PB2001-101840

Seismic Rehabilitation of Concrete Bridges: Verification Using In-Situ Tests at South Temple Bridge on Interstate 15

Final Report

Chris P. Pantelides, Ph.D., P.E.

Janos Gergely, Ph.D., P.E.

Nicole Marriott, M.Sc.

and

Lawrence D. Reaveley, Ph.D., P.E.

THE UNIVERSITY OF UTAH

Research Report UUCVEEN 00/1
Department of Civil & Environmental Engineering
University of Utah
Salt Lake City, UT 84112

July 2000

Seismic Rehabilitation of Concrete Bridges: Verification Using In-Situ Tests at South Temple Bridge on Interstate 15

Final Report

Chris P. Pantelides[1], Ph.D., P.E.

Janos Gergely[2], Ph.D., P.E.

Nicole Marriott[3], M.Sc.

and

Lawrence D. Reaveley[4], Ph.D., P.E.

[1]Professor, Department of Civil and Environmental Engineering, University of Utah, Salt Lake City, Utah 84112

[2]Assistant Professor, Department of Civil Engineering, University of North Carolina, Charlotte, North Carolina 28223

[3]Research Assistant, Department of Civil and Environmental Engineering, University of Utah, Salt Lake City, Utah 84112

[4]Professor, Department of Civil and Environmental Engineering, University of Utah, Salt Lake City, Utah 84112

FORWARD

University of Utah researchers, Professor Chris Pantelides and Professor Lawrence Reaveley, initiated a research effort after obtaining a grant from the National Science Foundation to perform research on lateral load testing of bridges retrofitted with carbon fiber composite materials. This funding was matched by the Federal Highway Administration, the Utah Department of Transportation, the Idaho National Engineering and Environmental Laboratory, and the University of Utah. The research included in-situ testing of a Bridge on Interstate 15 in Salt Lake City, using advanced carbon fiber composite materials. Principal Investigator for the project was Professor Chris Pantelides and Co-Principal Investigator was Professor Lawrence Reaveley, both of the Department of Civil & Environmental Engineering. The opportunity arose for testing actual bridges due to the Interstate 15 corridor reconstruction, which was already in progress. Dr. Janos Gergely was a Ph.D. candidate during the project, and is currently an Assistant Professor at the University of North Carolina, Charlotte. Nicole Marriott is a M. Sc. graduate student at the Civil Engineering Department of the University of Utah.

This document constitutes the Final Report for the in-situ tests of the South Temple Bridge at Interstate 15. The research was supported by a number of sponsoring agencies: Utah Department of Transportation, Federal Highway Administration, National Science Foundation, Idaho National Engineering and Environmental Laboratory, and University of Utah. In-kind support was provided by Geopier Foundation Company, Inc., and XXsys Technologies, Inc. The authors are also grateful to Wasatch Constructors for allowing them to perform the composite retrofit and lateral load tests during construction of the new Interstate 15 bridges.

This document is complemented by the following research reports:

1. Pantelides, C.P., and Reaveley, L.D. (1999). "In-Situ tests at South Temple Bridge on Interstate 15 – *Construction Report*", Research Report UUCVEEN 99-01, Feb. 1999, pp. 78.

2. Pantelides, C.P., Reaveley, L.D., and Gergely, J. (1999). "In-Situ tests at South Temple Bridge on Interstate 15 – *Interim Report*", Research Report UUCVEEN 99-03, Apr. 1999, pp. 36.

3. Cook, C., Lawton, E. C., and Pantelides, C.P., (2000). "Soil structure-interaction effects on bridge bent tests at South Temple Bridge on Interstate 15", Research Report CVEEN 00/2, July 2000.

ACKNOWLEDGEMENTS

The authors would like to thank the following individuals for their support and encouragement throughout this project. Mr. Doug Anderson, Mr. Sam Musser, and Dr. Steve Bartlett of the Research Division of the Utah Department of Transportation; Mr. James D. Cooper of the Federal Highway Administration, Dr. S. C. Liu of the National Science Foundation, and Mr. Bill Richins of the Idaho National Engineering and Environmental Laboratory.

The authors would like to thank the following individuals for their contribution to the success of the project: Mr. Yasuteru Okahashi, Ph.D. candidate, Mr. Vladimir Volnyy, Mr. Chris Hofheins, Mr. Paul McMullin, and Mr. Gavin Fitzsimmons, M.Sc. students at the University of Utah, and Mr. Shawn Black, undergraduate student at the University of Utah.

In addition, the following individuals made significant contributions to the project. Dr. Larry Cercone, Dr. Suresh M. Menon, and Mr. Frederick A. Policelli, Mr. Reinhard Ruf Safety Coordinator of the Utah Department of Transportation, Mr. Brian Welty of Valley Systems, Mr. Jim Reed and Mr. Jim Pudgett of Utah Corrections and Mr. David Blackbird of Penhall Company.

TABLE OF CONTENTS

LIST OF FIGURES

LIST OF TABLES

1. INTRODUCTION

In-situ tests of bridges allow verification of design methods and establishment of capacities for loads up to failure. This knowledge contributes to better designs for new bridges and better rehabilitation techniques for existing bridges. The lateral load capacity of bridges is of interest due to potential catastrophic failures in large earthquakes. Recent earthquakes such as the one in Loma Prieta in 1989, in Northridge in 1994, and in Kobe in 1995, have repeatedly demonstrated the vulnerabilities of older reinforced concrete bridges to seismic deformation demands. While experimental validation of retrofit concepts for such bridge columns exists (Priestley et al. 1996, Seible et al. 1997), full-scale in-situ tests of retrofitted bridge bents are rare.

In the Northridge earthquake of January 17, 1994, the primary cause of all collapse and major damage can be summarized as insufficient ductility in the bridge structural frames (Zelinski 1999). Most of the damage occurred within a zone bounded by a minimum of 0.25g ground surface shaking. The maximum horizontal ground acceleration in the Northridge earthquake was 0.91g, whereas the Caltrans design criteria for the maximum credible event for a bridge with period of 0.8 s is 2.5g. All bridge structures in the region of strong ground motion shaking during the 1994 Northridge earthquake, that were retrofitted since the 1989 Loma Prieta earthquake performed adequately without damage requiring repairs, thus demonstrating the validity of the adopted Caltrans retrofit procedures (Seible and Priestley 1999). The retrofitted structures as a whole resisted the earthquake motions much better than the unretrofitted structures. Assessment analyses, performed on the six bridges that collapsed due to column failure, showed that collapse of these bridges could have been prevented if existing column retrofit technology would have been implemented at the time of the 1994 Northridge earthquake.

In the 1995 Kobe earthquake, it was found that lateral reinforcement in the columns was spaced relatively far apart, and moreover the lateral bars were spliced at the corners. The arrangement of the lateral bars was not conducive to effective confinement of the rectangular section; there were no cross ties running through the thickness of the column to prevent outward buckling of longitudinal bars on the faces of the columns (Taylor 1999). Thus, because the volumetric ratio of lateral reinforcement was low, and the bars were not arranged for effective confinement or shear resistance, a plastic hinge could not be formed, and the columns exhibited a catastrophic shear failure. Therefore, not only must a sufficient quantity of confining reinforcement be present, but also the closure details of the hoops must be appropriate for developing confinement of the concrete core.

Lessons from recent earthquakes have modified the design concepts used in reinforced concrete bridges that are expected to resist significant earthquakes. The California Department of Transportation has adopted a ductile design philosophy, since developing the current seismic design specifications in 1973 (Roberts 1999). Seismic lateral forces are reduced using reduction factors based on ductility inherent in the structural framing of the bridge. However, joint displacements are not reduced from those actually calculated from the dynamic analysis. An acceptable design procedure is to allow local and controlled yielding at the base or top of columns, as plastic hinges. The ductility prevents the development of brittle failures and is helpful in retrofitting older existing bridges. Today, all main reinforcing in the columns is continuous into the footings and the superstructure; splices are not permitted in the plastic hinge zones.

In-situ tests of bridges have included dynamic tests for system identification and design evaluation of bridges (Douglas and Reid, 1982; Saiidi and Douglas, 1984), quick-release tests performed in the Dominion Road bridge in New Zealand (Buckle et al., 1989), and tests performed at the Meloland Road overpass in California (Douglas et al., 1990). A three span segment of the standing portion of the Cypress Street viaduct was instrumented and tested for evaluating retrofit techniques, including addition of external post-tensioning rods to each bent cap, and placement of external shear reinforcement over the column clear height. It was found that retrofitting had little effect on overall lateral stiffness but increased strength and displacement ductilities (Bollo et al., 1990). In-situ lateral load testing of a bridge in Washington was shown to be a feasible means of obtaining data on its large-displacement behavior (Eberhard et al., 1992). More recently, full-scale tests of reinforced concrete circular columns were performed in St. Louis (Gamble and Hawkins, 1996). Several columns were tested in the as-built condition, after being retrofitted with tensioned steel bands, or glass FRP (Fiber Reinforced Polymer) advanced composite jackets. All of the retrofits functioned properly, and prevented the lap splices from failure at significant force and deformation levels.

Rehabilitation techniques involving steel jacketing, concrete jacketing, and FRP advanced composite jackets for columns have been developed at the University of California San Diego (Priestley et al., 1996). Various circular and rectangular columns with carbon FRP advanced composite retrofits were tested in the laboratory (Seible at al. 1997). These retrofitted columns exhibited stable hysteretic load-displacement behavior up to large displacement ductilities, while maintaining a constant load capacity level without significant cyclic capacity degradation. The tests showed that the carbon FRP advanced composite jacket was as effective as a comparable steel jacket system.

Plate bonding technology, i.e. bonding plates externally on the surfaces of concrete members, is a structurally efficient method for rehabilitating beams for flexure and shear. Steel plates have initially been the natural choice for such rehabilitation work (Swamy and Gaul 1996), but FRP composites have also been used for strengthening reinforced concrete beams. Flexural strengthening of RC beams with glass FRP advanced composite plates was performed by Saadatmanesh and Ehsani (1991). The behavior of pre-cracked RC beams strengthened with carbon FRP advanced composite sheets in four-point bending was investigated by Arduini and Nanni (1997).

The effectiveness of externally applied advanced FRP composites in improving the shear capacity of RC beams was studied by Chajes et al. (1995). An increase in the beam ultimate strength of 50% to 150% was achieved. Norris et al. (1997) have studied the shear and flexural strengthening of RC beams with carbon FRP advanced composite sheets. Triantafillou (1998) studied the shear strengthening of RC beams using externally epoxy bonded FRP advanced composites. The failure of the beams was due to the advanced composite's delamination from the concrete surface at very low composite strain levels which was less than 0.17%. Malek and Saadatmanesh (1998) have quite recently studied the ultimate shear capacity of RC beams strengthened with web-bonded FRP advanced composite plates.

Experimental studies (Priestley et al. 1997) show that older RC concrete joints do not meet the confinement and shear reinforcement details specified in the ACI Committee 352R-91 recommendations (1991). Methods available for strengthening these weak joints include: (1) jacketing of the joint region (Alcocer and Jirsa 1993); (2) joint section increase with special dowels and post-tensioning rods (Lowes and Moehle 1995); (3) post-tensioning of the beam combined with fiberglass wraps on the beam and column (Sexsmith et al. 1997); and (4) corrugated steel jacketing of the beam-column connection (Biddah et al. 1997). Retrofit of RC joints using FRP advanced composites has not received much attention. Three columns, the beam cap, and the joints of the Highland Drive Bridge at Interstate 80 in Salt Lake City were wrapped with carbon FRP advanced composites in September 1996. The bridge was in service during the retrofit. The details of the field application were presented by Pantelides et al. (1997); the analytical techniques for the retrofit design and comparison with full-scale experiments of similar joints are presented elsewhere (Gergely et al. 1998). Detailed procedures for improving the shear capacity of RC T-joints using FRP advanced composites were recently established (Gergely et al. 2000).

As part of the Interstate 15 reconstruction project, 17 miles of I-15 in Salt Lake City are currently being replaced. The reconstruction is a $1.6 billion project and it involves the demolition and reconstruction of 142 bridges. This provided an opportunity to test two bents of the old freeway at the South Temple Bridge. The bridge under consideration was designed and built in 1962, before the 1971 San Fernando earthquake, and was missing the basic reinforcement and reinforcement details necessary to provide adequate lateral load capacity and ductility. These reinforced concrete bents presented several deficiencies, among which the seismic and corrosion related problems were the most serious. Three in-situ tests were performed on the South Temple Bridge bents at Interstate 15 before their demolition: (a) test of a bent in the as-built condition (Bent #5), (b) test of a bent rehabilitated with FRP advanced composites (Bent #6), and (c) test of the repaired Bent #5 rehabilitated with FRP advanced composites (Bent #5R). The report describes the results for in-situ tests (a), (b) and (c) of the as-built Bent #5, the rehabilitated Bent #6, and the repaired Bent #5R, respectively. The purpose of the tests was to evaluate the capacity of the existing bridges which were not built to current seismic codes, assess the performance of such bridges for credible earthquake events that could occur in Salt Lake City, and demonstrate the ability of advanced composite materials to restore structural integrity and improve resistance to seismic loading. Specifically, the FRP advanced composite retrofit of Bent #6 was designed to double the displacement ductility of the bent in the as-built condition. The FRP advanced composite design considered the shear capacity of the beam cap-column joints, beam cap and columns; the confinement of the plastic hinge zones of the columns and cap-beam; and the lap splice region clamping of the columns. In addition to evaluation of the as-built Bent #5 and the retrofitted Bent #6, a third evaluation was performed on the repaired Bent #5R. This represents a simulation of the performance of a bridge bent that was damaged in a previous earthquake and then was repaired and rehabilitated with FRP composites.

2. OBJECTIVES OF THE RESEARCH

The objectives of the in-situ tests were to: (a) determine the capacity of the bent in the as-built condition (test of Bent #5); (b) determine the improvement in strength and ductility of the undamaged bent with the FRP advanced composite retrofit (test of Bent #6); and (c) demonstrate that repair of a damaged bridge bent with FRP composites is feasible (test of Bent #5R); this damage could have occurred after an earthquake and the transportation agency might decide to repair a bridge rather than demolish it. In addition to evaluation of capacity of the bents in the three in-situ tests described above, the study has as its objective to determine the seismic demand on a typical bent for earthquakes which are likely to occur in Salt Lake City. The final objective was the assessment of the experimental results with respect to expected performance predictions according to current seismic codes.

Two bents (Bent #5 and Bent #6) and the deck between them, which were part of the Northbound lanes of the South Temple Bridge at I-15 in Salt Lake City, were made available for testing prior to demolition. The bents were identical, composed of three columns and a beam cap, and are classified as multi-column bents. The layout of the bents used in the tests is shown in Fig. 1. The figure shows the elevation and plan of the portion of the bridge that was made available for testing between Bents #5 and #6. The elevation of Bent #5 and Bent #6 and the deck, after demolition of the remaining South Temple Bridge, are shown in Fig. 2. The columns are square in cross-section and are relatively flexible with a length to width ratio approximately equal to 8. The exterior pile caps are supported by four piles while the interior cap is supported by five piles. The beam cap has a cross-section, which is 3 ft (914 mm) wide and 4 ft (1219 mm) deep except at the two cantilever portions where it tapers to a 3 ft x 3 ft (914 x 914 mm) section.

A picture of the bridge standing after demolition of the remaining bridge is shown in Fig. 3. Bent #6 is the one closest to the viewer and Bent #5 is the one furthest from the viewer. It should be noted that the southbound lanes of the South Temple Bridge at Interstate 15 were operational as can be seen in this figure. In addition, work on the new South Temple Bridge for the new Interstate 15 was well on its way. As a consequence, time constraints were imposed on the completion of the three in-situ tests. The three tests are shown graphically in Fig. 3.

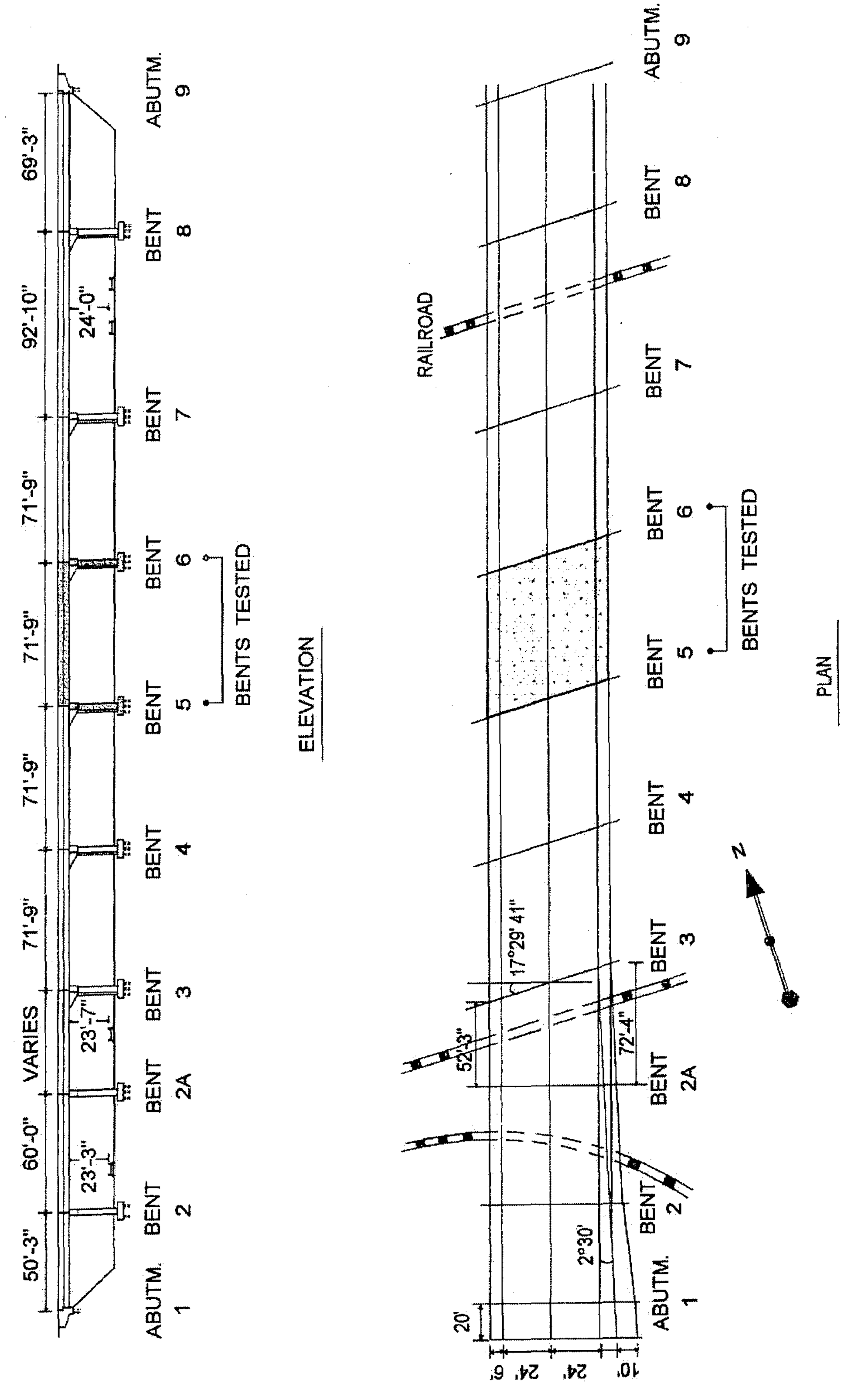

Figure 1. Northbound lanes of South Temple Bridge at Interstate 15 (1'=305 mm, 1"=25.4 mm)

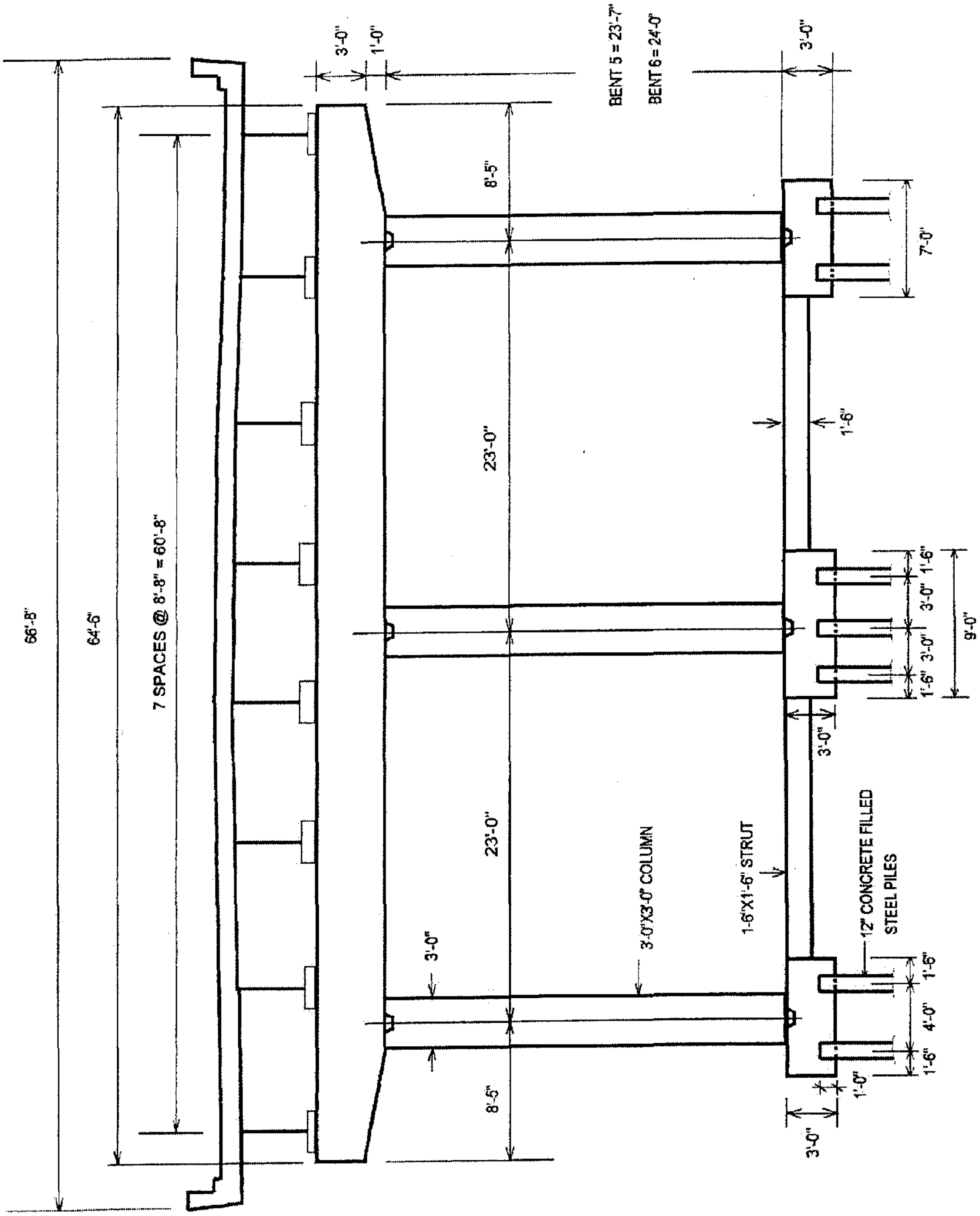

Figure 2. Elevation of Bent #5 and Bent #6 of South Temple Bridge at Interstate 15
(1'=305 mm, 1"=25.4 mm)

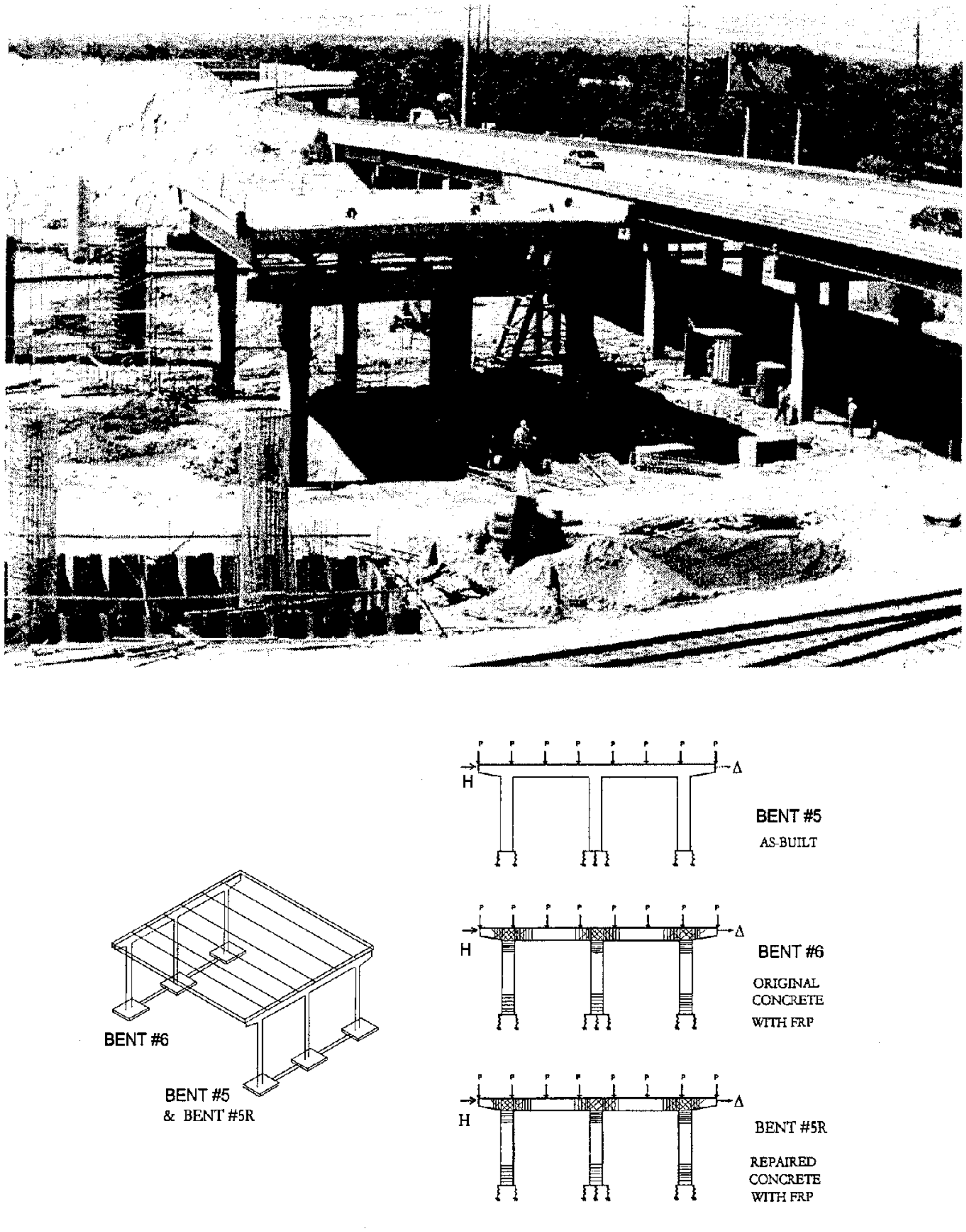

Figure 3. Bent #5, Bent #6, and the deck between the two bents on the Northbound lanes of South Temple Bridge at I-15: The three tests corresponding to Bent #5, #6 and #5R

3. CONDITION OF BENT #5 AND BENT #6 PRIOR TO IN-SITU TESTING

The South Temple Bridge at Interstate 15 was built in 1963, before the existence of any seismic codes. The bridge was designed for gravity loads as well as wind loads which met the requirements of the prevailing code. As such, the bridge bents had several deficiencies as can be seen by examining the reinforcement details shown in Fig. 4 and Fig. 5. These deficiencies include the confinement of the column reinforcement in the plastic hinge regions, the anchorage of the column reinforcement into the beam cap on the top and the pile cap on the bottom, the shear reinforcement at the top of the pile cap, the embedment of the reinforcement from the piles to the pile cap, the size and reinforcement of the grade beam connecting the pile caps, the column splice lengths, and the inadequate reinforcement in the beam cap and pile cap joints.

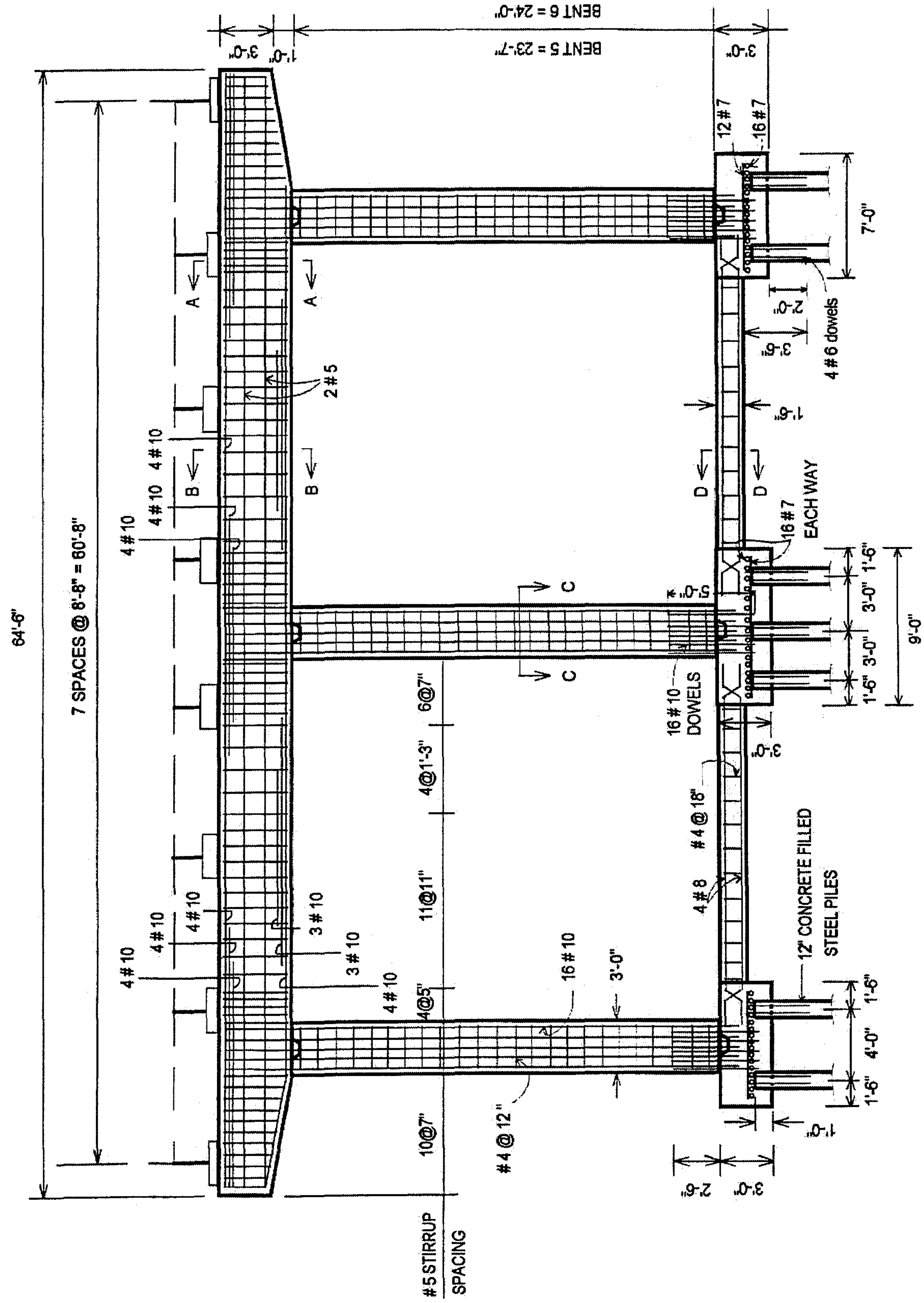

Figure 4. Reinforcement details for Bent #5 and Bent #6 (1'=305 mm, 1"=25.4 mm)

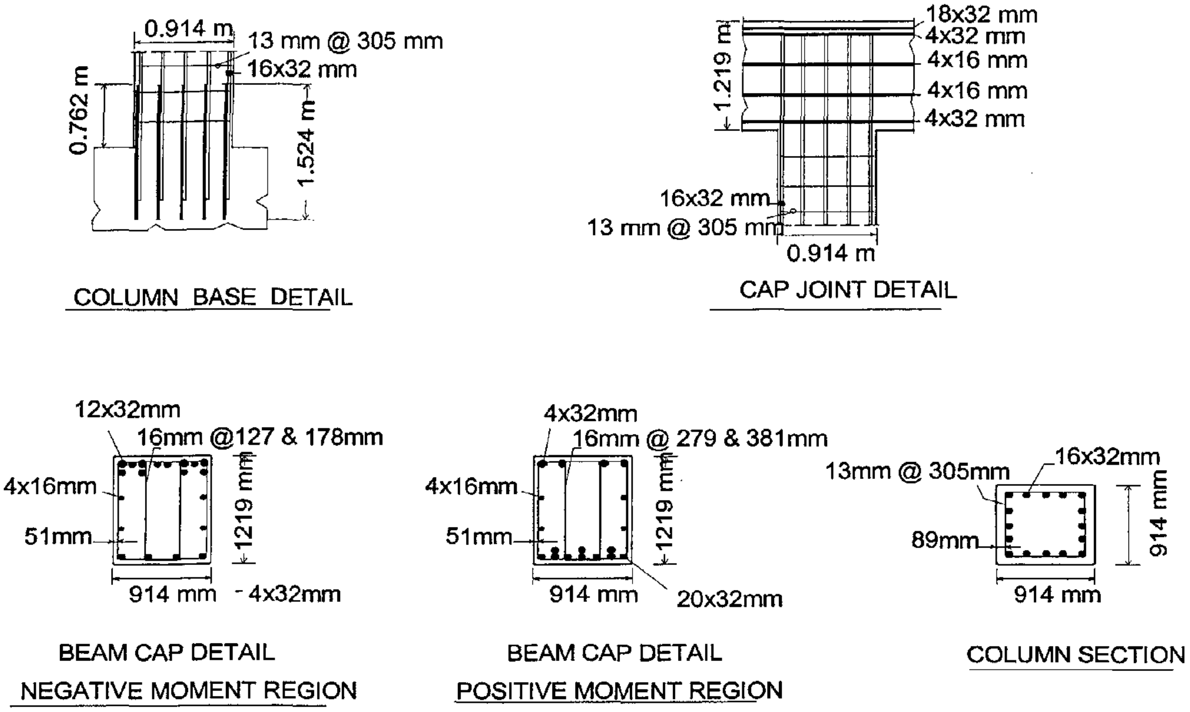

COLUMN BASE DETAIL

CAP JOINT DETAIL

BEAM CAP DETAIL
NEGATIVE MOMENT REGION

BEAM CAP DETAIL
POSITIVE MOMENT REGION

COLUMN SECTION

Figure 5. Column and beam cap cross-sections

Corrosion of Bent #5 and Bent #6 at South Temple Bridge

The amount of corrosion of the reinforcement is important for evaluating the remaining capacity of bridge bents. At the South Temple Bridge site, all of the beam caps had some corrosion, including the bents to be tested, as well as those that were not tested as part of this research. There was no obvious sign of corrosion in the columns of Bents #5 and #6. It is interesting that the majority of the observed corrosion occurred in the stirrups of the beam cap. There was only one observed occurrence of corrosion in the longitudinal column bars at one of the joints of Bent #6, as shown in Fig. 6. The diameter of the bar, which was originally 31 mm, was reduced to 30 mm. It should be noted, that the corrosion was visible at the north, south and bottom sides of the beam caps, where the concrete had spalled. Corrosion was present at the topside of the beam cap; however, the concrete was still in place and only after removal of the concrete cover with hydro blasting was the corrosion visible.

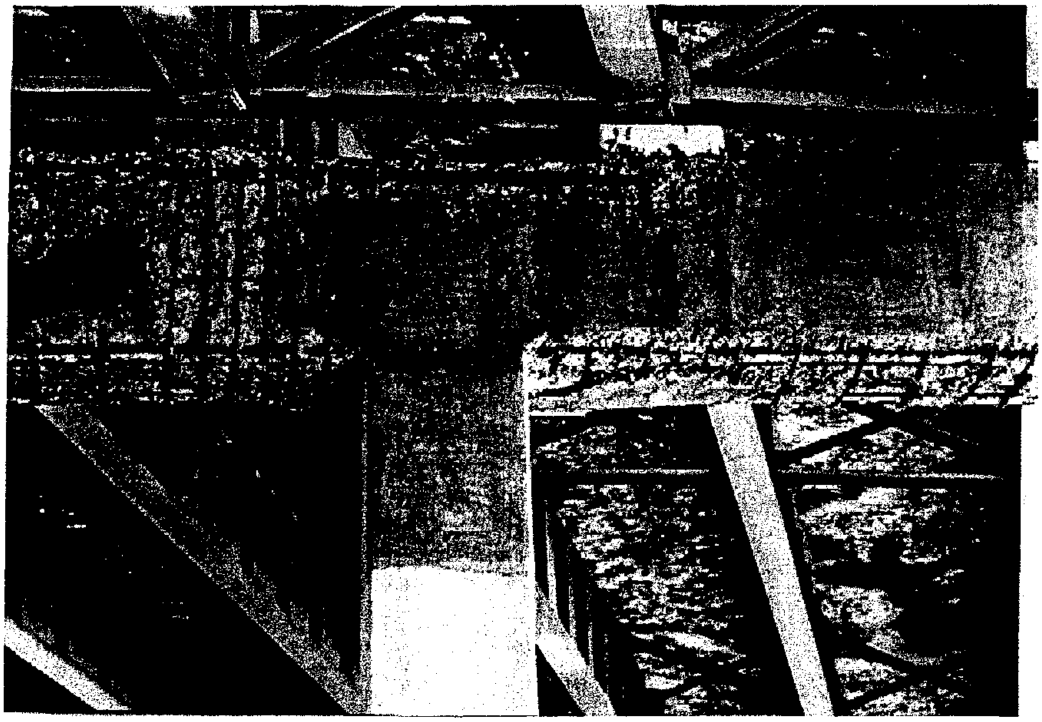

Figure 6. Corrosion in the beam cap of Bent #6

An analysis of the corrosion level is presented in what follows. The condition of a typical corroded bar is shown in Fig. 7.

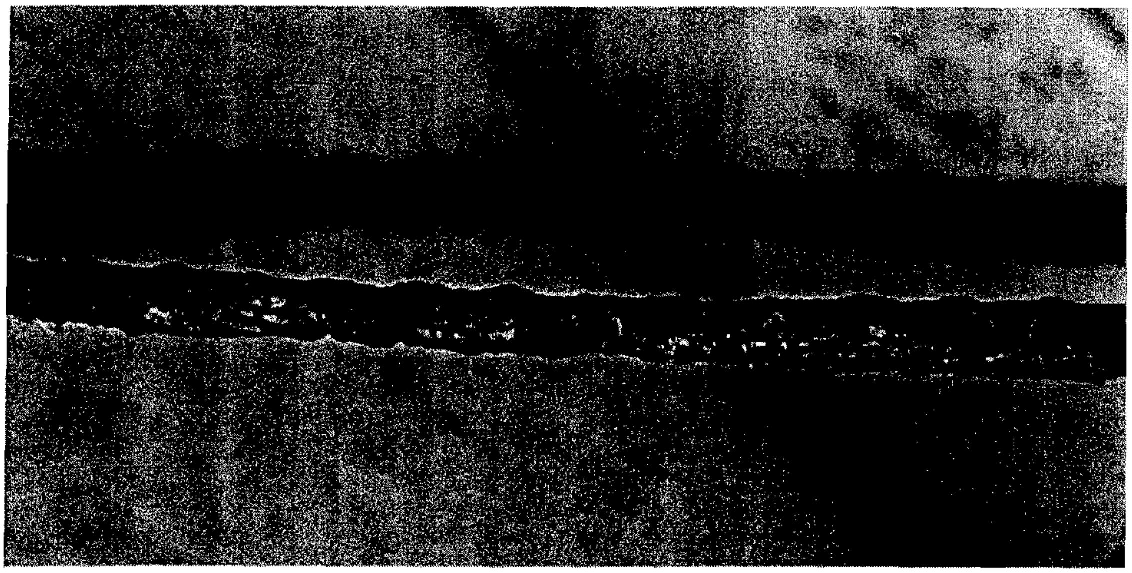

Figure 7. Close-up of corroded rebar from Bent #6

It should be noted that the beam caps were reinforced with double stirrups as shown in Fig. 5 and that the observed corrosion relates to the external legs of these stirrups. The original diameter of the stirrups was 16 mm (#5 bar). The measurements include the length of the exposed portion of the stirrups, as shown by the length of the lines in Figs. 8 and 9, and the loss of the area of the stirrups, expressed in terms of the remaining diameter of the stirrup. The notation used in Figs. 8 and 9 for expressing the remaining diameter of the stirrup is as follows:

Table 3.1. Notation for corrosion of reinforcement in beam cap

SYMBOL	DIAMETER RANGE (mm)	CROSS-SECTIONAL AREA RANGE (mm^2)	PERCENT LOSS OF CROSS-SECTIONAL AREA (%)
a	15 → 16	189	5
b	14 → 15	165	17
c	13 → 14	143	28
d	12 → 13	123	38
e	11 → 12	104	48
f	10 → 11	87	56
g	9 → 10	71	64
h	8 → 9	57	71
i	7 → 8	44	78
j	6→ 7	33	83
k	5 → 6	24	88

The two bents had a similar amount of corrosion. A detailed summary for each bent is presented below, as well as the effect of the observed corrosion on the shear capacity of the beam cap. The following assumptions are made in compiling the data: (1) the topside of the beam cap has identical corrosion as the bottom side, which is shown in Figs. 8 and 9, (2) even though the length of the exposed stirrup is drawn in Figs. 8 and 9, it is assumed that the total length of the stirrup on that face of the beam cap is corroded; this assumption was verified after hydro blasting.

Table 3.2. Corrosion of reinforcement for the bam cap of Bent #5 at South Temple Bridge

SYMBOL	NORTH FACE (NUMBER)	SOUTH FACE (NUMBER)	BOTTOM (NUMBER)
a	6	6	-
b	1	1	15
c	-	3	11
d	11	1	3
e	13	5	4
f	-	-	-
g	4	3	-
h	-	1	-
i	-	-	-
j	-	1	-
k	-	1	-
% TOTAL LOSS	19	12	12

Table 3.3 Corrosion of reinforcement for the bam cap of Bent #6 at South Temple Bridge

SYMBOL	NORTH FACE (NUMBER)	SOUTH FACE (NUMBER)	BOTTOM (NUMBER)
a	6	2	10
b	1	4	6
c	5	3	5
d	2	-	11
e	13	8	-
f	1	2	-
g	1	-	-
h	-	1	-
i	-	-	2
j	-	-	-
k	-	-	-
% TOTAL LOSS	14	10	12

It important to note that the actual shear capacity contributed by the stirrups is governed by the vertical area of the stirrups. Considering the vertical area of the stirrups reveals that Bent #5 shows an average loss of area of 15.5%, and Bent#6 an average loss of area of 12%. If one assumes that the same corrosion is possible for the interior stirrups, then these percentages represent the loss of shear strength contributed by the stirrups. This may be critical in the regions close to the column supports.

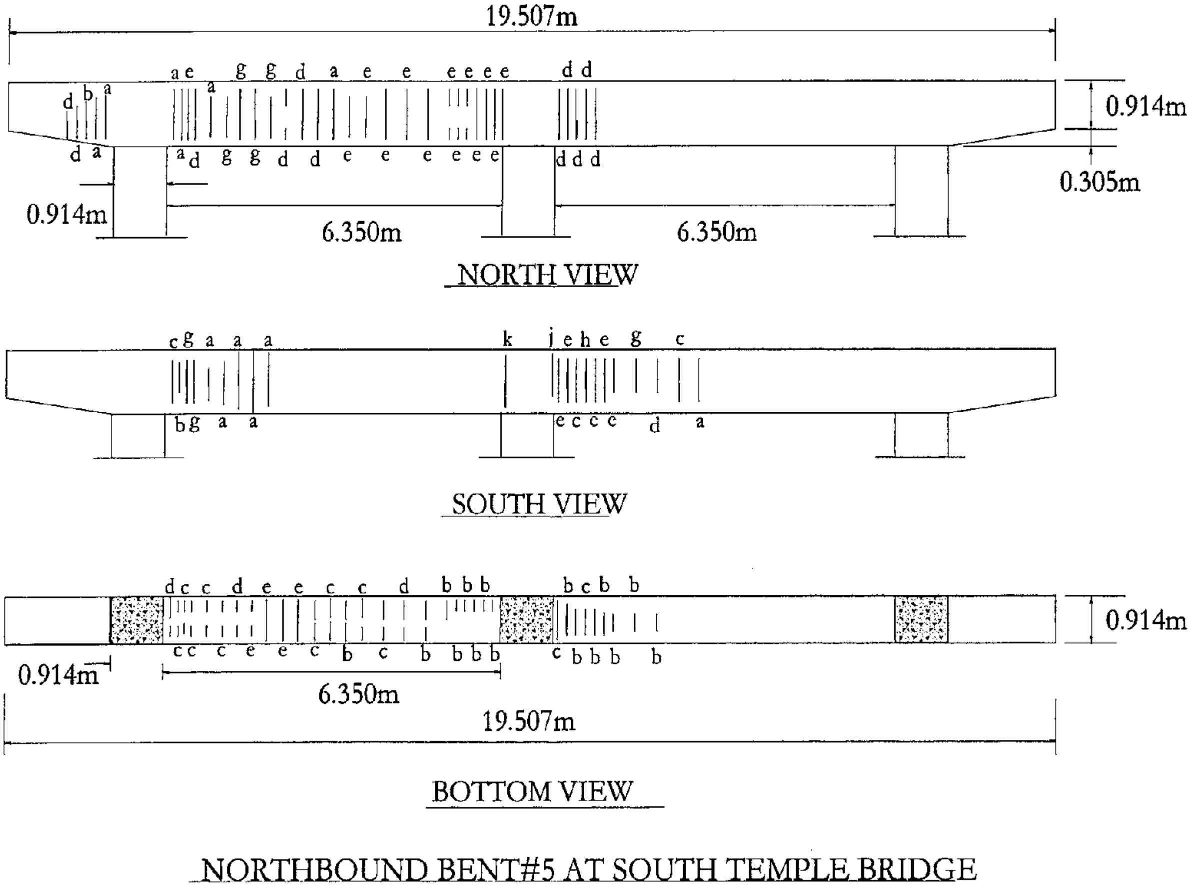

Figure 8. Corrosion map for Bent #5

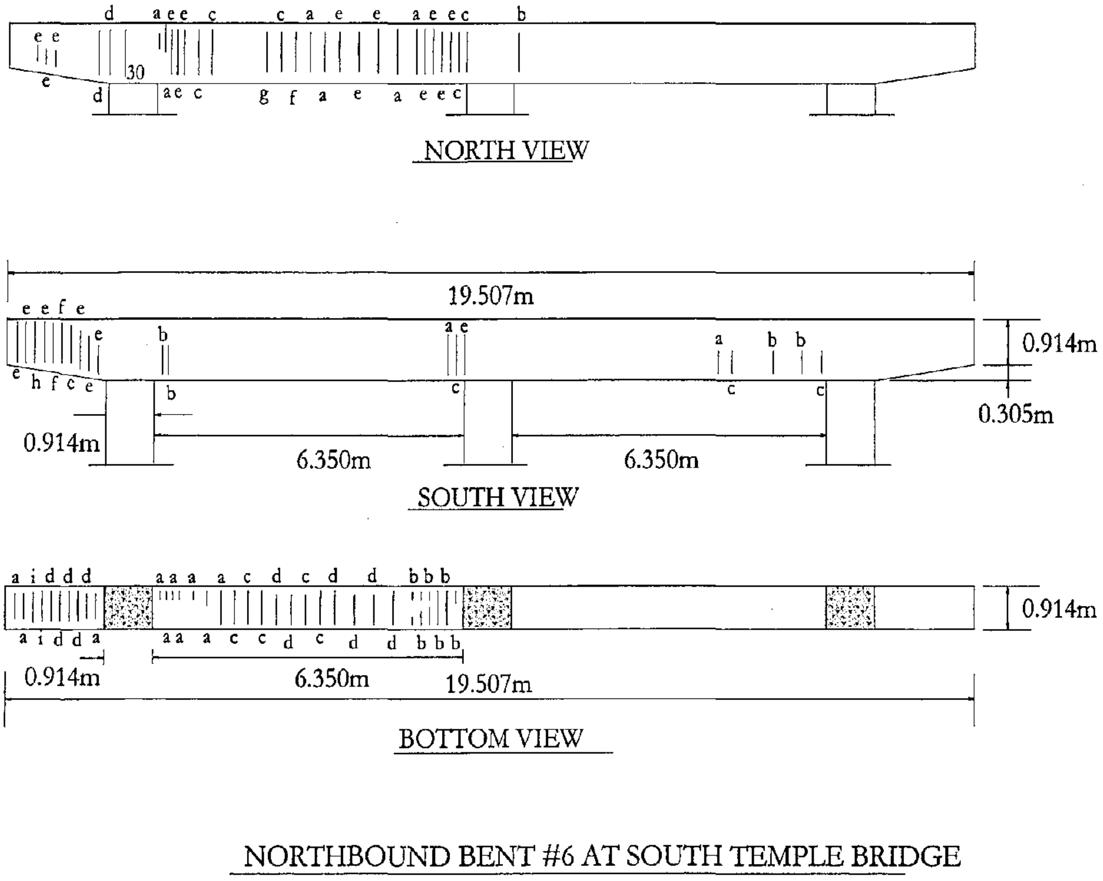

Figure 9. Corrosion map for Bent #6

4. MODIFICATION OF DECK SUPPORTS AND PIER FOUNDATION

Modifications were made to the substructure in order to resist the shear from application of the lateral load. The deck supports were also modified in order to perform the tests safely, without the danger of loosing support for the deck.

Modification of the Substructure

Each bent consisted of a beam cap and three columns, which were supported on three pile caps. Each of the exterior columns was supported on a 2.134 m square pile cap with four 0.305 m diameter concrete filled pipe piles. The center column was supported by a 2.743-m square pile cap with five piles. The piles had an average length of 19.81 m and were embedded into the 0.914 m thick pile cap a distance of 0.305 m as shown in Fig. 10. However, the connection of the piles to the pile cap consisted of four 19 mm bars (276 MPa yield strength) which extended only 0.305 m into the pile cap, as shown in Section A-A of Fig. 10. The capacity of these bars would be exceeded for the lateral loads anticipated in the test. In addition, the existing short bar anchorage would cause pullout failure of the piles. In order to avoid this, a 38-mm hole was cored through the pile cap and into the pile for a distance of 2.438 m as shown in Fig. 10 and Fig. 11. The pile was then anchored into the pile cap using a 32-mm Dywidag bar (1,030 MPa ultimate stress) epoxied into the hole. This detail was implemented for the four corner piles of the three pile caps.

Each of the pile to pile-cap connections was designed to transfer 100 kip (445 kN) from the pile-cap to each pile, even though analysis had shown that this was conservative. However, since failure of the pile to pile-cap connection could terminate the test, this conservatism was warranted. The ultimate strength of the 1.25 in (32 mm) diameter Dywidag bar is equal to the ultimate stress (specified by the manufacturer as 150 ksi (1030 MPa)) times the cross-sectional area of the bar which is 1.25 in^2 (806 mm^2), which equals 187 kip (833 kN); this is higher than the transfer design load of 100 kip (445 kN) by a factor of 1.87.

In addition to the strength of the bar, the development length was checked. The epoxy used to anchor the bar into the pile had a higher ultimate strength than the concrete; the nominal bond strength of the concrete controls the development length of the Dywidag bar and is given as:

$$u = \frac{9.5\sqrt{f_c'}}{d_b} \leq 800 \ psi \tag{4.1}$$

where u is the bond strength, d_b is the bar diameter of 1.25 in (32 mm) and f'_c is the compressive strength of the concrete which was conservatively assumed to be equal to the design strength of 3,000 psi (20 MPa). The development length is related to the nominal bond strength as:

$$L_e = \frac{P}{u \sum o} \tag{4.2}$$

where P = axial load of 100 kip (445 kN) and Σ_o is the bar perimeter = π d_b. From the information given above it was determined that the nominal bond strength is u = 416 psi < 800 psi , and that the required development length L_e = 61.2 in. (1555 mm). Therefore, the total length of the Dywidag anchor bar required is equal to the development length L_e plus the thickness of the pile cap of 36 in. (914 mm). This gives a total bar length of 97.2 in. (2469 mm). For convenience an 8 ft (2438 mm) length of the 1.25 in. (32 mm) Dywidag bar was provided for each pile. In addition, an A36 plate with a nut was used of dimensions 5x5x1.25 in. (127x127x32 mm) on top of the pile cap; the Dywidag bar was not post-tensioned.

The piles did not have adequate shear capacity to carry the lateral loads anticipated in the tests. For this reason, two 36 mm Dywidag bars (1,030 MPa ultimate stress) were connected by anchoring their ends to a wide flange beam on one side, and by casting them in the load frame footings on the other, as shown in Fig. 12; these Dywidag bars were not prestressed. The load for the test was applied at the top of the beam cap through a structural steel load frame specially designed for the test. The frame was 7.315 m high, 6.096 m long, and 1.829 m wide with the four legs resting on two footings. A concrete footing 2.515 m x 7.468 m in plan and 0.914 m deep supported two legs of the load frame. The frame footing was supported on ten geopiers of 0.914 m diameter that were 4.572 m deep. Geopiers are aggregate piers, which can support considerable pullout forces (Lawton et al. 1994). The load frame footings and horizontal Dywidag bars are shown in Fig. 13. A detail of the 32 mm Dywidag bars connecting the pile cap to the piles is shown in Fig. 14.

The bent was originally built with a 457 mm x 457 mm concrete strut linking the pile caps. The strut section had four 25 mm longitudinal bars (276 MPa yield strength), and nominal stirrups as shown in the dashed area of Section A-A of Fig. 12. In order to minimize lateral movement of the pile caps and complete the load path, the existing strut was widened with two sections of unreinforced concrete to carry the compression force as shown in Section A-A of Fig. 12. In addition, a 0.510-m long concrete strut reinforced with four 25-mm longitudinal bars, was used to join the pile cap to the load frame footing as shown in Section B-B of Fig. 12. The pile to pile-cap connections were reinforced using 32-mm Dywidag bars which were epoxied into the piles, and the concrete strut linking the pile caps was strengthened. As mentioned earlier, 36-mm Dywidag bars were used to connect the pile caps to the load frame footings to assist the piles in carrying the horizontal shear, as shown in Fig. 12.

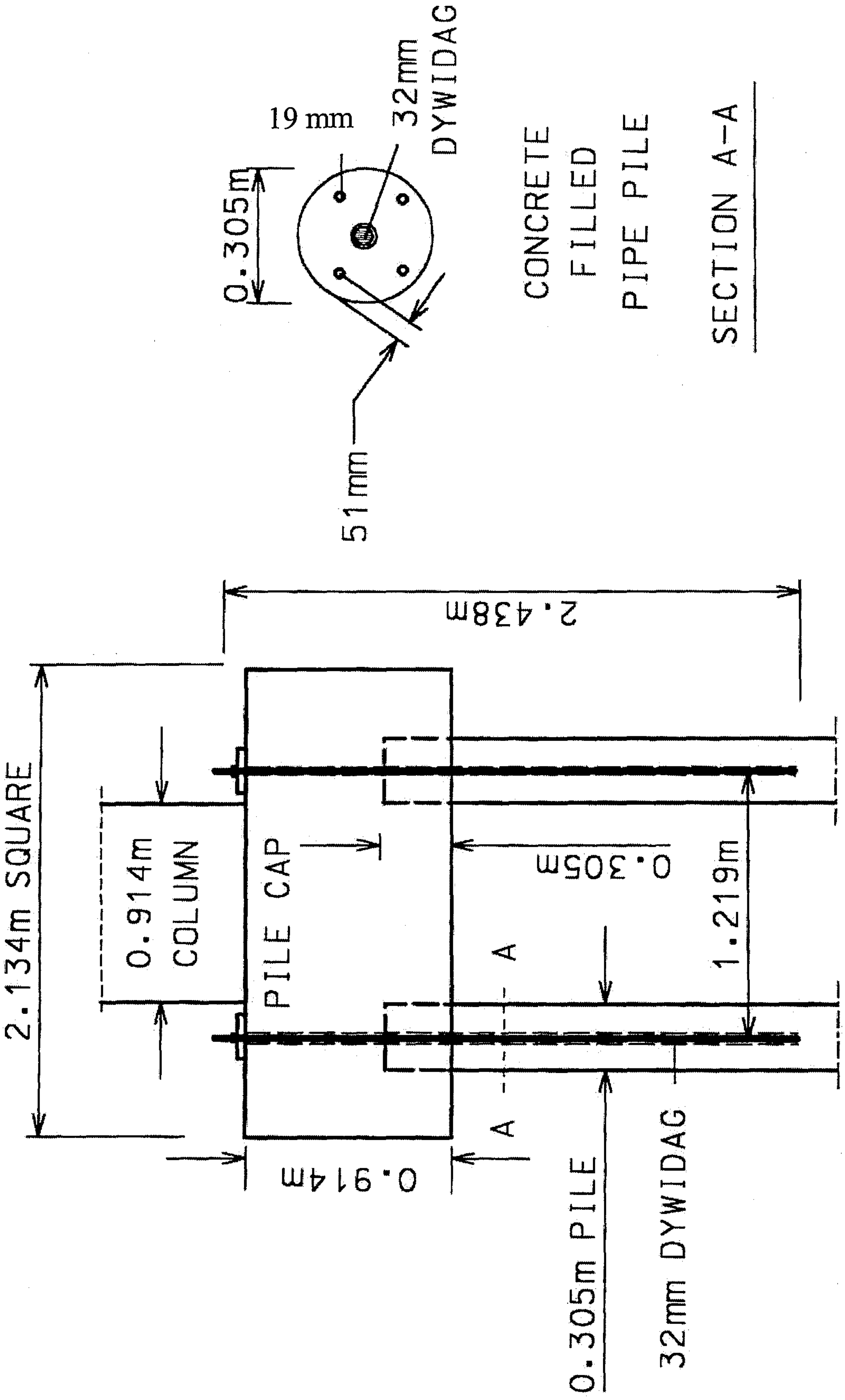

Figure 10. Detail of pile to pile cap connection

Figure 11. Driving the vertical Dywidag rods into the pile caps and piles

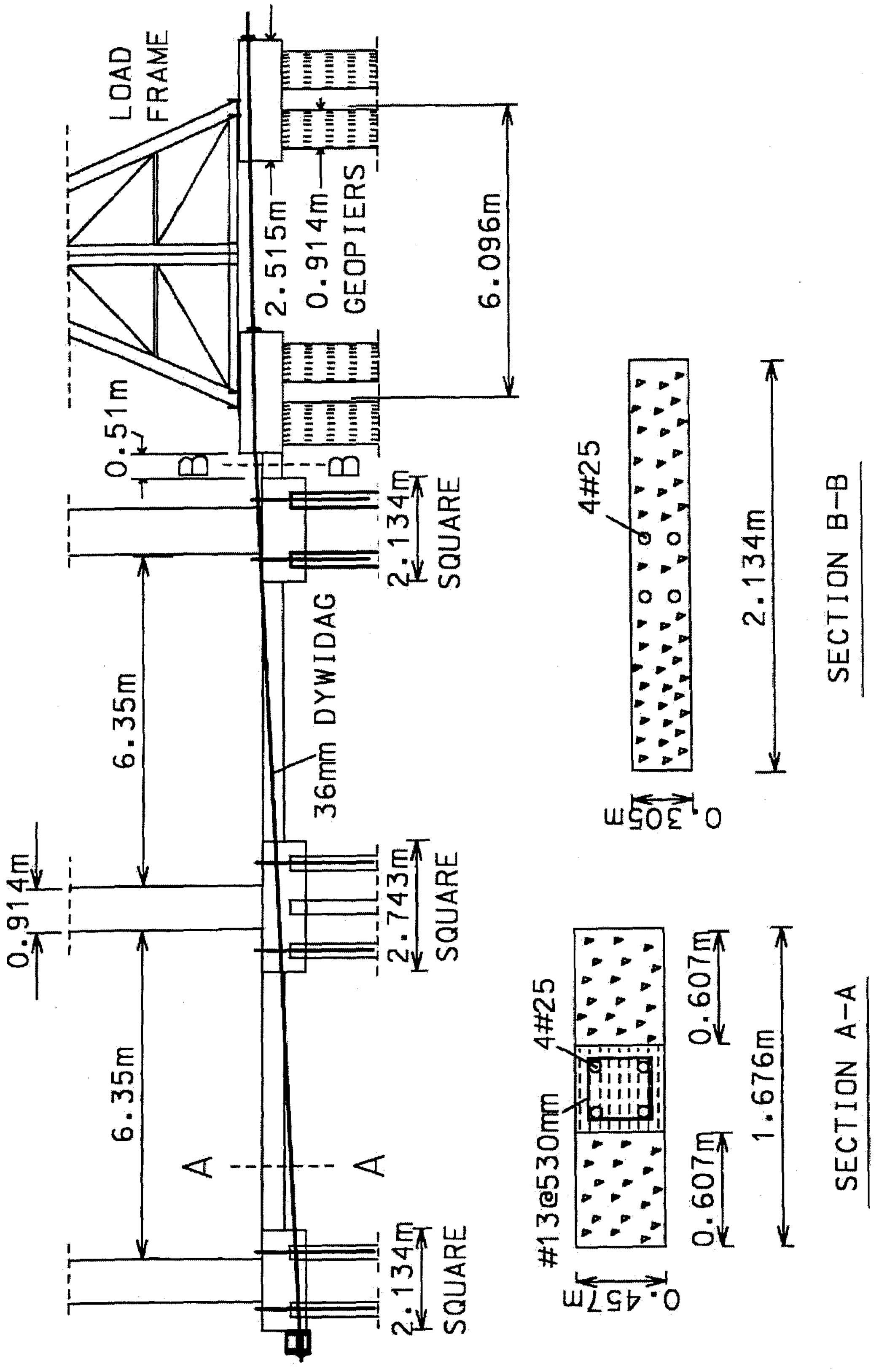

Figure 12. Detail of substructure arrangement and modifications

Figure 13. Detail of Geopier concrete cap and load frame support

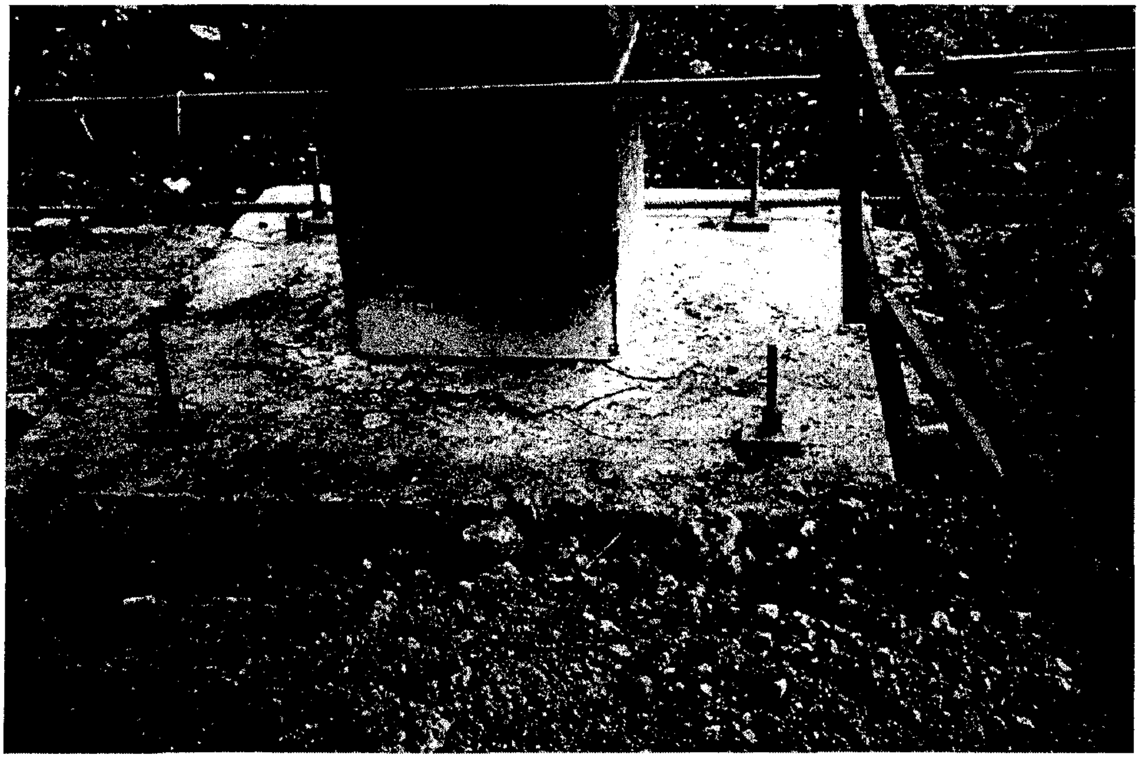

Figure 14. Detail of Dywidag bars in the pile cap

Modification of Deck Support Conditions

The composite deck was supported by eight steel plate girders. The original girder supports at Bent #5 were fixed by means of 254 mm x 102 mm x 152 mm steel bearing bars that were restrained by keeper plates on the top, and were welded at the bottom to 38 mm thick steel plates; the plates were anchored to concrete bearing pads using two 38 mm diameter steel anchors. The steel girder supports at Bent #6 were expansion bearings with the same details as those described for Bent #5, except that the bottoms of the bearing bars were restrained by keeper plates.

Consideration was given to the support conditions of the deck, which weighed approximately 3,840 kN. This weight was beneficial for the tests in that it provided approximately half the gravity load originally present, but it was also a serious concern for the following reasons: (a) the steel girders were resting on the beam cap at a skew angle of 17° 29' as shown in Fig. 15, (b) the concrete bearing pad supports were not in good condition, (c) some of the bearing bars were twisted or out of place. Analysis of the movement of the deck due to the imposed lateral loads, showed that the deck would not be able to withstand the large movements of the bents during testing, without the danger of losing support.

The support conditions of the deck were modified to "fixed" for Bent #5, and "roller" for Bent #6. The girder supports of Bent #5 were modified as shown in Detail "A" of Fig. 15. The bearing bar was welded on the top to the keeper plates, and a total of ten 13 mm diameter steel studs were welded to the top of the anchor plate and the bottom of the girder flange. Figure 16 shows details of the concrete support on top of Bent #5 shown as detail “A” in Fig. 15. The detail was completed by using a 10 mm closed stirrup as shown in Fig. 16. The bearing pad was enlarged by pouring additional concrete up to the bottom of the girder flange as shown in Fig. 17 and Fig. 18, which shows the finished supports. The girder supports of Bent #6 were modified as shown in Detail "B" of Fig. 15. The roller assembly consisted of two 102 mm diameter camyoke bearings as shown in Fig. 19. The girders were lifted one at a time, as shown in Fig. 20, the steel bearing bar was removed and in its place the roller assembly was welded to the bottom of the keeper plates. To complete the support conditions, a 25-mm steel plate, which was 305 mm wide and 1.118 m long, was welded on top of the steel plate to provide a "runway" for the roller assembly. The length of the plate was selected so that the maximum stroke of the actuator of ± 381 mm could be accommodated; the plate was supported by steel stiffener plates for carrying the vertical loads as shown in Fig. 21 and Fig. 22. The tests for the two bents proceeded with the testing of the as-built Bent #5 first, followed by testing of Bent #6 with the FRP advanced composite retrofit, and finally by testing the repaired Bent #5R.

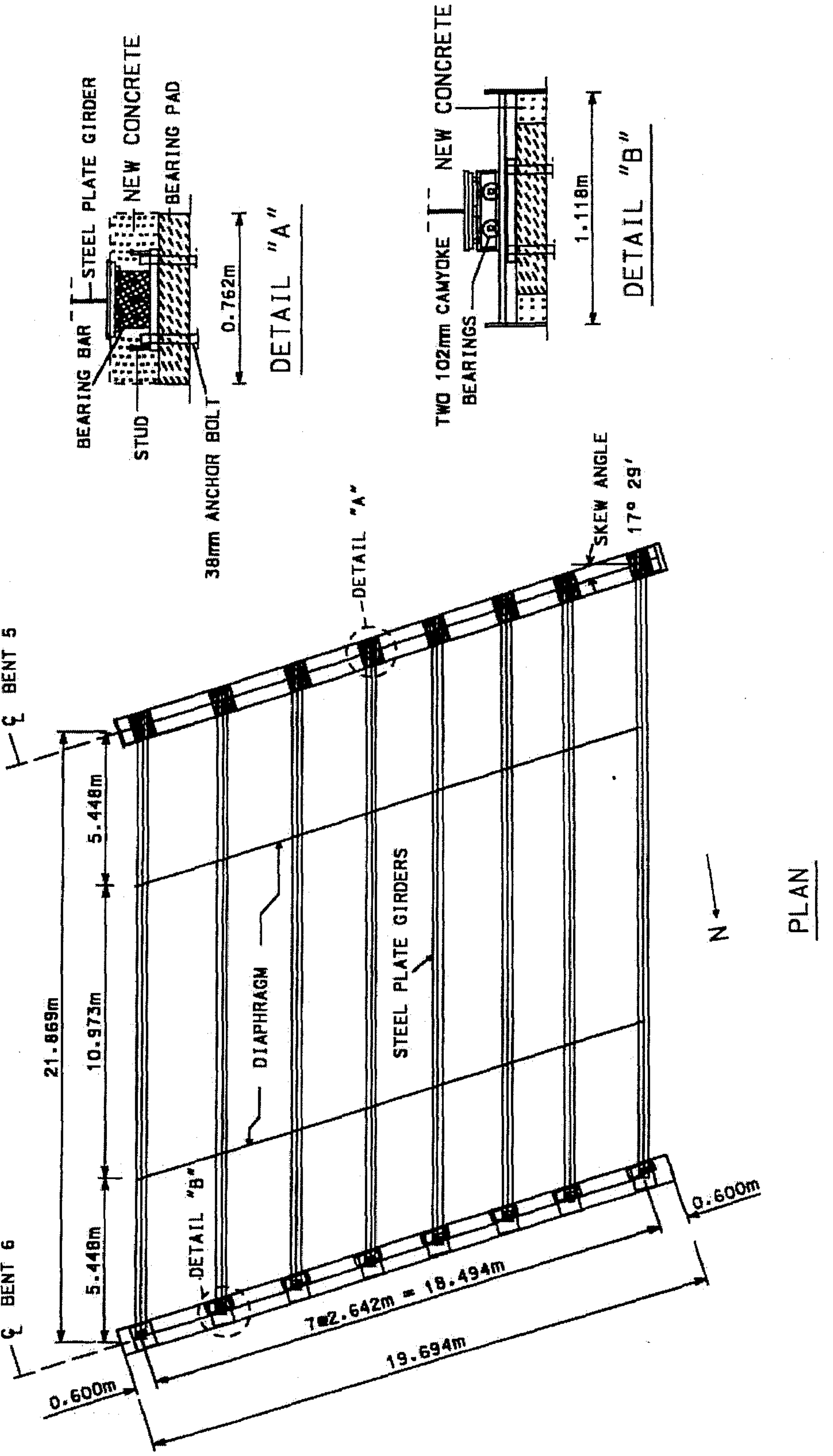

Figure 15. Plan of deck showing deck support modifications

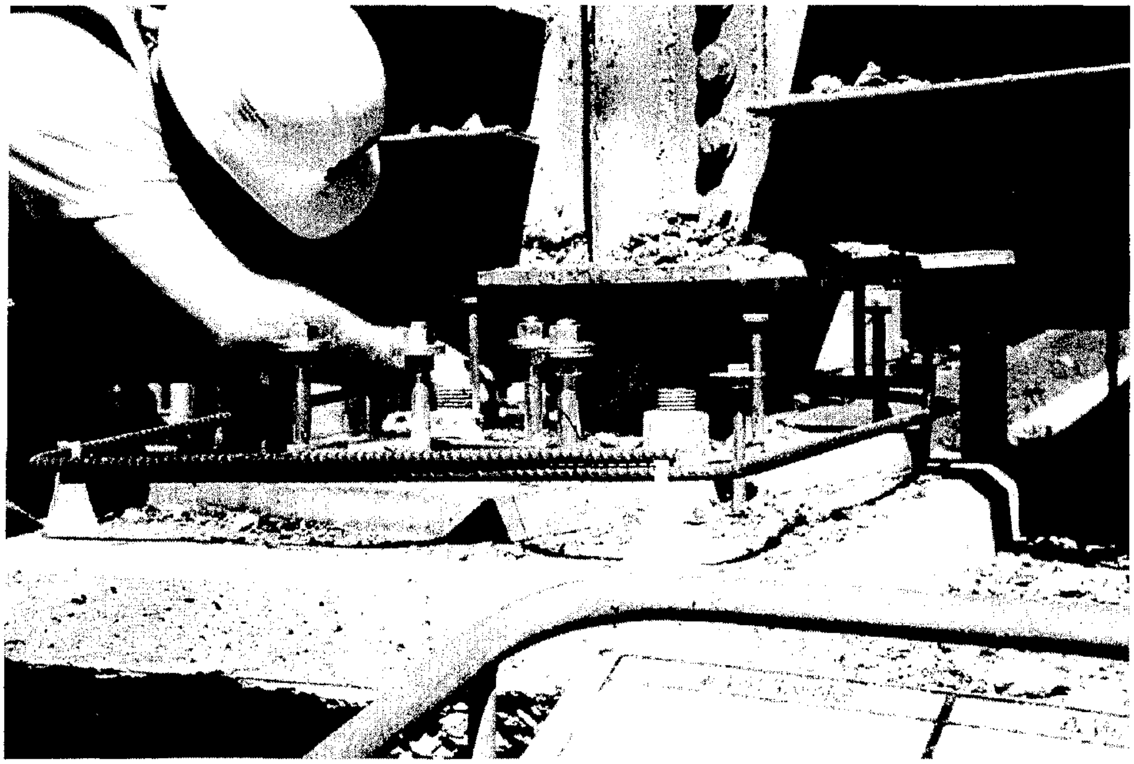

Figure 16. Detail of concrete support on top of Bent #5- Detail “A” in Figure 15

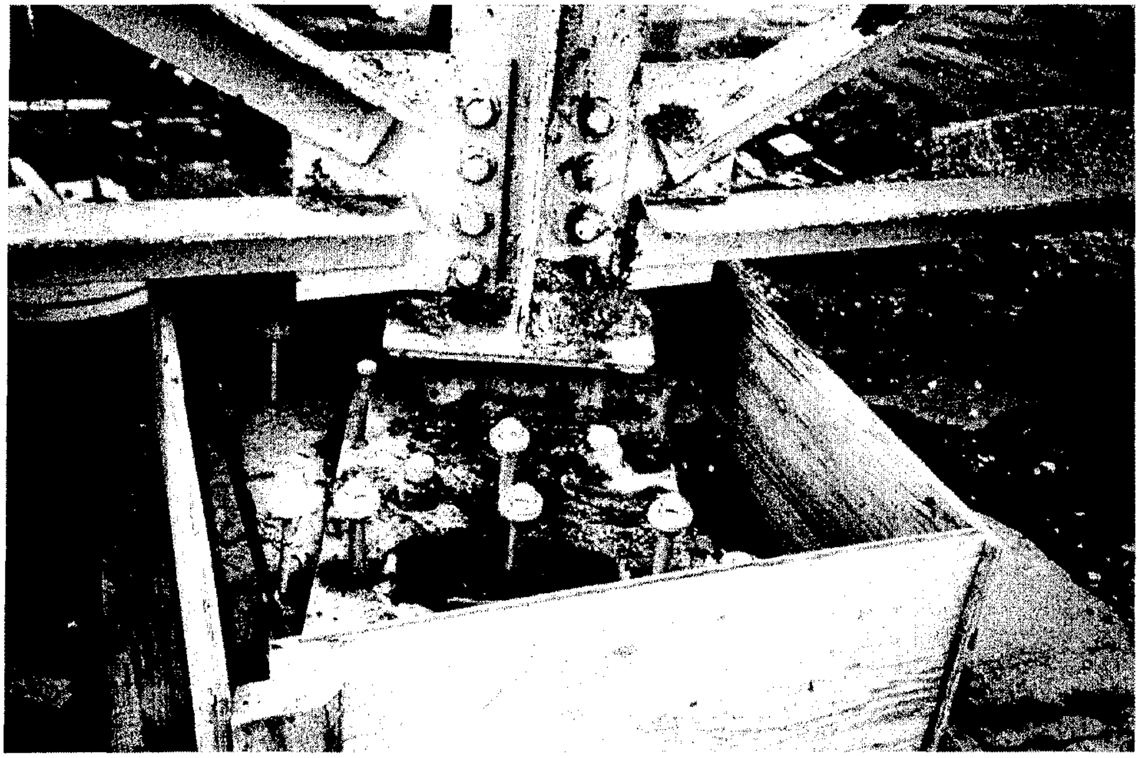

Figure 17. Formwork for concrete support on top of Bent #5

Figure 18. Finished concrete supports on Bent #5

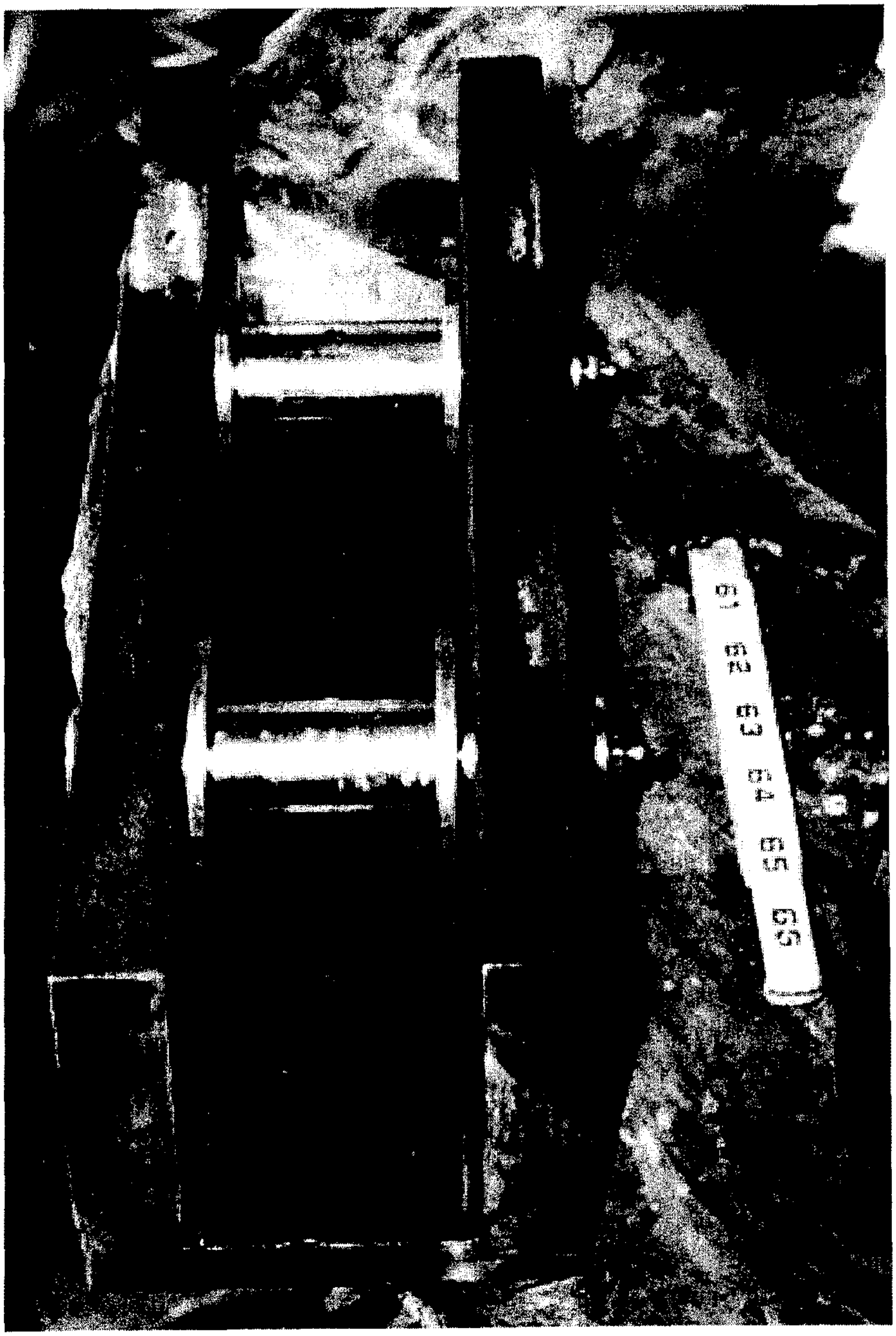

Figure 19. Detail of roller

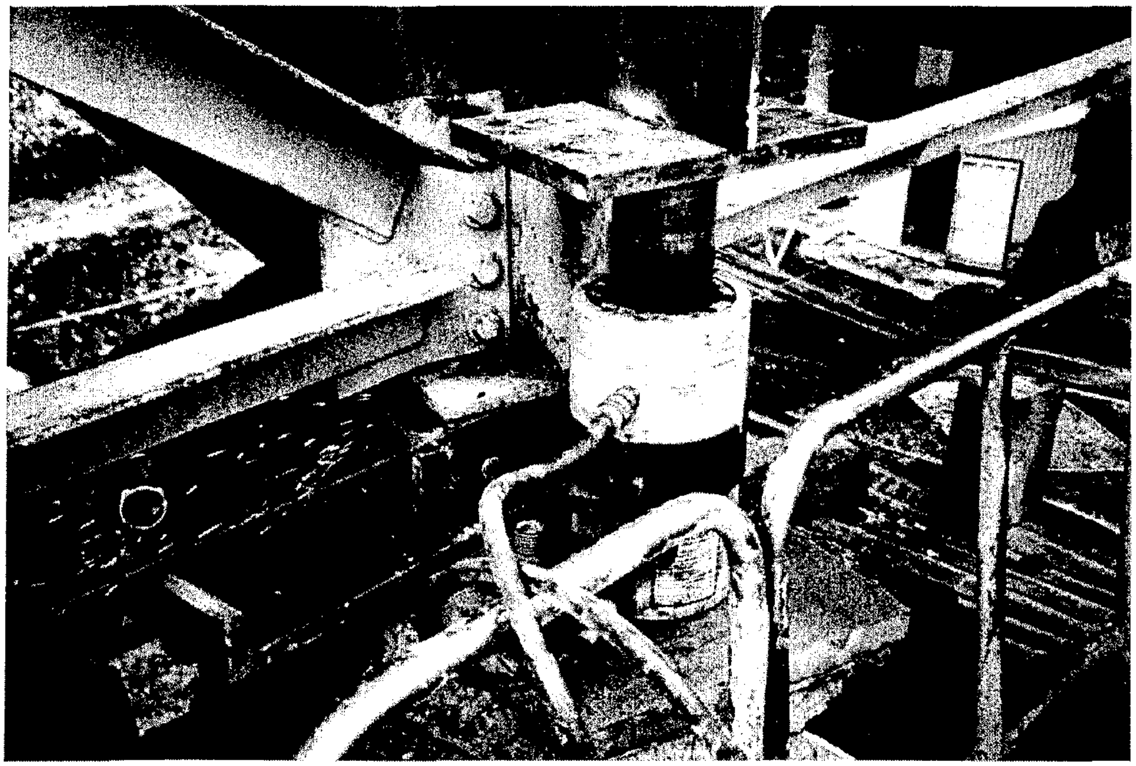
Figure 20. Lifting of steel girders on Bent #6

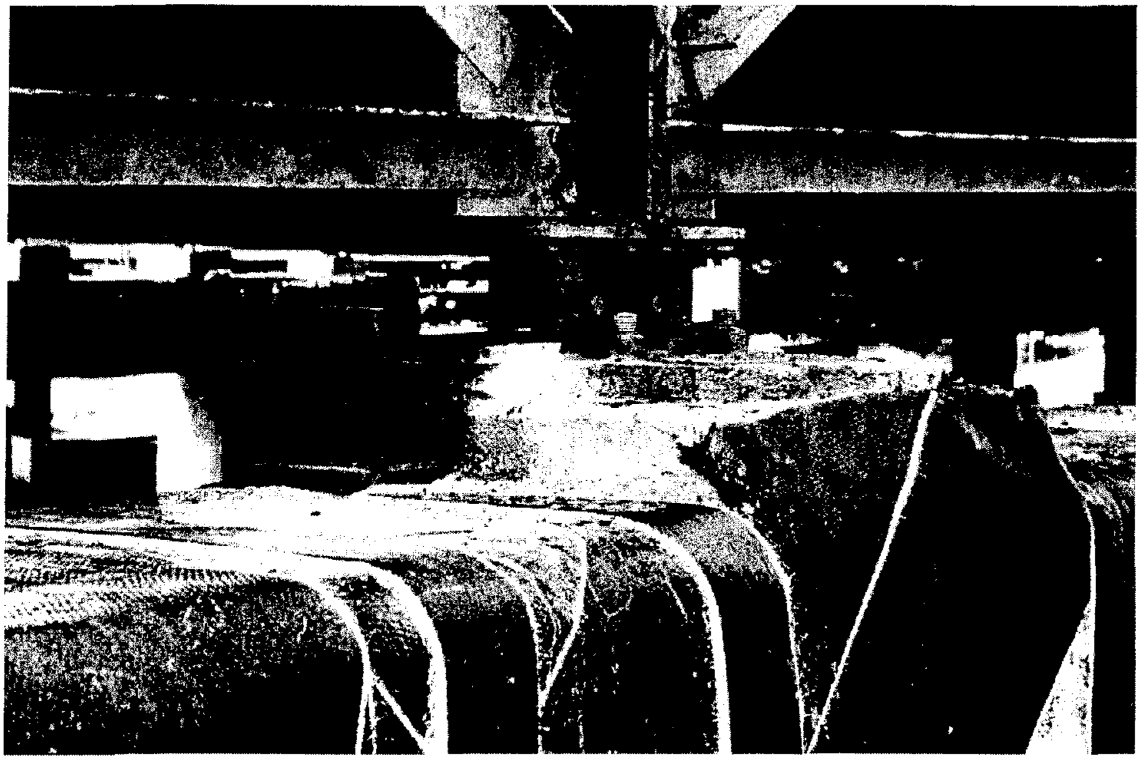
Figure 21. Roller in place on top of Bent #6

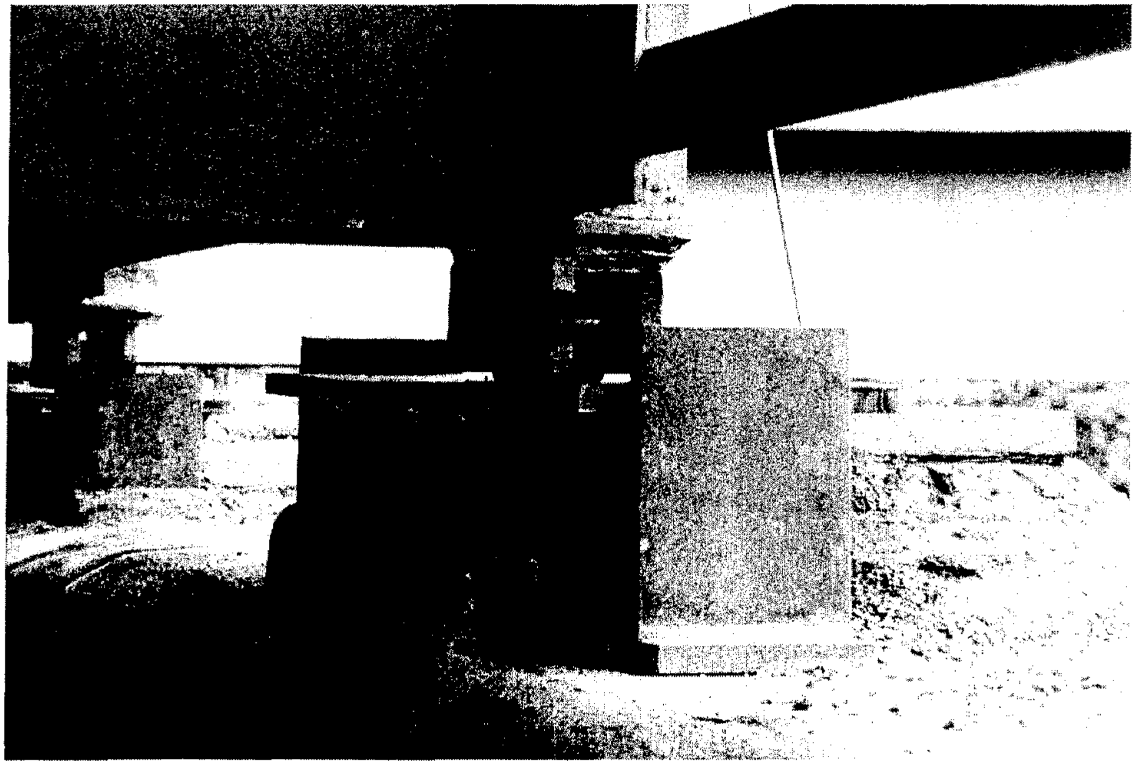

Figure 22. Finished roller assembly on top of Bent #6

The prestressing tendons shown in Fig. 18 were used to apply the pull cycle, and were prestressed only to approximately 4 N/mm^2 per tendon to take out the cable sag. Since there were 20 tendons (1/2 in. diameter, 7 strand) the total force applied axially as a compression on the beam cap was 7,896 N. This translates to an axial stress of only 0.0094 N/mm^2 (1.4 psi) which does not affect the results obtained in the lateral load tests.

5. LOAD FRAME, ACTUATOR, AND LOAD FRAME FOUNDATION

The design of the load frame and the load frame foundations is presented in this section. The load frame is essential in carrying out the transverse load tests; equally important is the need for resistance to significant vertical pullout and horizontal shear forces at the load frame supports.

Load Frame Design

The purpose of the in-situ tests was to evaluate the capacity of the bridge bents in the transverse direction. For this purpose, a special steel load frame was constructed for a design load of 400 kip (1779 kN), which was determined from nonlinear pushover analysis of the multi-column rehabilitated bent. The load frame was designed and constructed with a factor of safety of 1.5. The analysis of the load frame was performed using the computer finite element software SAP 2000 (Computer and Structures 1998). The final design of the side view of the load frame is shown in Fig. 23. The 3D load frame is composed of an identical frame to the one shown in Fig. 23, at a distance of 6 ft (1.829 m). The two frames were joined by a 6 ft-wide (1.829 m) truss as shown in Fig. 24. A 3D rendering of the load frame before construction is shown in Fig. 25. The load frame in its final form is composed of two identical A-frames with the member dimensions and sections as shown in Fig. 26. All connections between the two A-frames were bolted connections since the two half A-frames could be disassembled with a resulting width of 10 ft (3.048 m) to facilitate transportation. All members were designed using Grade 50 ksi (345 MPa) steel. The final dimensions were 20 ft (6.096 m) long, 24 ft 11 7/8 in. (7.617 m) tall, and 6 ft (1.829 m) wide.

Figure 27 shows the detail of one of the four legs of the load frame, which was reinforced to resist a significant horizontal shear. Figure 28 shows the detail at the top of the load frame, and the location where the actuator is anchored. The detail showing the connection of the two half A-frames at the bottom of the load frame is shown in Fig. 29. Figure 30 shows the details at typical braces on the connection point of the half A-frames. Figure 31 shows details of the braces along the side of the load frame. Figure 32 is a close-up of the detail shown in Fig. 30, between the half A-frames. Figure 33 shows the members of the load frame before assembly. The assembled frame in position for a lateral load test is shown in Fig. 34.

Actuator

The actuator used in the tests was a Hydroline hydraulic cylinder with a 30 in. (762 mm) stroke capability and a 600 kip (2670 kN) push, and a 420 kip (1870 kN) pull capacity. The actuator operated through a 30-gallon power supply. Figure 34 shows the actuator and the mounting bracket where the load is applied from the actuator to the beam cap. Figure 35 shows the actuator in a close up and the detail of the mounting onto the beam cap. The actuator connection on top of the load frame is shown in detail in Figs. 36-38. Details of the mounting bracket are shown in Figs. 39-41. The locations of the holes for the tendons going through the mounting bracket are shown in Fig. 40, and the actual detail is shown in Fig. 41.

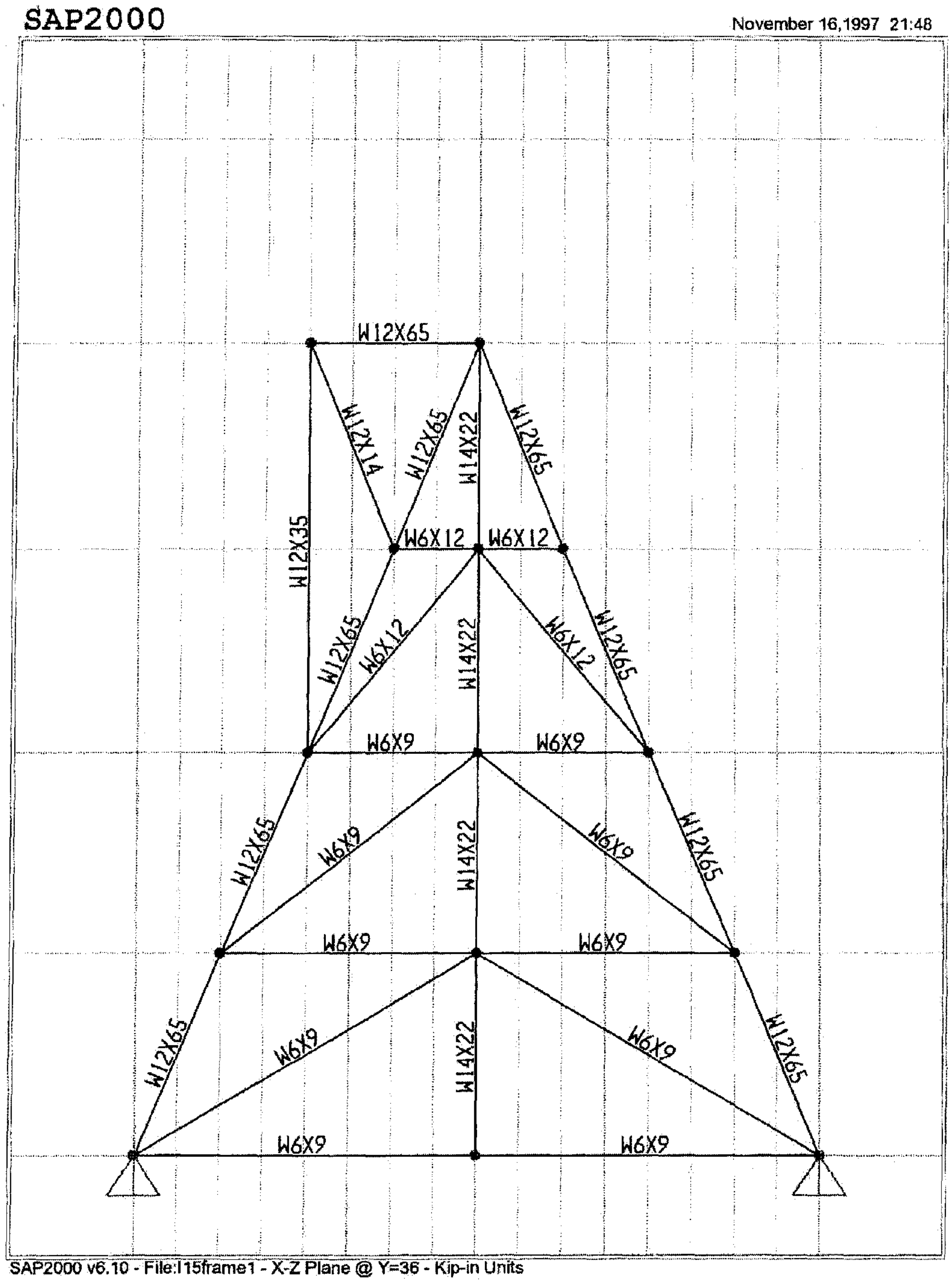

Figure 23. Final design of load frame

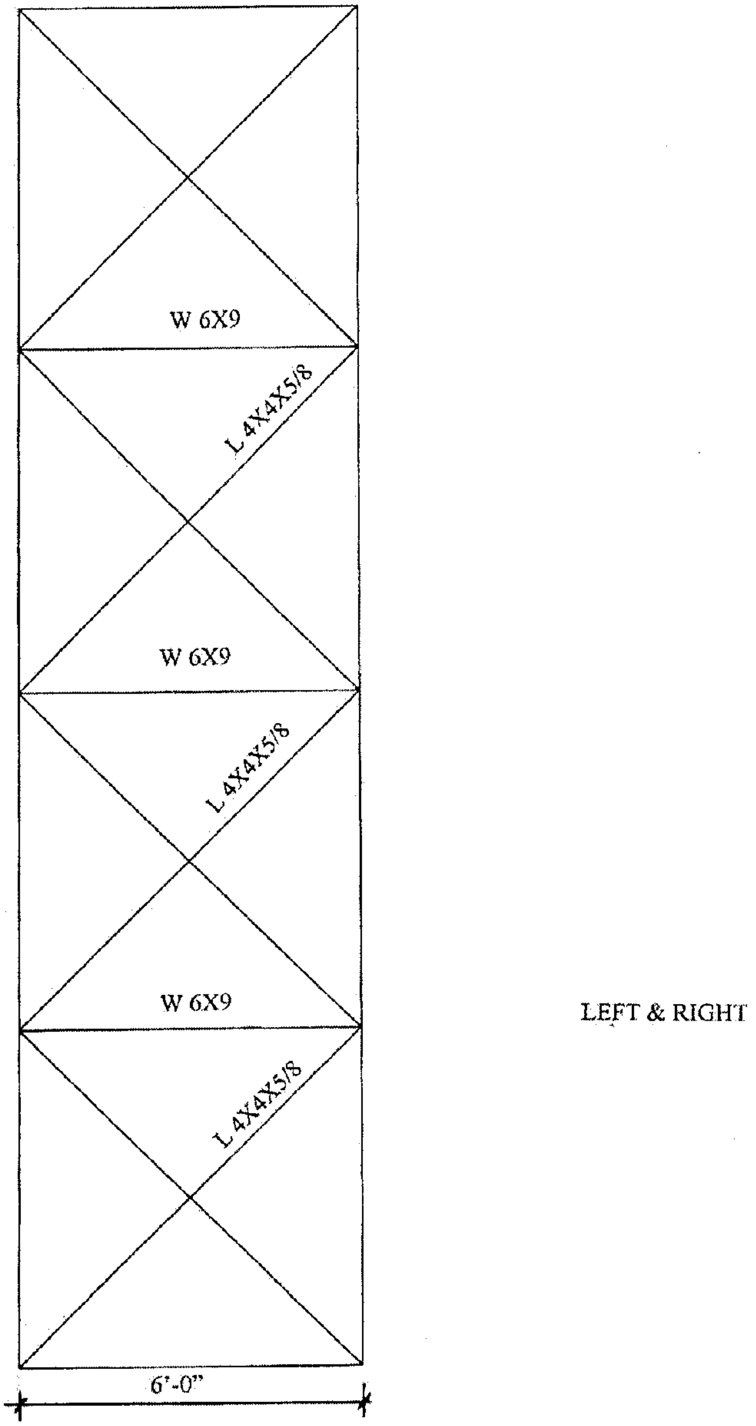

Figure 24. Bracing of load frame in the out-of-plane direction (1'=305 mm, 1"=25.4 mm)

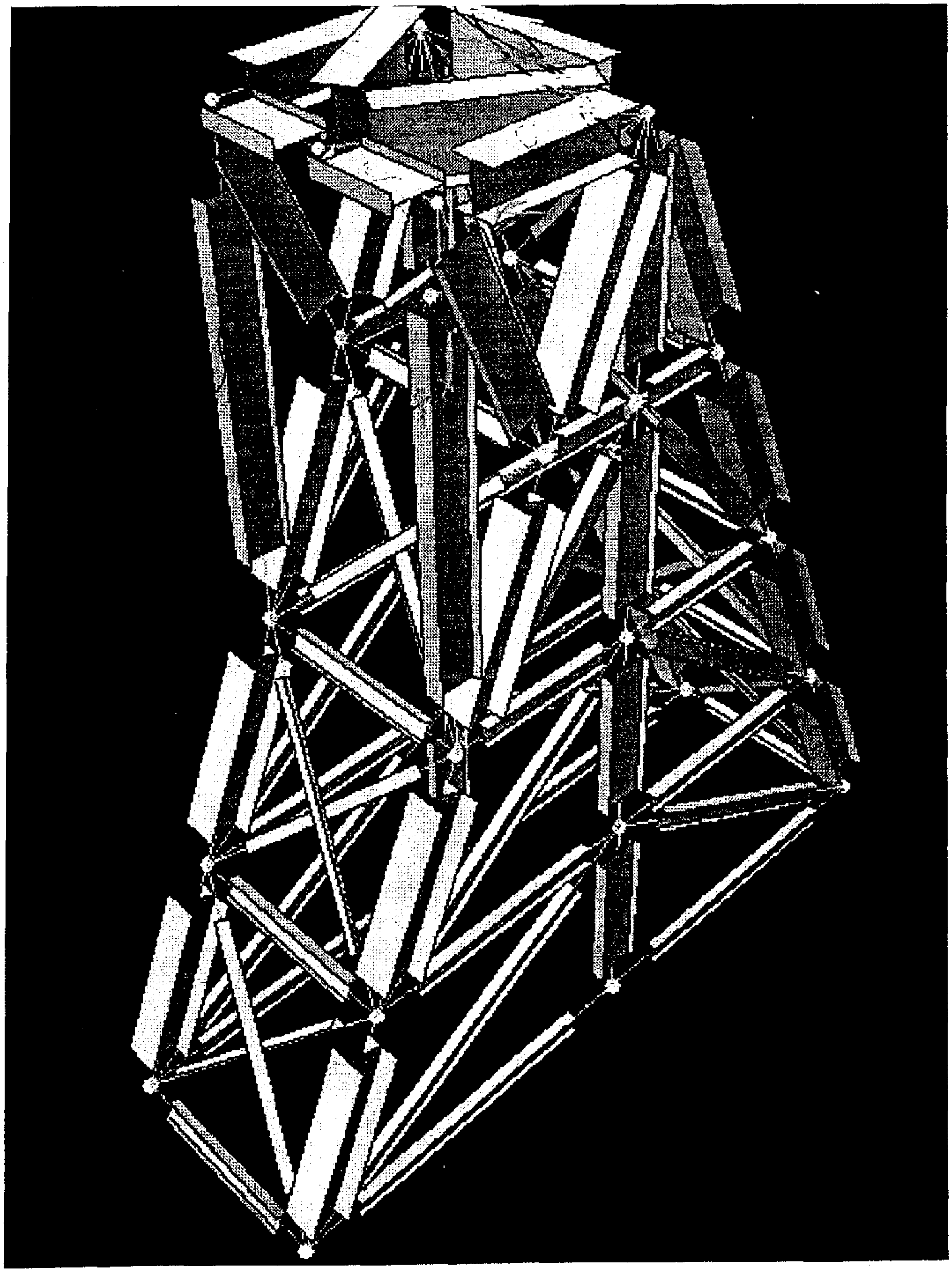

Figure 25. Three-dimensional rendering of load frame design

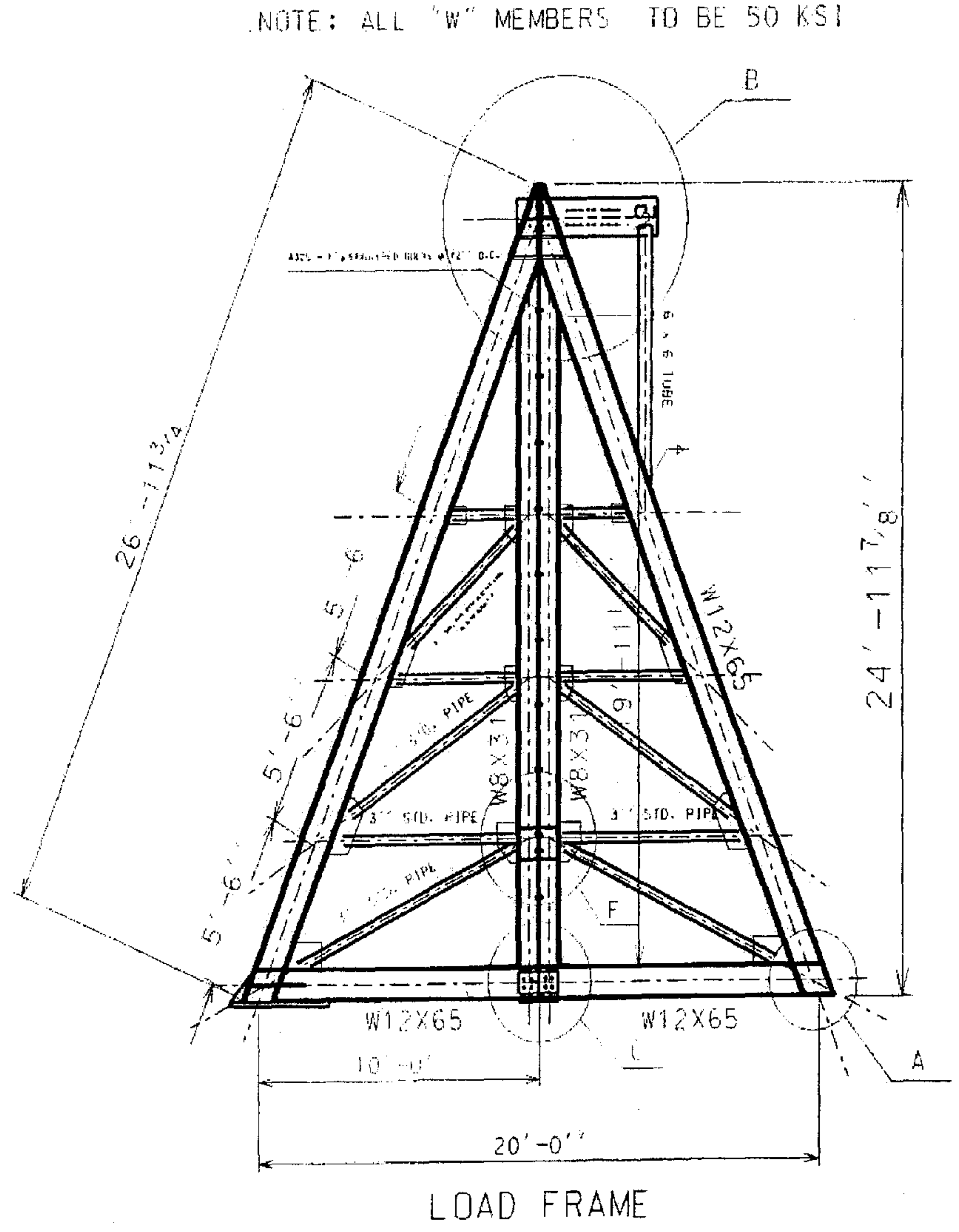

Figure 26. Construction drawing of load frame: Overall view (1'=305 mm, 1"=25.4 mm)

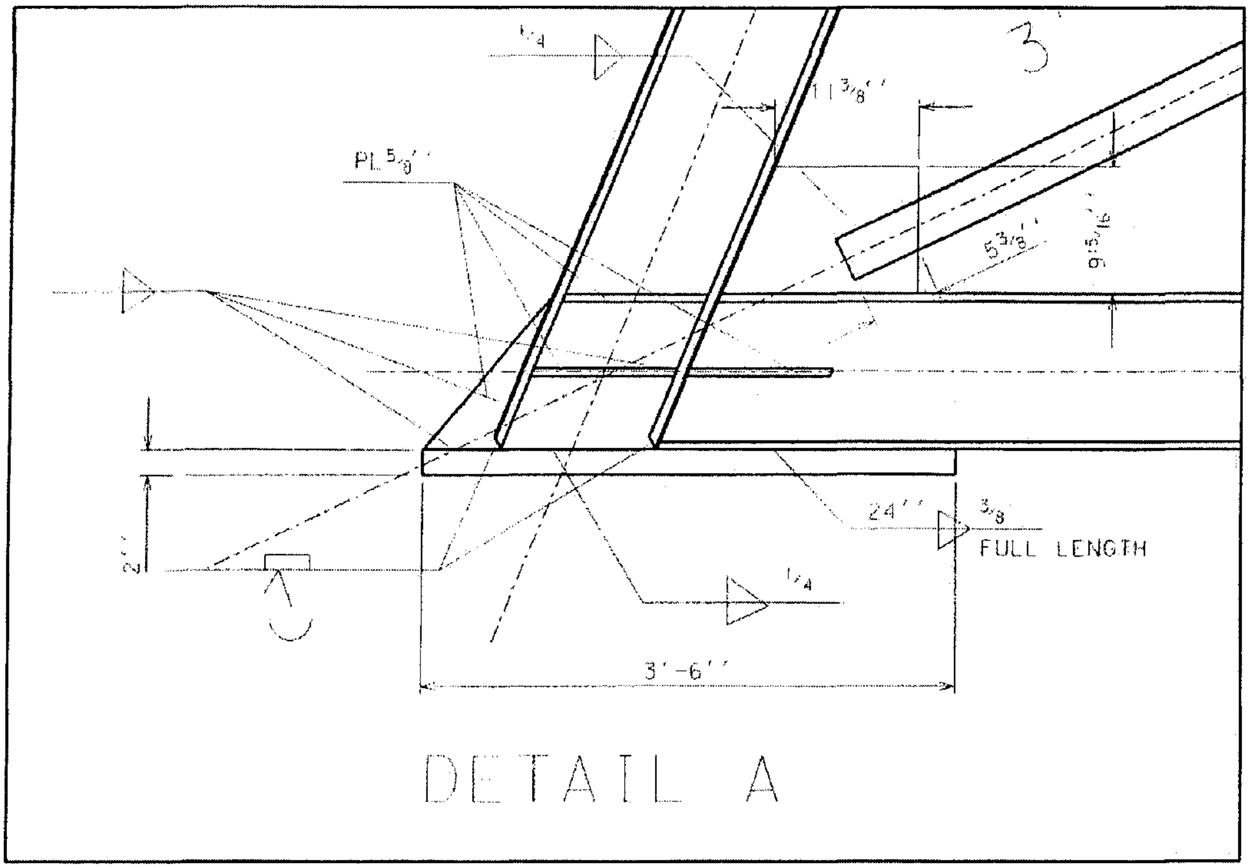

Figure 27. Construction drawing of load frame: Detail "A" (1'=305 mm, 1"=25.4 mm)

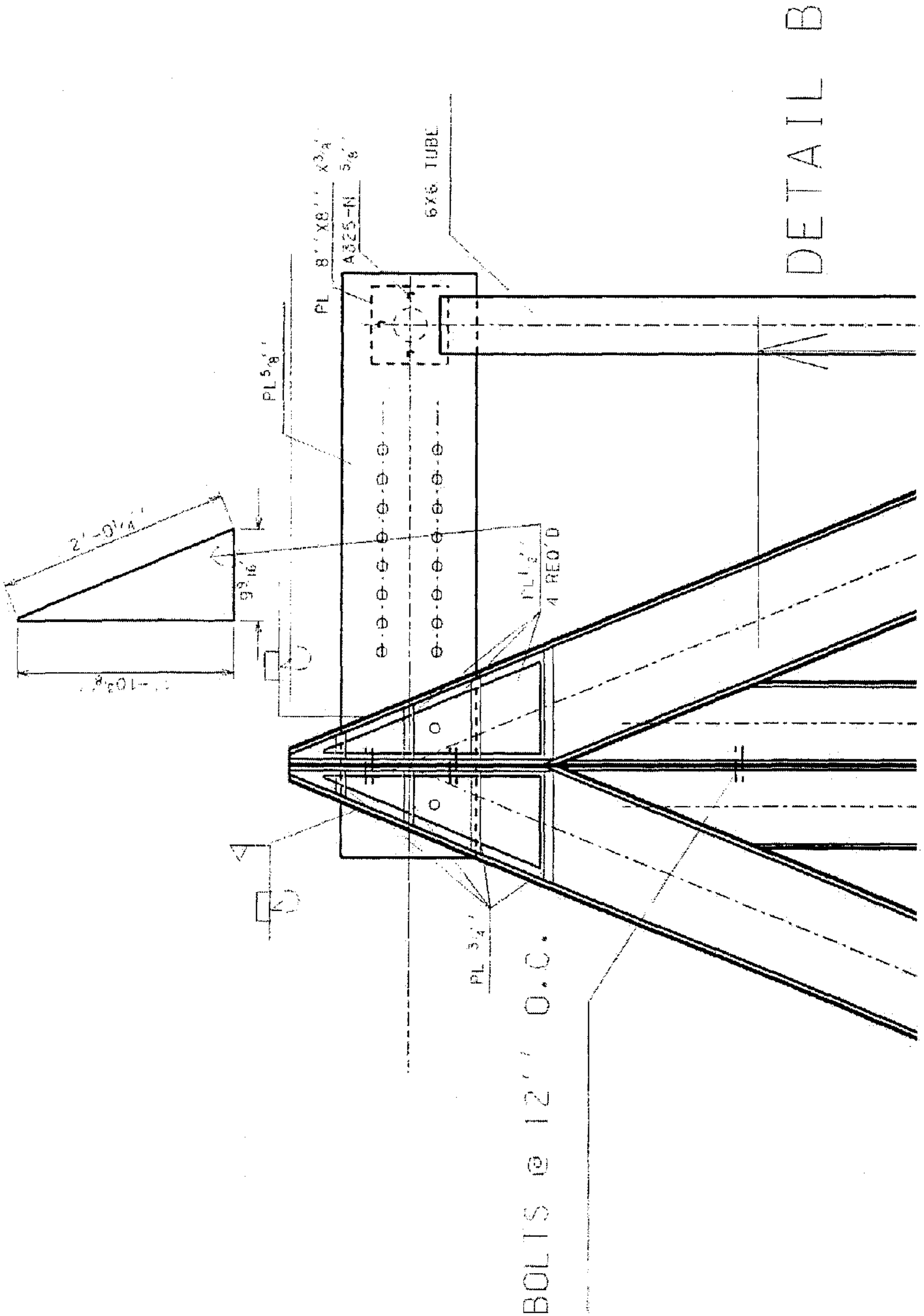

Figure 28. Construction drawing of load frame: Detail “B” (1’=305 mm, 1”=25.4 mm)

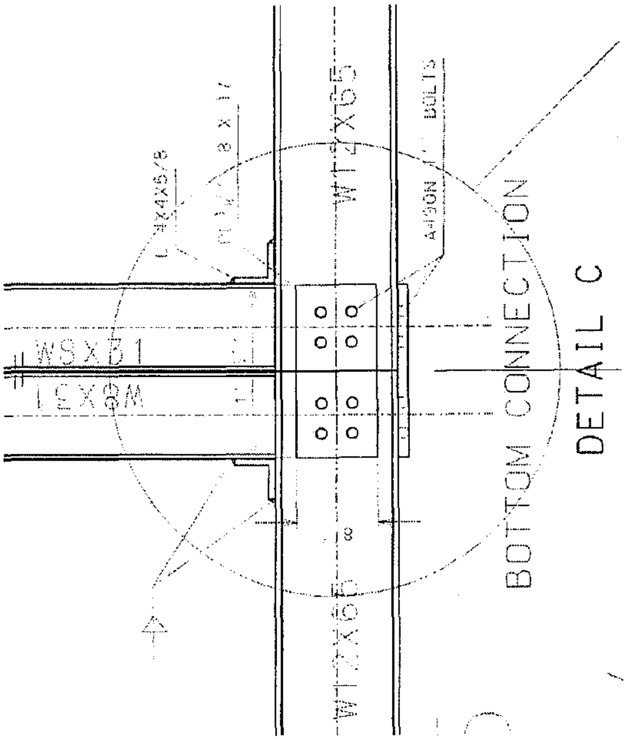

Figure 29. Construction drawing of load frame: Detail "C"

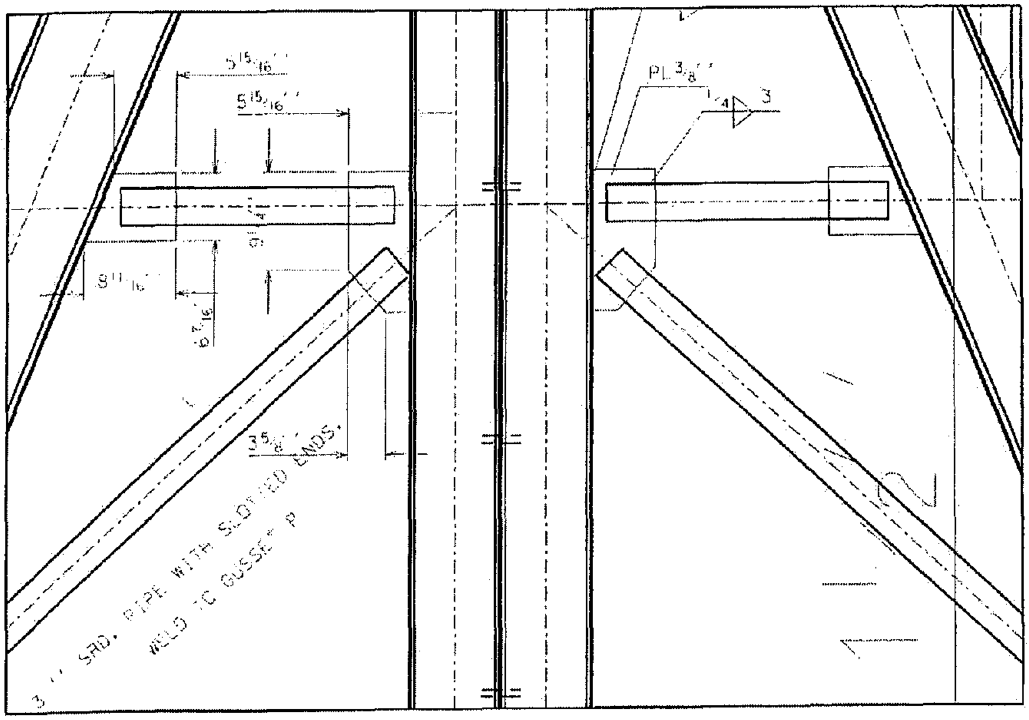

Figure 30. Construction drawing of load frame: Additional "A-Frame" detail (1"=25.4 mm)

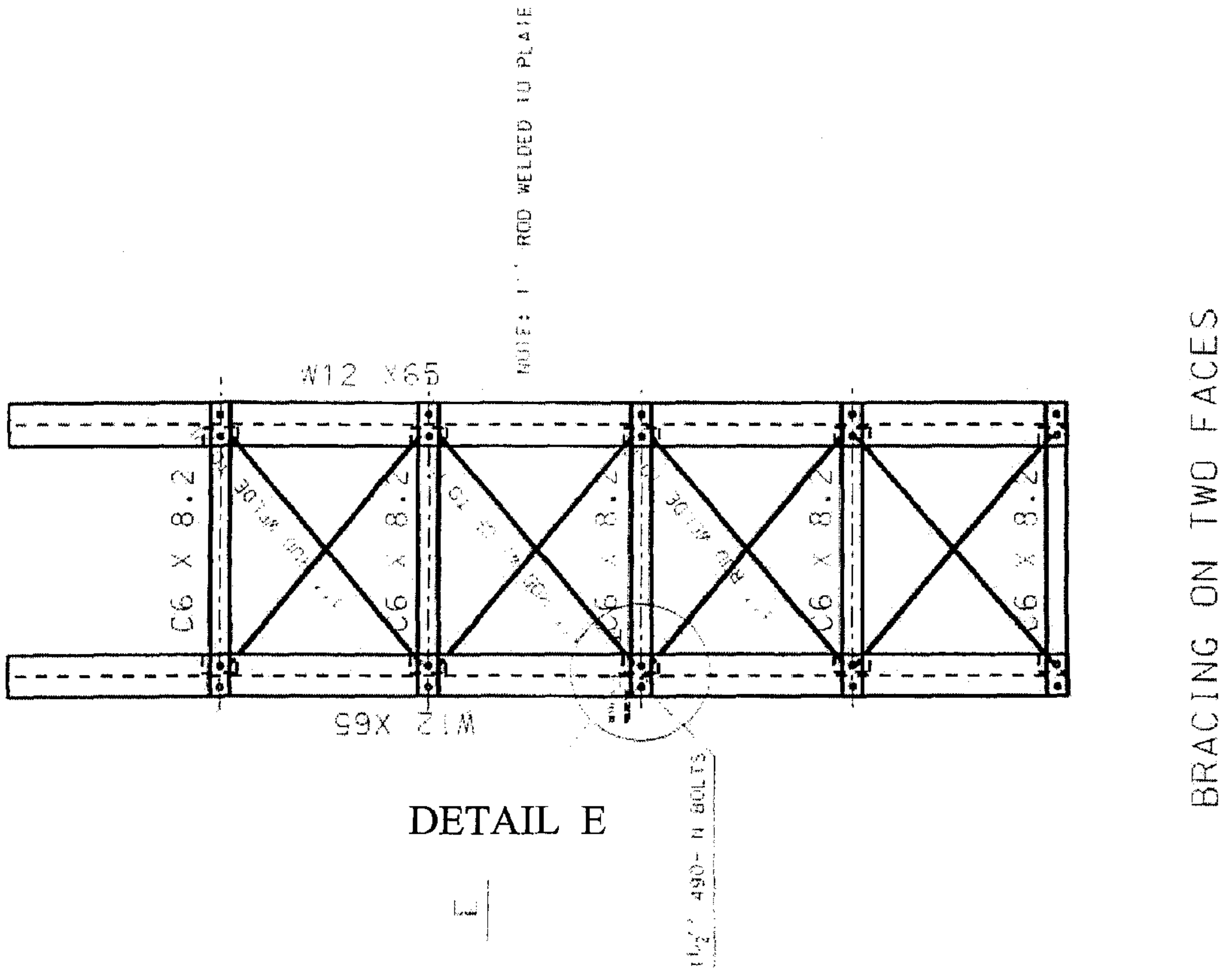

Figure 31. Construction drawing of load frame: Side view

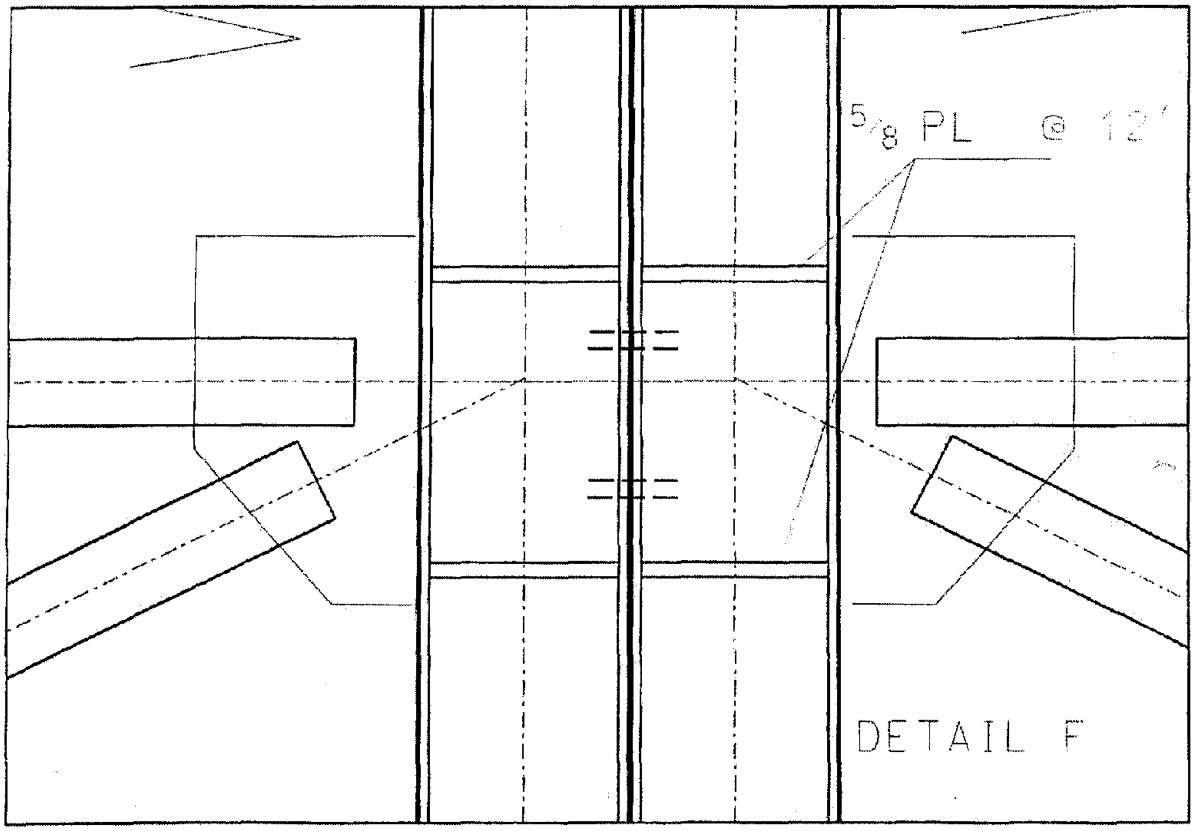

Figure 32. Construction drawing of load frame: Detail "F"

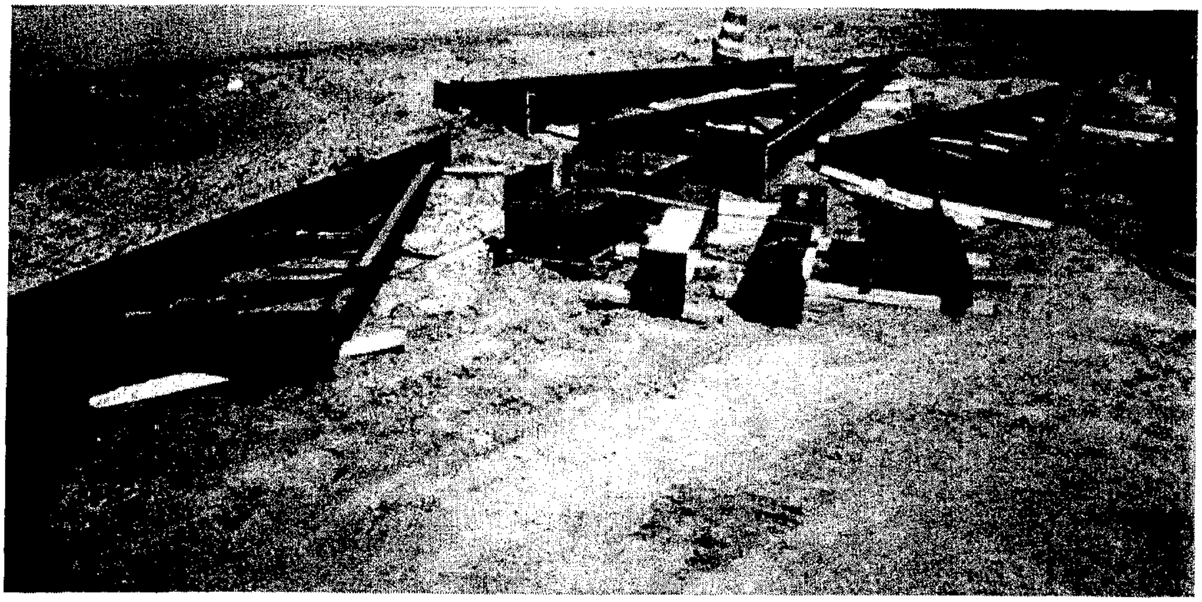

Figure 33. Constructed elements of load frame before final assembly

Figure 34. Assembled load frame

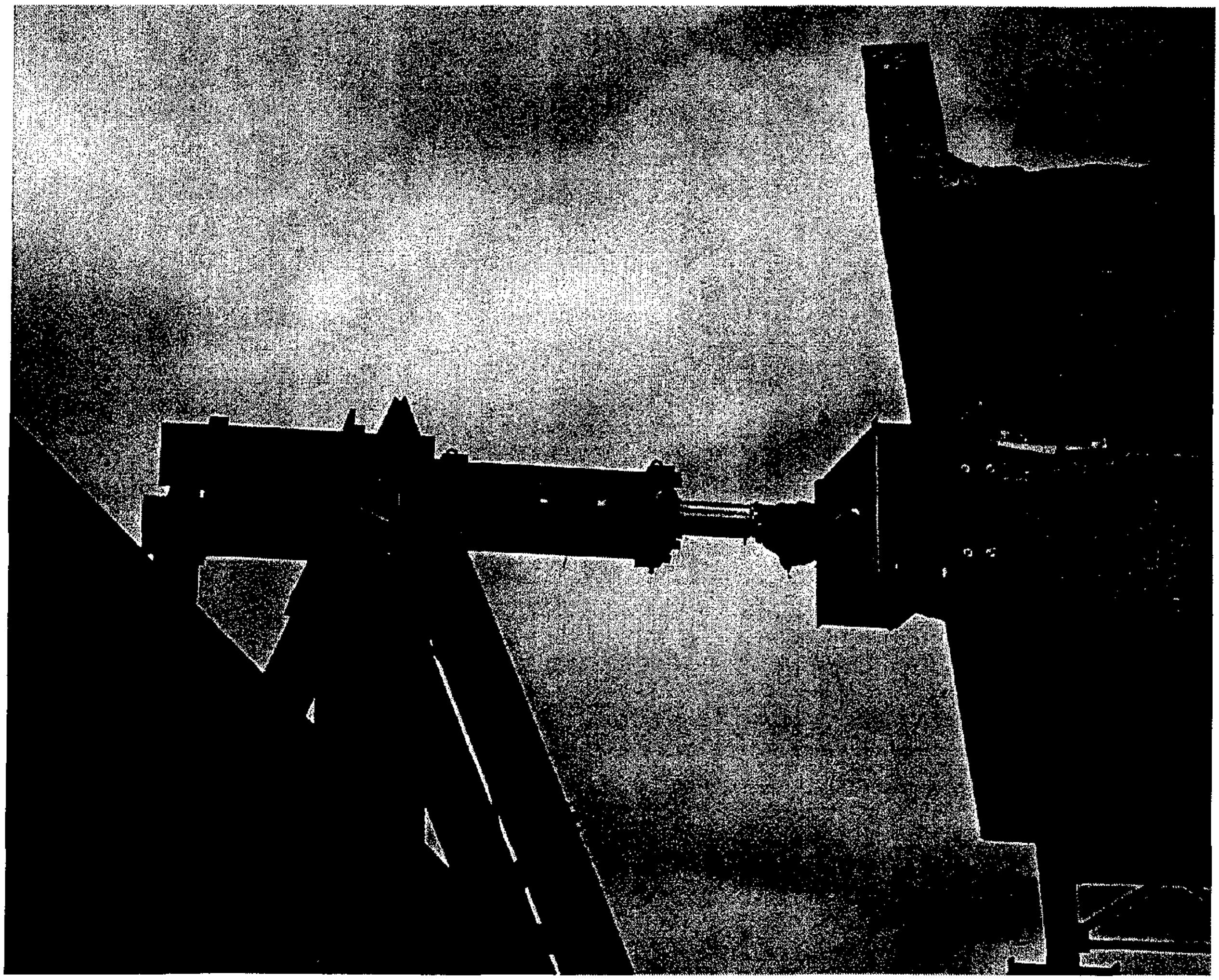

Figure 35. Close-up of actuator connection to the beam cap

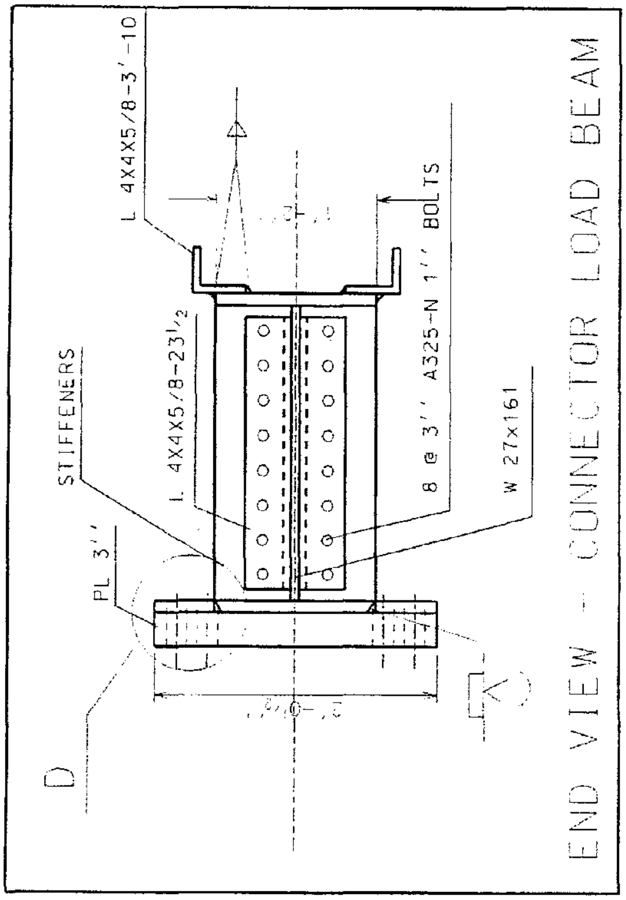

Figure 36. Construction drawing of load frame: End view of actuator connector

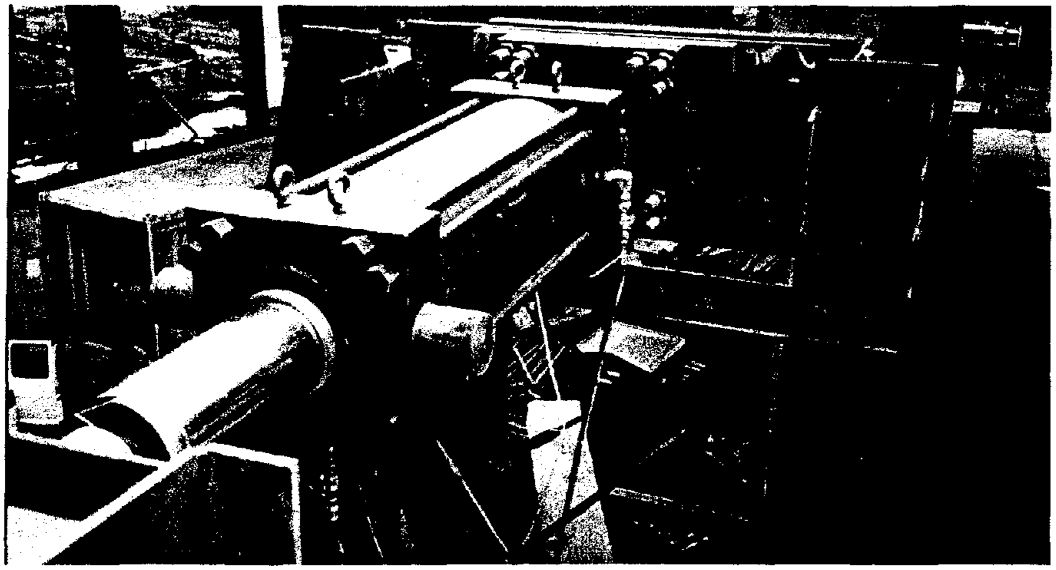

Figure 37. Detail of actuator and actuator connector to the load frame

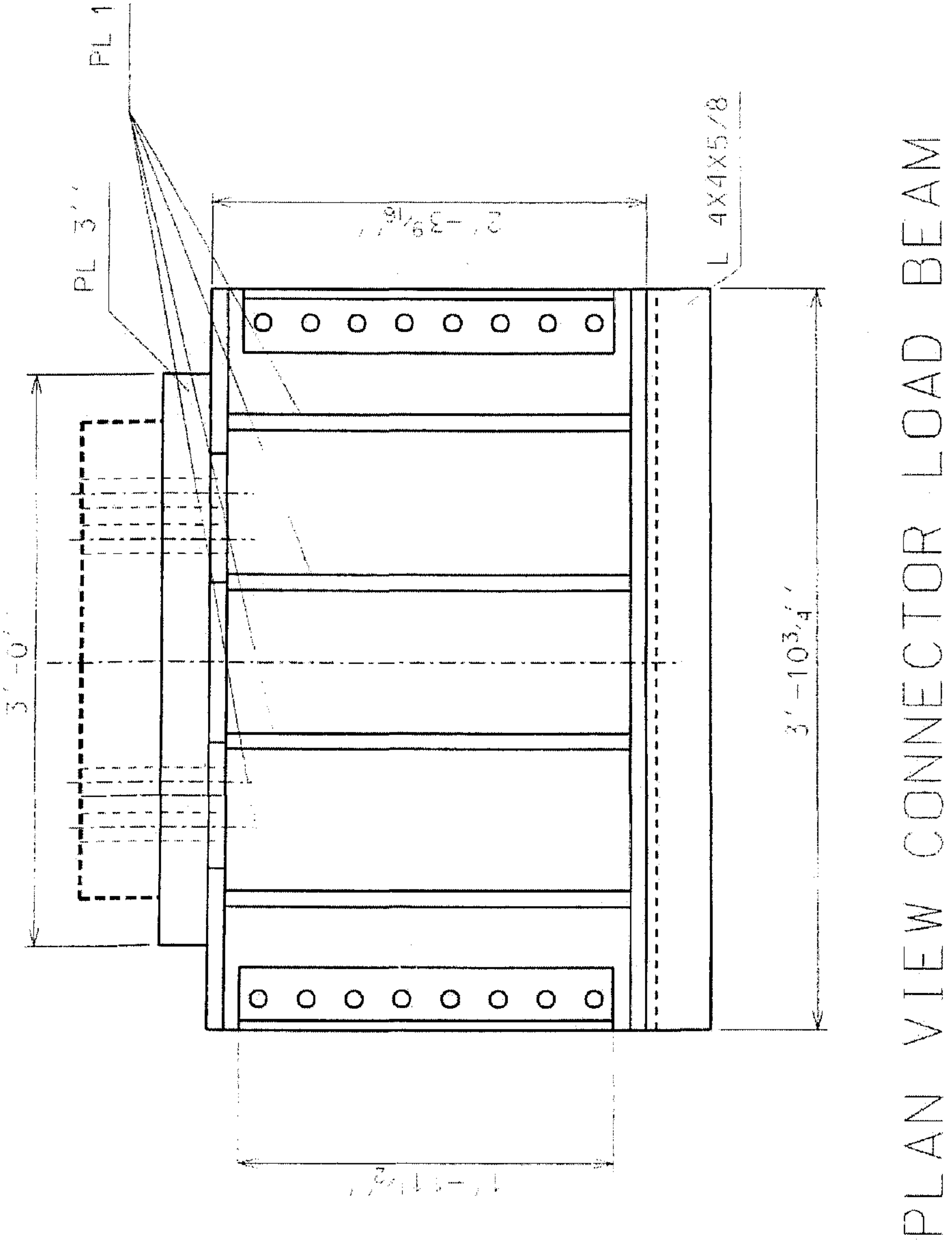

Figure 38. Construction drawing of load frame: Plan view of actuator connector (1'=305 mm, 1"=25.4 mm)

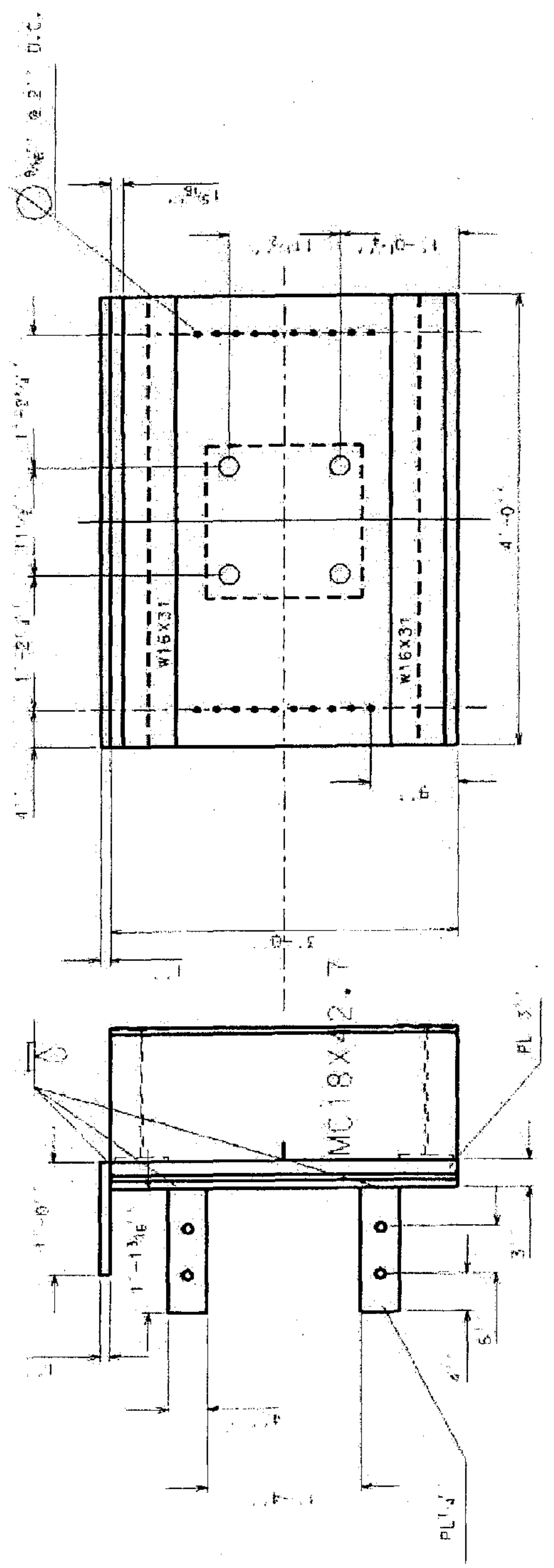

Figure 39. Construction drawing of beam cap mounting bracket (1'=305 mm, 1"=25.4 mm)

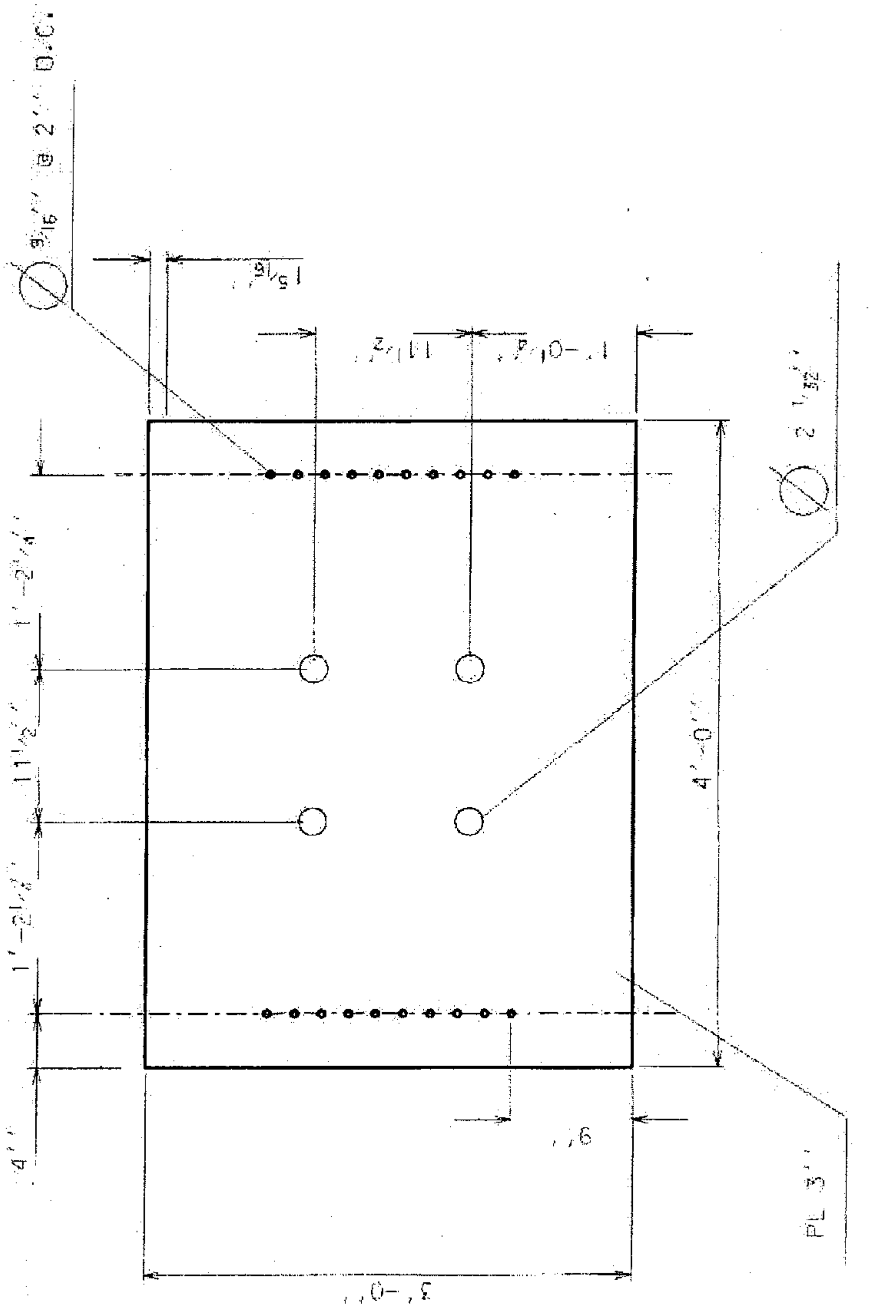

Figure 40. Construction drawing of beam cap mounting bracket detail showing holes for the prestressing tendons (1'=305 mm, 1"=25.4 mm)

Figure 41. Detail of actuator, beam cap mounting bracket, and tendons

Load Frame Foundation Design

The load frame was supported at the base by two reinforced concrete footings, which were reinforced with special channels and threaded rods, that were used to hold down the load frame. The two footings were supported for uplift and shear resistance by Geopiers (Lawton et al. 1994), which are aggregate piers in the soil, that provide the uplift and shear required to secure the load frame during the lateral load test. The configuration of the test setup is shown in Fig. 42. The lateral load was applied to the bent at the beam cap level, and the horizontal and vertical reactions generated from the load applied to the bent were transferred to the load frame footings and finally from the load frame footings they were transferred to the Geopiers. Each of the four legs of the frame had a steel frame base plate support, with four A490 1 1/2 in. (38 mm) diameter rods extending above the load frame footing, as shown in Fig. 43. The details of the base plate support are shown in Fig. 44. Embedded channels held the four rods in position. Details of the embedded channel are shown in Fig. 45 and Fig. 46.

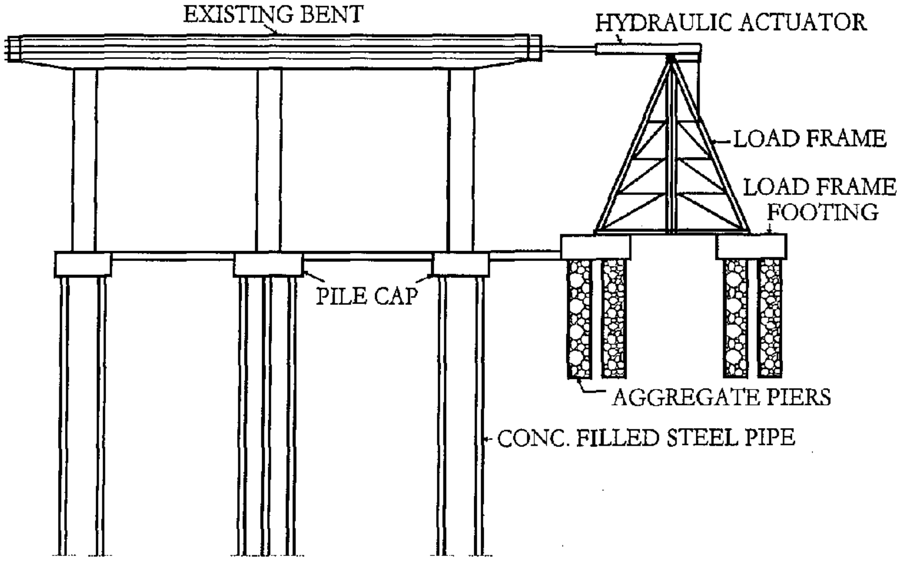

Figure 42. Load frame and load frame foundation

Figure 43. Detail of embedded channel and 1 1/2 in. diameter threaded rods in one leg of the load frame footing

The dimensions of the load frame dictated the location of the load frame footings and consequently the location of the Geopiers. The center-to-center longitudinal distance between the four rods of each of the four base plates of Fig. 44 is 20 ft (6.096 m). This is shown schematically as the location of the embedded channels in Fig. 47. The transverse direction requires a distance of 6 ft (1.829 m) between each of the two channels on both ends of the load frame as shown in Fig. 47. The detail of the plan view of the embedded channel is shown in Fig. 48, where the four rods extending above the concrete foundation are also shown. The actual load frame footing is supported by ten 36 in. (914 mm) diameter Geopiers as shown in Fig. 49. The Geopiers were located so as not to interfere with the two base plates in each of the two identical footings, one of which is shown in Fig. 49.

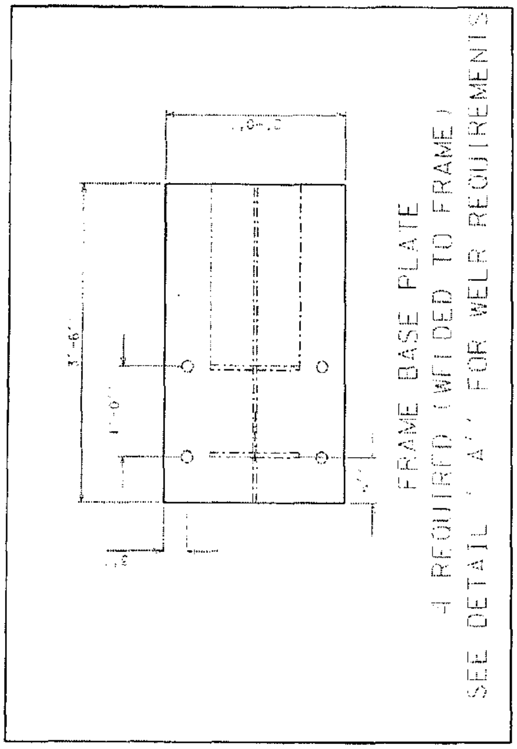

Figure 44. Construction drawing of the base plate support at one of the four legs of the load frame (1'=305 mm, 1"=25.4 mm)

Figure 45. Embedded channel showing threaded rods

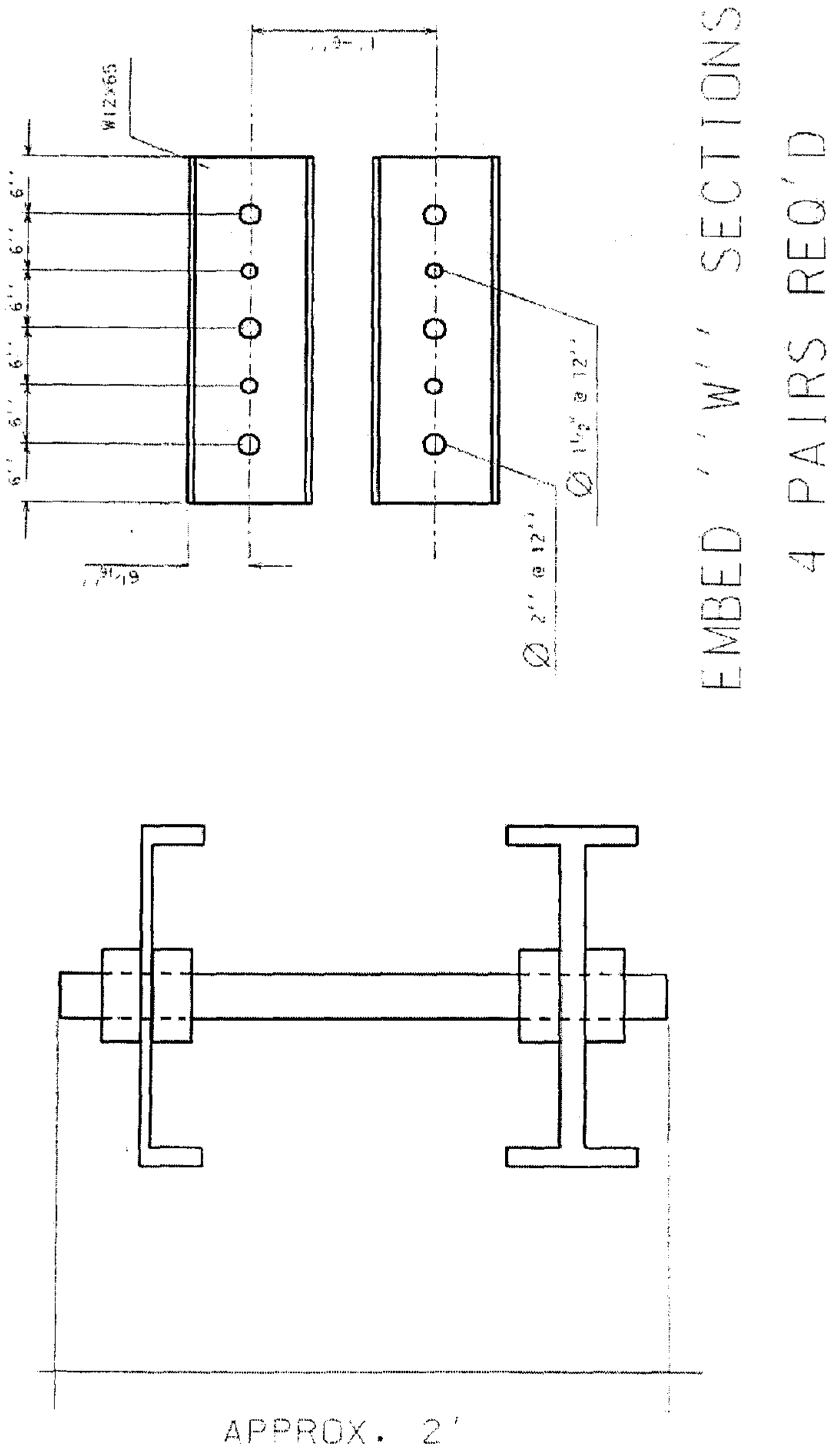

Figure 46. Dimensions and details of embedded channel (1'=305 mm, 1"=25.4 mm)

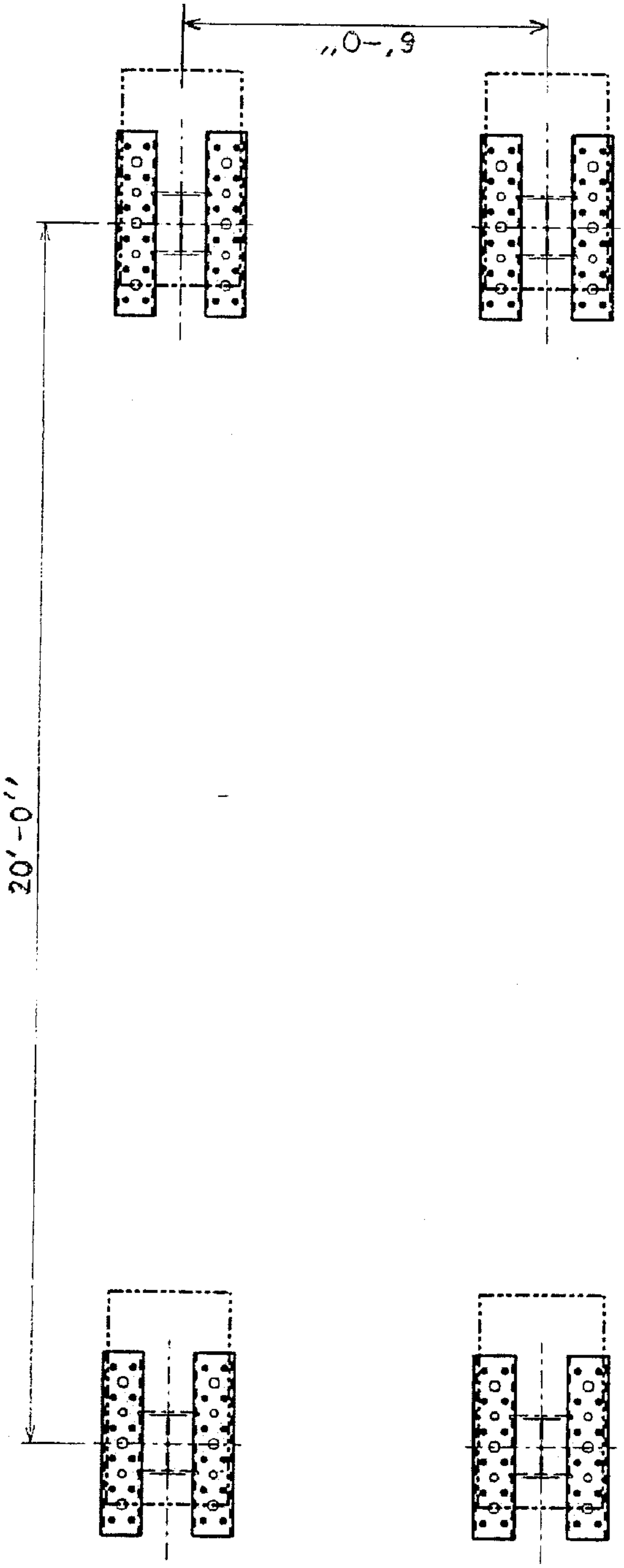

Figure 47. Load frame foundation supports showing four embedded channels (1'=305 mm, 1"=25.4 mm)

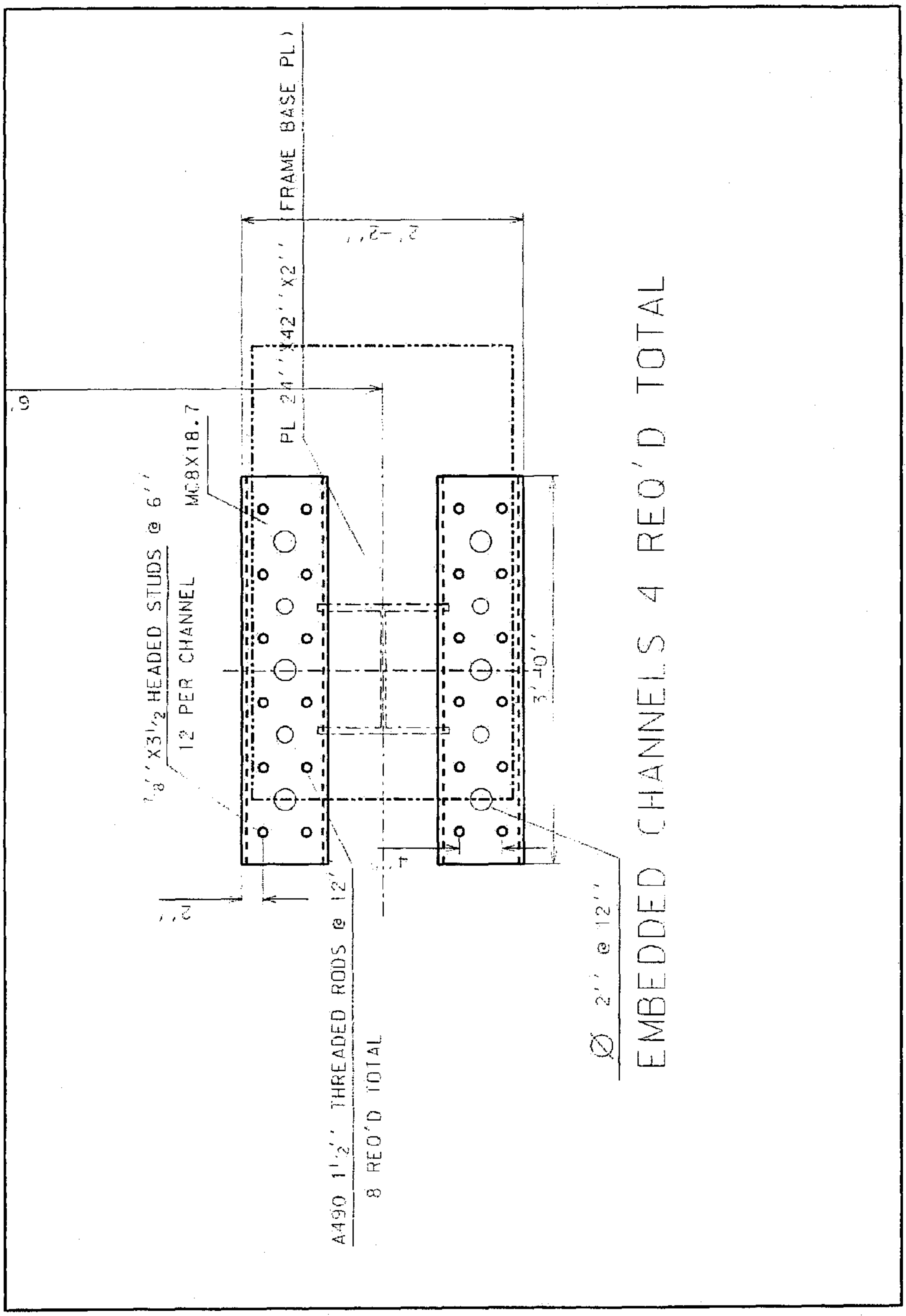

Figure 48. Detail of embedded channel and load frame base plate (1'=305 mm, 1"=25.4 mm)

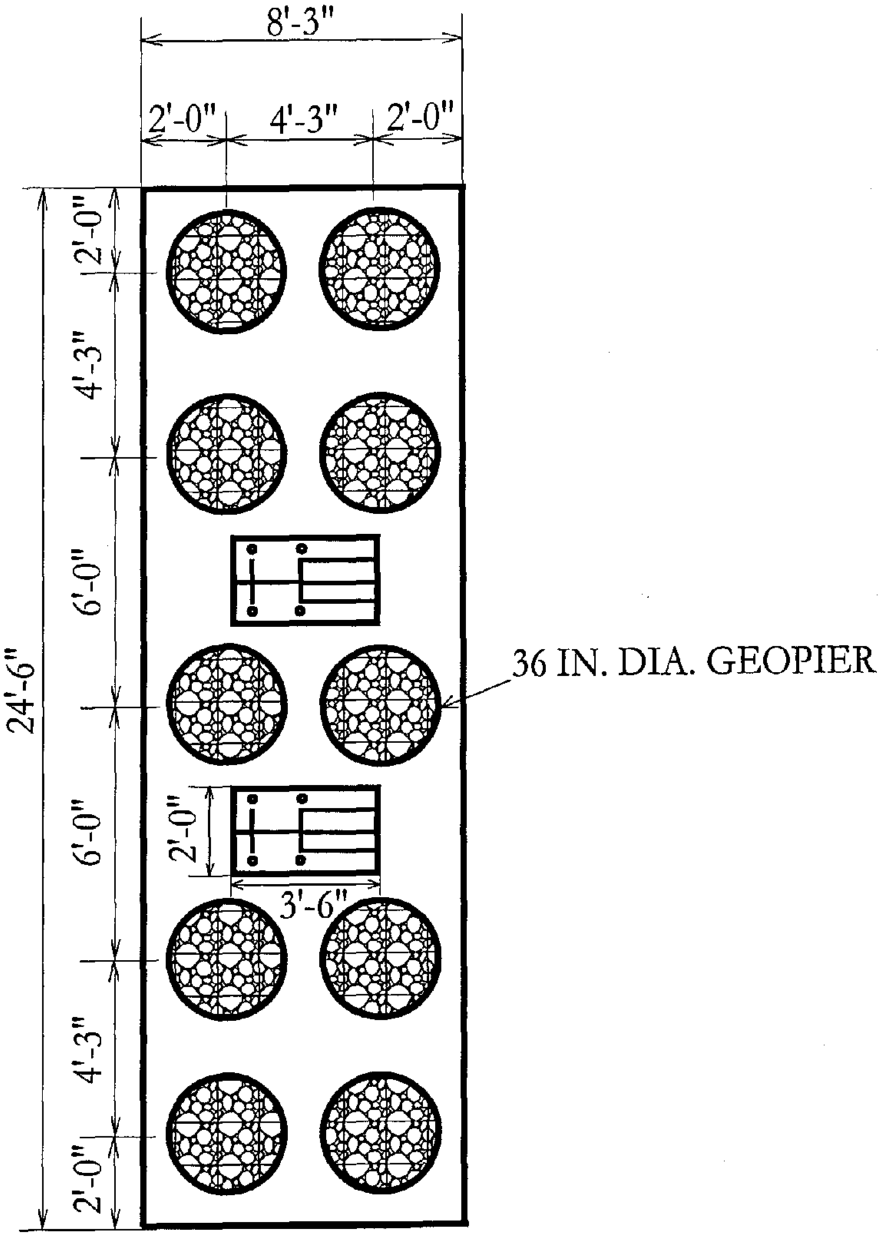

Figure 49. Construction drawing of load frame footing showing location of base plate and ten Geopiers (1'=305 mm, 1"=1 in.=25.4 mm)

The design of the load frame footing foundations was carried out according to the ACI (ACI 1995) provisions, with special details for the base plates and Geopiers. The plan dimensions of the footing are shown in Fig. 49. The footing overall depth was assumed as 39 in. (990 mm), and #8 (25 mm) bars were used. Assuming a 3 in. (76 mm) cover, the effective depth of the footing was d = 35 in. (889 mm). Bars would be provided both top and bottom, with a 3-in. (76-mm) cover. In addition, the reinforcement would be both in the transverse .and longitudinal directions.

Punching shear at embedded channels

The punching shear around the embedded channels was checked using a critical section of 24+35=59 in (1499 mm) parallel to the long direction of the footing and 42+35=77 in. (1956 mm) perpendicular to the long direction of the footing. Note that the base palate dimension is 24 x 42 in. (610 x 1067 mm) as shown in Fig. 44. The critical perimeter per support is thus calculated as b_0 = 272 in. (6909 mm). The concrete specified for the load frame footings was a high early strength concrete that was supposed to reach a compressive strength of 4,000 psi (26 MPa) in two weeks. However, in order to be conservative the design calculations were carried out using a compressive strength of concrete equal to f'_c = 3,000 psi (21 MPa). The concrete capacity in punching shear was calculated as

$$\phi V_c = 0.85\sqrt{f_c^{'}}(4b_0 d) \tag{5.1}$$

which yields a punching shear capacity of 1773 kip (7886 kN). The applied loads of 280 kip (1245 kN) per load frame leg were obtained from the DRAIN-2DX analysis as reactions at the four legs of the load frame and are shown in Fig. 50.

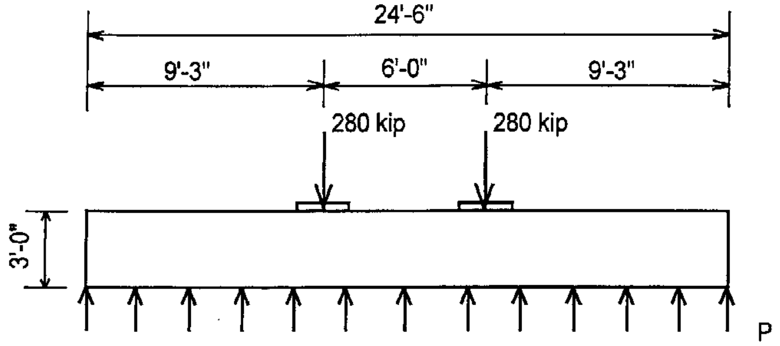

Figure 50. Assumed loads from load frame to load frame footing (1'=305 mm, 1"=25.4 mm)

The pressure P is calculated as the load divided by the planar dimensions of the footing (24'-6" x 8'- 3") which results in 19.24 psi (133 kPa). The applied shear is then found as :

$V_u = [294x99 - 2\,x77x59]\,x\,(19.24/1{,}000) = 385$ *kip (1713 kN).* Since the capacity was found from equation (5.1) to be equal to 1773 kip (7886 kN), the factor of safety is 4.6, which is adequate.

One-way shear

The shear diagram corresponding to the footing sketch shown in Fig. 50 results in the maximum one way shear applied at the embedded channel equal to 212 kip ((943 kN). The concrete capacity in one-way shear is

$$\phi V_c = 0.85\sqrt{f_c'}\,(2b_w d) \tag{5.2}$$

Using a concrete compressive strength of f'_c = 3,000 psi (21 MPa) yields the capacity as 323 kip (1437 kN), which gives a factor of safety equal to 1.5 which is acceptable.

Flexure

In the long direction the bottom reinforcement is determined from the line-factored load by a using a load factor equal to 1.6. The factored load is: $P_u = 1.6\ (19.24\ x\ 144\ ) = 4432\ psf$ which when multiplied by the width of the footing gives the line load as: P_{lu} = 4432 x 8.25 /1000 = 36.6 kip /ft (534 kN/m). The factored moment at the critical section is thus: $M_u = 36.6\ (9.25)^2/2 = 1566$ *ft-kip (2123 kN-m).* Using the moment capacity of a rectangular section gives

$$\phi M_n = 0.9 A_s f_y jd \tag{5.3}$$

Using 12#8 bars gives a capacity within 5 percent of the demand, which is considered satisfactory since a load factor of 1.6 was used.

The top reinforcement in the long direction is calculated similarly to the bottom reinforcement with the difference being the weight of the concrete. The required reinforcement is calculated as 16 #8. Another way to look at the top reinforcement is to resist the moment provided by the Geopiers. From Fig. 49, the moment to be resisted equals the moment created by the weight of the footing and the moment created by the two sets of Geopiers at 3 ft and 7.25 ft from the critical section. Assuming that the Geopiers at 3 ft provide an uplift of 50 kip, and the two Geopiers at 7.25 ft provide an uplift of 68 kip gives a moment of 1574 ft-kip which is less than the capacity provided by 16 #8 bars.

In the short direction, a similar calculation yields 12 #8 bars in both the top and bottom of the footing within the 6 ft in-between the load plates shown in Fig. 49. As is common in two-way footings, the reinforcement outside the 6 ft region is scaled by the ratio of the long to the short side of the footing equal to 24.5/8.25= 2.97; this yields a ratio of $\beta = 2/(2.97 + 1) = 0.5$. Thus, 50% of the 12#8 bars are provided in the 9'-3" cantilever sections of the footing. This corresponds to #7 bars at 12 in. Similar calculations were performed for Bent #6 and the results for both are given in Fig. 51 and Fig. 52.

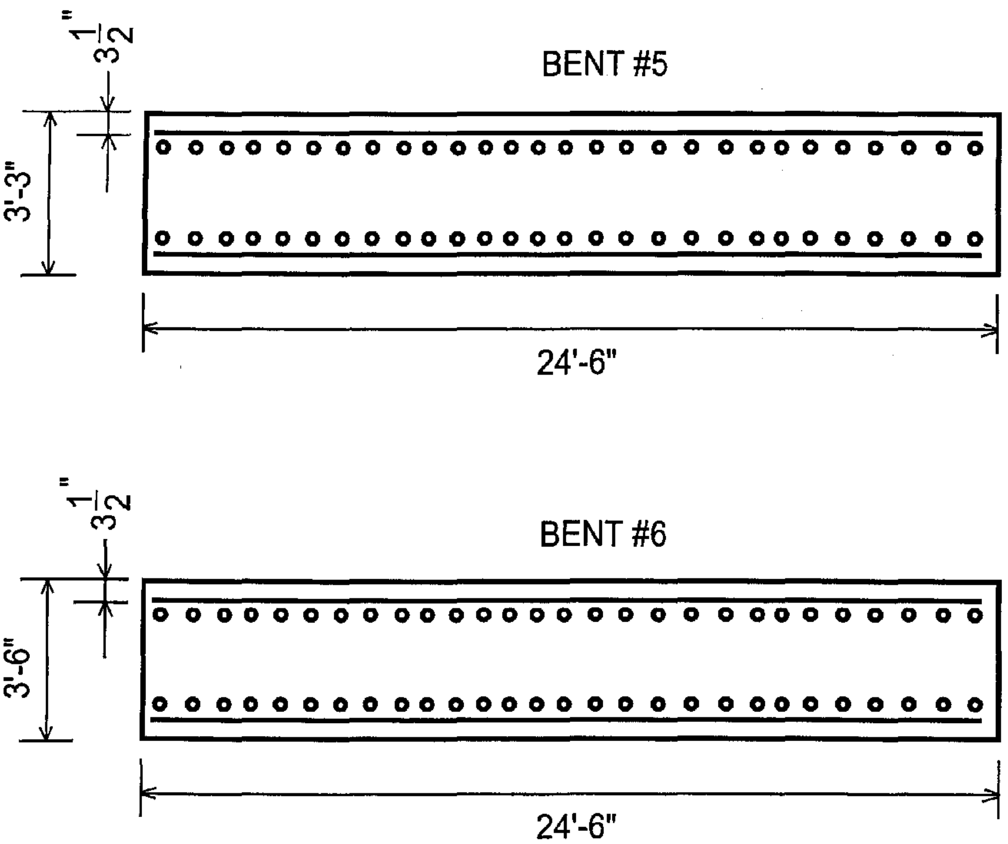

Figure 51. Dimensions and reinforcement for load frame footings (1'=305 mm, 1"=25.4 mm)

It should be noted that in the analysis of Bent #6, a larger lateral load was predicted to be carried by the bend. This resulted in larger forces in the supports which required a footing 42 in. (1067 mm) thick. Otherwise, the planar dimensions and reinforcement are identical to the footings of Bent #5.

The final configuration of the load frame, load frame footings and horizontal Dywidag bars and grade beam completing the load path are shown in Fig. 53.

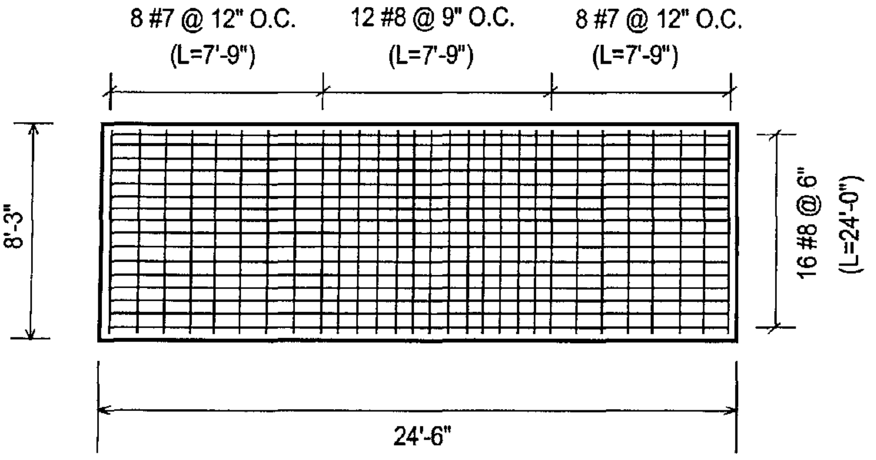

TOP

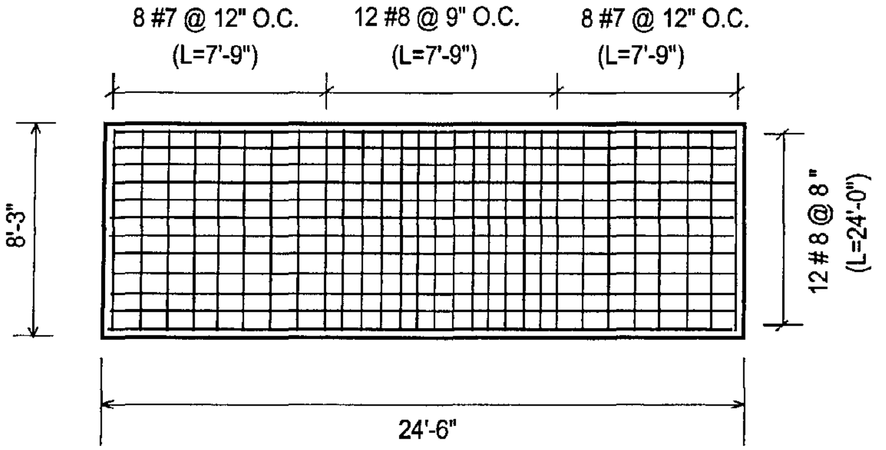

BOTTOM

Figure 52. Reinforcement details for load frame footings (1'=305 mm, 1"=25.4 mm)

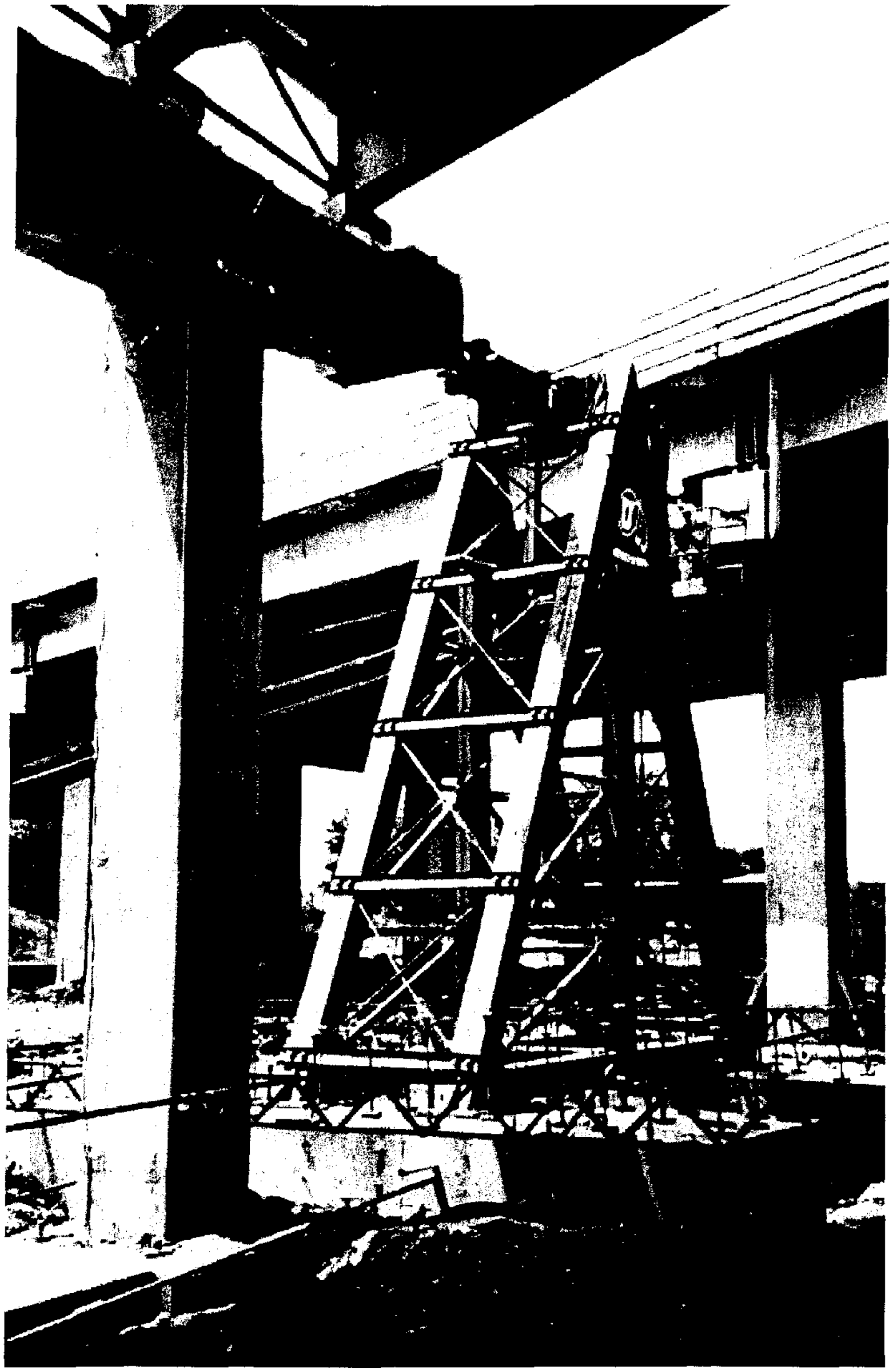

Figure 53. Load frame showing footing details and horizontal Dywidag bars

6. BENT #5 IN THE AS-BUILT CONDITION

After the 1994 Northridge earthquake, inelastic pushover analyses were performed of the failed bridges and predictions of the analyses were compared with observed behavior (Seible and Priestley 1999). This provided a rapid and valuable insight into the ability of simple pushover analyses, based on rational section analyses, to predict observed location and type of damage. Bridges designed and built before the 1971 San Fernando earthquake did not include considerations for inelastic structural response or ductile design detailing. For example, low transverse reinforcement ratios in columns, typically #4 bars at 12 in. centers (12 mm bars at 300 mm centers) were provided nominally without consideration of column size or strength. Current engineering capacity requirements would have resulted in transverse reinforcement ratios exceeding the nominally provided ones by a factor of 8 to 10 or more.

In this research, the finite element program DRAIN-2DX (Prakash et al. 1992) was used to perform static nonlinear pushover analyses of Bent #5 in the as-built condition. An estimate of the peak lateral load and maximum horizontal displacement were obtained for the as-built Bent #5. The bent dimensions and support conditions are shown in Fig. 54; the cyclic lateral load for the test was applied at the top of the beam cap through the steel load frame described in section 5. The support conditions at the foundation were neither fixed nor pinned. Therefore, the resistance of the piles was modeled using vertical springs. The location of the springs corresponded with the piles, and the spring constants were estimated based on the axial stiffness of the pile and Dywidag system. The specified concrete strength was 3 ksi (21 MPa), and the yield strength of the longitudinal and the transverse reinforcement was 40 ksi (276 MPa). Fiber element meshing was used to represent the cross-sections.

Analysis of as-built Bent #5

By performing a static pushover analysis for the bent, an estimate of the peak lateral load and the maximum horizontal displacement were determined. The yielding sequence of the structural members was observed, and member forces were calculated at the ultimate displacement. This information was necessary for the rehabilitation design of Bent #6 using FRP composites. To construct the 2-D model of the structure, the existing conditions had to be evaluated and compared with the original design plans. The reinforcement details of the bent were presented in Fig. 4; the columns had a reinforcement ratio of 1.6%. It can be seen that the column transverse reinforcement was inadequate in the lap-splice region, and the anchorage of the longitudinal reinforcement in the pile cap and in the cap joint was insufficient. In addition, there are no transverse hoops in the column cap-beam connection. Since the lap splice in the column base is mostly unconfined, it would break down under cyclic inelastic action. The spacing of ties in the plastic hinge region at the top of the columns was insufficient. In addition, the anchorage of the piles into the pile cap was insufficient. These deficiencies are identified in Fig. 55.

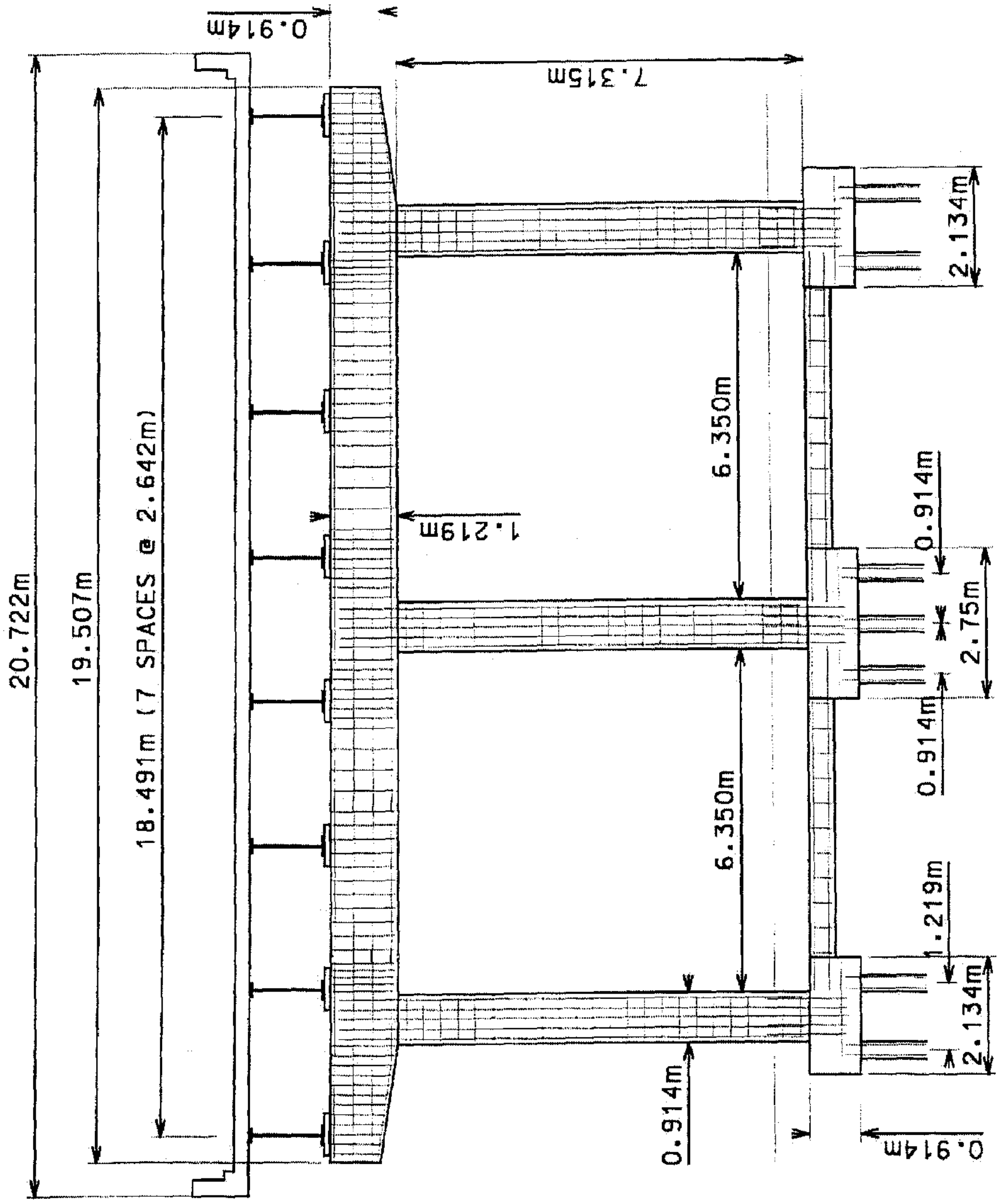

Figure 54. As-built Bent #5 dimensions and support conditions

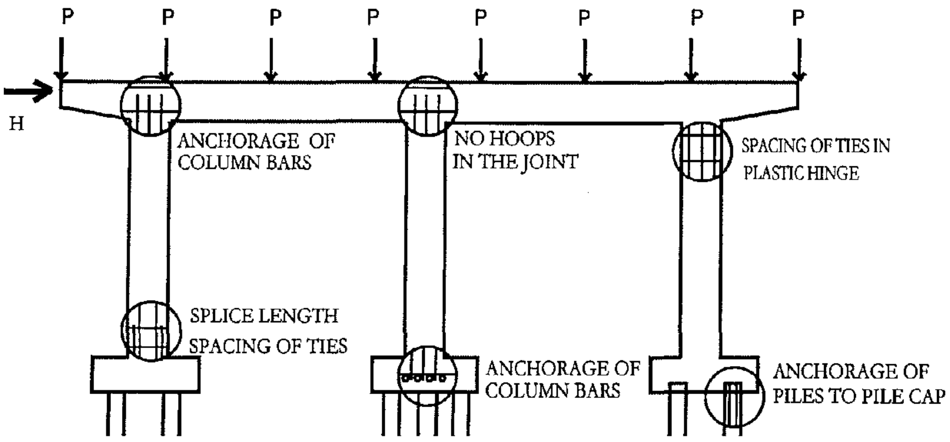

Figure 55. Reinforcement details showing deficiencies of Bent #5 for resisting large earthquakes

The support conditions after implementing the modifications, described in Fig. 12 were neither fixed nor pinned. These modifications involved anchoring of the piles to the pile cap by epoxying a 32-mm Dywidag bar into the four corner piles of each footing. Therefore, the tension-compression resistance of the piles was modeled using axial spring elements. The location of these elements corresponded with the piles, and the spring constant values were estimated based on the axial stiffness of the Dywidag bar-pile system. Values ranging from pinned to fixed support conditions were assumed. From the results of the analysis it was obvious that the values of the spring constants have a great influence on the outcome. After testing Bent #5, and based on the maximum observed pile cap vertical movement (3.8 mm), the spring constant values (K_1 and K_2 in Fig. 4) were calibrated to provide a more realistic model. This soil spring calibration was done by matching the measured pile cap rotations at any force level, with the pile cap rotations from analysis.

The majority of the concrete cover on the beam cap was loose and was removed; therefore, in the model, the outside 50 mm concrete was not included. A stress-strain curve corresponding to the specified concrete strength of 3 ksi (21 MPa) was used; the steel reinforcement was modeled using an elasto-plastic stress-strain behavior with a yield stress of 40 ksi (276 MPa). Strain hardening was not considered. Figure 56 shows the model of the bent, including the location of the elements, the gravity and horizontal loads, and the boundary conditions. Each of the eight steel girders carried a gravity load equal to 240 kN (54 kip) which was modeled as a point load at that location on the beam cap. The weight of the columns was 144 N (32 kip) was included as a concentrated load at the bottom of the columns. Fiber element meshing was used to represent member cross-sections. Due to the loading system configuration, lateral movement was partially prevented at the level of the pile caps (nodes 1, 2 and 3); the three supports were modeled as springs in compression with axial stiffness only.

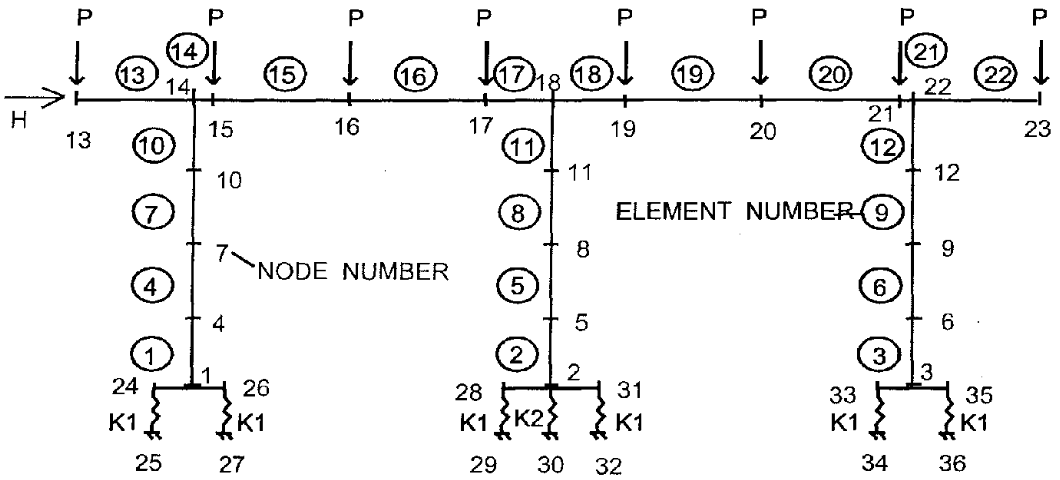

Figure 56. Finite element model for Bent #5

The pushover curve for Bent #5 in the as-is condition from the analysis is shown in Fig. 57 as a solid line. The magnitude of the peak lateral force from the analysis was 1,552 kN (349 kip) after which the load decreased gradually. The first yielding occurred at the top section of the middle column at a displacement of 30 mm (1.18 in.), and a horizontal load of 876 kN (197 kip). A total of seven elements yielded in the sequence shown in Fig. 57, where the yielded elements can be identified using Fig. 56. The beam cap yielded in one location and was assisted in its performance by the high axial loads. It is clear that a mechanism was formed, and with the extensive generation of plastic hinge regions, the structure could not take additional horizontal load.

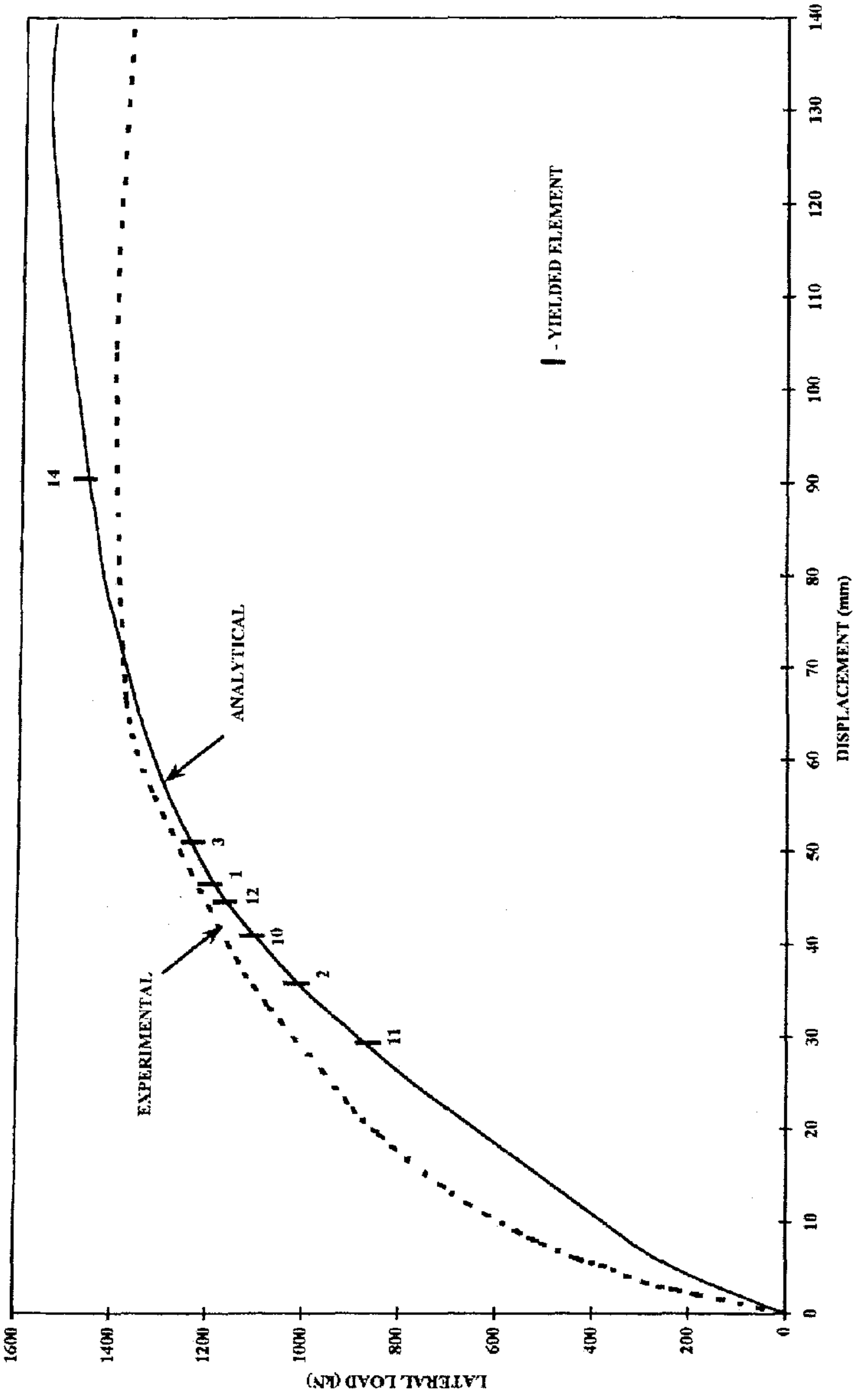

Figure 57. Comparison of analysis and experiment for Bent #5

Test of the as-built Bent #5

The loading condition is shown in Fig. 58 and Fig. 59. The reaction frame was positioned between the Southbound (which was in service) and the Northbound bridges. The horizontal load was applied at the beam cap level. To pull on the bent, the load was transferred to the far end of the bent by twenty 13-mm (1/2 in.) diameter prestressed tendons of ultimate strength 1,725 GPa (250,000 ksi) as shown in Fig. 41 and 42. The tendons were prestressed to only 6 MPa (870 psi) to take out the sag in the tendons and the slippage in the anchorage system. This corresponds to an axial compressive stress of 14 kPa (2 psi) which is not significant. The connection details were such that there is no difference between pulling from the far end and pushing from the near end. Half of the originally present dead load from the deck was acting on each bent. This dead load was transmitted to the beam cap by welded plate girders, bearing on eight reinforced concrete pedestals.

In order to monitor the behavior of the structure during the test, strain gages, displacement transducers, LVDT-s, and a load cell were used, as shown in Fig. 58 and Fig. 59. A horizontal quasi-static cyclic load was applied at the beam cap level. This was the most convenient and economical manner for applying the transverse load. The beam cap joints were in compression and shear. In the first part of the test, a force-controlled test was performed with increasing load steps starting at 180 kN (40 kip). In each load step, the load was applied for three cycles, and each cycle had a push and a pull segment. The applied load is shown in Fig. 60 and the applied displacement history is shown in Fig. 61. The maximum load reached was 1566 kN and the maximum displacement was 137 mm (5.4 in). After the first yielding had occurred, the test was continued by controlling the lateral displacement. The displacement was increased by a fraction of the yield displacement in subsequent steps. The displacement ductility of the bent was calculated as the ratio of the ultimate displacement to the yield displacement.

The load-displacement hysteresis curve for Bent #5 is given in Fig. 62. The first yielding occurred at the top of the middle column. The first yielding of the column occurred at a lateral displacement of 29 mm (1.14 in.), corresponding to a lateral load of 801 kN (180 kip). These values are within 4% and 9% of the values obtained form analysis, respectively. From a bilinear approximation of the load-displacement behavior, the displacement ductility of the bent at the end of the test was found to be equal to 2.8, as shown in Fig. 62. This is reasonable for bridges of this type built in the 1960's, which were not designed for earthquakes. However, the bridge was designed for lateral wind loads.

To draw the "backbone curve," the FEMA 273 (1997) guidelines were followed. The envelope of the load-displacement curve with the analytical pushover curve is shown with a dashed line in Fig. 57. There is general agreement between the analytical and experimental results. The experimental backbone curve shows a higher initial stiffness, but the peak loads are within 10%. This is due to discrepancies in the material properties, modeling issues of the analysis program, as well as movement of the pile caps.

The location of the plastic hinges was identical to the analytical results given in Fig. 57. Plastic hinges formed at the base and the top of the columns, and in the beam cap at one location. The sequence of plastic hinge formation is shown in Fig. 57 from node 11 to node 14. Current seismic design guidelines allow for development of plastic hinges at both the top and bottom of the column.

For the purpose of comparing the as-built Bent #5 results to the other two tests performed in this research, the overall envelope of the hysteresis curves was constructed according to the FEMA 273 (1997) guidelines and is shown in Fig. 63. The envelope shows a higher load capacity in the pull direction as compared to the push direction.

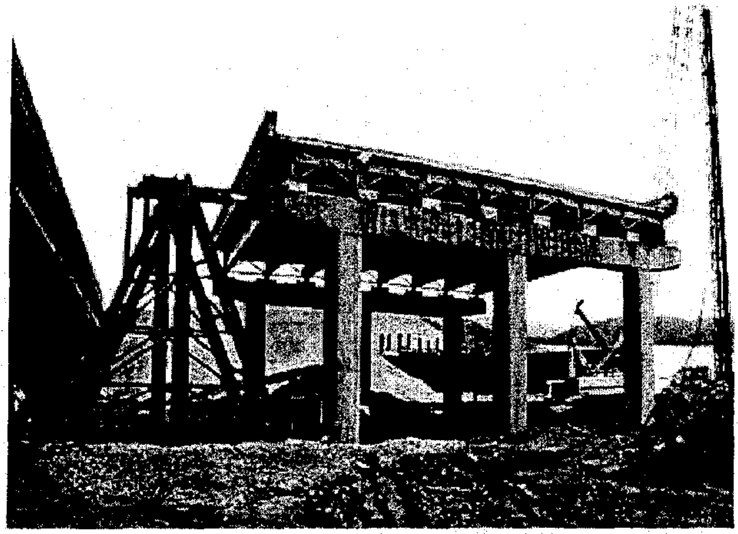

Figure 58. In-situ lateral load test of Bent #5

Damage assessment of Bent #5

Significant diagonal tension cracks formed in the beam cap-column joint region, revealing a gradual degradation of the concrete as shown in Fig. 64. After the test, the loose concrete was removed from the joint, and it was apparent that there was not much left from the outside 100 mm (3.9 in.) to 150 mm (5.9 in.) layer. Flexural cracks developed at the top of the columns that opened as the bending capacity was reached. These cracks had various widths with the largest being at the interface of the column and the beam cap which reached approximately 2 mm (3/32 in.) as shown in Figs. 64-66. The cracks went all around the column perimeter in the plastic hinge region. The first layer of the column longitudinal reinforcement extending into the joint was exposed on the south

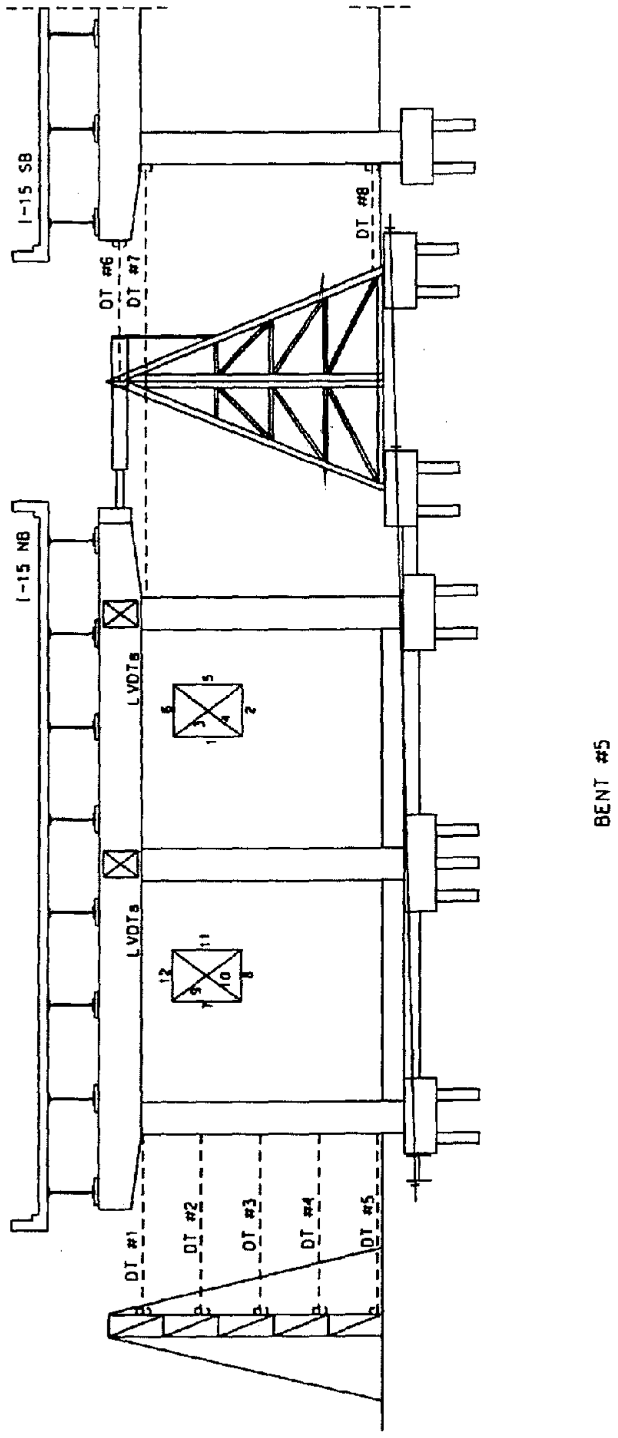

Figure 59. Displacement transducer and LVDT locations for Bent #5

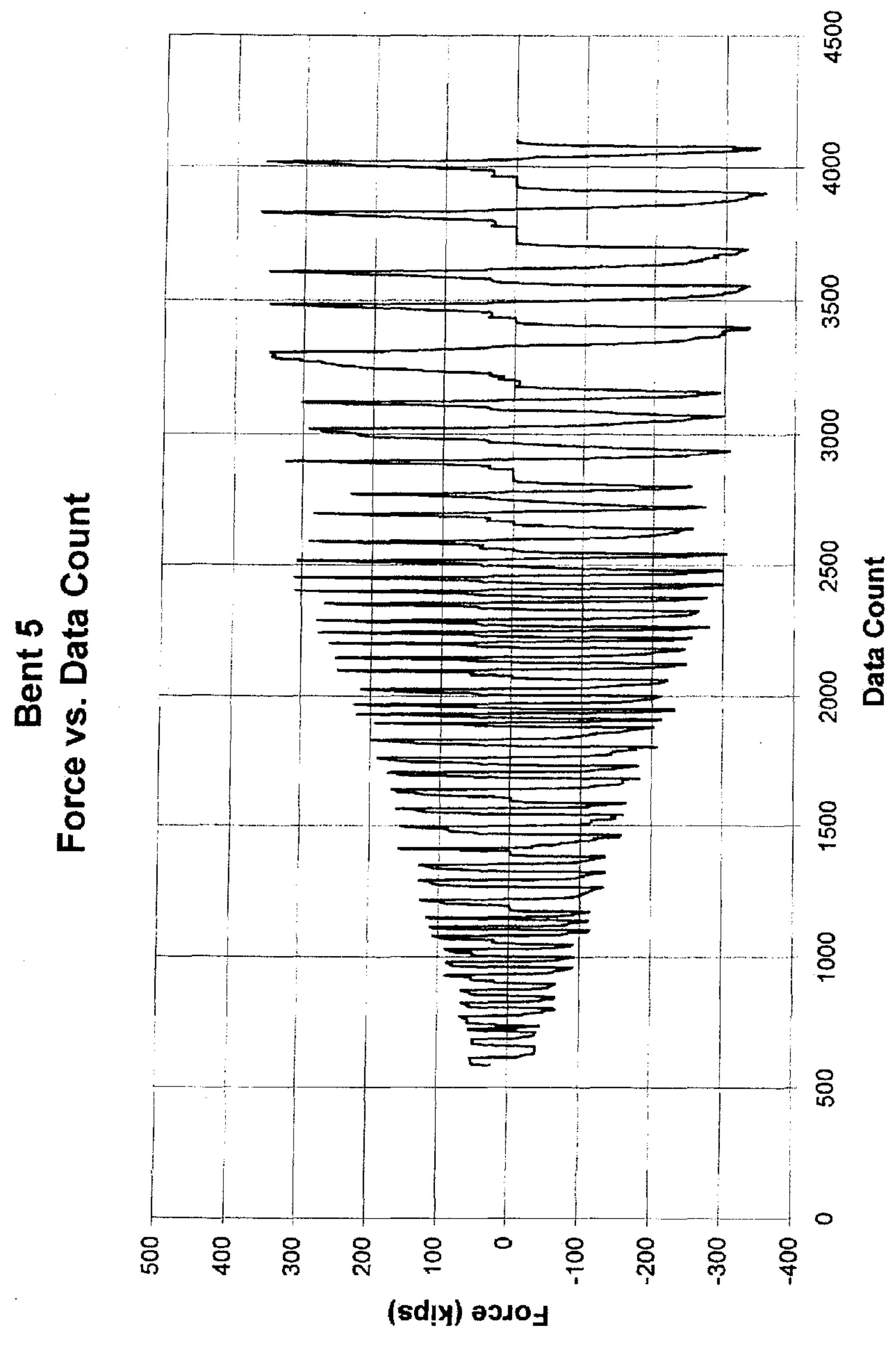

Figure 60. Actual applied lateral load history on Bent #5 (1 kip = 4.448 kN)

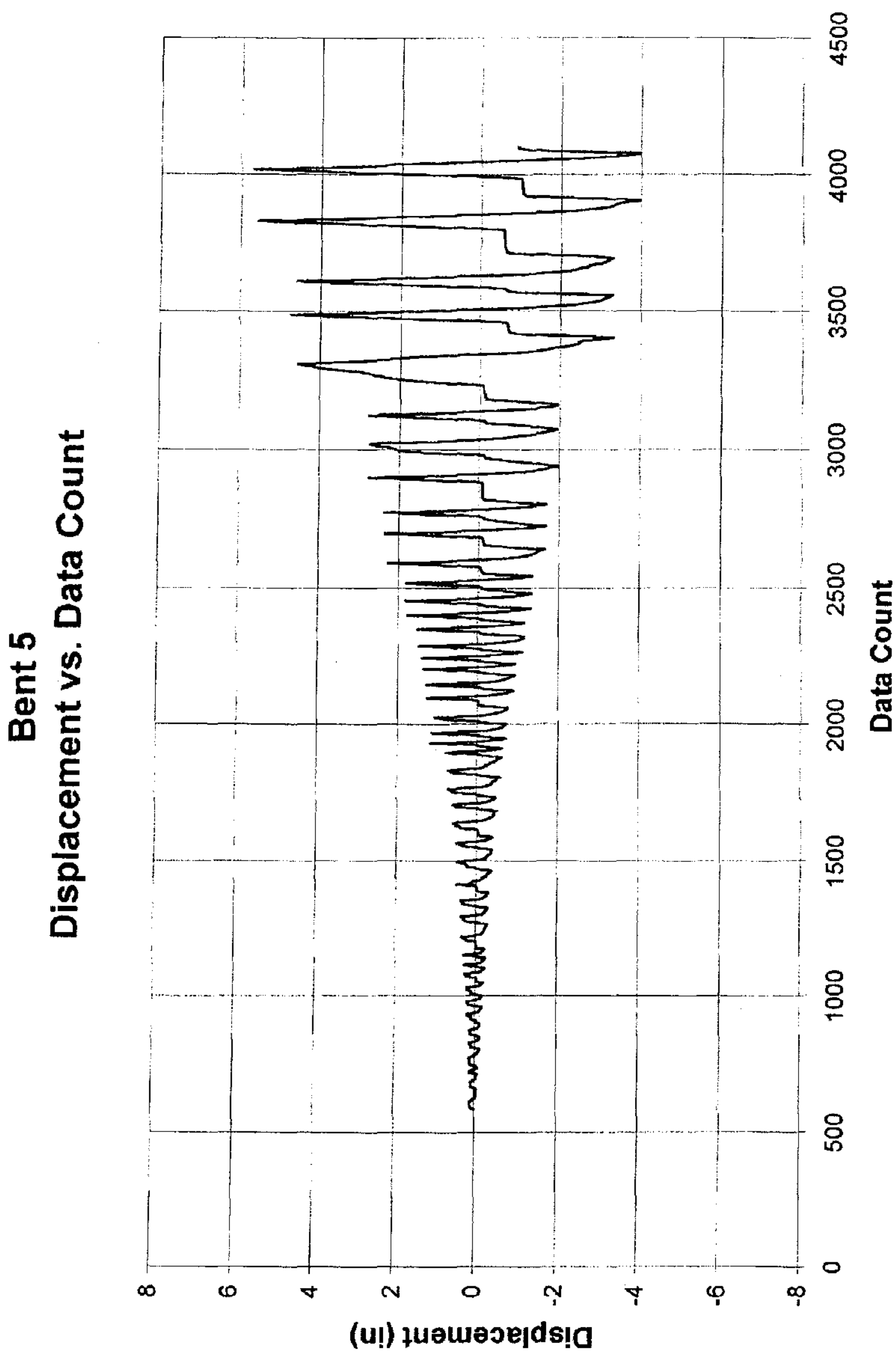

Figure 61. Applied lateral displacement history on Bent #5 (1 in. = 25.4 mm)

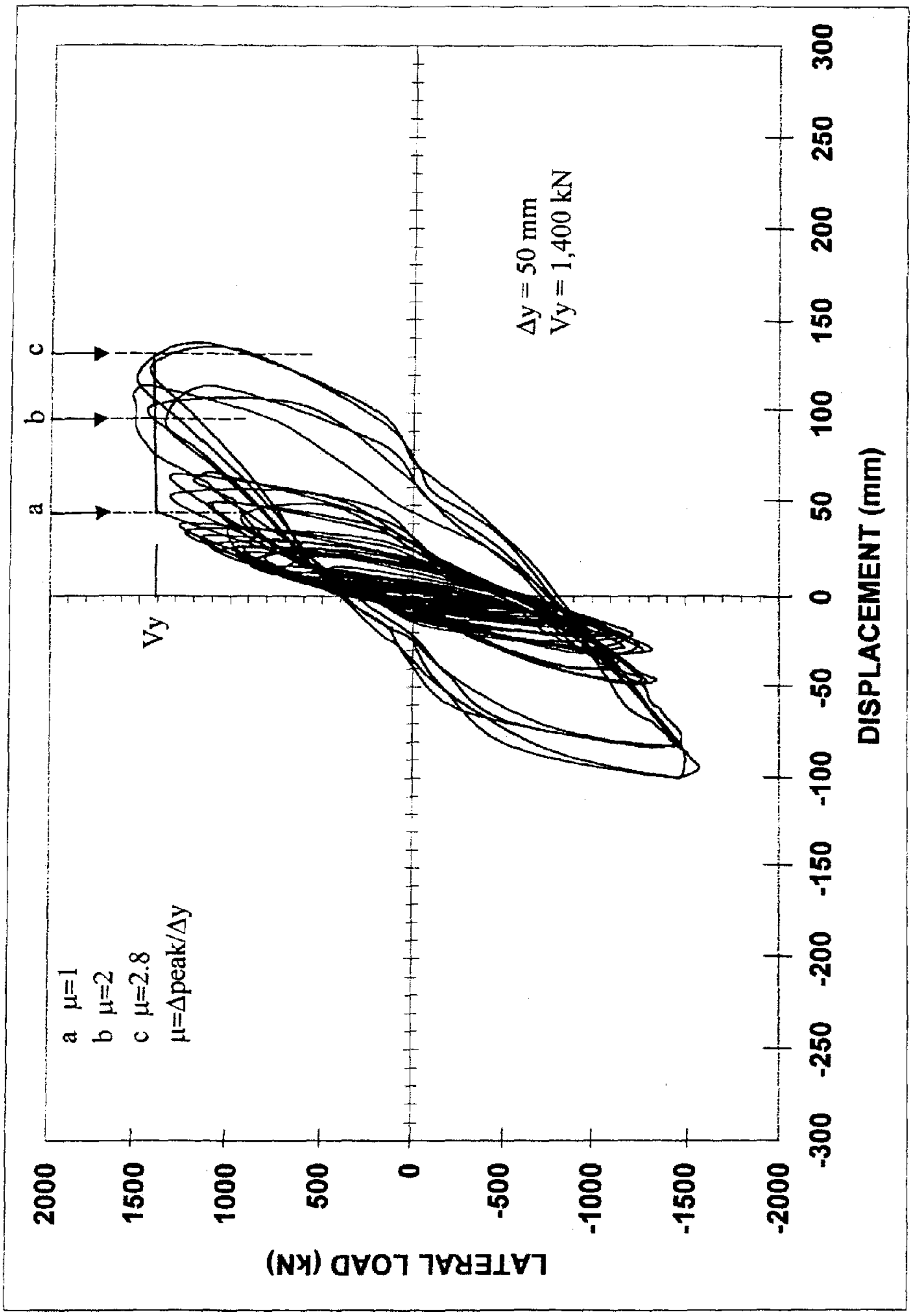

Figure 62. Hysteresis curves for Bent #5

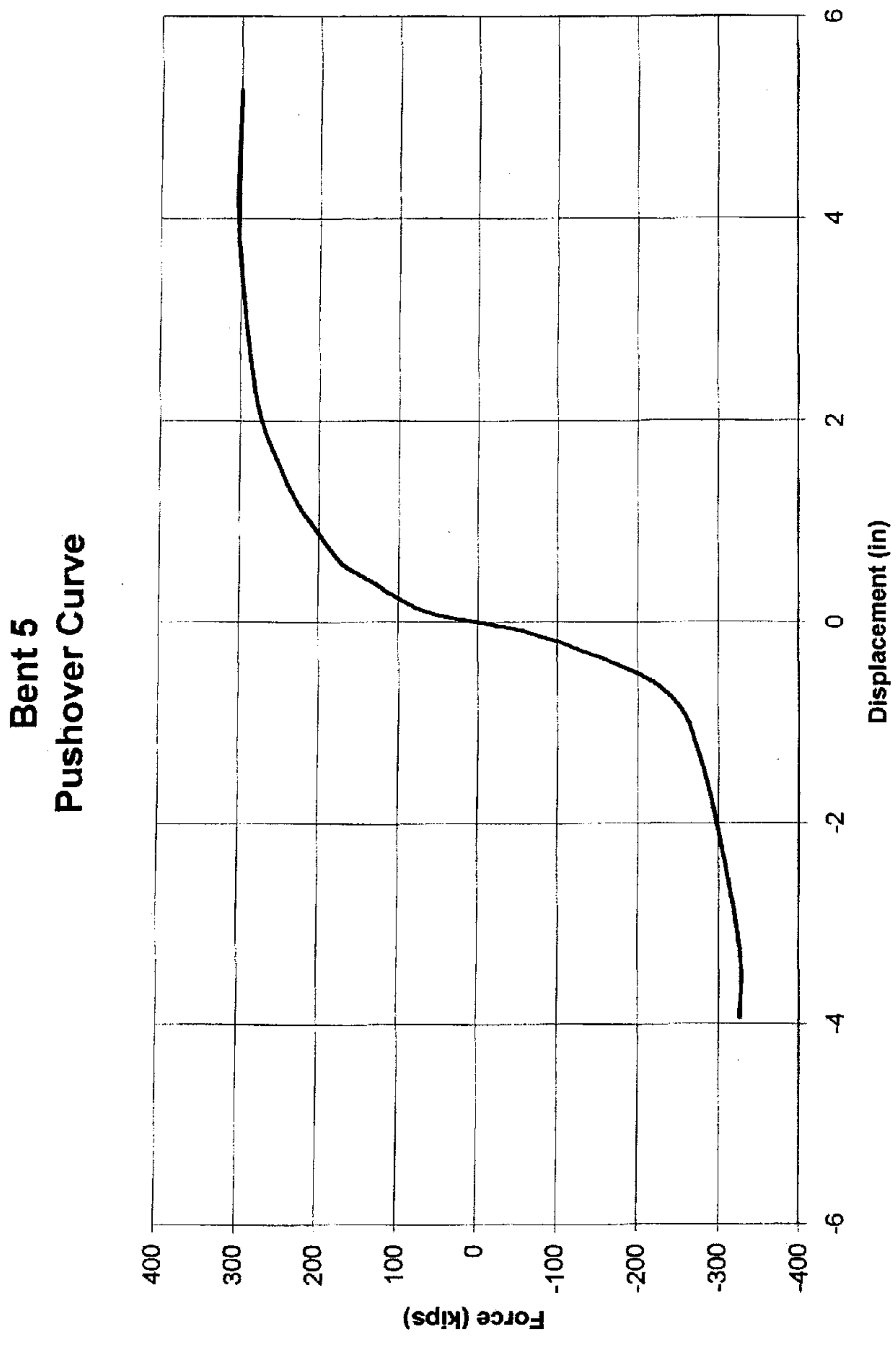

Figure 63. Envelope of hysteresis behavior for Bent #5 (1 kip = 4.448 kN, 1 in. = 25.4 mm)

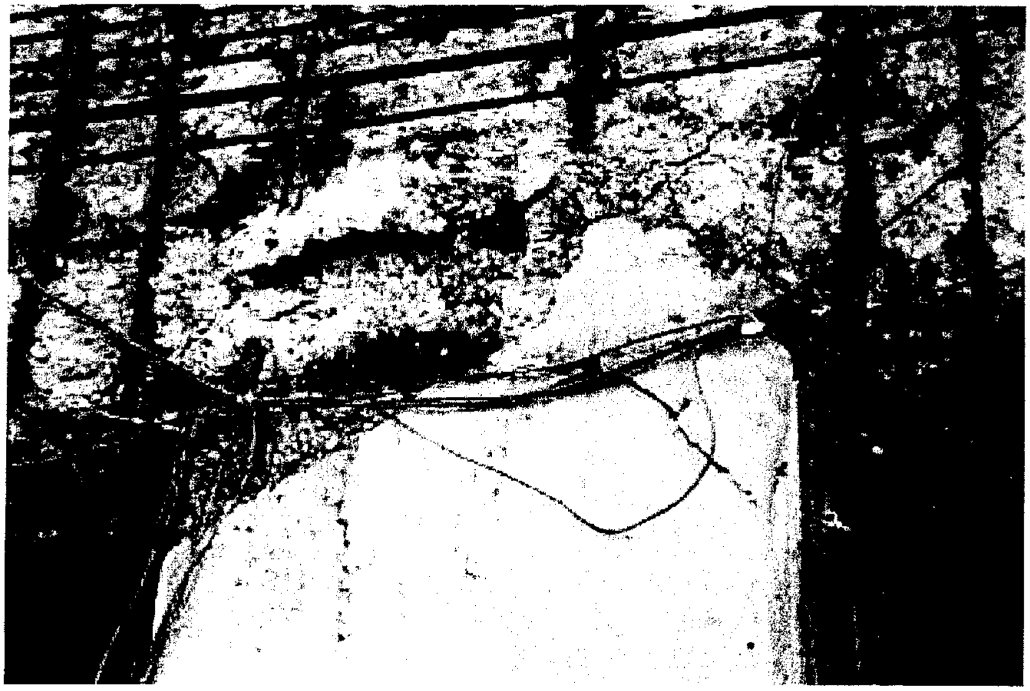

Figure 64. Damage in the interior joint of Bent #5

Figure 65. Close up of beam cap – column joint on Bent #5

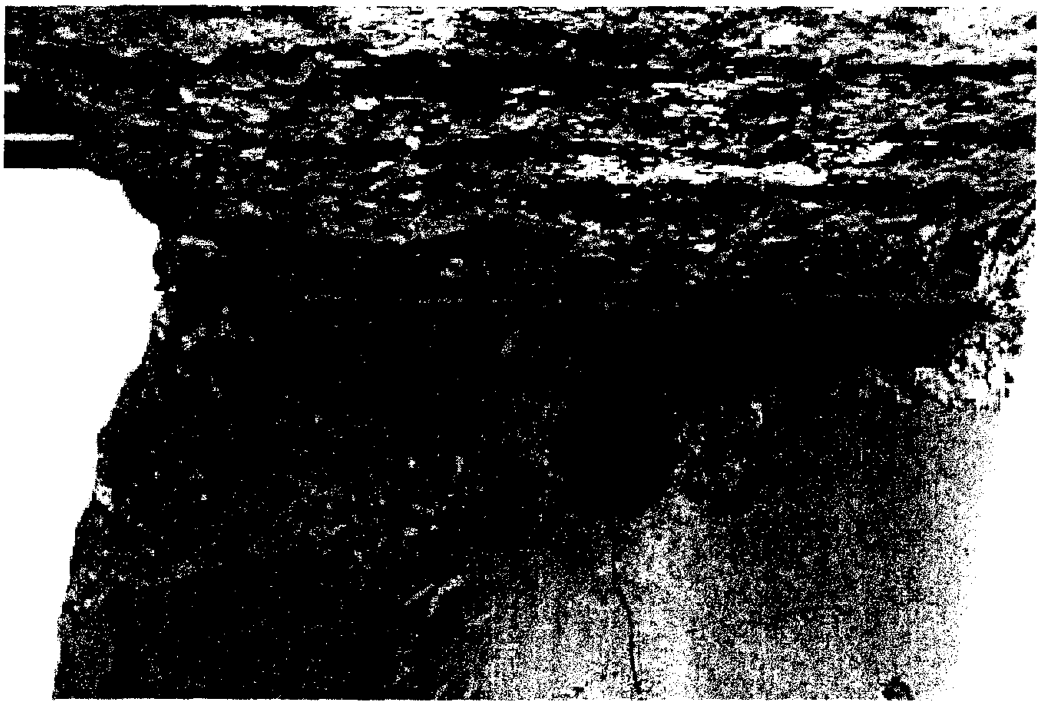

Figure 66. Damage at the beam cap – column joint of the interior column of Bent #5

side, suggesting bar slippage and severe deterioration of reinforcement bond. This was observed after removal of the concrete for the joint of the interior column as shown in Fig. 67. In addition, at the substructure level, considerable spalling of the concrete at the top of the pile cap around the column perimeter was observed.

The actual distortion of the beam cap – column joints was determined from the LVDT measurements. Figure 68 shows the diagonal displacement of the beam cap to column joint nearest to the actuator. The maximum diagonal measurement was 3 mm (0.12 in). The shear strain in the same joint is shown in Fig. 69; the maximum strain is 0.003 in compression. The principal tensile stress in the interior beam cap – column joint was evaluated as shown in Fig. 70. The horizontal and vertical shear forces in the joint are: $V_{jh} = 1109+511=1620\ kN$; $V_{jv} = 3118-784 = 2334\ kN$. The corresponding horizontal and vertical joint shear stresses are:

$$v_{j,v} = \frac{V_{j,v}}{h_b b_b};\ v_{j,h} = \frac{V_{j,h}}{h_c b_c} \tag{6.1}$$

where h and b are the effective depth and beam of a section and subscripts b and c denote beam and column, respectively. The resulting stresses are $v_{j,v} = 2.28\ MPa$ *and* $v_{j,h} = 2.20\ MPa$. The axial compressive stress in the joint is calculated as: $\sigma_a = -\ 553{,}000/(914\ x1118) = -\ 0.54\ MPa$. The principal tensile and compressive stresses are obtained as:

$$\sigma_{t,c} = \frac{\sigma_a}{2} \pm \sqrt{\frac{\sigma_a^2}{4} + v_j^2} \tag{6.2}$$

where v_j is the average of the horizontal and vertical joint shear. From equation (6.2), the principal tensile stress is obtained as $\sigma_t = 1.99\ MPa$, and the principal compressive stress as $\sigma_c = 2.53\ MPa$. Thus, the principal tensile stress is $0.44\ (f'_c)^{0.5}\ MPa$ or $5.26\ (f'_c)^{0.5}\ psi$, which indicates that the joint has developed full diagonal cracks and joint degradation is anticipated (Priestley et al. 1996). This is clearly shown in Fig. 67.

Figure 67. Bond detrrioration and bar slippage at interior beam cap – column joint

Strain gages were attached to reinforcement in the columns, beam cap and on the Dywidag bars going from the pile cap into the piles of Bent #5 as shown in Fig. 71. These gages demonstrated the presence of flexural hinges when the strain exceeded the yield strain of 1380 microstrain. As illustrated in Fig. 72, strain gage 6 at the bottom of the exterior column closest to the actuator exceeded the yield strain early in the loading cycles. The strain at the end of the test reached 1.3% in./in. or approximately 10 times the yield strain. Figure 73 shows the strain in gage 24, at the top of the same column, and it exhibits similar behavior. Figures 74 and 75 show a force versus strain diagram for two of the columns of Bent #5. The diagrams show that the gage at the top of the column (gage 24) yields in the push direction whereas, strain gage 2 at the bottom of the column yields in the opposite direction. This suggests the development of an S–shape deformation pattern.

The displacements of the exterior column were recorded at 6 ft (1.829 m) intervals using displacement transducers 1 to 5, as shown in Fig. 59. The envelopes of the displaced shape at various drift levels both in the push and pull direction are shown in Fig. 76. The curve shows the displaced shape of an exterior column but it represents the overall transverse deformation of the bet. It can be seen that an S-shape has begun to form due to the yielding occuring at the top and bottom of the columns.

It must be noted that the data presented to this point do not include the effect of soil-pile-structure interaction, which as shown in Fig. 77 are significant. Figure 77 shows the displacement of the pile cap for Bent #5 which reveals that a maximum displacement of 0.8 in (20 mm) was reached. This is approximately 13 percent of the displacement reached at the beam cap of Bent #5. The topic of soil-pile-structure interaction is treated in detail in a companion report (Cook, Lawton and Pantelides 2000).

The energy dissipated during the cyclic loading of the bridge bent represents a measure of the damage suffered by the bent. The cumulative dissipated energy was calculated as the area under the hysteresis loops and is shown in terms of the load cycle number in Fig. 78. It can be seen that approximately 50% of the energy is dissipated in the last six cycles. A plot of the cumulative energy dissipation versus maximum displacement at each load step is shown in Fig. 79. The curve is almost linear after an initial steep slope at small displacements, indicating that the energy is heavily dependent on the maximum displacements reached during testing. As observed in Fig. 78, half of the energy was dissipated after the load step corresponding to the maximum deformation of 3 in. (76 mm).

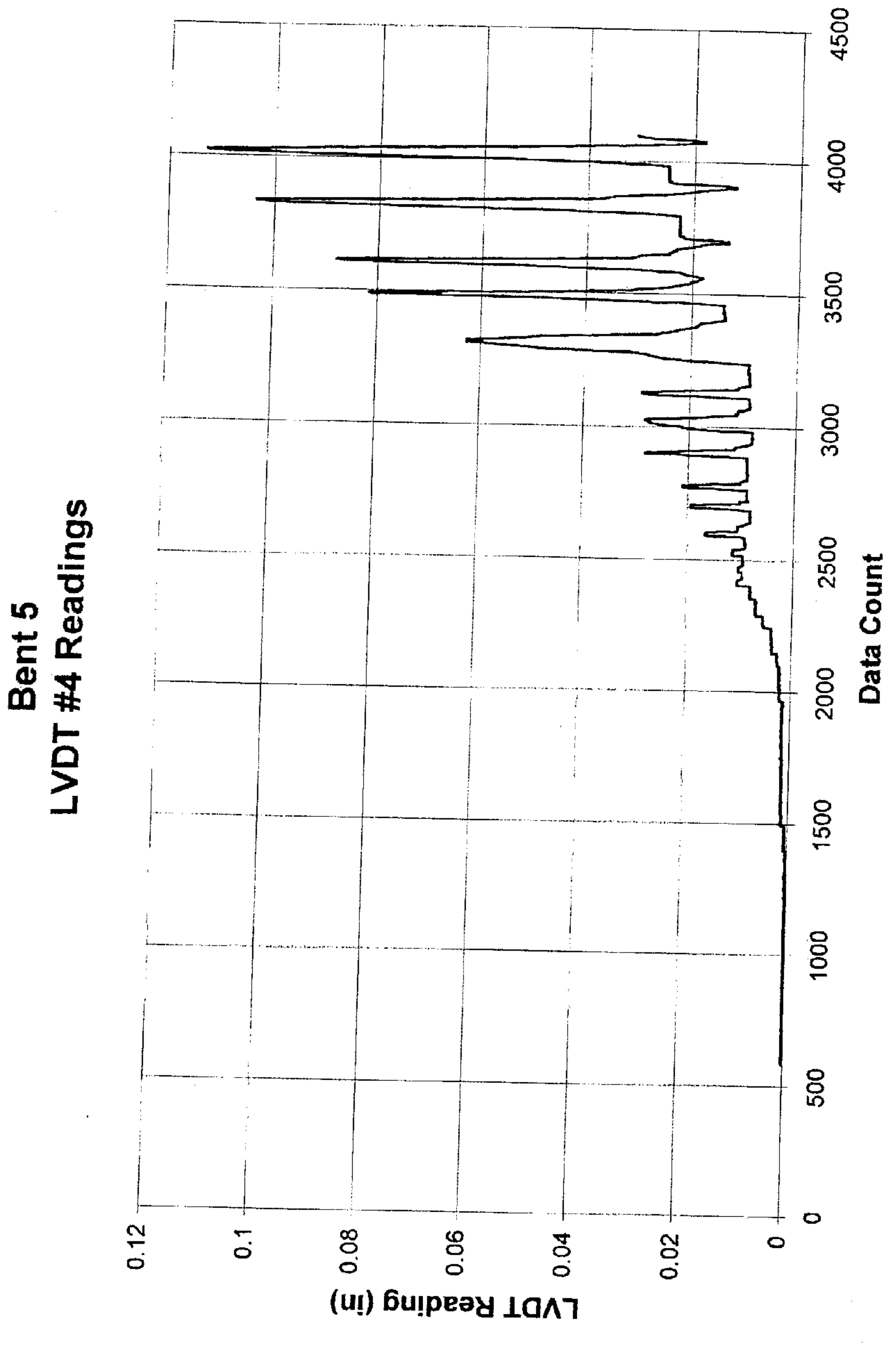

Figure 68. Displacement of diagonal along exterior beam cap – column joint on Bent #5 (1 in. = 25.4 mm)

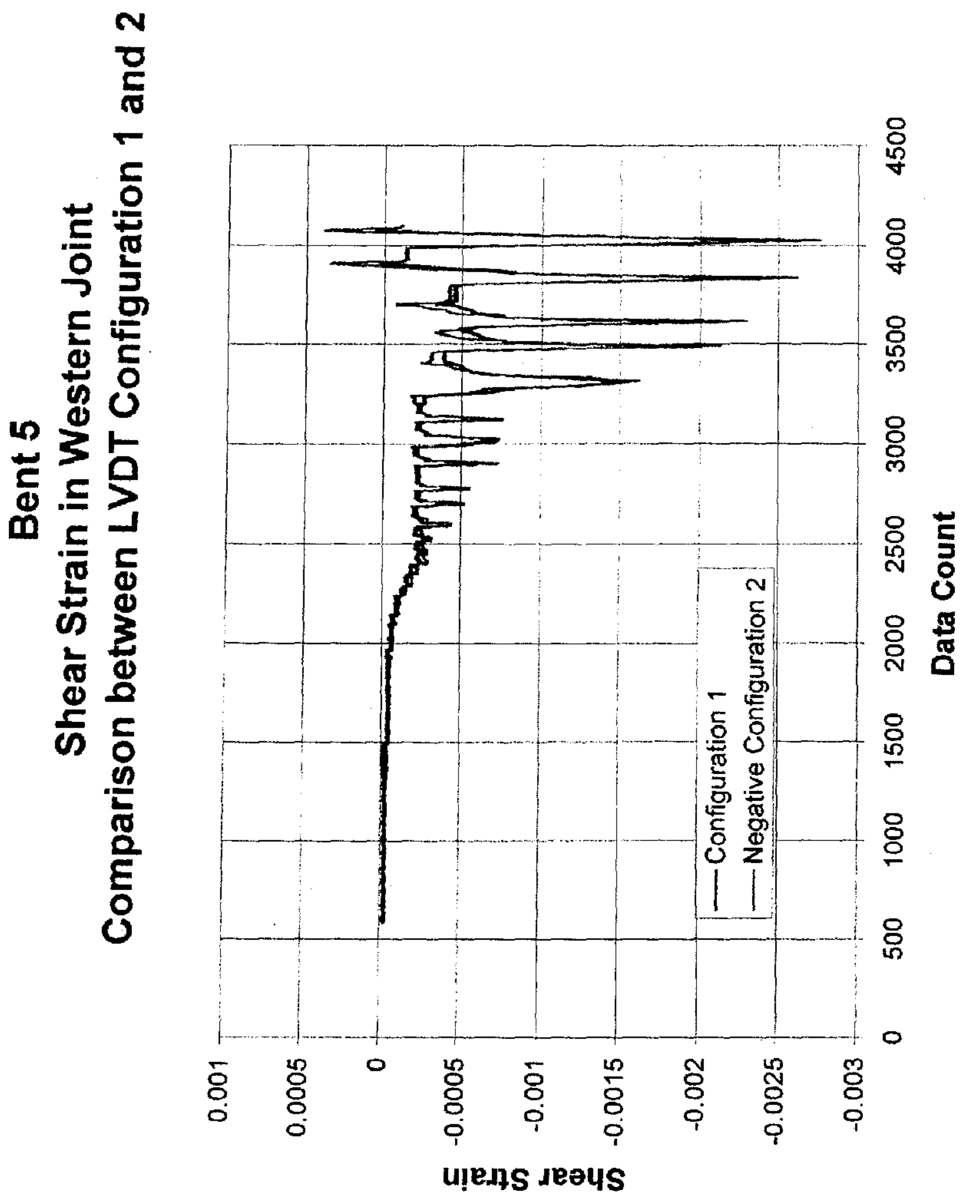

Figure 69. Shear strain at exterior beam cap –column joint of Bent #5

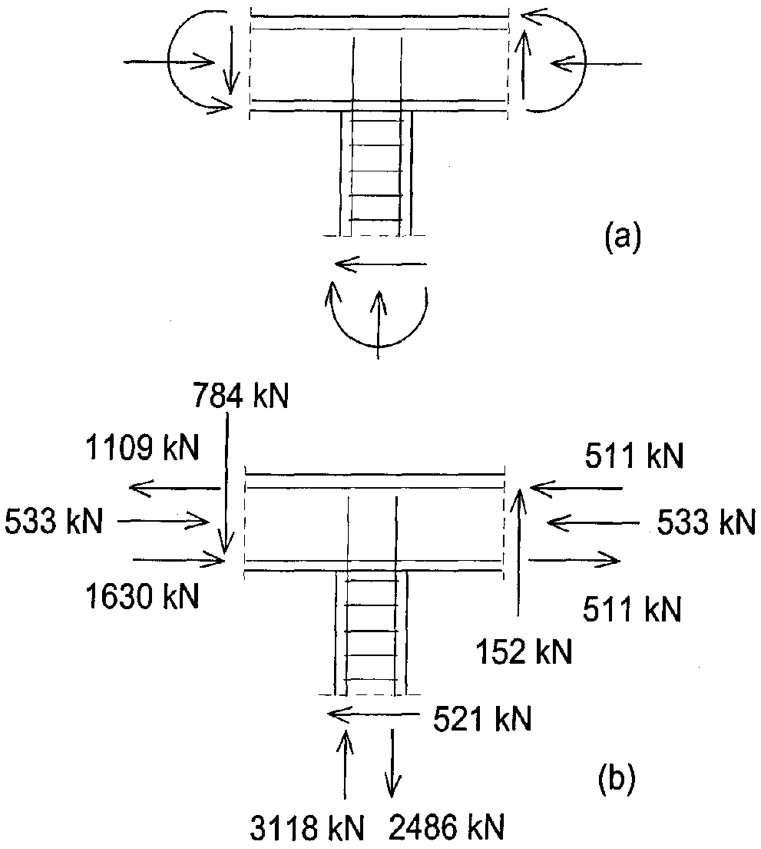

Figure 70. Joint forces at beam cap –column interior joint: (a) member forces, (b) corresponding force couples

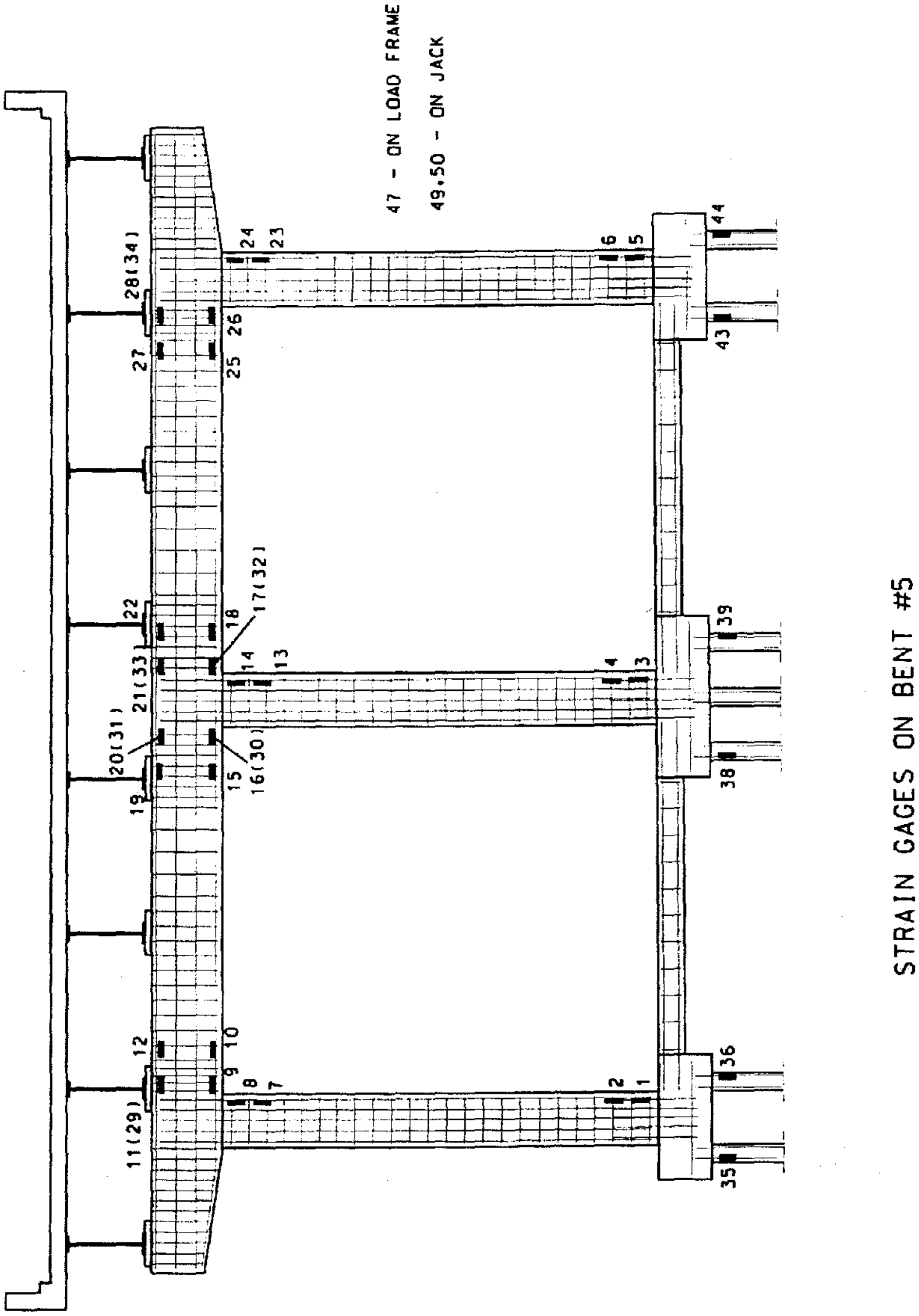

Figure 71. Strain gage locations for Bent #5

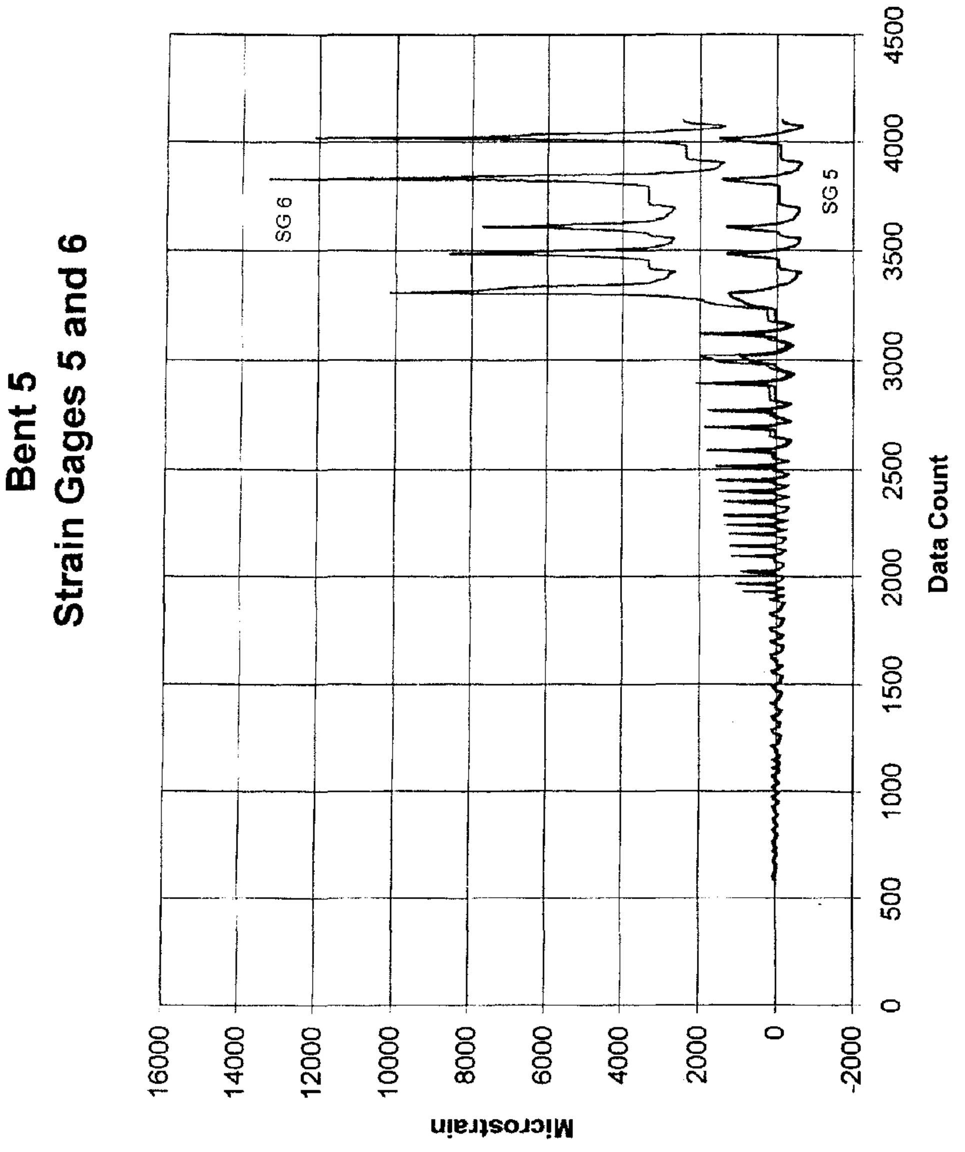

Figure 72. Strain gages 5 and 6 at the bottom of the exterior column on Bent #5

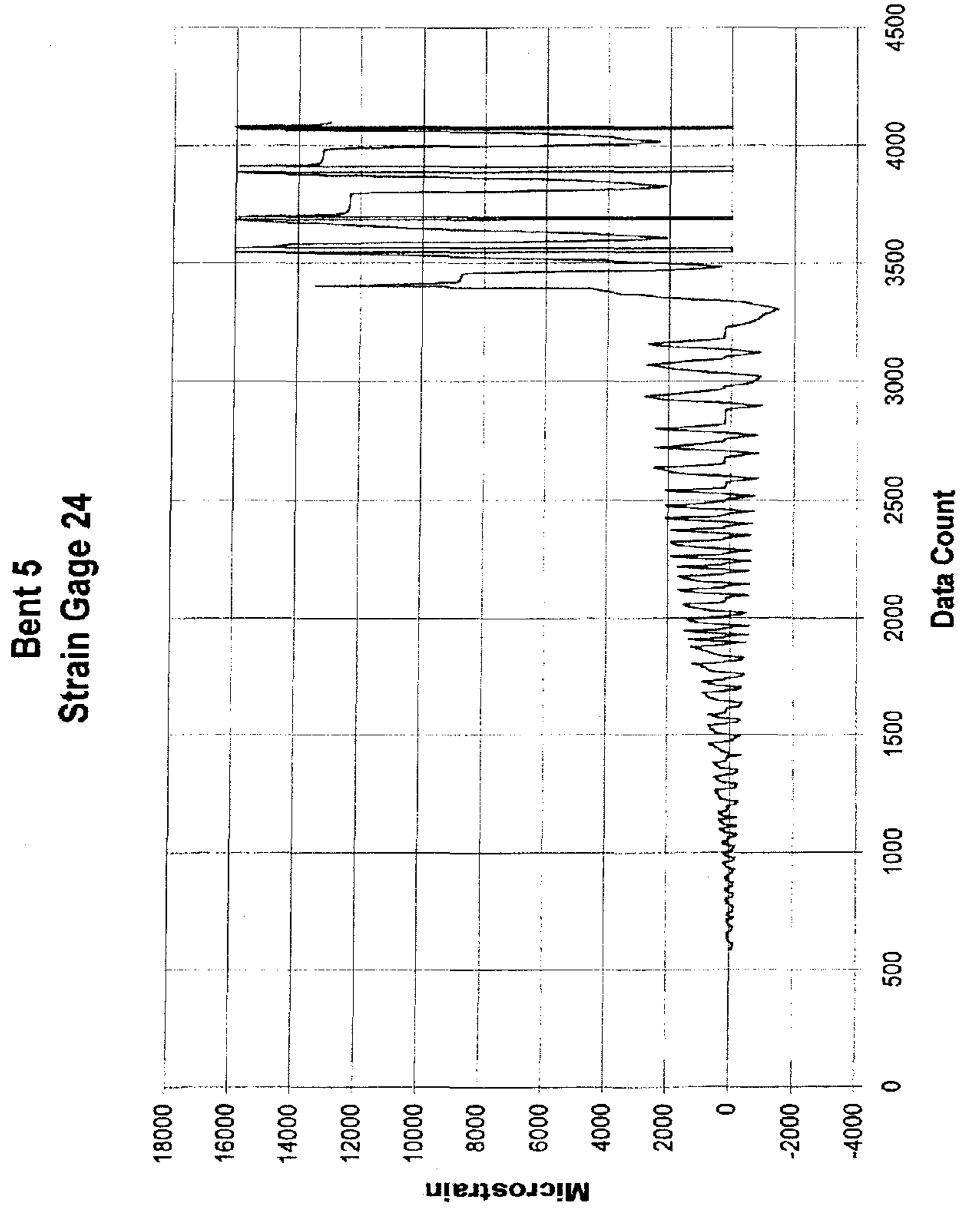

Figure 73. Strain gage 24 at the top of the exterior column of Bent #5

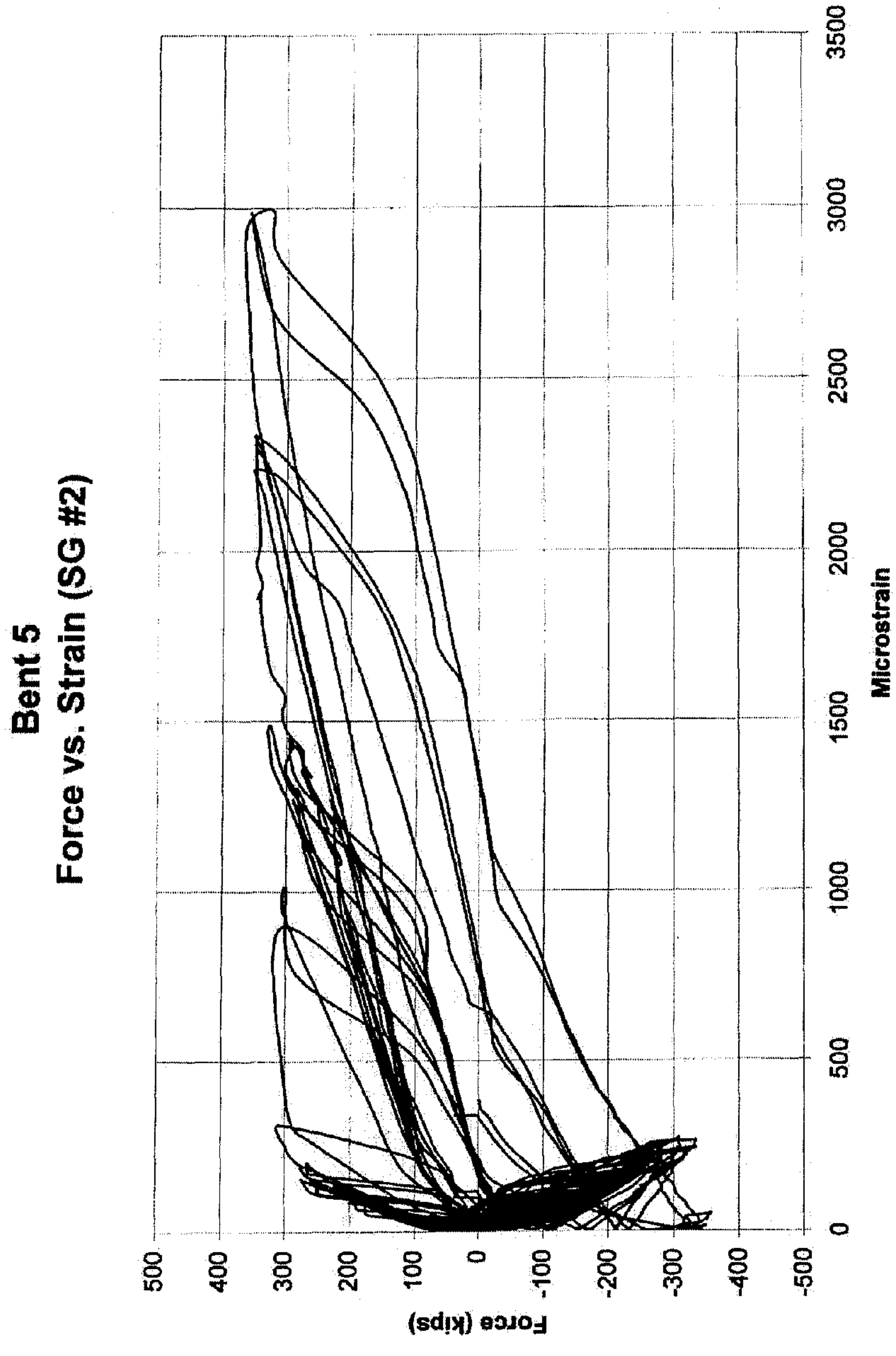

Figure 74. Force versus strain diagram for gage 2 at bottom of the exterior column of Bent #5 (1 kip = 4.448 kN)

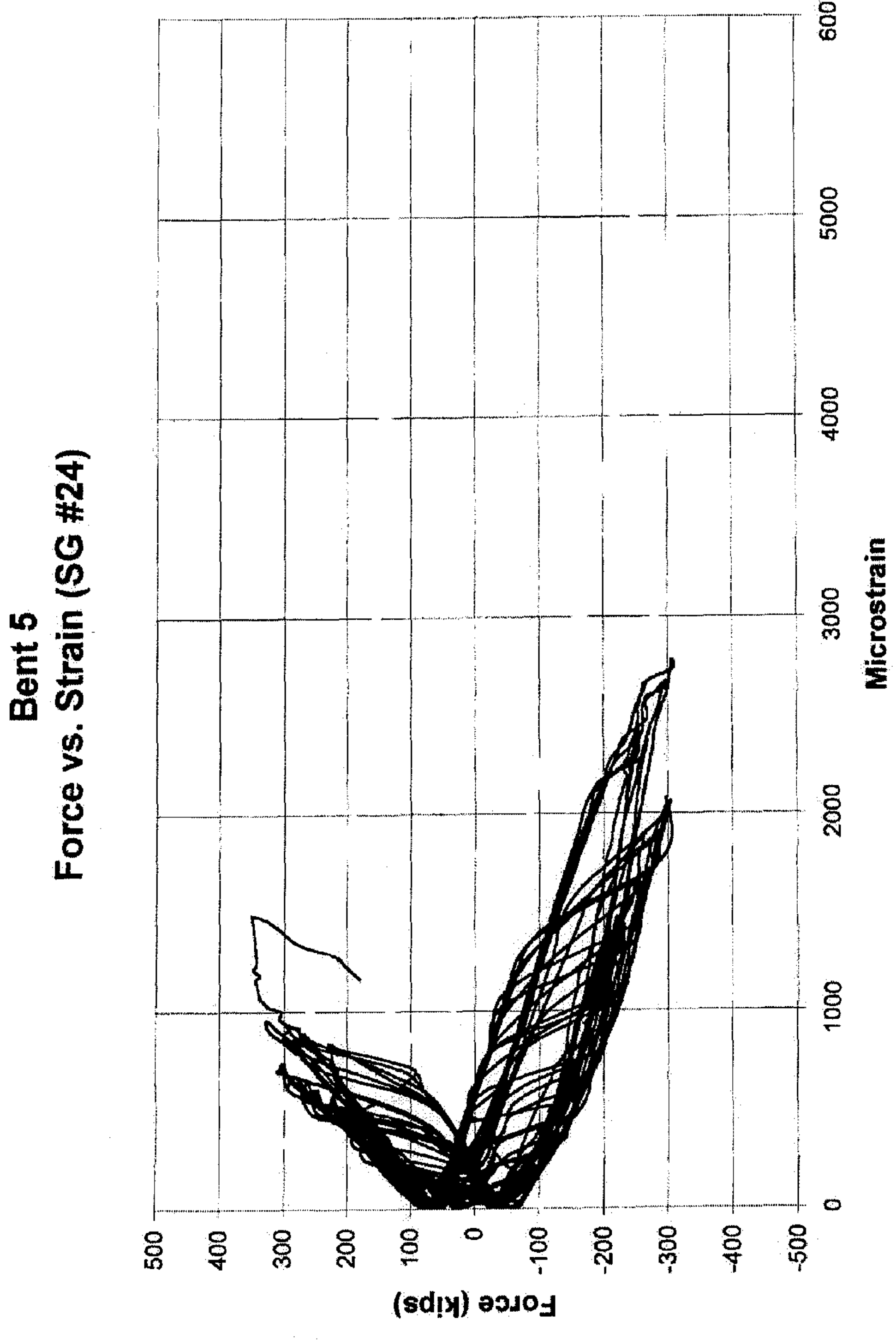

Figure 75. Force versus strain diagram for gage 24 at the top of exterior column of Bent #5 (1 kip = 4.448 kN)

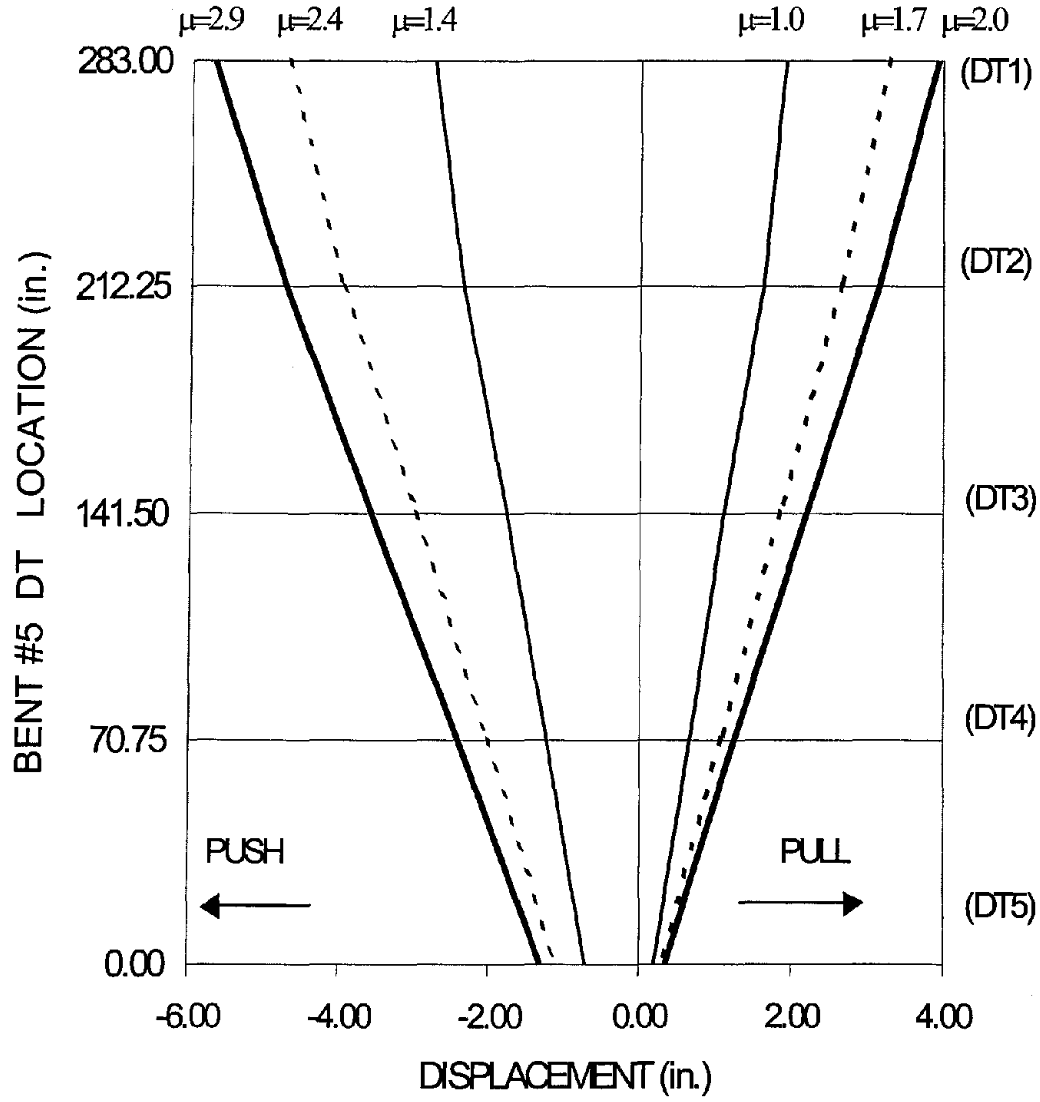

Figure 76. Displacement envelopes for exterior column of Bent #5 (1 in. = 25.4 mm)

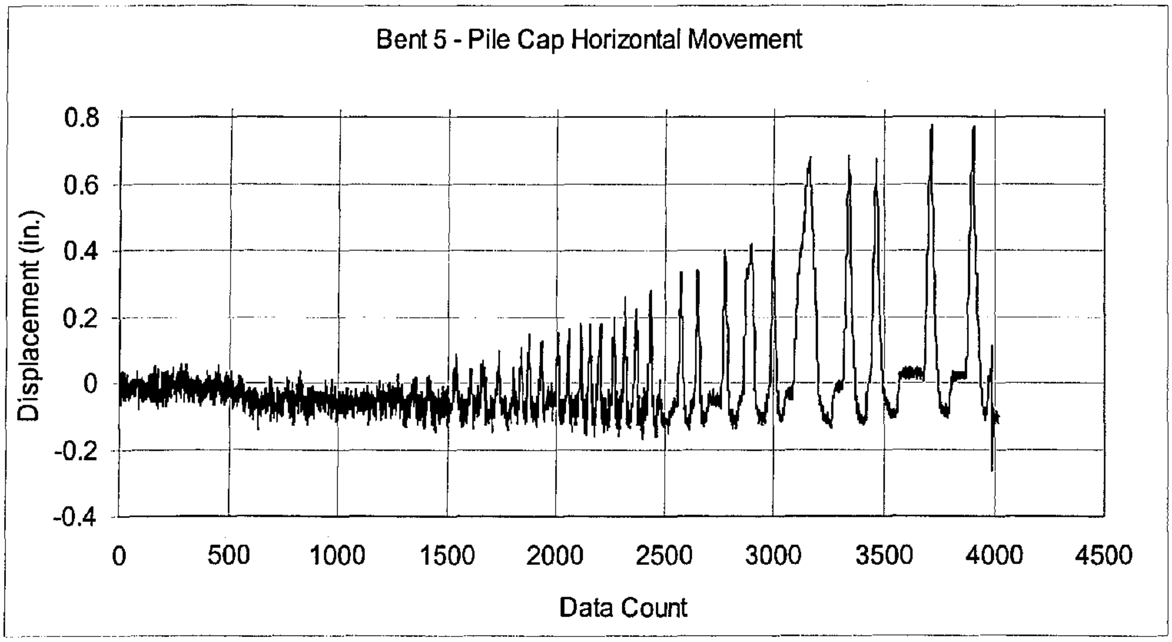

Figure 77. Horizontal movement of pile cap of Bent #5 (1 in. = 25.4 mm)

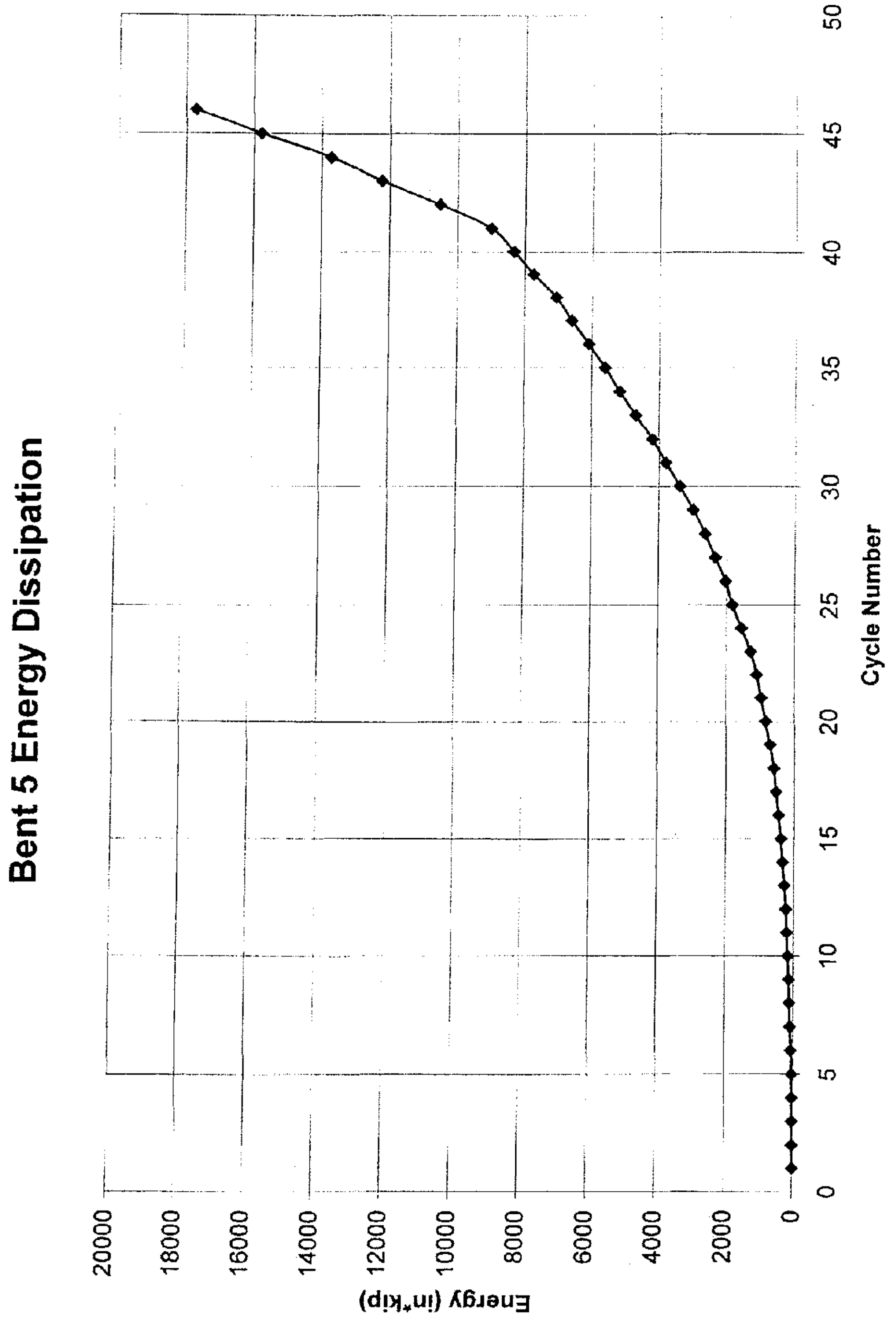

Figure 78. Cumulative energy dissipation of Bent #5 versus load cycle number
(1 in-kip = 0.113 kJ)

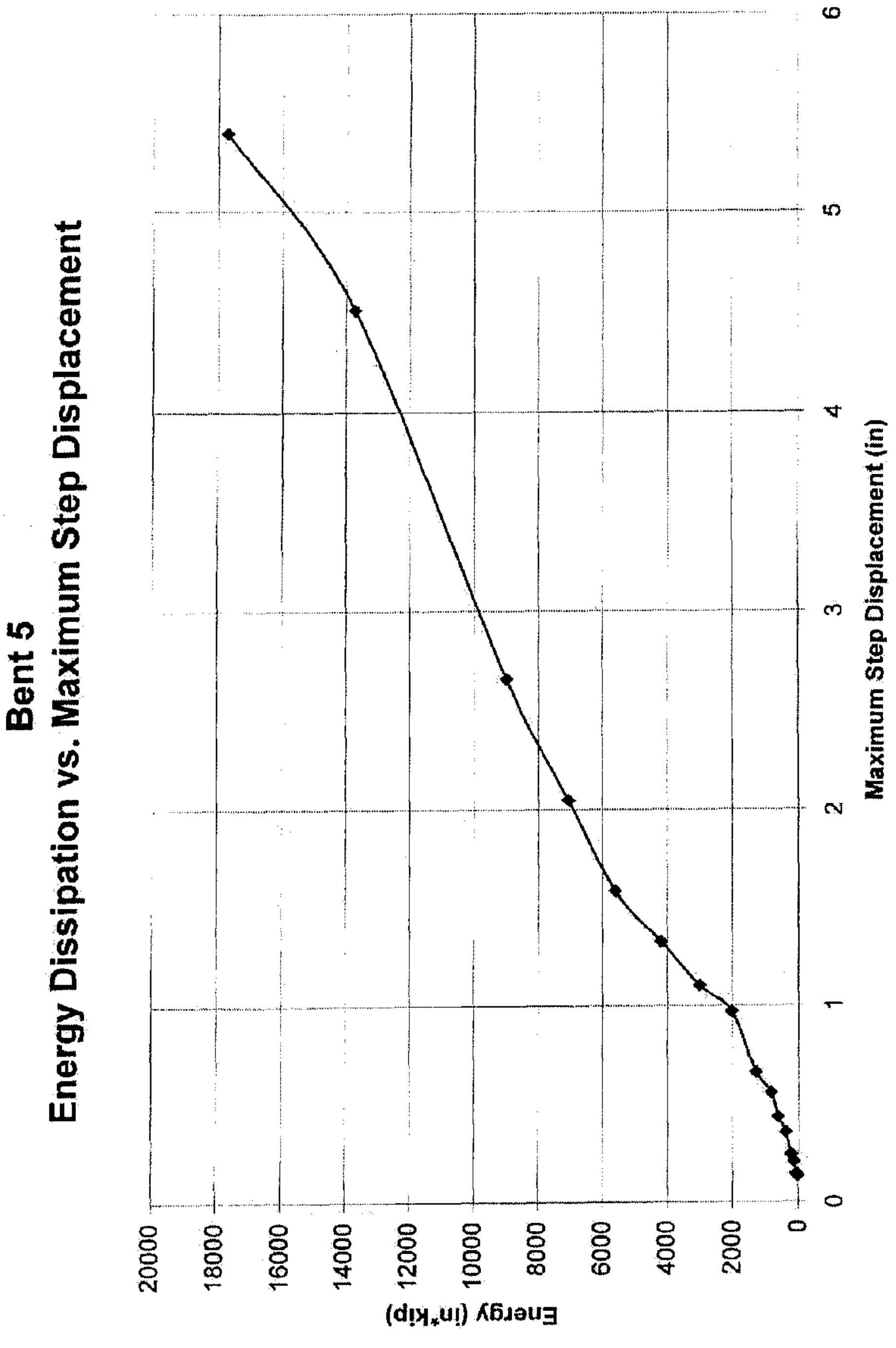

Figure 79. Cumulative energy dissipation of Bent #5 versus maximum load step displacement (1 in-kip = 0.113 kJ, 1 in. = 25.4 mm)

7. REHABILITATED BENT #6 WITH FRP COMPOSITES

As in new bridge design, rehabilitation designs for bridges are developed in a manner which provides ductility, including a reliable load resisting path. According to CALTRANS, the seismic retrofit design begins with an elastic dynamic analysis (Zelinksi 1999). After the elastic dynamic analysis, the generated maximum elastic forces are reduced by a force coefficient (for loaded piers the factor is equal to 2.0). Existing column and abutment seismic demands are compared to calculated capacities. The designer develops a strategy whereby existing properties are modified. The analytical model is then modified to more closely represent probable retrofit conditions. The model is then dynamically analyzed a second time in the modified condition. Demands are once again compared to established standards. The modification and comparison process is then repeated as often as required to satisfy the standards.

After the 1994 Northridge earthquake, inelastic pushover analyses were performed of the failed bridges, and predictions of the analyses were compared with observed behavior (Seible and Priestley 1999). This provided a rapid and valuable insight into the ability of simple pushover analyses, based on rational section analyses, to predict observed location and type of damage. Bridges designed and built before the 1971 San Fernando earthquake did not include considerations for inelastic structural response or ductile design detailing. For example, low transverse reinforcement ratios in columns, typically #4 bars at 12 in. centers (12 mm bars at 300 mm centers) were provided nominally without consideration of column size or strength. Current engineering capacity requirements would have resulted in transverse reinforcement ratios exceeding the nominally provided ones by a factor of 8 to 10 or more.

Advanced composite retrofit design for Bent #6

As was stated earlier, the goal of the retrofit was to improve the displacement ductility of Bent #6 by a factor of two. The shear capacity of the beam cap-column joints had to be improved to allow this ductility increase. From the analytical results it was concluded that the bent had deficiencies in the following areas: the confinement of the column lap splice region, the confinement of the plastic hinges, the column shear, the shear in the joint region, and the anchorage of the column longitudinal reinforcement into the beam cap. The column shear capacity for example, was 300 kN including the contribution of the concrete, the ties, and the axial load, whereas the demand for the required displacement ductility level was 743 kN. To address these issues, each element was analyzed and the structural retrofit using FRP advanced composites was specified.

Seismic rehabilitation techniques involving steel jacketing, concrete jacketing, and composite material jacketing for columns have been developed by Priestley et al. (1996). Various circular and rectangular columns with carbon fiber retrofits were tested in the laboratory, which exhibited large displacement ductilities while maintaining a constant load capacity level without significant cyclic capacity degradation (Seible et al. 1997). Bonding plates externally on the surfaces of concrete members is a structurally efficient method for rehabilitating beams for flexure and shear. Steel plates have initially been the natural choice for such rehabilitation work (Swamy and Gaul 1996), but CFRP composites have also been used for strengthening reinforced concrete beams. The effectiveness of externally applied composites in improving the shear capacity of RC beams has been studied (Chajes et al. 1995). An increase in the beam ultimate strength of 50% to 150% was achieved. The shear strengthening of RC beams using externally epoxy bonded CFRP composites was investigated by Triantafillou (1998). The shear strengthening of RC T-joints using CFRP composites was recently investigated by Gergely et al. (2000).

Methods available for strengthening older reinforced concrete joints, which are known to have seismic deficiencies, include: (a) joint section increase with special dowels and post-tensioning rods (Lowes and Moehle 1995); (b) jacketing of the joint region (Alcocer and Jirsa 1993); (c) corrugated steel jacketing of the beam-column connection (Biddah et al. 1997); and (d) post-tensioning of the beam combined with glass FRP wraps on the beam and column (Sexsmith et al. 1997). Details of a field application in which the columns and joints of the Highland Drive Bridge in Salt Lake City were wrapped with carbon fiber composites were given by Pantelides et al. (1997); the analytical techniques for the retrofit design were presented by Gergely et al. (1998).

The objectives of the retrofit were to determine the improvement in strength and ductility of the bent with the CFRP advance composite materials, and evaluate the shear strengthening of the beam cap-column joints. The retrofit of the bent was designed to double its displacement ductility in the as-built condition. The CFRP composite design considered the shear capacity of the beam cap-column joints, beam cap, and columns; the confinement of the plastic hinge zones of the columns, and beam cap; and the lap splice region strengthening of the columns. The bridge was built in the 1960's and had deficiencies in the amount and detailing of the column transverse reinforcement in the plastic hinge and lap-splice regions, and in the anchorage of the longitudinal reinforcement.

Flexural plastic hinge confinement of columns

The benefits of confining the concrete in a column with suitable methods such as concrete jackets, steel jackets or FRP composite jackets are well known. The efficiency of FRP composites in confining columns that have deficiencies such as the ones of the South Temple Bridge can be demonstrated using a simple example of confining the column core with either steel hoops or an FRP composite jacket. The confinement pressure of a column with steel hoops in the core as shown in Fig. 80(a) is given as:

$$f_l = \frac{2 f_y A_s}{D' s} \tag{7.1}$$

The confinement pressure that can be developed by the FRP composite jacket shown in Fig. 80(b) per unit length of the column is:

$$f_l = \frac{2T_j}{D} \leq \frac{2t_j E_j \varepsilon_j}{D} \tag{7.2}$$

where, as shown in Fig. 80(b), t_j is the FRP composite thickness, ε_j is the strain in the FRP composite, and E_j is the modulus of elasticity of the FRP composite. It should be noted that the second expression in equation (7.2) usually controls the design, since the FRP composite will not always reach its ultimate strain. The two equations will be compared to investigate the spacing of steel hoops versus the FRP composite thickness for providing the same confinement pressure.

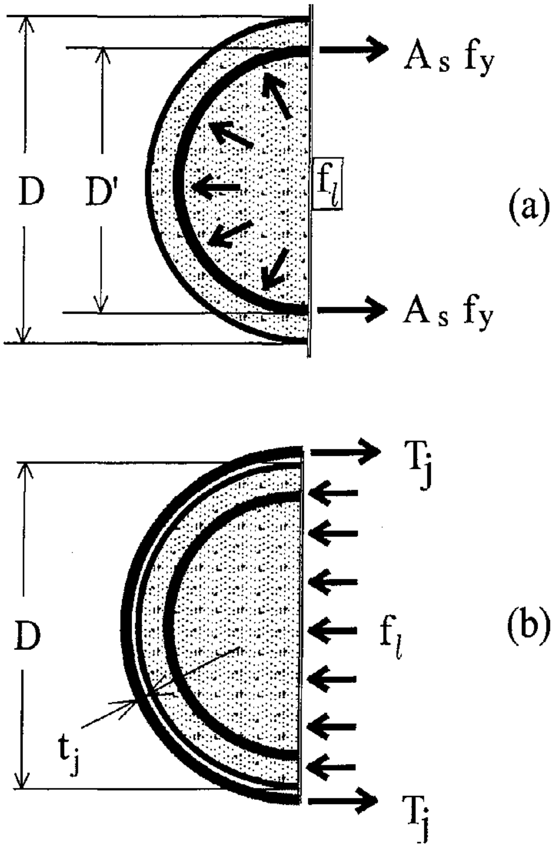

Figure 80. Confinement of concrete column using : (a) steel hoops and (b) FRP composite jacket

Consider a circular column with the following dimensions: Diameter=36 in. (914 mm), diameter of #4 steel hoops D'=29.5 in. (749 mm), A_s=0.2 in^2 (129 mm^2), yield stress of the reinforcement, f_y=48 ksi (330 MPa). Using a confinement pressure requirement of f_l=300 psi (2.07 MPa) gives a required hoop spacing s=2.2 in. (56 mm). Consider the modulus of elasticity of the FRP composite to be E_j = 10,000 ksi (69 GPa), and the maximum strain that is allowed to develop in the jacket as ε_j = 0.004, which is approximately 40% of the ultimate strain of the carbon FRP composite used in this research. The thickness of one layer of FRP composite used in this example is 0.045 in. (1.14 mm). For a confinement pressure of f_l=300 psi (2.07 MPa), the required thickness of FRP composite is t_j = 0.135 in. (3.43 mm) or 3 layers. Thus, the ability of the FRP composite to rehabilitate columns that need additional confinement is demonstrated.

The FRP composite was custom designed for the conditions of the bent at South Temple Bridge (Pantelides et al. 1999a). To confine the plastic hinge region, the composite layout was designed as a square jacket using twice the CFRP thickness required for the equivalent circular jacket; the effective circular diameter D_e was calculated as 1.292 m. The thickness of the composite layers was calculated as (Seible et al. 1997):

$$t_j = 2\left[\frac{0.09D_e(\varepsilon_{cu} - 0.004)f'_{cc}}{\phi_f f_{ju}\varepsilon_{ju}}\right] \tag{7.3}$$

where ε_{cu} = required ultimate concrete strain which was taken as 0.0065 based on the required ductility increase; f'_{cc} = compressive strength of confined concrete assumed as 24 MPa; f_{ju} = ultimate composite strength evaluated according to ASTM D-3039 specifications (ASTM 1996) as 628 MPa; ε_{ju} = ultimate composite strain evaluated using ASTM D-3039 as 0.01; and ϕ_f = flexural capacity reduction factor taken as 0.9. The factor 2 in front of the expression reflects the fact that this is a rectangular section. It should be noted that the material used in this application was 48,000 fibers per tow unidirectional carbon fibers. The number of tows per 25.4 mm of sheet (pitch) was 6.5, and the width of the carbon fiber sheets used was 457 mm. The required thickness calculated from (1) was 2.48 mm. The thickness of one composite layer was 1.32 mm; approximately two layers of CFRP composite were required for flexural plastic hinge confinement of the columns. The location of these layers with respect to the column length is governed by the plastic hinge length, in terms of column depth and the distance from the column hinge to the point of contraflexure (Seible et al. 1997).

Lap splice clamping of columns

The thickness of the composite required for clamping the lap splice region was determined based on an equivalent circular jacket and was then multiplied by a factor of two. The lateral clamping pressure is defined as (Seible et al. 1997):

$$f_l = \frac{A_s f_{sy}}{\left[\frac{p}{2n} + 2(d_b + cc)\right]L_s} \tag{7.4}$$

where A_s = area of one longitudinal column reinforcing bar (819 mm^2); f_{sy} = yield strength of the longitudinal column bar (275 MPa); p = inside crack perimeter along the longitudinal lap-spliced bars (4x648 mm); n = number of longitudinal bars (i.e. 16); d_b =

diameter of longitudinal bars (32 mm); cc = concrete cover to the longitudinal bars (102 mm); and L_s = lap splice length (762 mm). Equation (2) gives $f_l = 0.85$ MPa.

The contribution of the reinforcing steel ties to the clamping force was calculated as:

$$f_h = \frac{0.002 A_h E_h}{D_e s} \tag{7.5}$$

where A_h = area of the transverse ties (200 mm^2); E_h = elastic modulus of ties (200 GPa); D_e = effective column diameter (1.292 m); and s = spacing of ties (305 mm). The resulting stress was found as f_h = 0.20 MPa. Based on the values calculated using equations (7.4) and (7.5), the thickness of the composite to clamp the lap splice region is given as (Seible et al. 1997):

$$t_j = 2\left[\frac{500 D_e (f_l - f_h)}{E_j}\right] \tag{7.6}$$

where, the only unknown is E_j, the modulus of the composite jacket which was determined experimentally using tensile coupons as 64,730 MPa (9,390 ksi). The required thickness was found to be 12.97 mm. The thickness of one composite layer was 1.32 mm; approximately ten layers of CFRP composite were required for lap splice clamping of the columns. The location of these layers is at the bottom of the column for a length of the column equal to the splice length (Seible et al. 1997).

Shear strengthening of columns

In order to design the composite jacket for shear, first, each of the shear resisting components were evaluated and then subtracted from the design shear. The design shear was estimated as 1.5 times the column shear at yielding. No shear strengthening was necessary outside the plastic hinge region. The thickness of the composite jacket inside the plastic hinge region was calculated as (Seible et al. 1997):

$$t_j = \frac{\frac{V_0}{\phi_v} - (V_c + V_s + V_p)}{2x0.004 E_j D} \tag{7.7}$$

where V_0 = design shear estimated at 743 kN; V_c = shear contribution of concrete equal to 68 kN; V_s = shear contribution of ties equal to 186 kN; V_p = effect of axial load taken as 46 kN; D = width of the column (0.914 m); and ϕ_v = shear strength reduction factor equal to 0.85. The required thickness was calculated as 1.28 mm which is approximately equal to one CFRP composite layer. The location of these layers is at the top and bottom of the column for a length of the column equal to 1.5 times the column depth (Seible et al. 1997).

Flexural plastic hinge confinement of beam cap

Since the shear capacity of the beam cap was found to be adequate (outside the joint region), only the confinement of the plastic hinge was considered. The design of the advanced composite followed the procedure presented earlier for the columns. Due to the different geometry and dimensions of the beam, the effective diameter D_e of the equivalent oval jacket was found to be 2.079 m, and the thickness of the jacket was calculated using equation (7.3) as 3.42 mm.

Shear strengthening of beam cap-column joint

In order to design the thickness of the composite in the joint region, the joint shear forces had to be evaluated. This was achieved by modeling the retrofitted bent, including the wrapped columns using DRAIN-2DX. However, the DRAIN-2DX model did not include the CFRP composite at the joint region. Figure 81 shows the sequence of the analyses required to design the FRP composite for the beam cap-column joint. The peak lateral load for the second analysis was increased compared to the as-built condition, which resulted in higher joint shear forces. The calculated shear forces and stresses at the ultimate displacement, in the middle joint, were: (a) the horizontal joint shear was 2,176 kN, and the horizontal joint shear stress calculated according to the ACI-352 Recommendations (ACI 1991) was 2.99 MPa; (b) the vertical joint shear was 3,139 kN, and the vertical joint shear stress was 3.02 MPa; and (c) the joint compression stress resulting from the axial force was - 0.63 MPa.

To calculate the principal tension and compression stresses, equation (6.2) was used where $\nu_j = 3.00$ MPa, is the average of the joint horizontal and vertical shear stresses and $\sigma_a = -0.63$ MPa, is the axial stress in the horizontal direction. The resulting principal stresses are: (a) tension $\sigma_t = 2.70$ MPa, and (b) compression $\sigma_c = -3.33$ MPa. The principal angle, θ, is given by the expression

$$\cos 2\theta = \frac{\sigma_a}{2\sqrt{\left(\frac{\sigma_a}{2}\right)^2 + \left(\nu_j\right)^2}} \tag{7.8}$$

which yields a principal angle $\theta = 42^0$. Thus, to maximize the contribution of the composite layers, the orientation of the fibers should be at $\pm 48^0$ from the longitudinal axis of the beam cap. However, in the test the sheets were outlined and laid at $\pm 45^0$ which did not affect the results significantly.

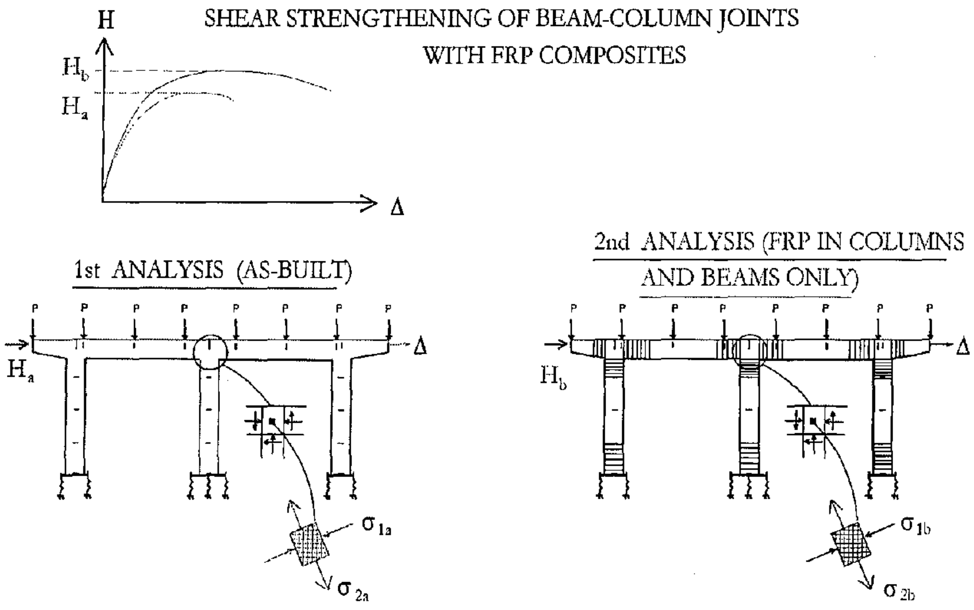

Figure 81. Required analyses for FRP rehabilitation design of beam cap – column joints

It can be seen from the calculations for the retrofitted bent that, with the increase in lateral load capacity of the entire system, the demand for the joint principal tensile stress was increased by $\Delta\sigma = 0.71$ MPa, from 1.99 MPa (value for the as-built bent) to 2.70 MPa for the retrofitted bent. To find the number of composite layers inclined at 48^0 required to provide the higher shear capacity, a diagonal tension crack in the joint region was analyzed. Figure 82 shows the beam cap–column joint with the composite layer perpendicular to the crack. The direction of the crack is parallel to the principal compression stress. The force F_2 acting normal to the crack is the force resisted by one composite layer stressed in the fiber direction. The magnitude of F_2 can be calculated as:

$$F_2 = t_j \varepsilon_f E_j \frac{d_e}{\cos\theta_p} \tag{7.9}$$

where θ_p = angle between the longitudinal axis of the member and the optimal fiber direction (48°); t_j = thickness of composite sheets (1.32 mm); ε_f = average axial strain in the fiber direction at peak horizontal load (0.0021 was used, which was later verified in the test by strain gage measurements on the composite); E_j = elastic modulus of the composite material (64,730 MPa); and d_e = effective joint depth which is the height of the joint minus twice the effective bond length of the composite sheets to the concrete, which from previous studies was found to be approximately 51 mm. The dimension of the joint and the inclination of the principal planes control the value of the joint effective depth d_e which is equal to 823 mm. The resulting force F_2 was found as 221 kN.

To find the tensile stress in one composite layer, the value of the force F_2 is divided by the width of the joint (b = 0.914 m) and by the inclined length (along the crack) bordered by the effective depth as:

$$\sigma_f = \frac{F_2 \cos\theta_p}{bd_e} \tag{7.10}$$

This calculation yields $\sigma_f = 0.197$ MPa. Enough layers, each of a tensile stress capacity equal to σ_f, have to be used in order to resist the $\Delta\sigma = 0.71$ MPa stress increase from the as built to the retrofitted bent. Therefore, the total number of layers required is given by:

$$n = \frac{\Delta\sigma}{\sigma_f} \tag{7.11}$$

which yields 3.65 layers. In order to have a symmetric composite jacket around the joint, four layers of unidirectional fibers were applied. These layers were provided in both directions to take into account the cyclic nature of the applied test loads.

The material properties of the FRP composite were determined prior to the tests using tensile coupons prepared according to the ASTM D-3039 specifications (ASTM 1996). A typical stress-strain curve of the FRP carbon fiber composite is shown in Fig. 83, and a typical tensile failure of the FRP composite coupons is shown in Fig. 84. A simple stress-strain confinement model was used to represent the columns with the FRP composite jacket. The model uses simple theory to determine the additional compressive stress and strain in the axial load direction which can be reached due to the confining effect of the FRP composite (Gergely et al. 1998). The constitutive model used in the analyses for the tests carried out in this research is shown in Fig. 85. Figure 85 also shows the constitutive model for the unconfined concrete. Both of these models were used in the DRAIN-2DX analyses of the frame.

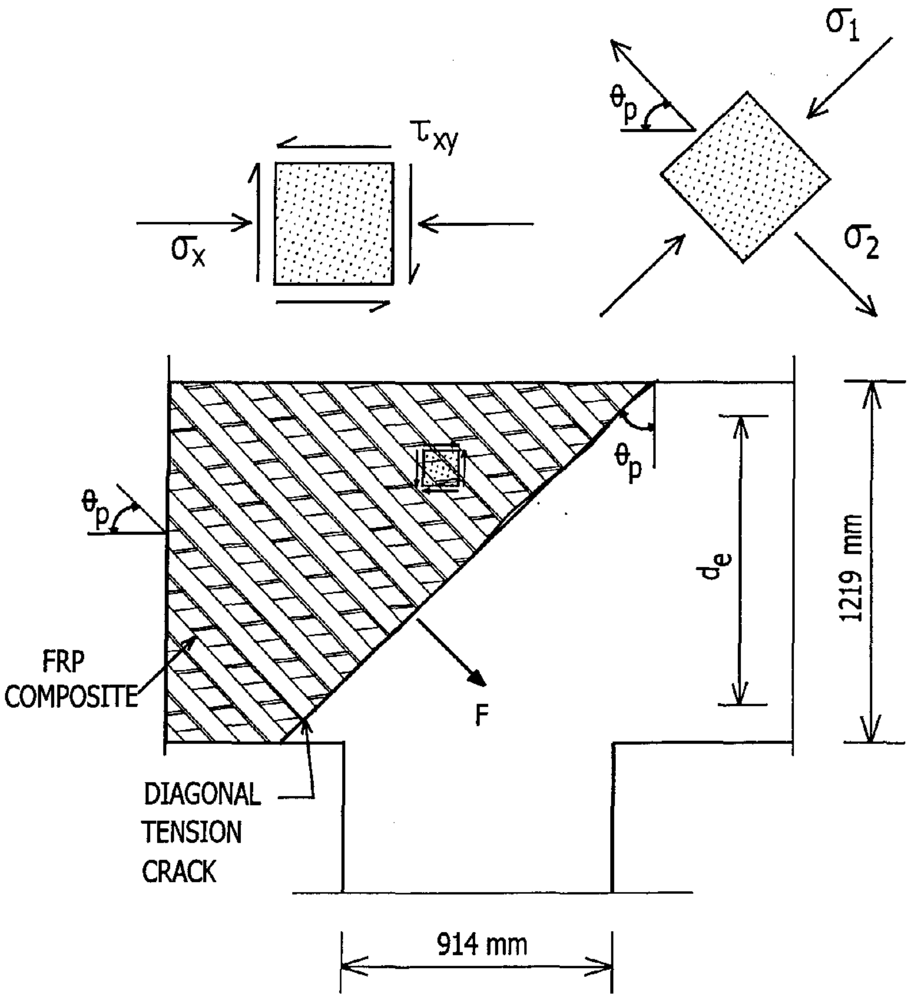

Figure 82. FRP composite rehabilitation design of beam cap-column joint

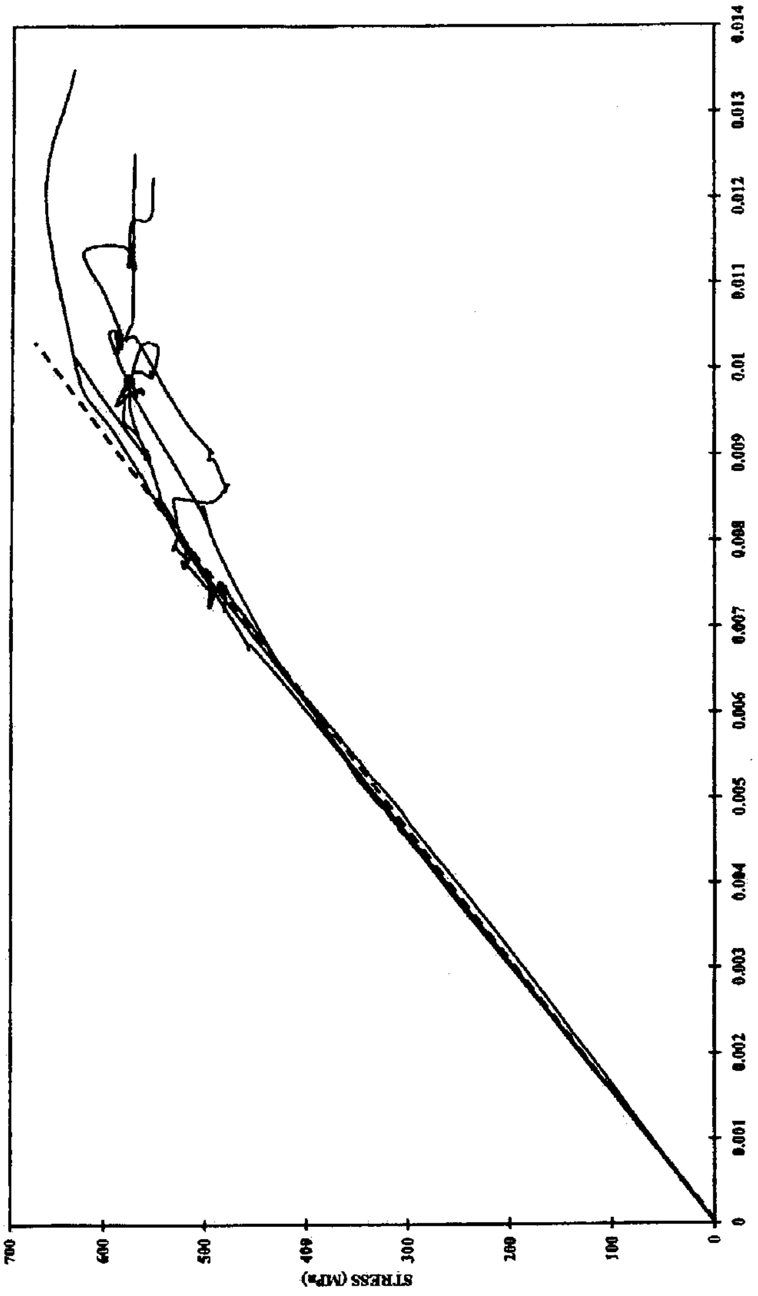

Figure 83. Stress-strain diagram of FRP composite

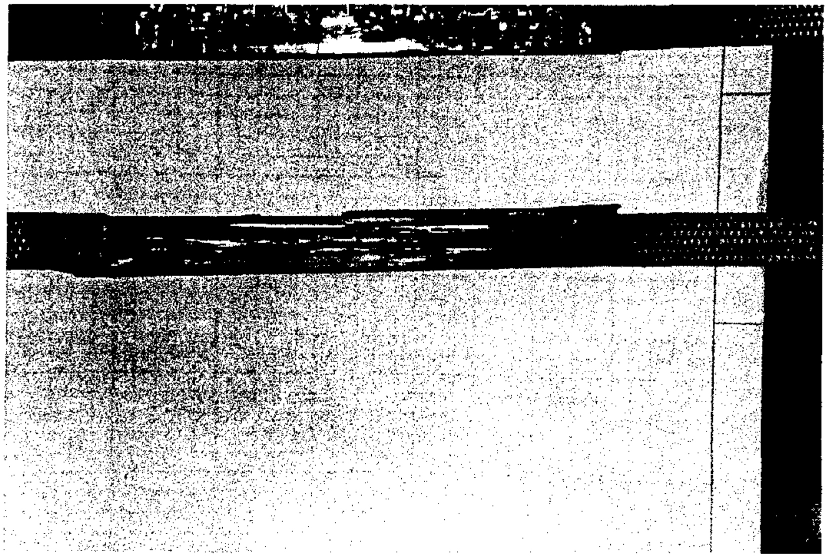

Figure 84. Tensile failure of FRP composite coupons

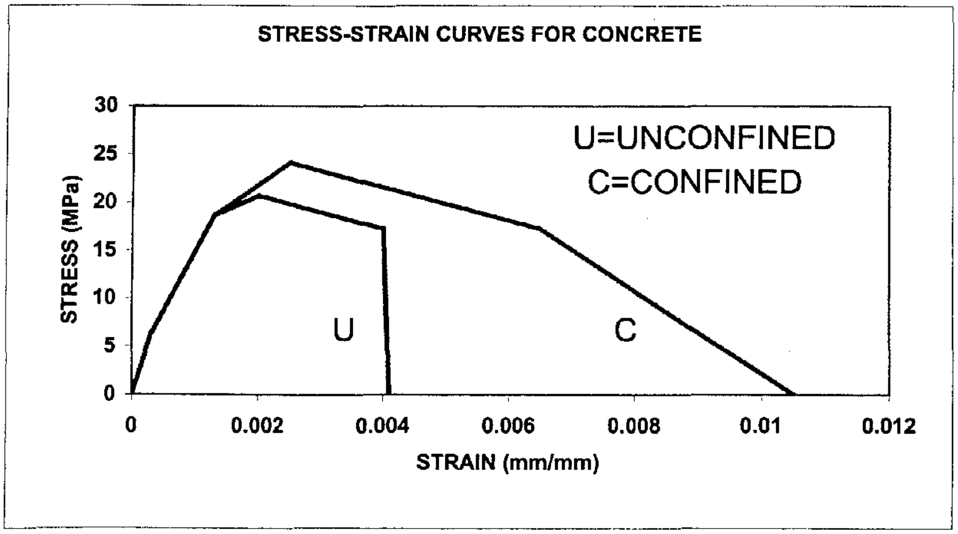

Figure 85. Stress-strain model for unconfined and confined concrete with FRP composites

Layout of FRP composite retrofit for Bent #6

The composite layout for the retrofitted bent is shown in Fig. 86 and Fig. 87. The required thickness was divided by the thickness of one layer which was 1.32 mm (0.052 in.). In Fig. 86 there are ten layers extending to a distance of 914 mm (36 in.); the majority of these layers is for lap splice clamping, with the remainder contributing to flexural plastic hinge confinement and shear strengthening. Next, two layers were placed for a distance of 457 mm (18 in.) for flexural plastic hinge confinement and shear strengthening, and finally one layer was placed for a distance of 457 mm (18 in.) for flexural plastic hinge confinement. The jacket for the top of the column is similar to the jacket for the bottom of the column, except that there is no requirement in this case for lap splice clamping. However, an additional six layers of 152 mm (6 in.) wide CFRP composite sheets (tapes), shown in Fig. 87, were provided in order to decrease the level of stresses in the column longitudinal steel reinforcement extending into the joint. In addition, this steel reinforcement had insufficient development length in the joint. These CFRP composite tapes were clamped down using a single layer of fibers, which was placed over the tapes in the transverse direction as shown in Fig. 87. The beam cap required two 457 mm (18 in.) wide layers of unidirectional fibers on either side of the column, as shown in Fig. 86, for flexural plastic hinge confinement.

Four layers of unidirectional fibers were provided on both sides of the beam cap at $\pm 45°$ in the joint region, as shown in Fig. 86. A 51 mm (2 in.) gap was left between the column and the pile cap, and the column and the beam cap, as shown in Fig. 86 to avoid any strength and stiffness increase from the retrofit. In addition, the corners of the beam cap and columns were rounded to 51 mm (2 mm) to provide better anchorage and confinement. Figure 88 shows the overall retrofit of the bent. The details of the retrofit at the top of the exterior columns were slightly different, only at the beam cap.

Application and validation of FRP composite retrofit for Bent #6

The application of the composite included: (a) removal of loose concrete using jack hammers and surface preparation with high pressure water jet; this involved mainly the beam cap surface area and it was necessary to remove the cover outside the stirrups; this operation is extremely important in order to ensure a good bond to the existing concrete that is in good condition; (b) shotcreting of the surface of the beam cap to bring it to its original shape; a wire mesh was used at the bottom of the beam cap for the shotcrete to adhere; (c) application of a structural adhesive; and (d) application of the carbon FRP sheets using hand layup and a room temperature curing system. Good surface preparation and the use of a high strength adhesive prolong the onset of delamination of the composite from the concrete surface; this was the dominant mode of failure of the composite, which occurred at about only one fifth of the composite's tensile capacity. Strain gages measured the peak value of the strain in the composite at the joint which was found to be 0.22%. The ultimate value for tensile strain in the CFRP composite was determined experimentally as 1%. The low strain level observed in the FRP composite during the tests verifies the validity of the value used in the design of the

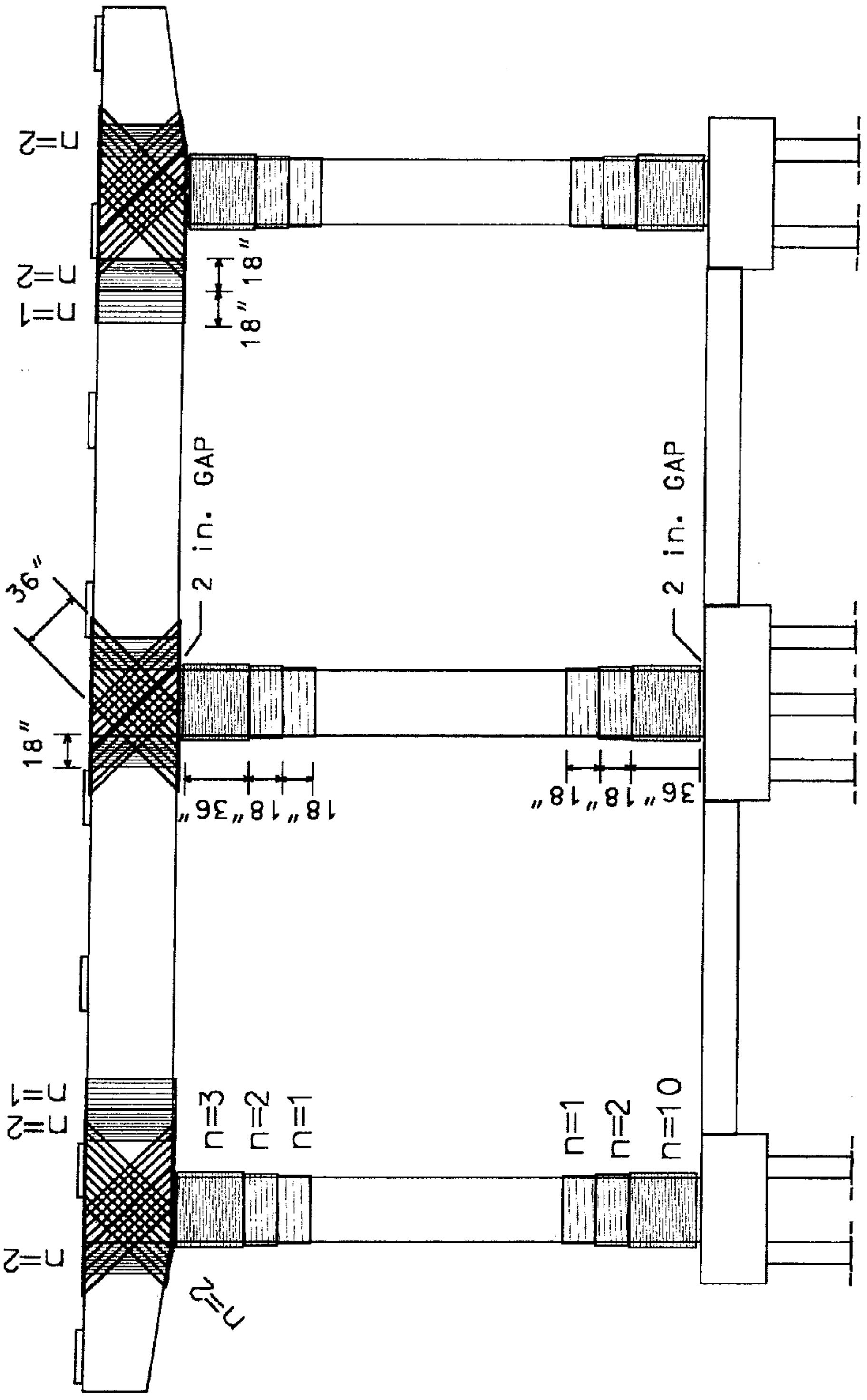

Figure 86. FRP composite layout for rehabilitated Bent #6: – First Part (1" = 25.4 mm)

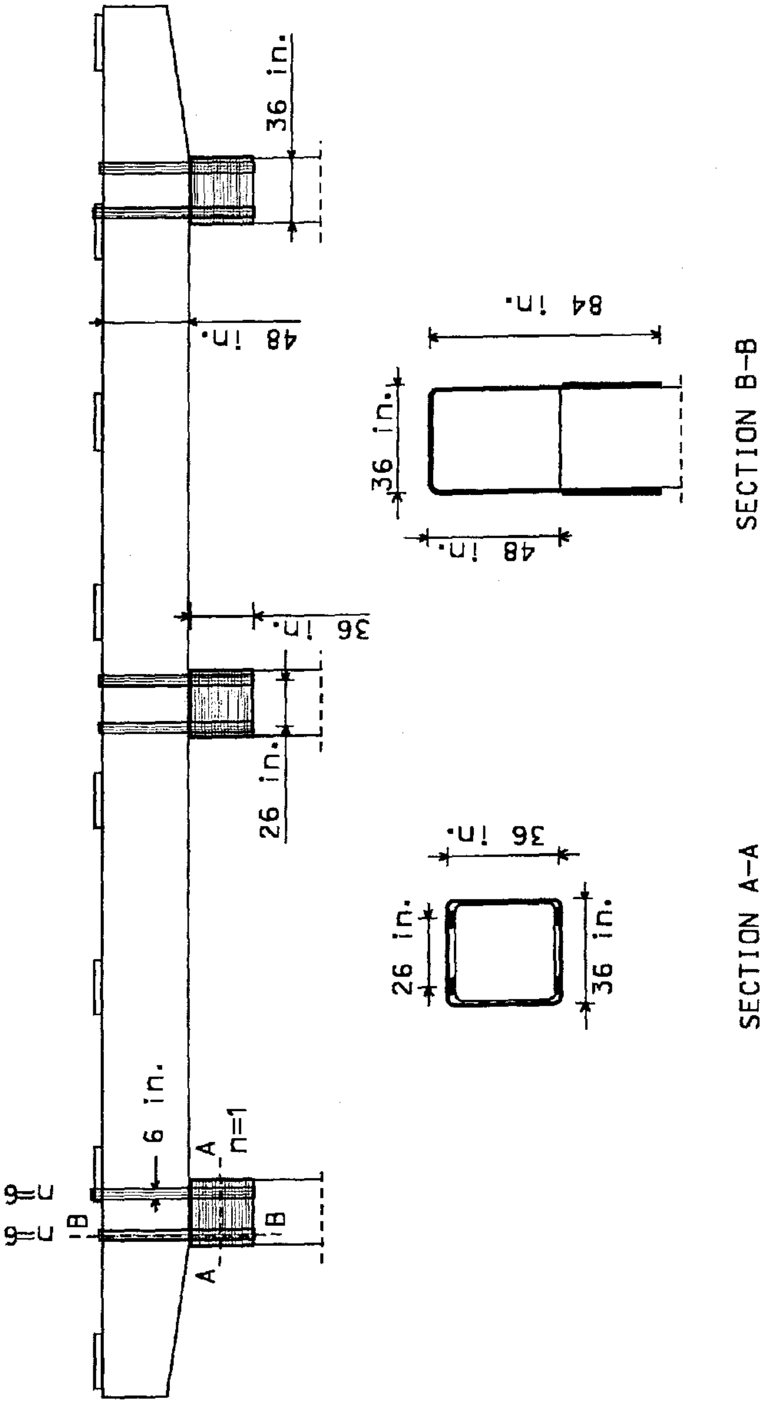

Figure 87. FRP composite layout for rehabilitated Bent #6: – Second Part
(1 in. = 25.4 mm)

FRP composite for the joint.

The carbon fiber was 48,000 fiber tows at six picks per 25.4 mm, and weighed 9.14 N/m^2. The curing system consisted of Epon 826 as the resin and Epi-cure 3251 as the curing agent; the resin/curing agent kits were prepared using 40 parts of curing agent to 100 parts of resin by weight. A profiling material was used prior to the application of the composite. The profiling material was custom made and was a two part thixotropic epoxy. The part A (CR-50 epoxy resin) to part B (CH-50 hardener) ratio was 3 to 1 by weight. The profiling material was used for patching holes in the concrete and in the shotcrete. The adhesive was also custom made for these tests and was a two part epoxy resin with strong adhesive characteristics. Moreover, it had a rating of 0 second burn using the ASTM 3801 test, which classifies it as fire retardant. Part A of the adhesive consisted of CR-38 fire-retardant epoxy resin; part B of the adhesive consisted of CH-38 epoxy hardener. The adhesive was mixed at a ratio of 3 parts A to 1 part B by weight.

The following quantities were used in the CFRP composite retrofit: (1) Carbon=2,730 N of which the 457 mm–wide unidirectional fibers were 609 m long, and the 152 mm-wide fibers were 165 m long; (2) the profiling material weighed 267 kN, (3) the adhesive weighed 1,423 N and the resin weighed 2,922 N. It took approximately 640 man-hours to prepare the concrete surface, apply the adhesive and the CFRP composite wrap for one bridge bent. However, this is by far less time than a traditional method, such as concrete encapsulation would require. This factor is important in the overall cost of the retrofit, not only because of the time duration of the project, but also from the point of view of traffic control; the latter can be a substantial portion of the retrofit budget. Detailed information on the application procedures and implementation can be found in the related Construction Report (Pantelides and Reaveley 1999).

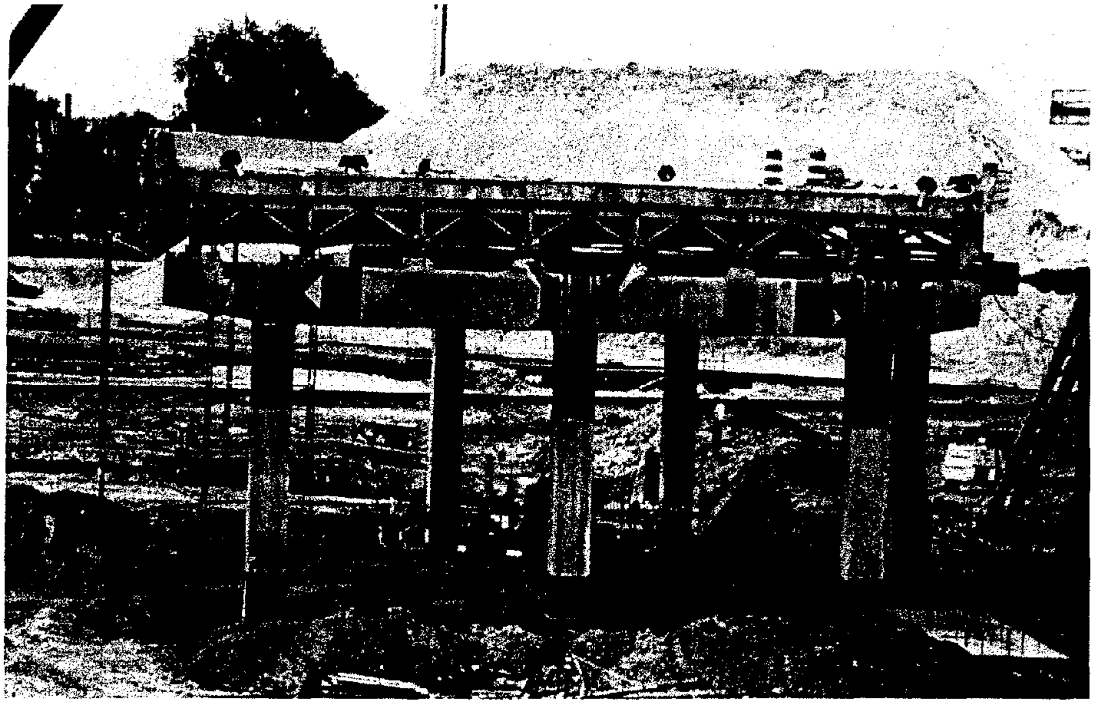

Figure 88. Overall rehabilitation of Bent #6 with FRP composites

Analysis of rehabilitated Bent #6

A static pushover analysis of the retrofitted Bent #6 with FRP composites was carried out to compare the analytical results to the experimental hysteresis curves. The yielding sequence of the structural members was observed and member forces were calculated at the ultimate displacement. The finite element model of Fig. 56 was used but the constitutive properties of the column and beam elements were modified as shown in Fig. 85. The confined stress-strain curve was used in the columns and beams where the FRP composite jacket was present. The result of the static nonlinear pushover analysis is presented in Fig. 89 as a solid line. The magnitude of the peak lateral force was 1800 kN (405 kip), after which the load decreased gradually.

Test of rehabilitated Bent #6

The test setup, the location of instruments, and the testing procedures are similar to the ones described for Bent #5. A force-controlled test was first performed up to a lateral load of 801 kN, and a displacement-controlled test was performed after that by gradually increasing the lateral deflection in each step. The lateral load at first yield was 956 kN and the first yield displacement was equal to 25 mm. Figure 89 shows a comparison of the analytical and experimental envelope obtained using FEMA 273 (1997) procedures. The curve also shows the number of elements that yielded with respect to Fig. 56. Comparing the yielding sequence of Bent #5 shown in Fig. 57 and that of Bent #6 one can observe that the sequence is almost identical and that the same mechanism forms in both cases, i.e., flexural hinges at the top and bottom of the columns.

The location of the instruments used in the test is shown in Fig. 90, and the LVDT detail on an exterior beam cap-column joint is shown in Fig. 91. The test procedure and monitoring of the data was carried out in an identical manner as that for Bent #5. The applied load history is shown in Fig. 92. The peak load is 2203 kN (495 kip) and is seen to drop by approximately 20 percent. The applied displacement history is shown in Fig. 93, with a maximum displacement of 265 mm (10.45 in.). From a bilinear approximation of the load-displacement behavior, the displacement ductility of the bent at the end of the test was found to be equal to 6.3, as shown in Fig. 94. Thus, the goal set out in the FRP advanced composite design of doubling the displacement ductility of the as-built Bent #5 was achieved. In addition, the ductility achieved during the test is higher than the target design displacement ductility of $\mu_\Delta = 5$ used by Caltrans for multicolumn bents (Caltrans 1999). The overall envelope of the hysteresis curves was constructed according to the FEMA 273 guidelines (1997) and is shown in Fig. 95. This was done in order to compare with the other two tests performed during this research. The figure shows a slightly higher load capacity in the pull direction as compared to the push direction. However, the maximum displacements in the push and pull direction are approximately equal.

Damage assessment of rehabilitated Bent #6

Large cracks in the concrete were visible at the interface between the column and the beam cap, which reached 6 mm in width as shown in Fig. 96. These interface cracks propagated from the concrete into the FRP composite as shown in Fig. 97. In addition, at both column ends, shallow spalling cracks in the 51 mm gaps were formed. The FRP advanced composite layers

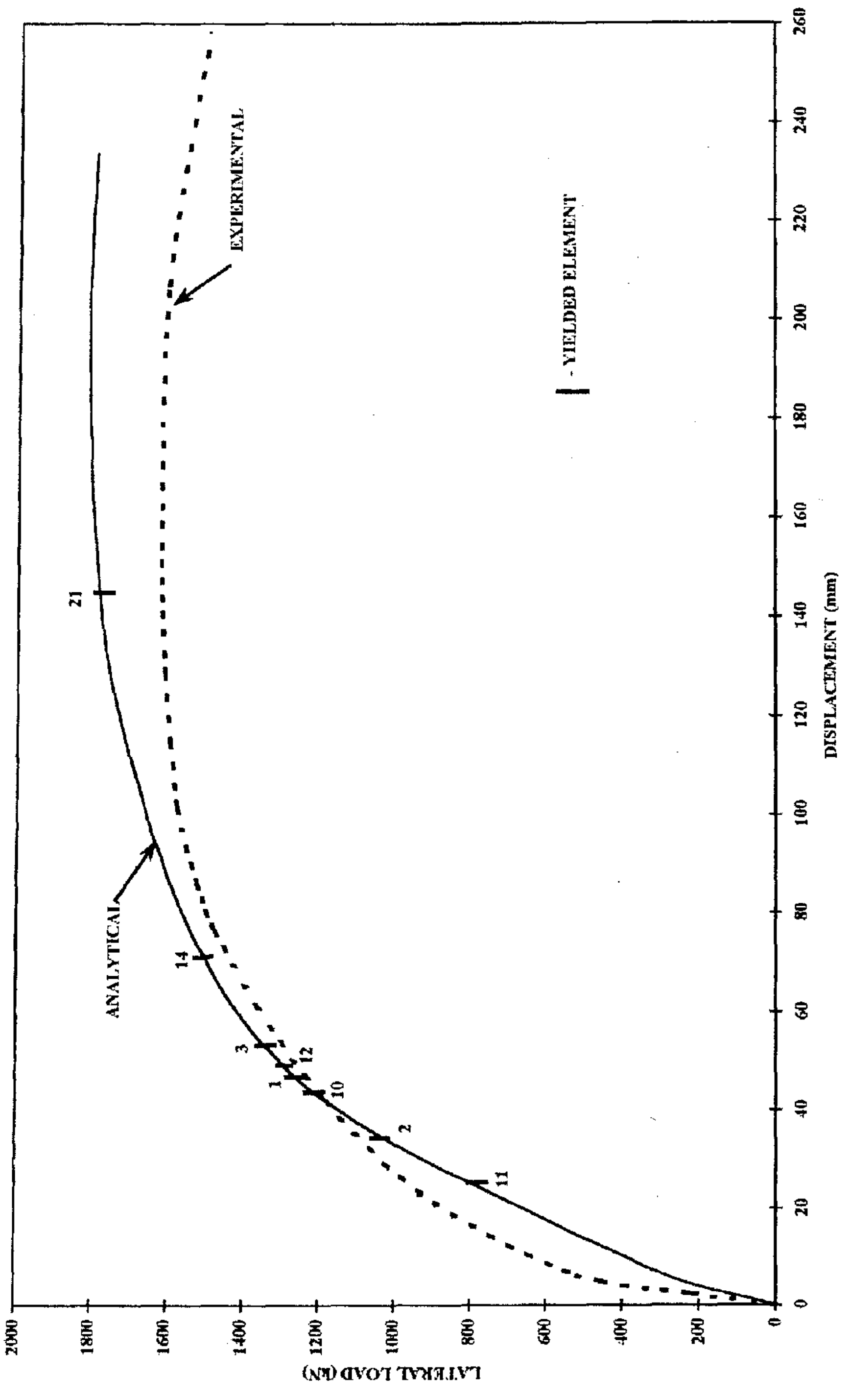

Figure 89. Comparison of analysis and experiment for rehabilitated Bent #6

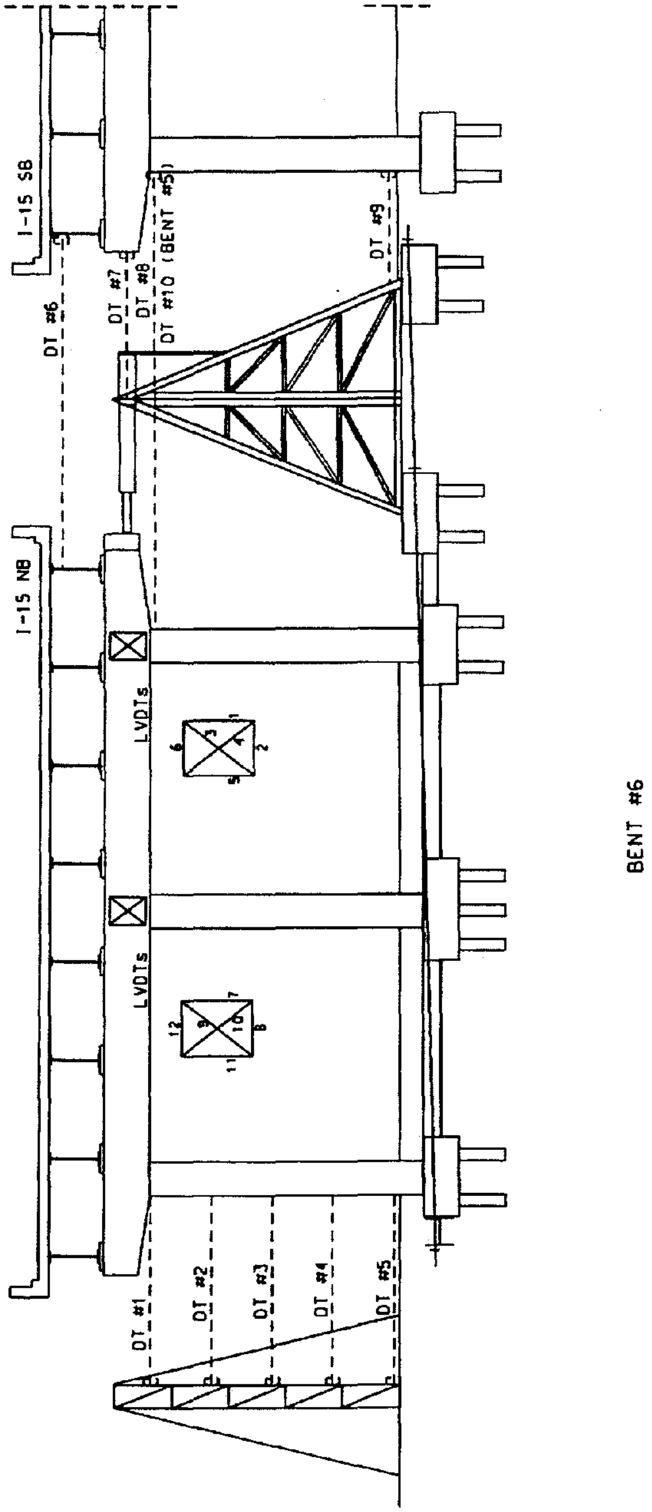

Figure 90. Displacement transducer and LVDT locations on Bent #6

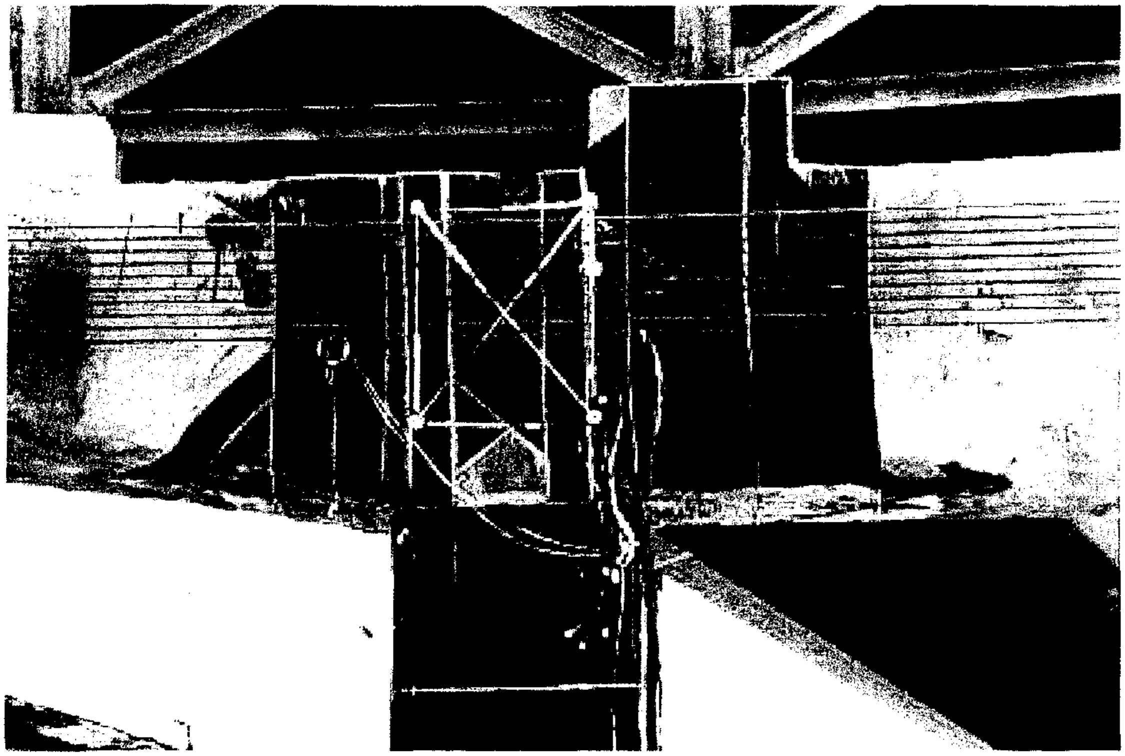

Figure 91. Detail of LVDT's and FRP composite on exterior beam cap-column joint

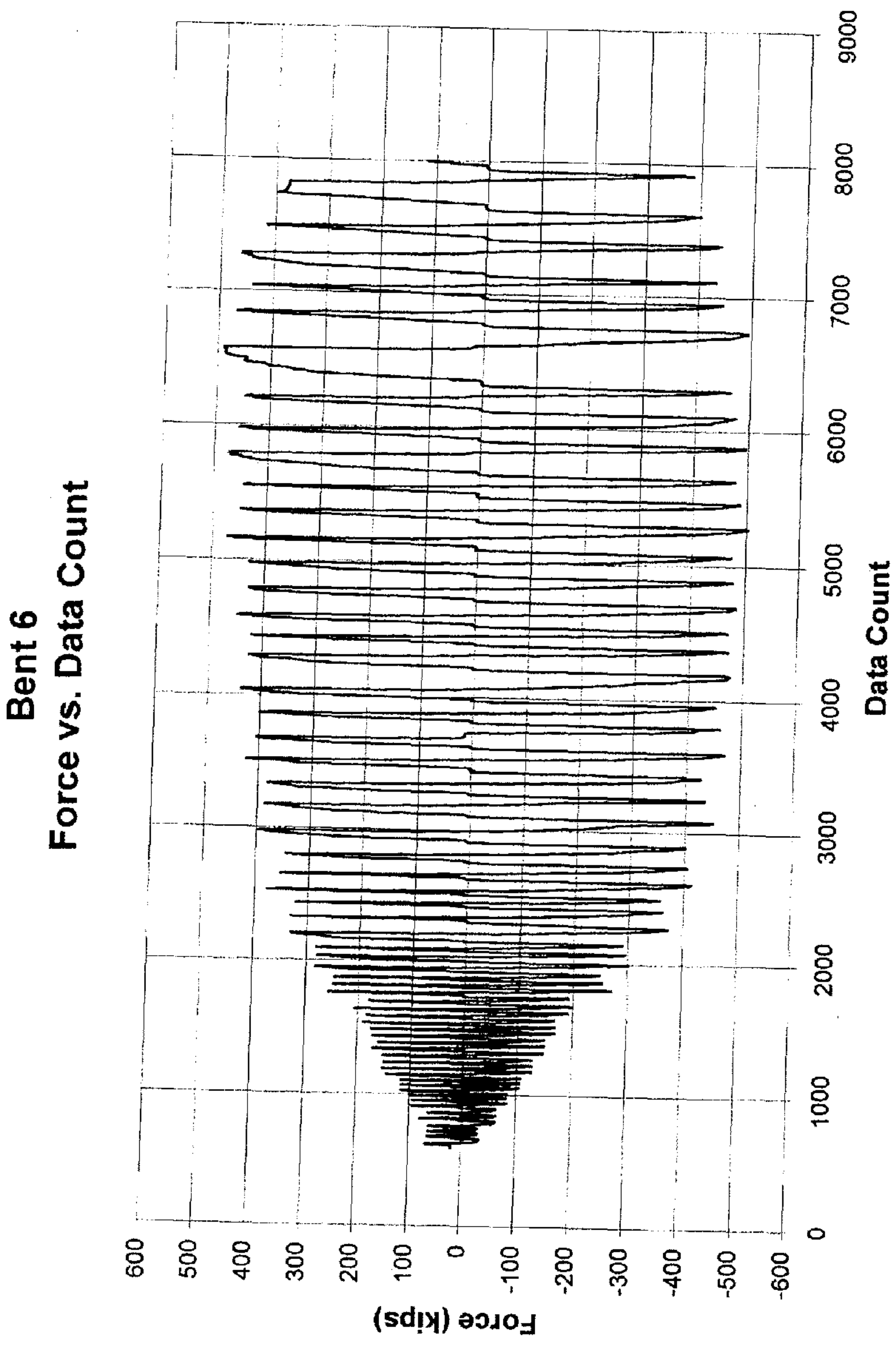

Figure 92. Actual applied lateral load history on Bent #6 (1 kip = 4.448 kN)

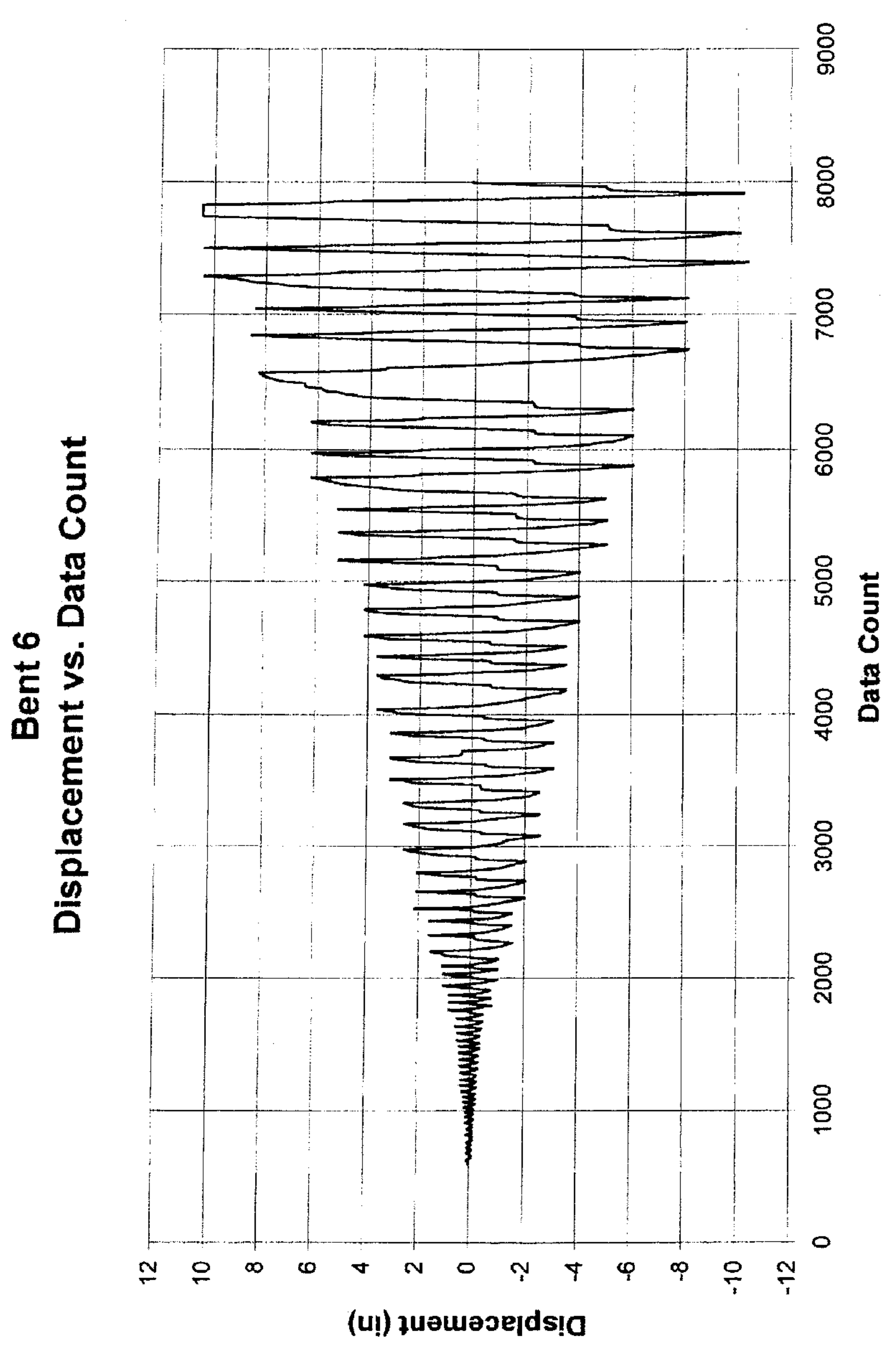

Figure 93. Applied lateral displacement history on Bent #6 (1 in. = 25.4 mm)

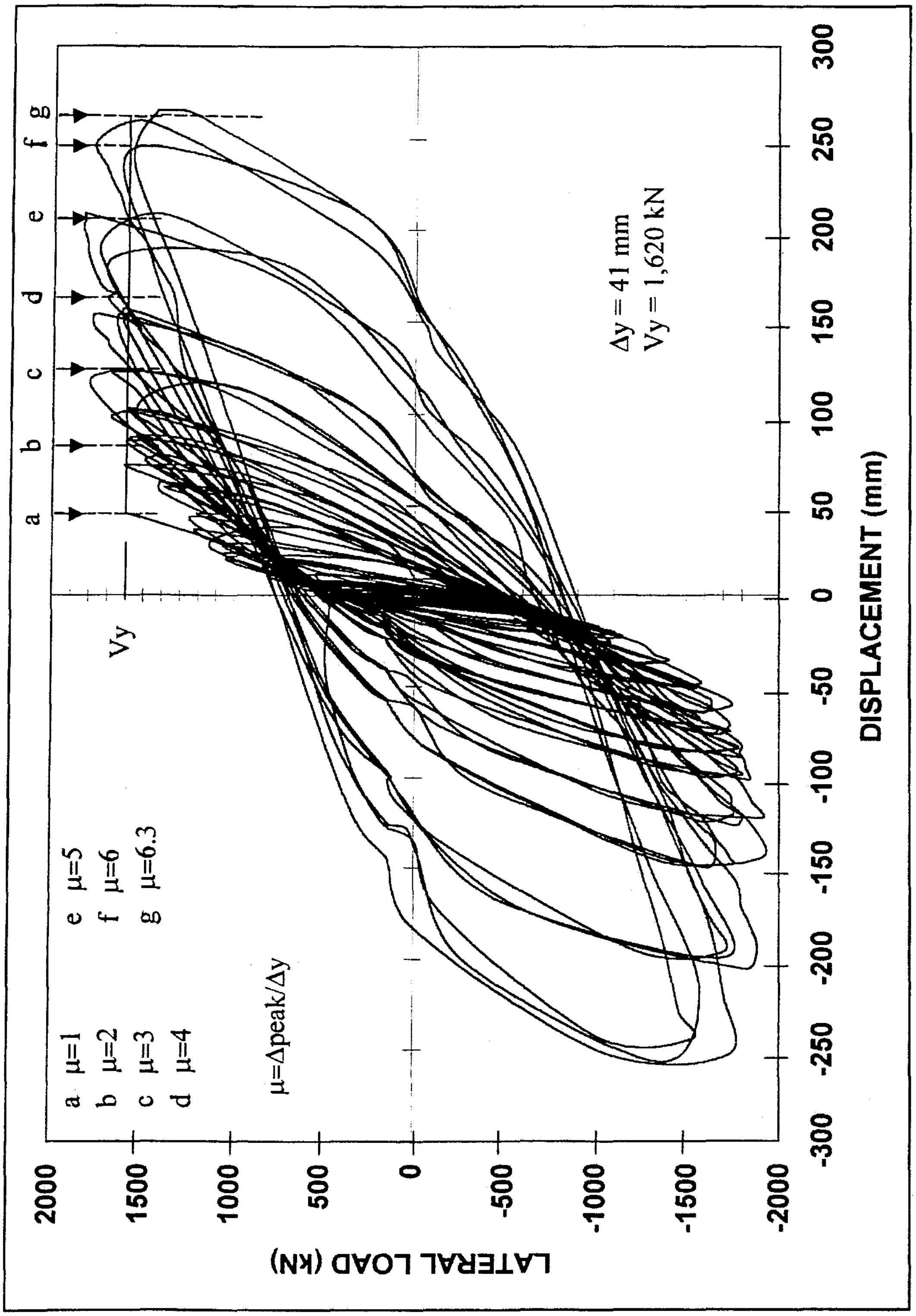

Figure 94. Hysteresis curves for Bent #6

]

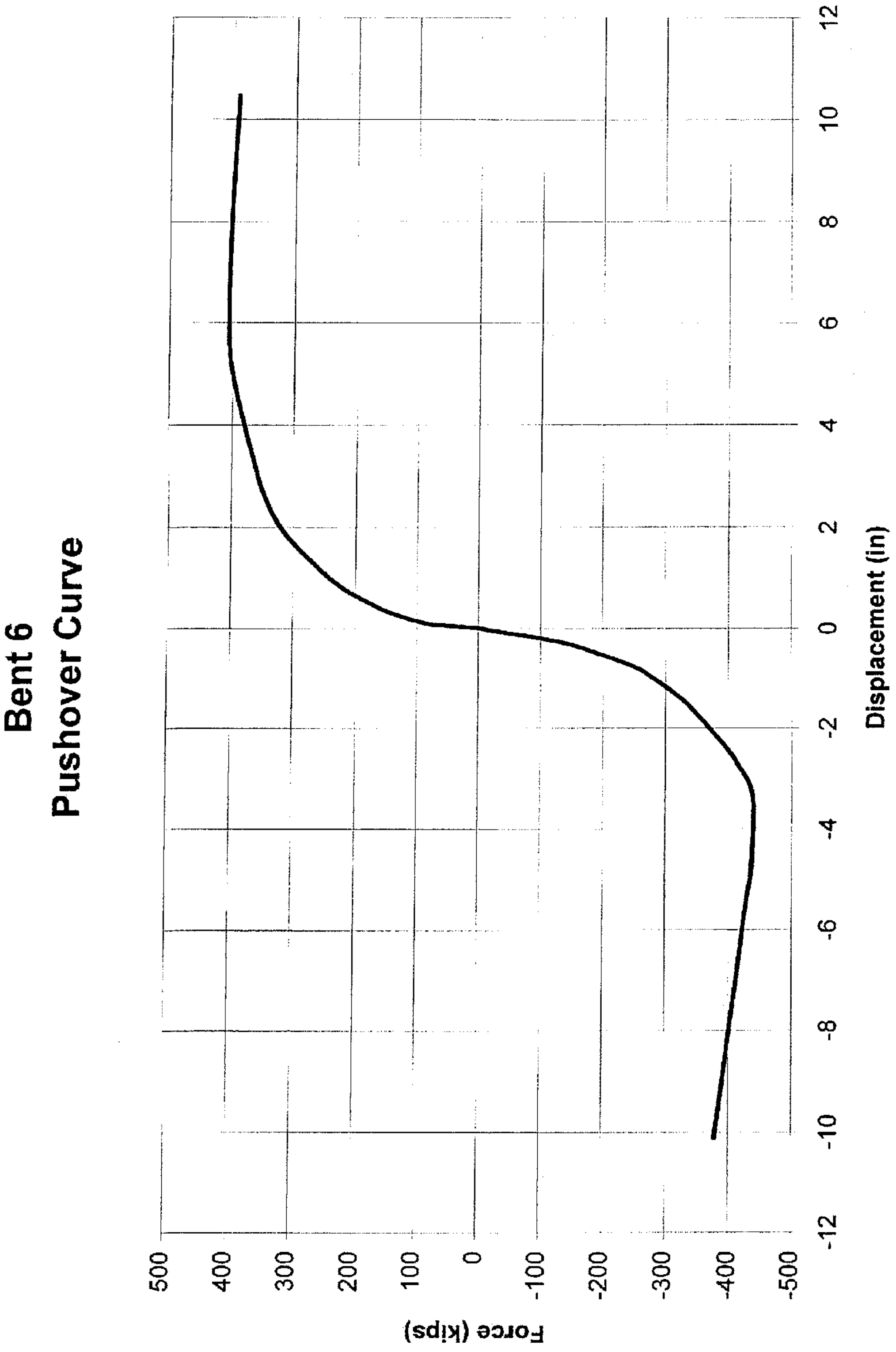

Figure 95. Envelope of hysteresis behavior for Bent #6 (1 kip = 4.448 kN,
1 in. = 25.4 mm)

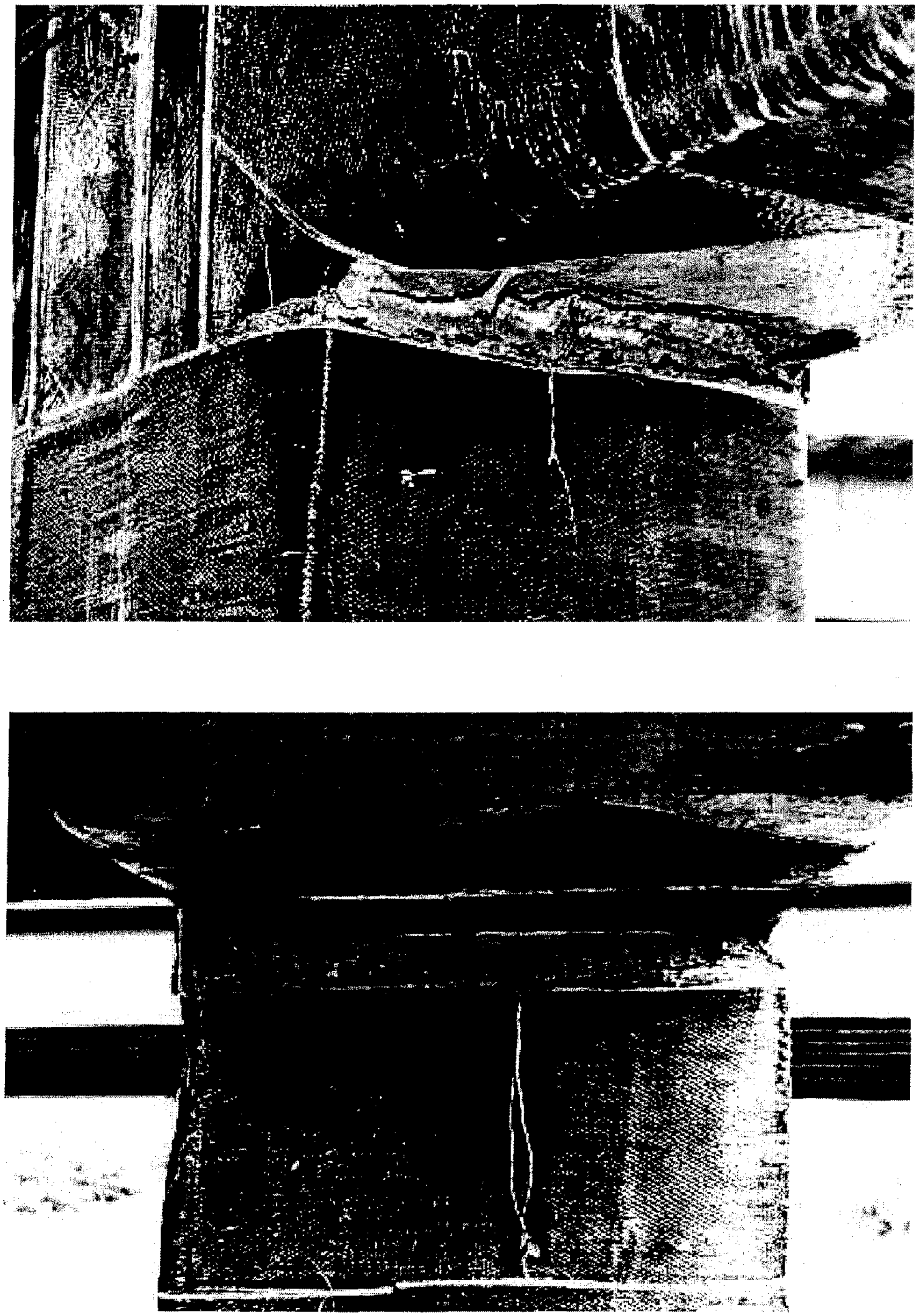

Figure 96. Cracking at the beam cap-column interface of Bent #6

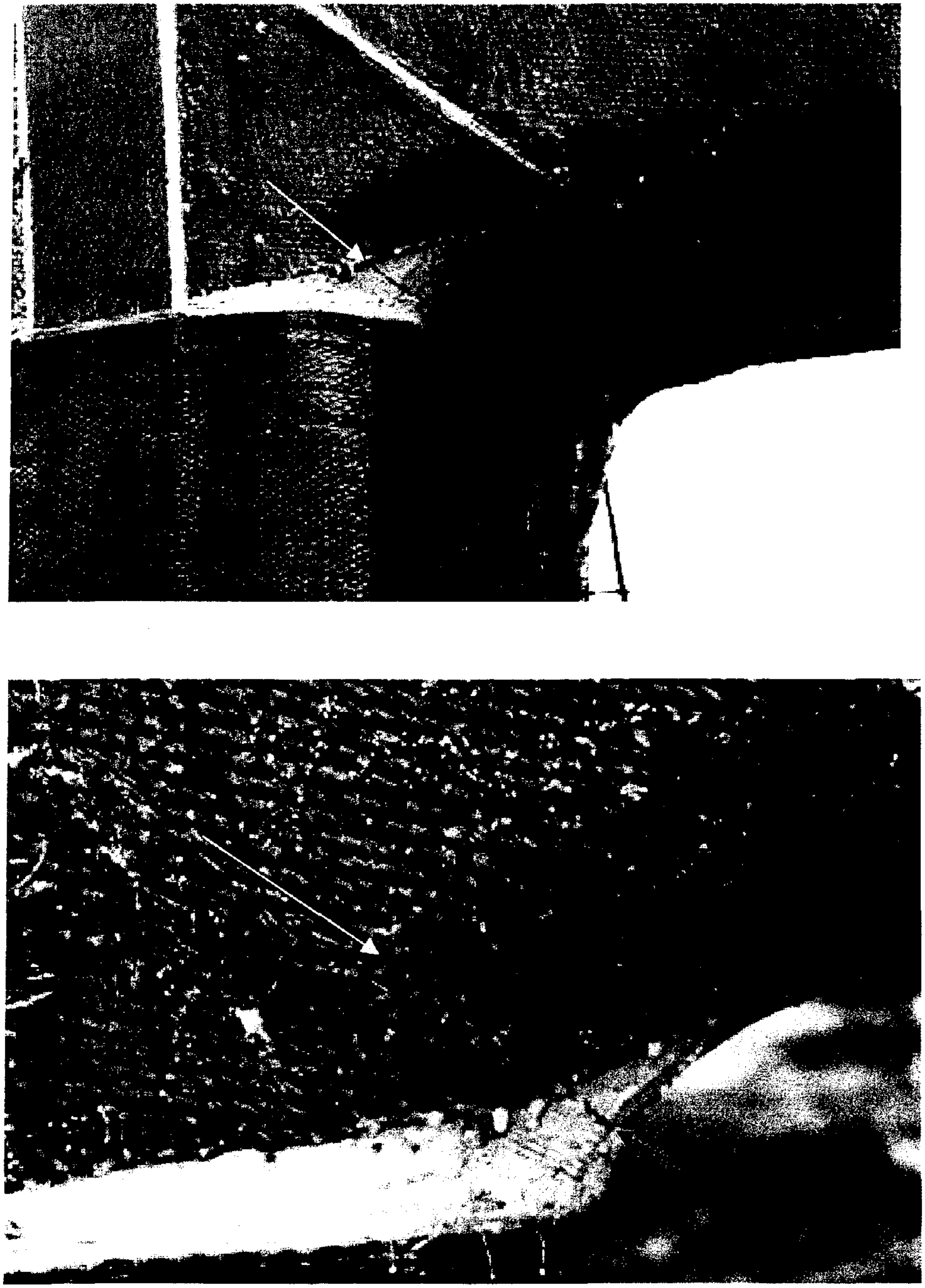

Figure 97. Cracks at the beam to column interface propagating into the FRP composite

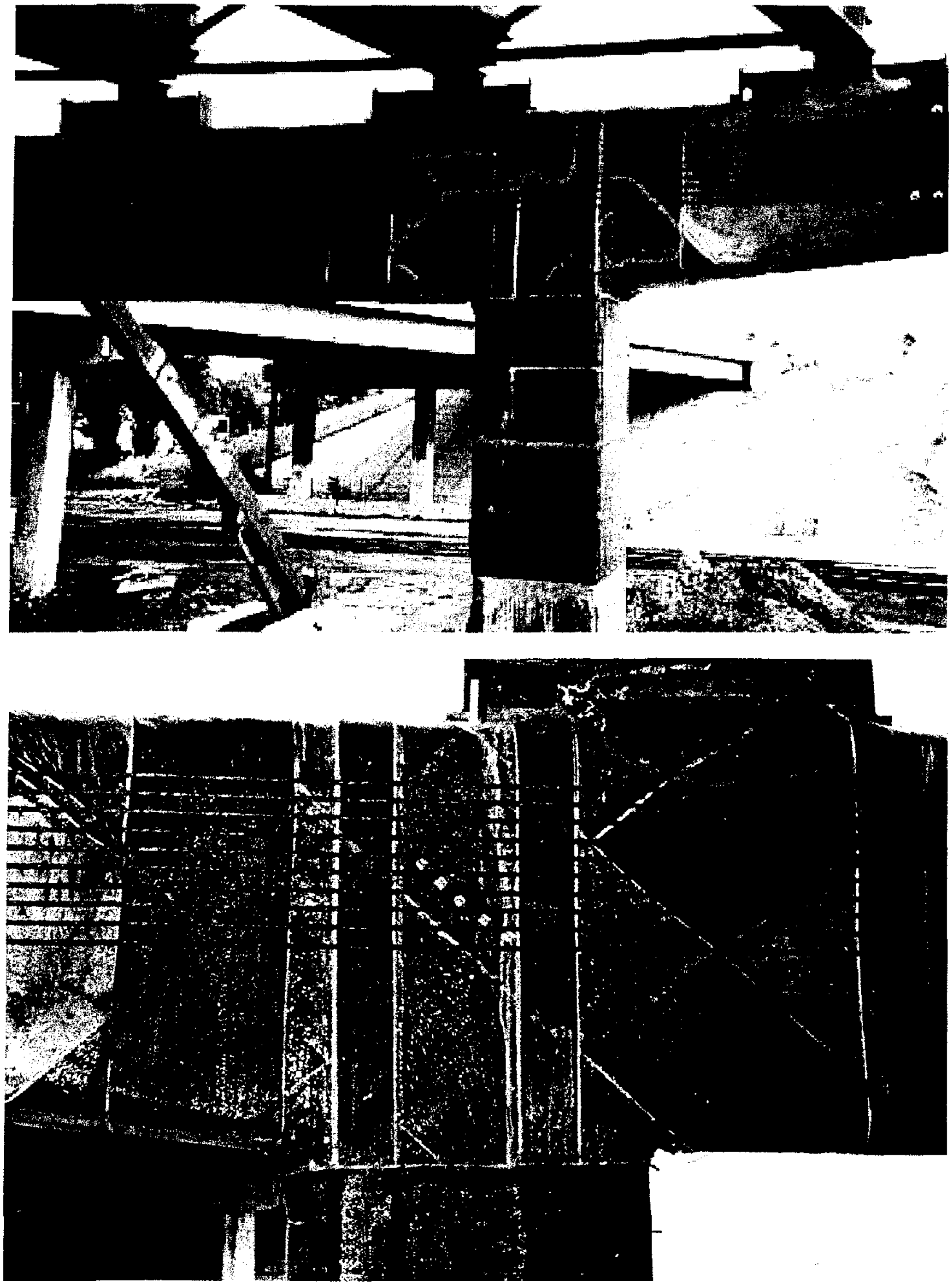

Figure 98. Delamination of FRP composite at the beam cap-column joints

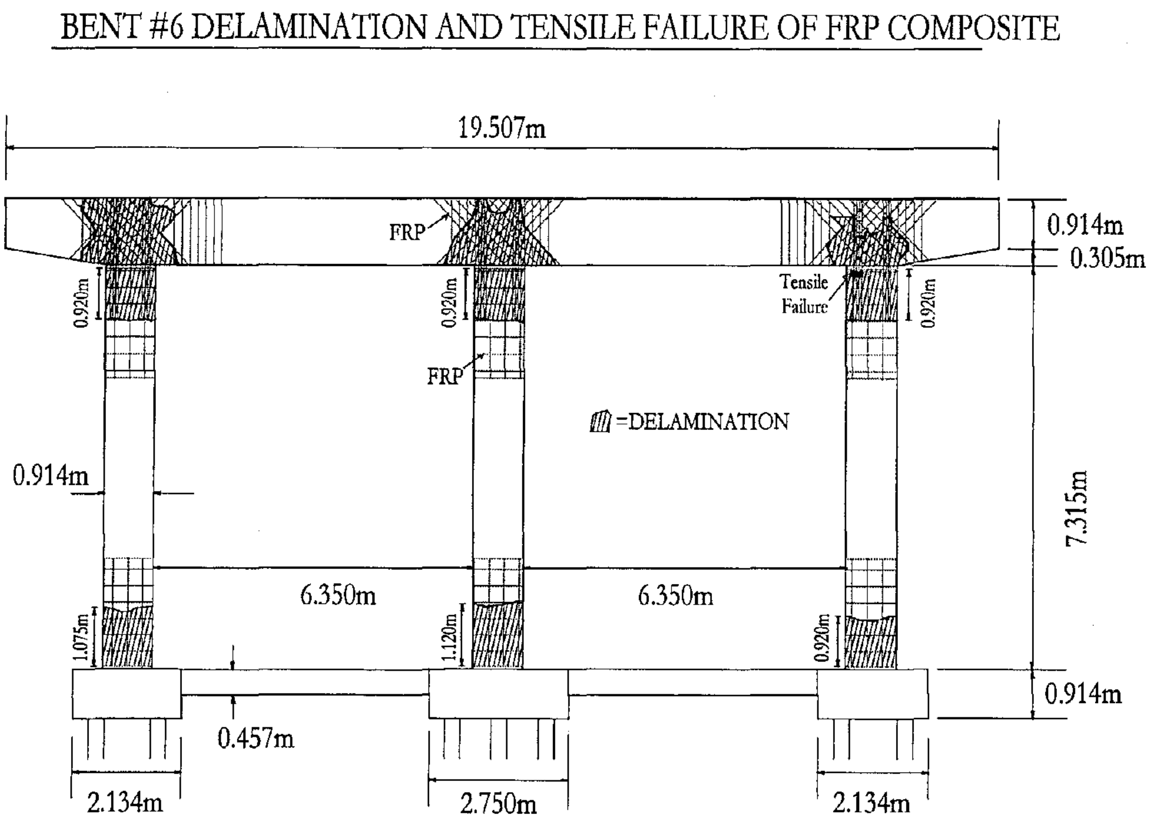

Figure 99. Delamination and tensile failure of FRP composite in Bent #6

delaminated in the beam cap-column joint region, as shown in Fig. 98, and at the top and bottom of the columns as shown in Fig. 99. This occurred because of the low concrete strength in surface tension. The outside carbon fiber layers had visible flexural cracks along the fiber direction. Tensile failure of the 152 mm tensile composite tapes was observed as shown in Fig. 99 and Fig. 100. Strain gages measured the peak value of the strain in the composite at the beam cap-column joints which was found as 0.22%, which was about a fifth of the ultimate strain value of 1%. This low strain level in the advanced composite verifies the value used to design the FRP composite design for shear strengthening of the beam cap-column joints.

The connection of the piles to the pile cap, which was reinforced by anchoring the piles into the pile cap using 32 mm Dywidag bars, was successful; this was evidenced by the severe cracking of the pile caps which was observed for Bent #6 around the columns, indicating improvement of the strength of the lap splice as shown in Fig. 101. The rigid link beam between the pile cap and the footing suffered severe damage and extensive cracking. The failure and cracking patterns of the columns are similar to those observed in laboratory experiments (Seible et al. 1994). The failure mechanism of the FRP advanced composite at the beam cap-column

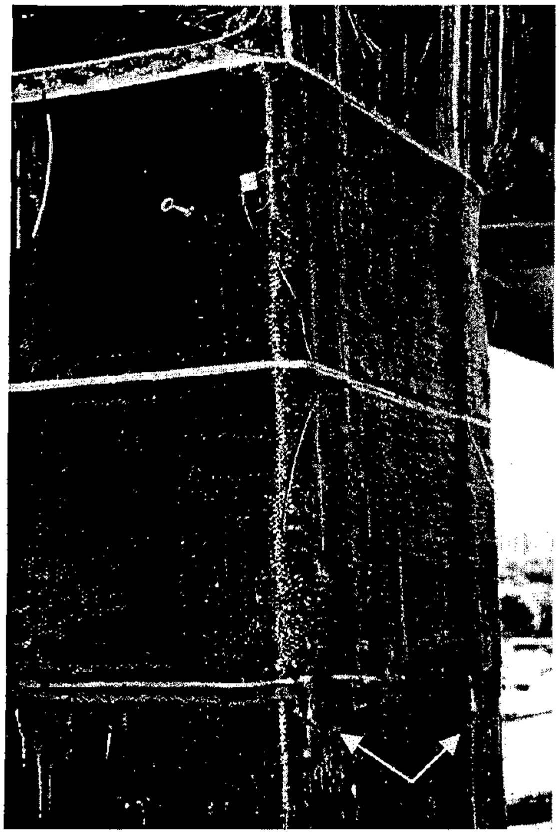

Figure 100. Tensile failure of FRP composite in the U straps on the columns

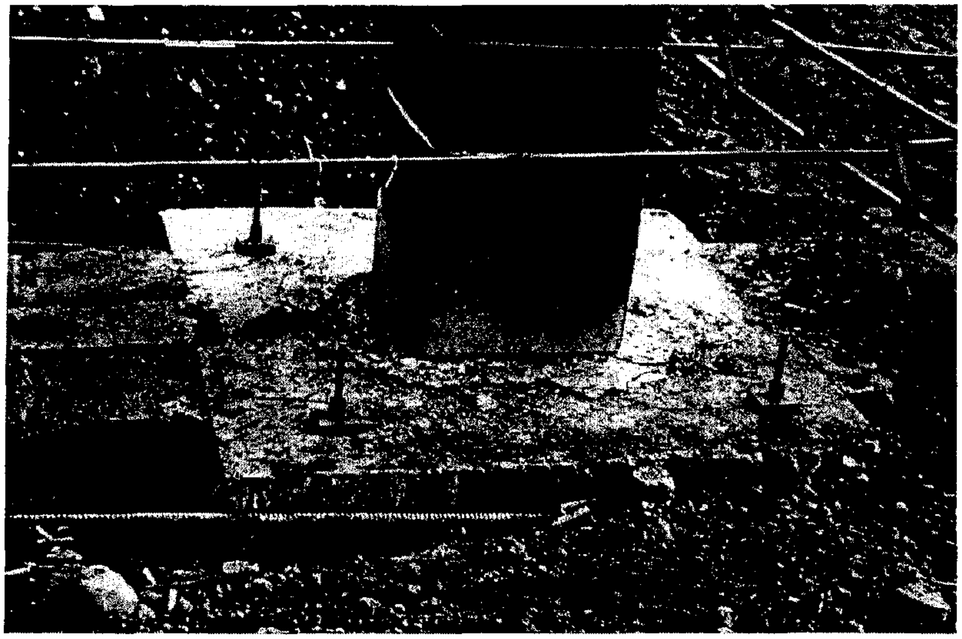

Figure 101. Radial and circular cracks at top of pile cap around the column

joints was also observed previously in laboratory experiments (Gergely et al. 2000). After completion of the test, the FRP composite was removed from the faces of the column, as shown in Fig. 102. It was found that the concrete had minor cracks, and the condition of the plastic hinge region was remarkably intact. It was found that the FRP composite confined the column and maintained its integrity even at the relatively high displacement ductility of $\mu_\Delta = 6.3$. This observation supports laboratory experimental evidence of the effectiveness of FRP composites to increase the ductility of concrete columns with relatively little concrete degradation (Priestley et al. 1996).

Figure 102. Condition of middle column below beam cap-column interface after removal of FRP composite at the completion of the test on Bent #6

The quality of the FRP composite application and the FRP composite material itself was examined after the test on Bent #6 after demolition. For the most part the saturation of the fibers was good even though some dry fibers were occasionally found as shown in Fig. 103. The use of a saturator would alleviate this problem. The bonding of the FRP composite to the concrete substrate was varied. Even though the old concrete was removed and shotcrete was applied in the beam cap, there were still areas were the FRP composite delaminated with little resistance from the substrate concrete. However, in most areas a sufficiently good bond was observed as shown in Fig. 103. The water jet procedure is recommended after application of shotcrete for an even better bond. This is critical in areas such as the beam cap-column joint where the FRP composite contribution depends on the bond between concrete and FRP composite.

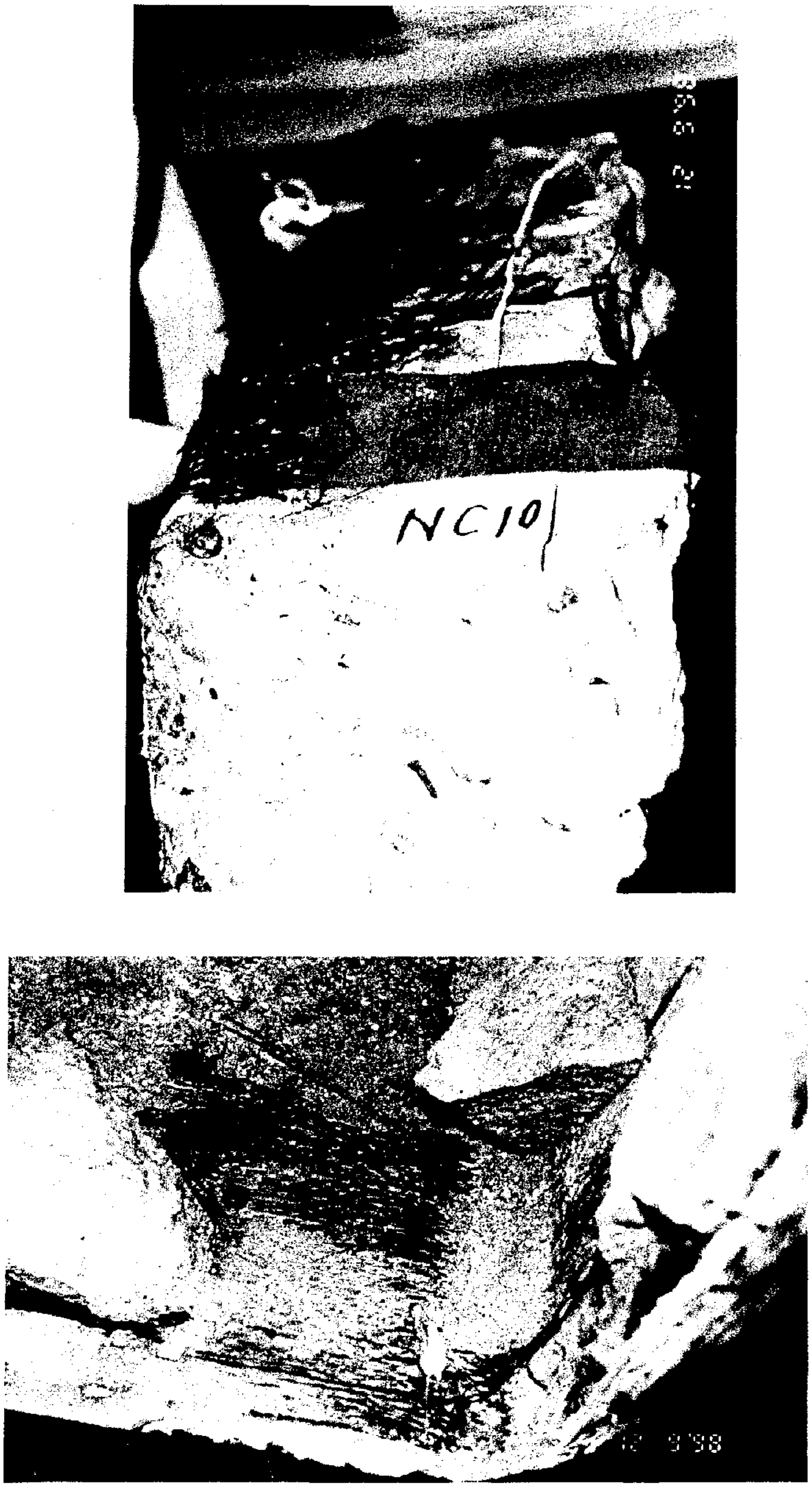

Figure 103. Condition of FRP composite and adhesion of FRP composite to the concrete

The distortion of the beam cap-column joints was determined from LVDT measurements. Figure 104 shows the diagonal displacement of the beam cap-column joint at the middle column. The maximum diagonal measurement was 10 mm (0.4) in, which is three times larger that the corresponding movement for Bent #5. The shear strain in the same joint is shown in Fig. 105; the maximum strain is 0.013 which is four times the strain observed in Bent #6 and well beyond the ultimate compressive strain usually obtained in reinforced concrete sections which is about 0.004. The shear strain is also shown at an exterior joint in Fig. 106, where the maximum strain is observed as 0.0038. The principal tensile stresses at the interior beam cap-column joint were evaluated in a manner similar to that described for Bent #5, using equations (6.1) and (6.2). The principle tensile stress was found as 2.73 MPa (396 psi), which corresponds to a stress of $0.60\ (f'_c)^{0.5}$ *MPa or* $7.20\ (f'_c)^{0.5}$ *psi*, which is 37 percent higher than that developed in Bent #5. It is also approximately 44 percent higher than the stress predicted to cause joint degradation (Priestley et al. 1996).

Strain gages were attached to the steel reinforcement in the columns, beam cap, the Dywidag bars, and the FRP composite. Figure 107 shows the location of the strain gages on all the steel and Figure 108 shows the location of the strain gages on the FRP composite. Details of the strain gages attached to the FRP composite on the beam cap-column joint are shown in Fig. 98 and on the column in Fig. 100. Figure 109 displays the strain gage readings on three of the vertical 32 mm Dywidag bars in the middle pile cap as shown in Fig. 107. It is clear that all three bars have yielded and consequently, large movements are expected at the pile cap-pile interface. Figure 110 shows the strain gage readings on the horizontal Dywidag bar shown in Fig. 107. These Dywidag bars are providing the tension forces in completing the load path for the structure and are shown in Fig. 12. As can be seen the two bars have yielded quite early in the loading sequence. Figure 111 shows the strain gage readings from gage 24, which shows that the steel has yielded at the top of the exterior column in the plastic hinge region. Figure 112 shows the strain gage readings from gage 21 on the FRP composite, which is adjacent to gage 24 in the exterior column. As can be seen, the FRP composite reaches a strain of 0.002, and the readings from gages 21 and 24 show that the reinforcing steel and FRP composite work together to resist the applied load in opposite directions. That is, the steel reinforcement is seen to carry the compression and the FRP composite carries the tension.

Strain gages 16 and 17 are on the FRP composite on the diagonal in the middle beam cap-column joint at a 45 degree angle with respect to the horizontal whose records are shown in Fig. 113. Strain gage 16 shows that a strain of 0.002 was reached at a lateral displacement of approximately 8 in. (drift of 2.8%); after this point the strain in the FRP composite drops dramatically signifying that the bond between the FRP composite and the concrete has been lost. From that point on, at approximately data count 6800, the strain in the FRP composite steadily decreases and as Fig. 92 shows the lateral load capacity starts to drop. Thus, the contribution of the FRP composite is effectively lost after a tensile strain in the composite of 0.002, which agrees with similar experiments carried out in the laboratory (Gergely and Pantelides 1998); this shows that the value of FRP composite maximum strain used to determine the joint shear design of 0.0021 in equation (7.9) was a good approximation. A very similar behavior was observed in the FRP composite from strain gage 31 at the exterior beam cap-column joint, as can be observed from Fig. 114.

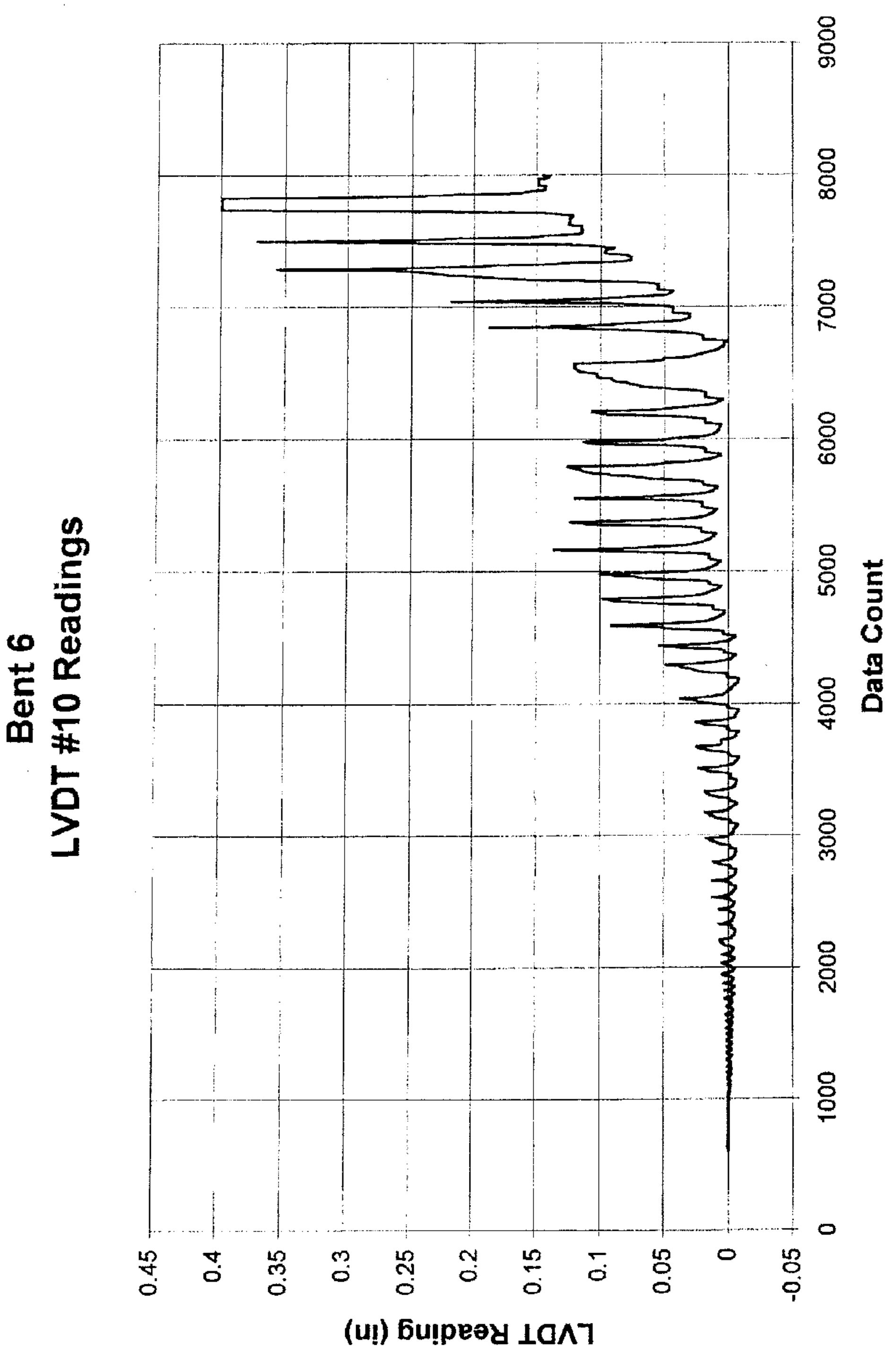

Figure 104. Displacement of diagonal along interior beam cap-column joint on Bent #6
(1 in. = 25.4 mm)

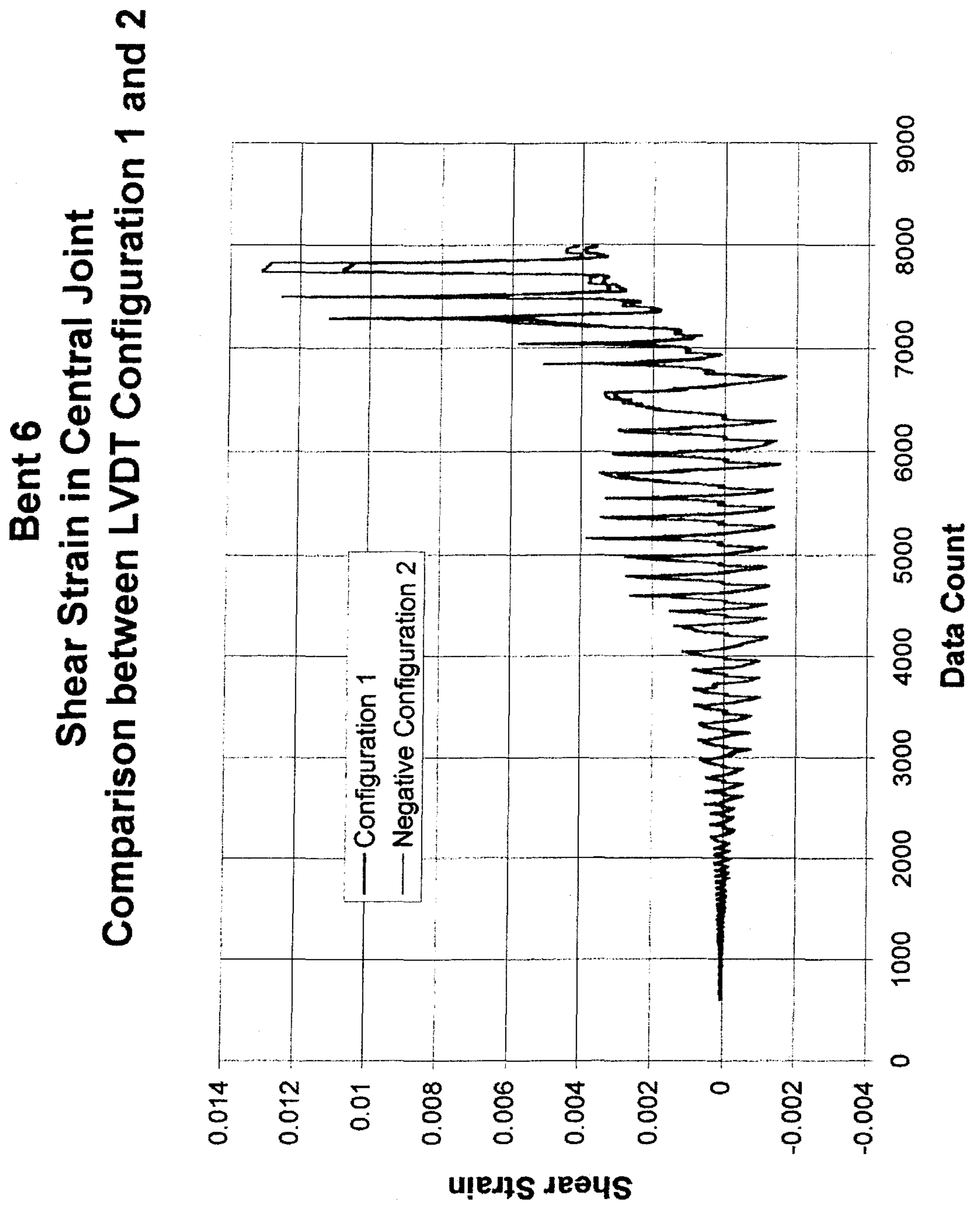

Figure 105. Shear strain at interior beam cap-column joint on Bent #6

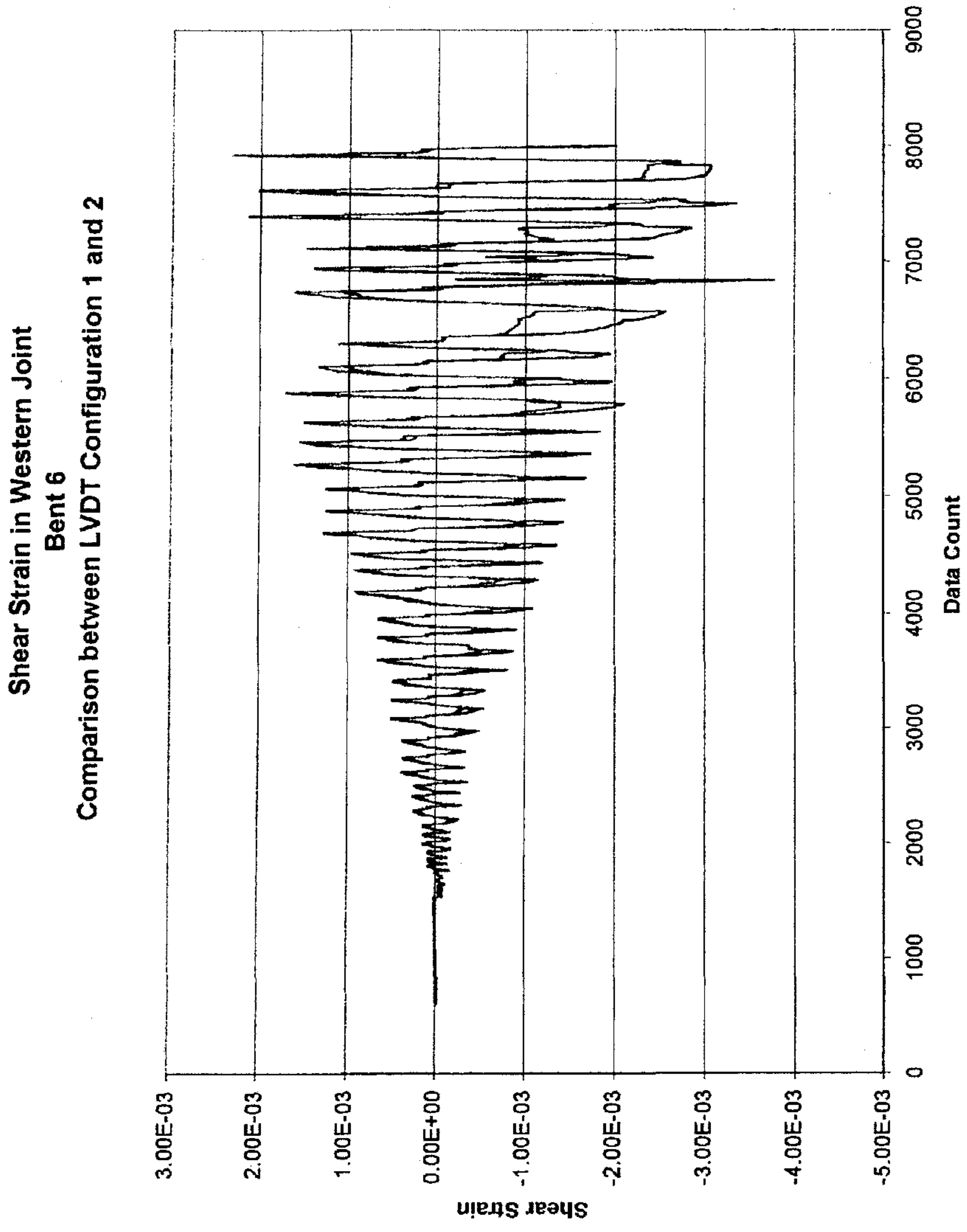

Figure 106. Shear strain at exterior beam cap-column joint on Bent #6

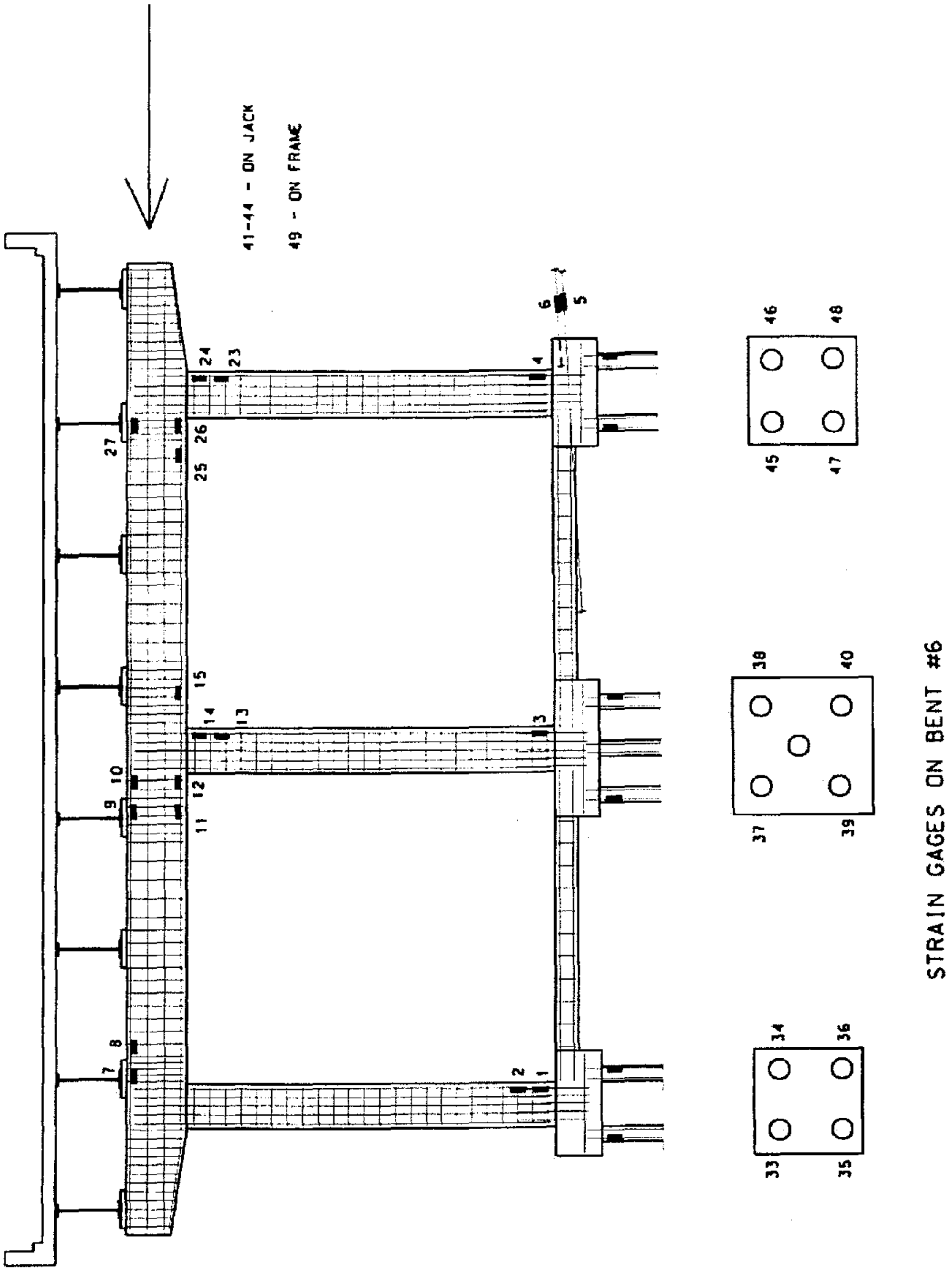

Figure 107. Strain gage locations on reinforcement of Bent #6

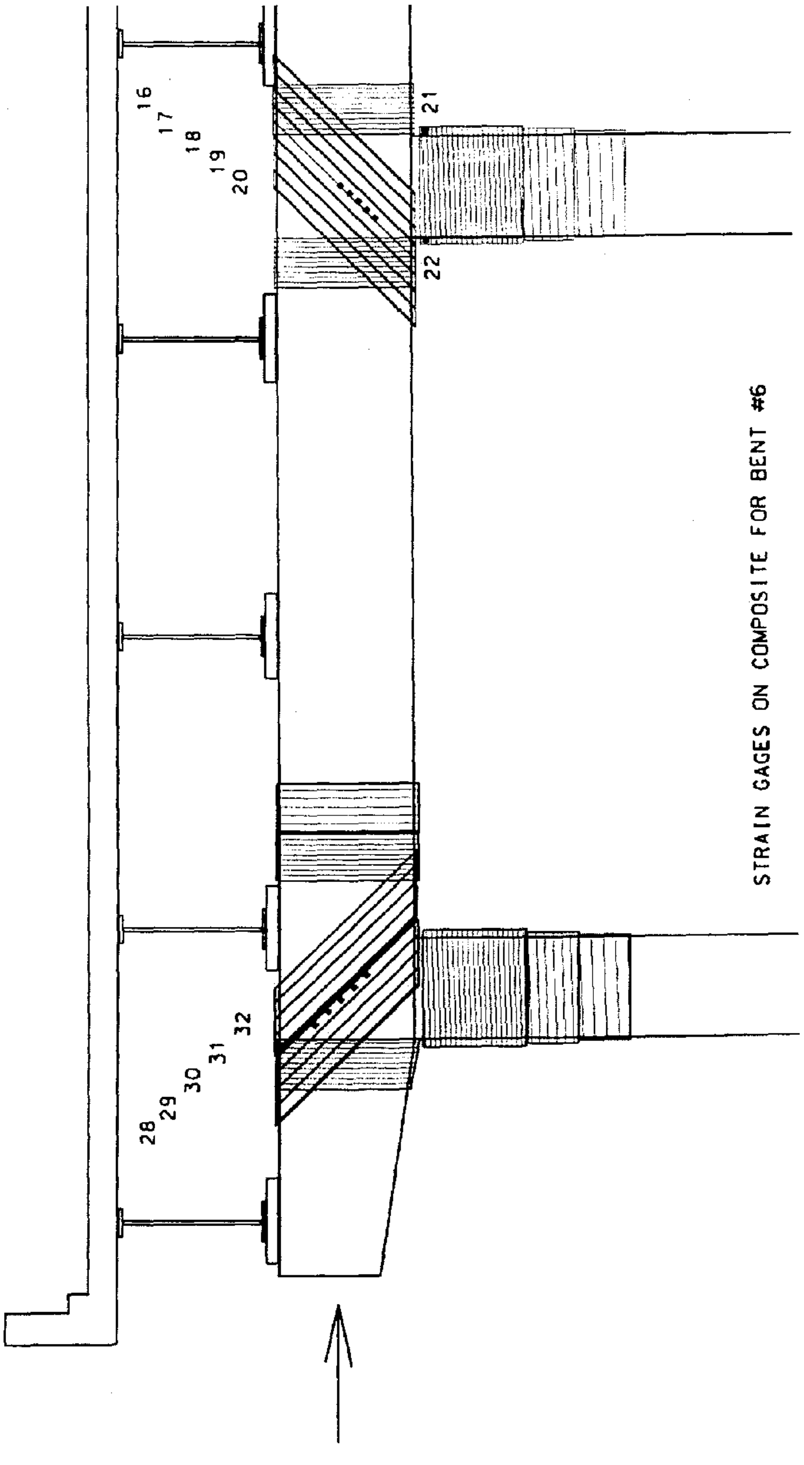

Figure 108. Strain gage locations on FRP composite of Bent #6

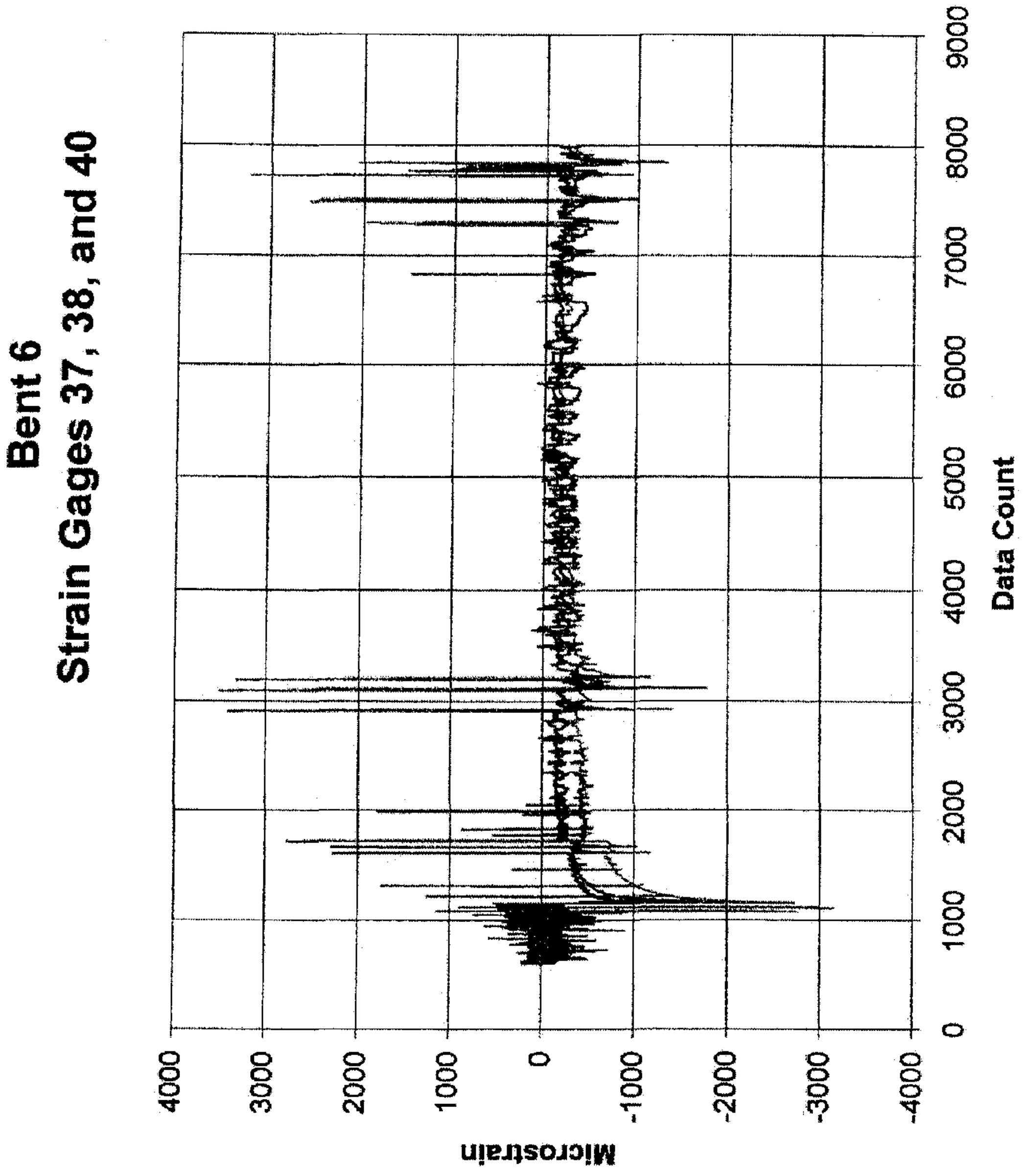

Figure 109. Strain gage readings on vertical Dywidag bars in the middle pile cap

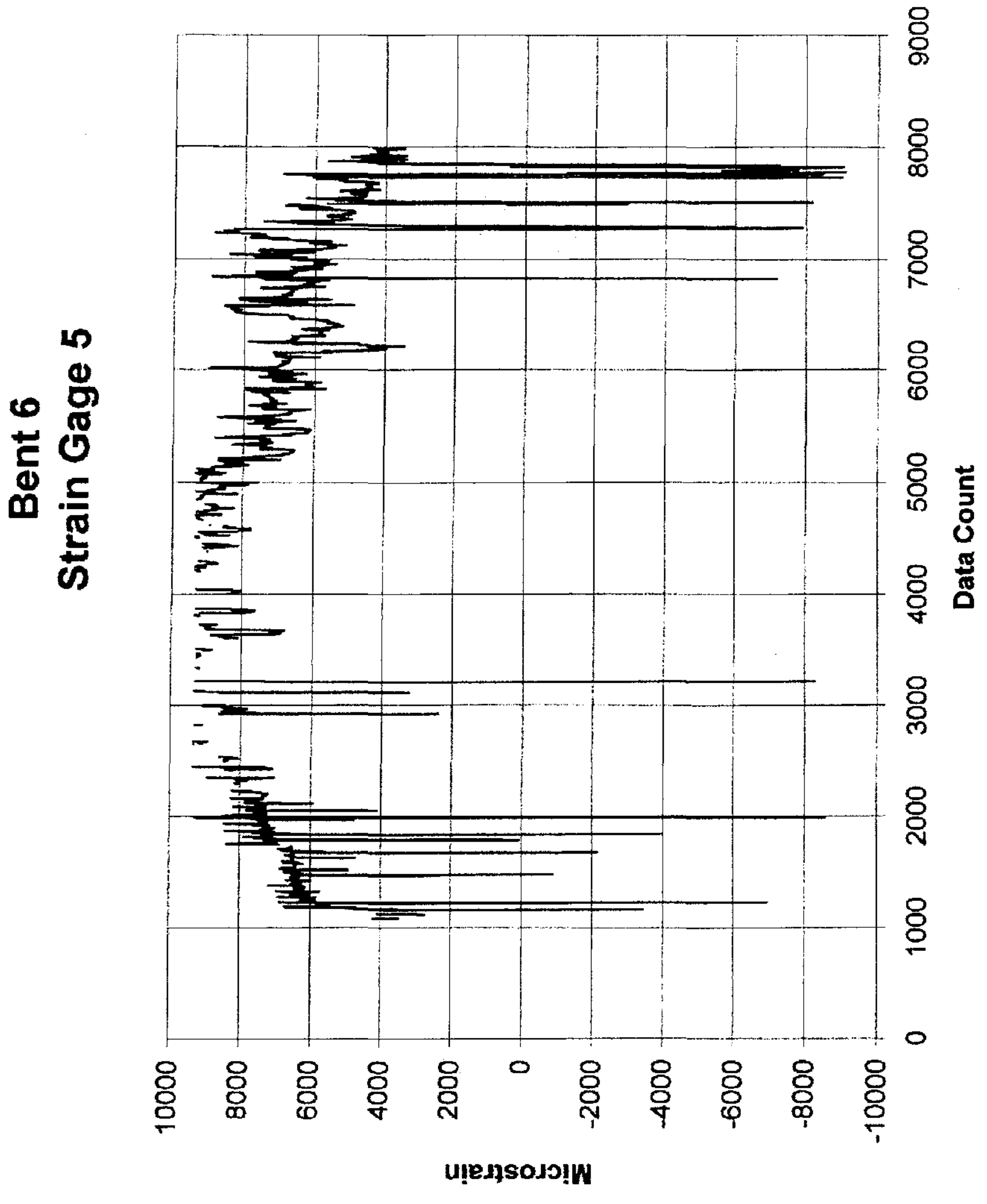

Figure 110. Strain gage readings on horizontal Dywidag bar

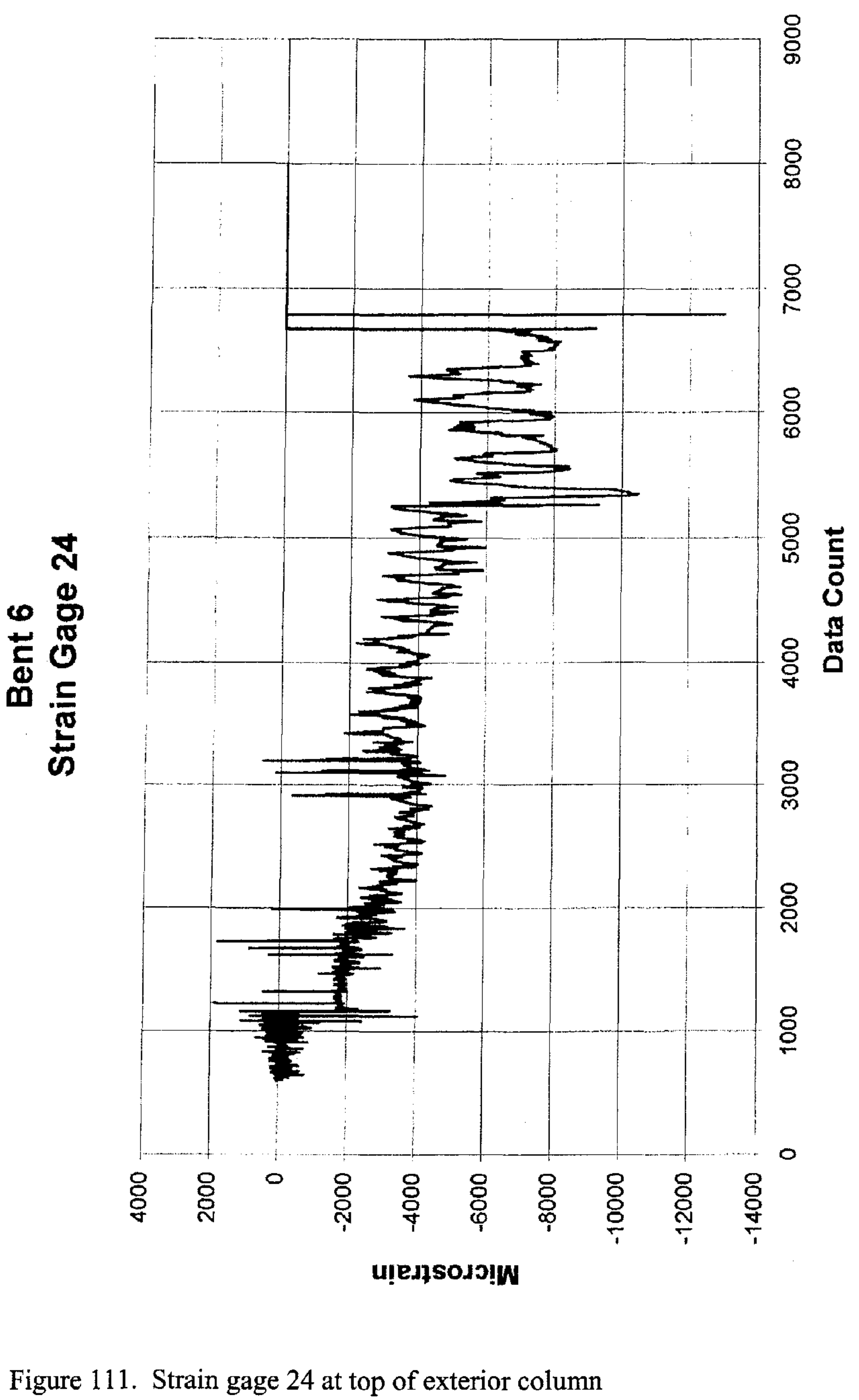

Figure 111. Strain gage 24 at top of exterior column

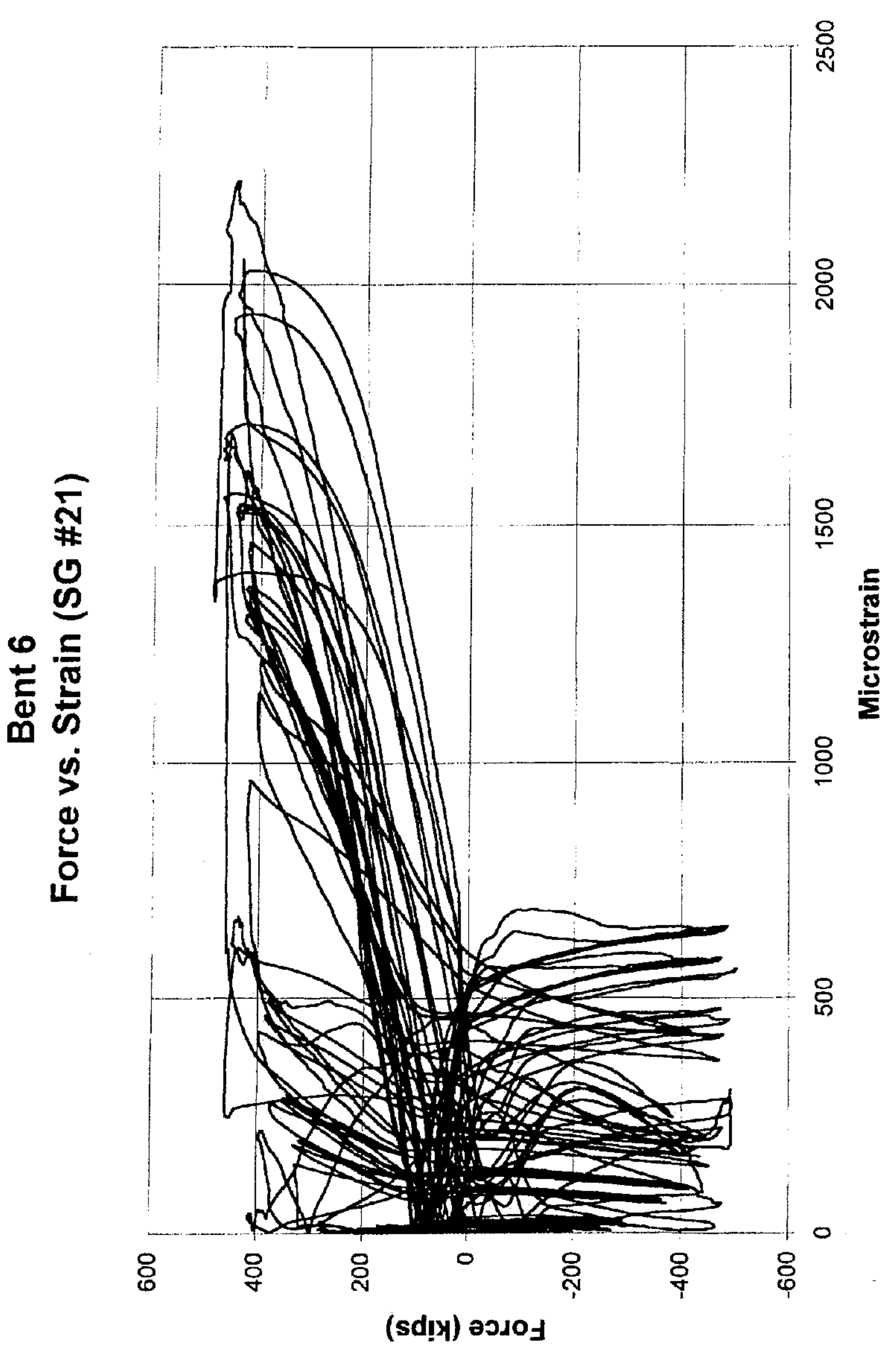

Figure 112. Strain gage on FRP composite at top of exterior column (1 kip = 4.448 kN)

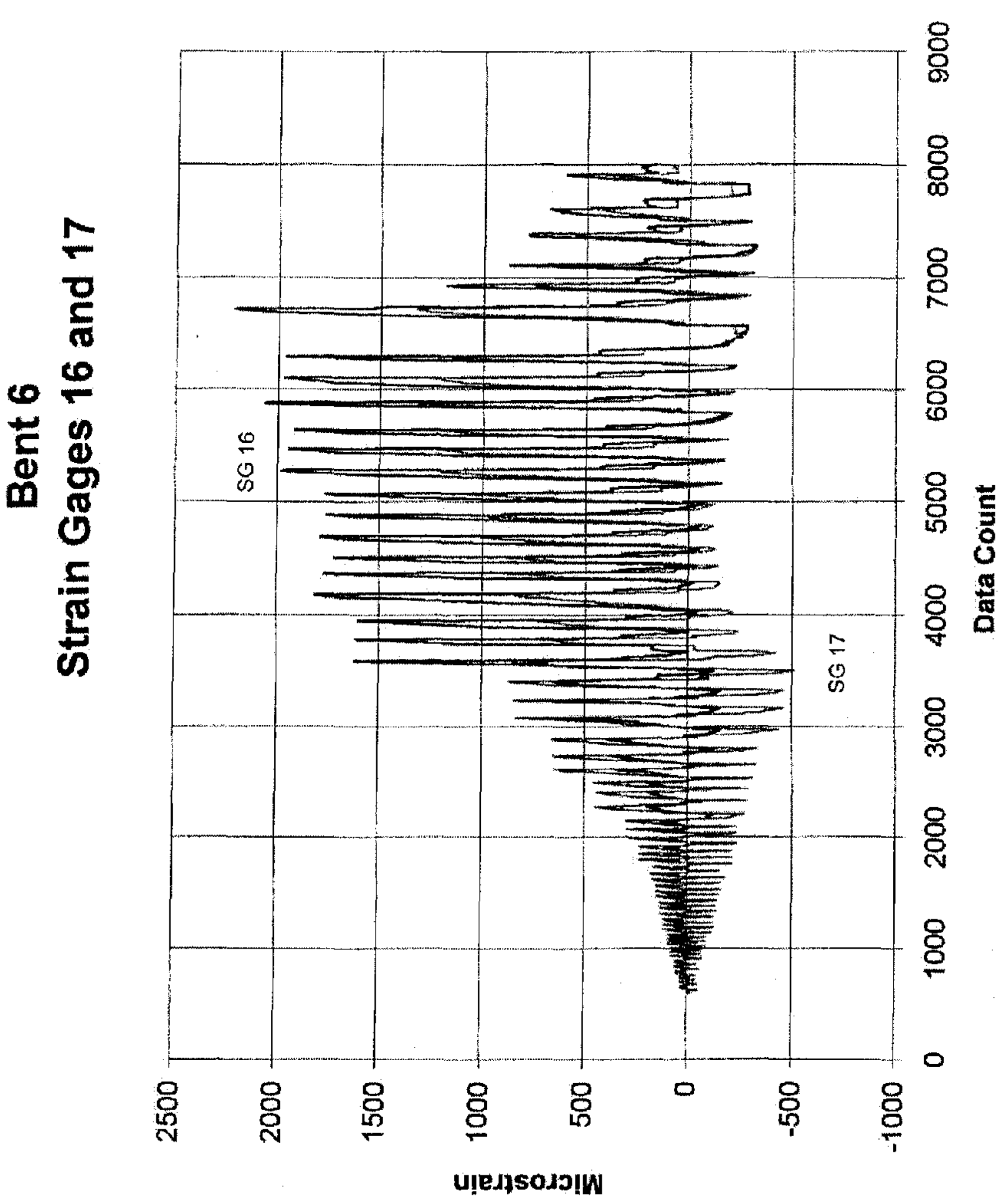

Figure 113. Strain gages on FRP composite in the beam cap-column joint at top of interior column

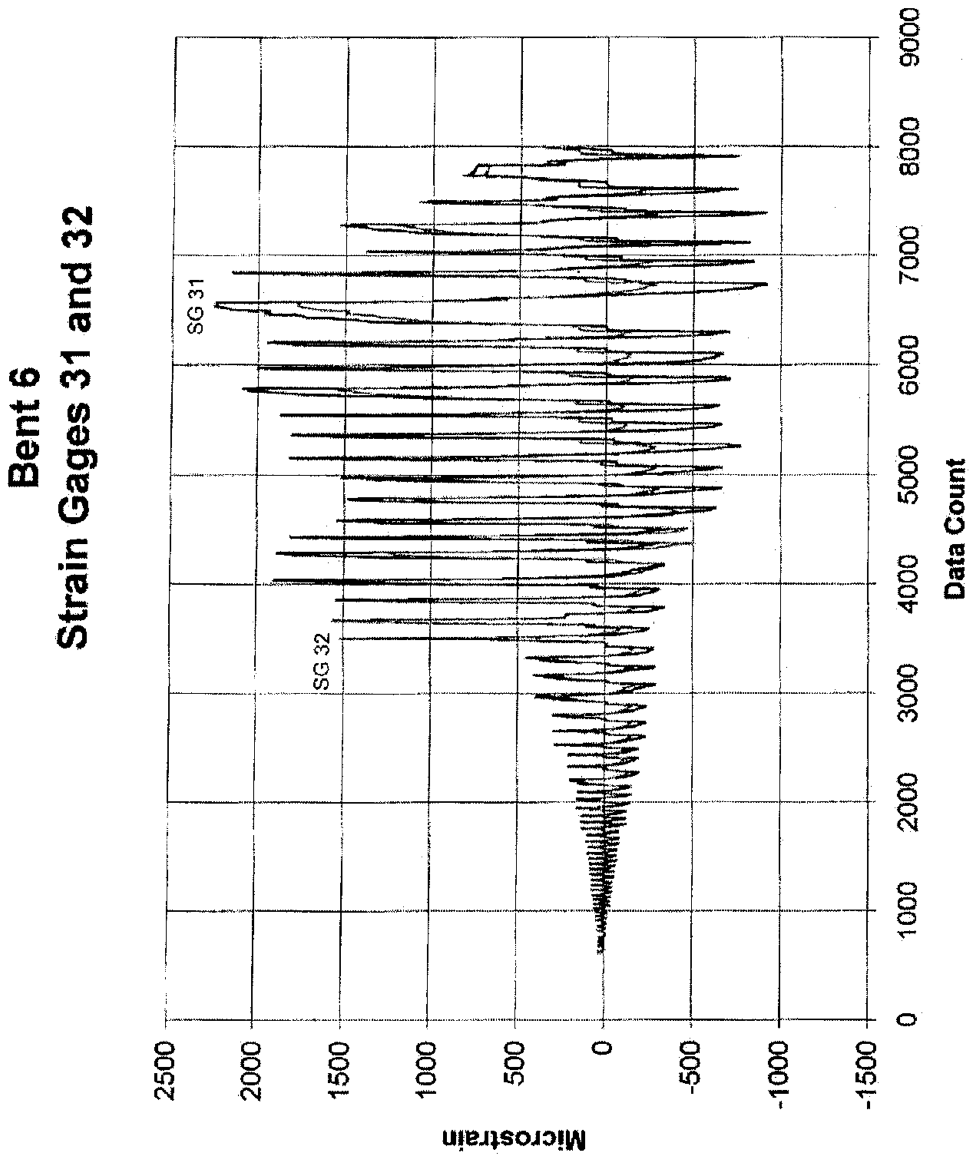

Figure 114. Strain gages on FRP composite in the beam cap-column joint at top of exterior column

The displacements of the exterior column were recorded throughout the test at 6 ft (1.829 m) intervals, as shown in Fig. 90 using displacement transducers DT1 to DT5. The envelopes of the displaced shape at various drift levels both in the push and pull direction are shown in Fig. 115. Even though the curve shows the displaced shape of one of the exterior columns, it closely represents the overall transverse deformation of the bent. As can be seen from Fig. 115, initially up to a ductility of approximately 2.2 in push and 3.1 in pull, the displacement envelope resembles that of the as-built Bent #5 shown in Fig. 76. However, beyond this point and at increasingly higher ductilities the displaced shape begins to change shape and becomes more of an S-shape and the quarter points form an almost perfect line. This is shown more vividly in Fig. 116 which shows the interior column at a ductility approximately equal to 6. Note that the points in Fig. 115 were connected only by straight lines.

The energy dissipated during the cyclic loading of the bridge bent represents a measure of the damage suffered by the bent. The cumulative dissipated energy was calculated as the area under the hysteresis loops and is shown in terms of the load cycle number in Fig. 117. It can be seen that approximately 50% of the energy is dissipated in the last six cycles, which is similar to the energy dissipation of Bent #5. A plot of the cumulative energy dissipation versus maximum displacement at each load step is shown in Fig. 118. The curve is almost linear after an initial steep slope at displacements near 100 mm (4 in.), indicating that the energy is heavily dependent on the maximum displacements reached during testing. As observed in Fig. 117, half of the energy was dissipated after the load step corresponding to the maximum deformation of 7.4 in. (188 mm).

Comparing the performance of the as-built Bent #5 and the rehabilitated Bent #6, it can be seen that the FRP advanced composite retrofit significantly increased the ductility capacity of the as-built bent, and allowed the bent to achieve a higher lateral load capacity while maintaining a significant gravity load (Pantelides et al. 1999b). In addition, the energy dissipated by Bent #6 is more than twice that dissipated by the as-built Bent #5.

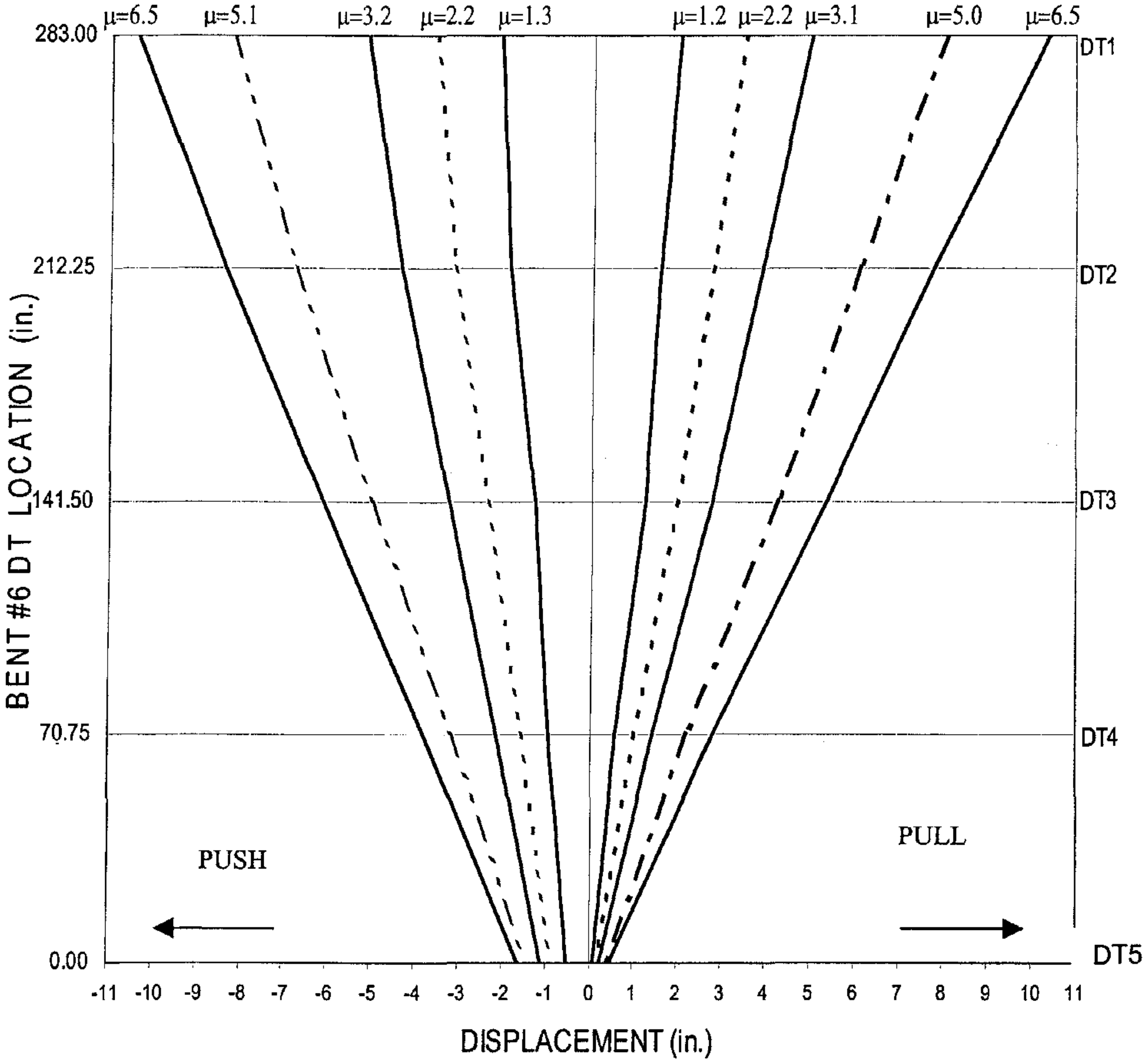

Figure 115. Displacement envelopes of exterior column of rehabilitated Bent #6
(1 in. = 25.4 mm)

Figure 116. Displaced shape of interior column of Bent #6 at approximately a displacement ductility equal to 6

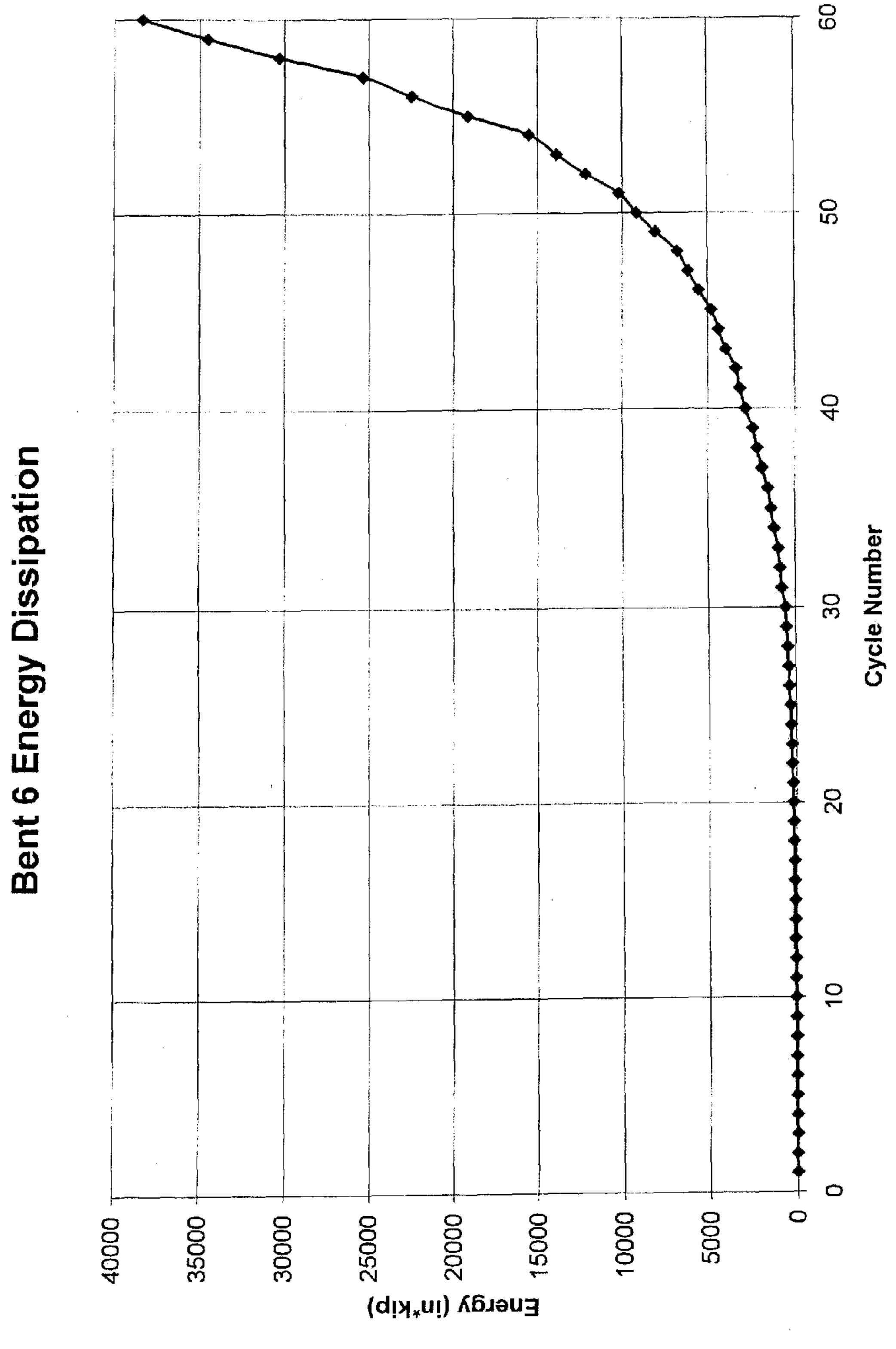

Figure 117. Cumulative energy dissipation of Bent #6 versus load cycle number
(1 kip-in. = 0.113 kJ)

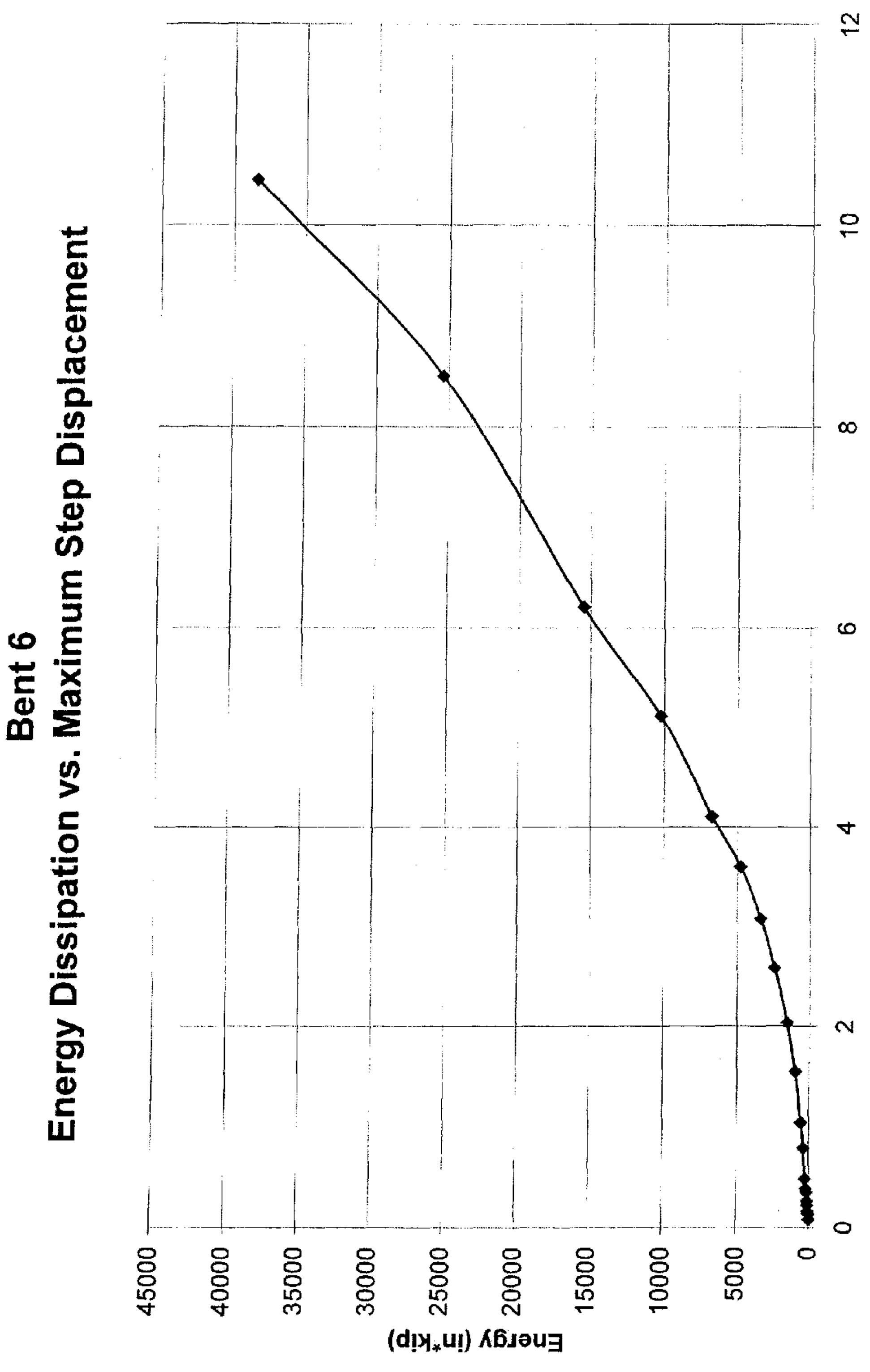

Figure 118. Cumulative energy dissipation of Bent #6 versus maximum load step displacement (1 kip-in. = 0.113 kJ)

8. REPAIRED BENT #5R WITH FRP COMPOSITES

As was stated in section 7 for Bent #6, the goal of the retrofit was to improve the displacement ductility by a factor of two. However, a more modest increase in ductility was expected to occur in the test for Bent #5R, since the bent had already been damaged. Every reasonable effort was made to repair the bent using shotcrete and epoxy injection so that it would regain as much of the strength it had before the original test for Bent #5 as possible. It was felt that the presence of the FRP composite retrofit would reinforce the bent and assist the weak areas of the structure in resisting the loads and displacements imposed during this second test. A decision was made not to alter the FRP composite design for Bent #6, so that direct comparisons could be made.

Layout of FRP composite retrofit for Bent #5R

The composite layout for the repaired Bent #5R was identical to that for Bent #6 and is shown in Figs. 86 and 87 in section 7. There were some additional difficulties present in the application of this FRP composite as compared to those encountered in retrofitting Bent #6, due to the presence of cracks which resulted from the first testing of Bent #5. These cracks were filled to a great extend using a resign grout.

The application of the composite included: (a) removal of loose concrete both originally present and also resulting from extensive cracking after the first test for Bent #5; this involved using jack hammers and high pressure water jet on all four surfaces of the beam cap down to the concrete cover, as well as in the columns in the area of the plastic hinges on the top as shown in Fig. 119; this length of the plastic hinge area did not exceed the size of the column which was 36 in. (914 mm); (b) crack injection using Sho-Bond Bics system in the columns, which is used to repair cracks in concrete structures, as shown in Fig. 119, and the beam-column joints as shown in Fig. 120; the system makes use of the contraction pressure of a rubber tube to reliably inject a special epoxy resin grout deep into cracks over time; this involved the marking of the cracks, applying fitting pipes along the crack 12 in. (305 mm) apart, and at branch points as shown in Figs. 119-121; a seal is applied around the fitting pipes and along the crack as shown in Fig. 121; the two part epoxy grout is then mixed and a DD injector balloon is connected to the injector and the epoxy grout mix is applied into the balloons, which are shown in Fig. 122; a more detailed explanation of the epoxy grout crack injection is given in the Construction Report (Pantelides and Reaveley, 1999); (c) shotcreting of the surface of the beam cap to bring it to its original shape; a wire mesh was used at the bottom of the beam cap for the shotcrete to adhere; (d) application of a structural adhesive; and (e) application of the carbon FRP sheets using hand layup and an ambient temperature curing system.

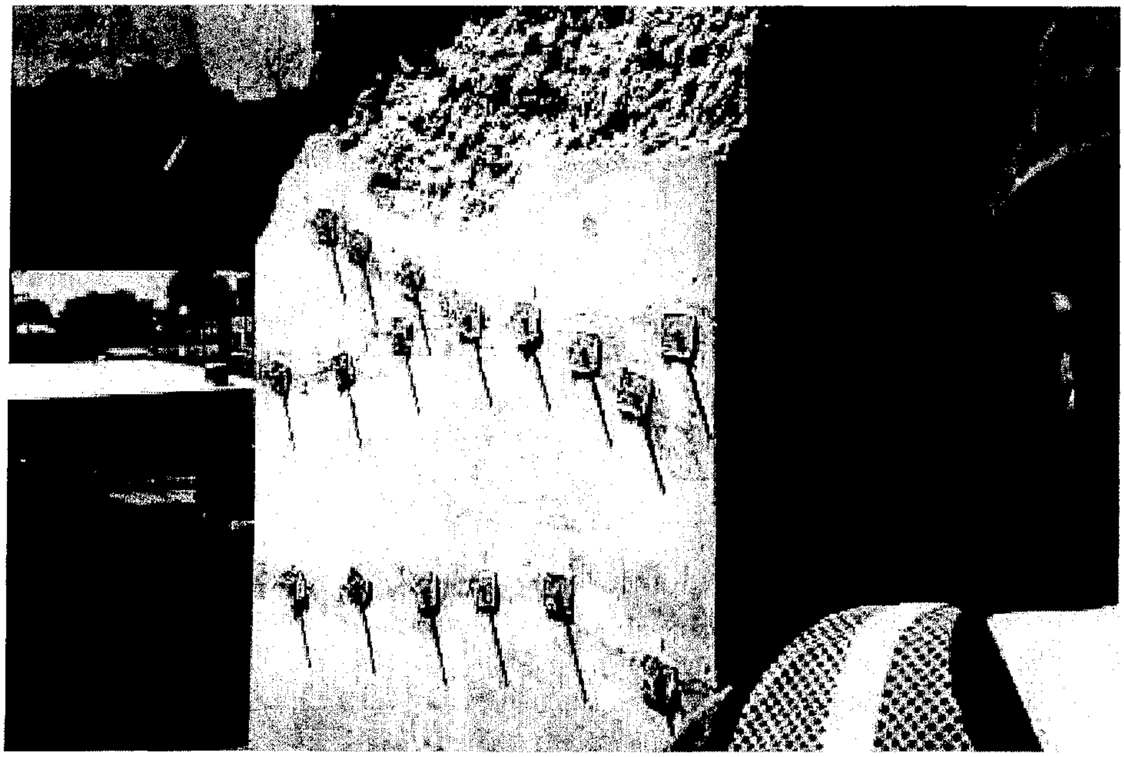

Figure 119. Repair of center column cracks of Bent #5R using resin grout injection

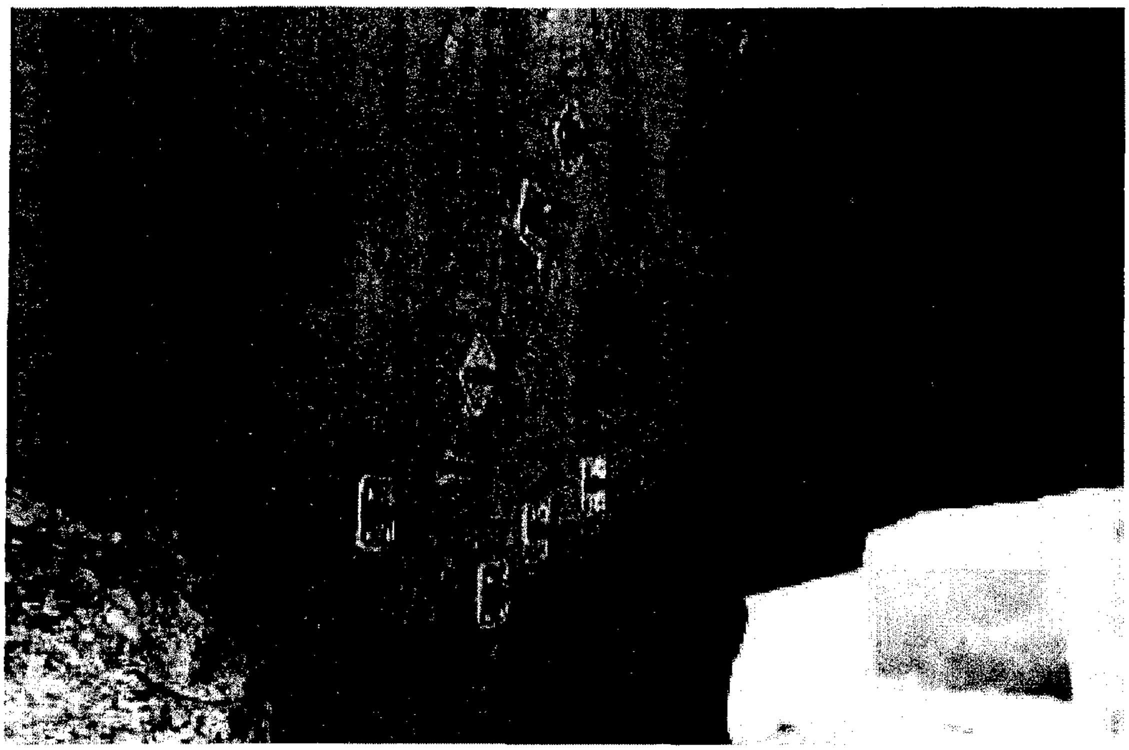

Figure 120. Repair of beam column joint cracks of Bent #5R using epoxy grout injection

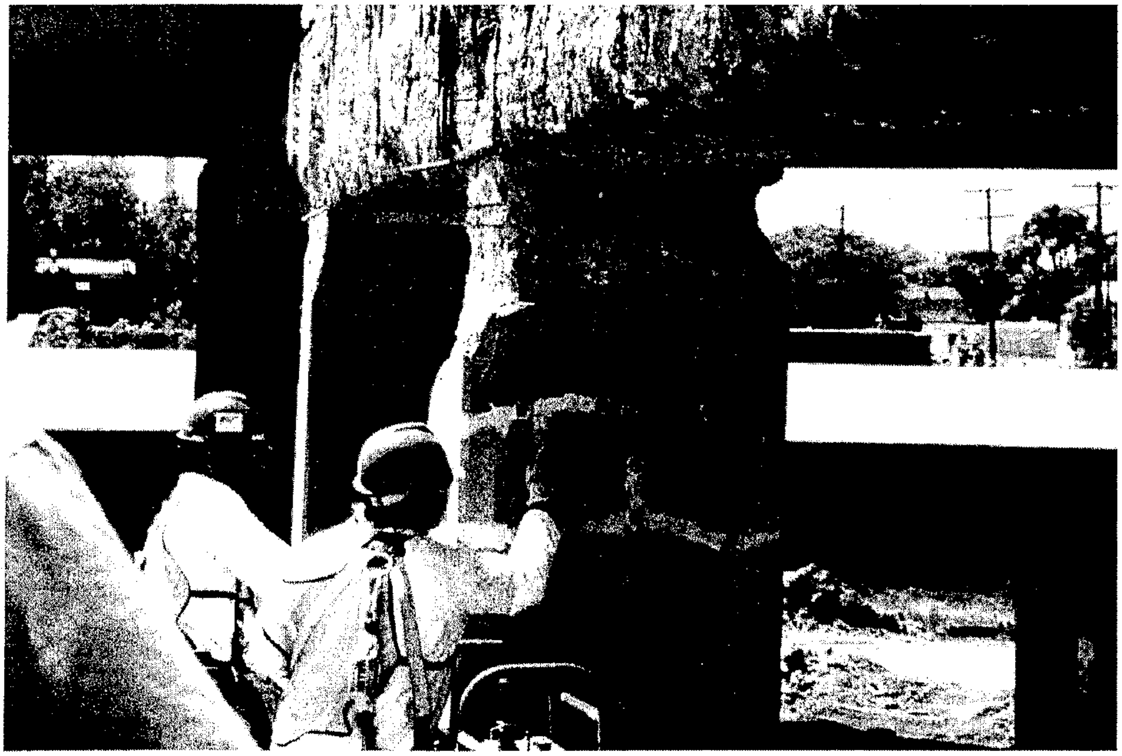

Figure 121. Repair of Bent #5R using the Sho-Bond DD Bics method of resin grout injection

Figure 122. Repair of Bent #5R showing injection balloons on east column

Test of repaired Bent #5R

The test setup, the location of instruments, and the testing procedures are similar to the ones described for Bent #5. A force-controlled test was first performed up to a lateral load of 900 kN, and a displacement-controlled test was performed after that by gradually increasing the lateral deflection in each step. The location of the instruments used in the test is shown in Fig. 123. The test procedure and monitoring of the data was carried out in an identical manner as that for Bent #5. The applied load history is shown in Fig. 124. The peak load is 2033 kN (457 kip) and is seen to drop by approximately 13 percent at the end of the test. The applied displacement history is shown in Fig. 125, with a maximum displacement of 267 mm (10.50 in.). From a bilinear approximation of the load-displacement behavior, the displacement ductility of the bent at the end of the test was found to be equal to 4.0, as shown in Fig. 126. This compares well with the ductility of Bent #6 which had a ductility of 6.3; it can be observed that the ductility of the repaired bent is 63 percent of the ductility of the undamaged Bent #6 retrofitted with FRP composites. Compared to Bent #5 tested in the as-is condition, which had a displacement ductility of 2.8, the repaired Bent #5R has a higher ductility by an amount of 143 percent. Thus, the goal set out in the FRP advanced composite design of doubling the displacement ductility of the as-built Bent #5 was achieved by Bent #6, while Bent #5R even though it did not reach that goal improved the performance of Bent #5 considerably. This implies that even damaged bridges from previous earthquakes can benefit from application of FRP composite seismic retrofit measures. In addition, the ductility achieved during the test of Bent #5R was 80 percent of the target design displacement ductility of $\mu_\Delta = 5$ used by Caltrans for multicolumn bents of new bridges (Caltrans 1999).

The overall envelope of the hysteresis curves was constructed according to the FEMA 273 guidelines (1997) and is shown in Fig. 127. This was done in order to compare with the other two tests performed during this research. The figure shows that the initial stiffness of the bent in the push direction was only 44 percent of that in the pull direction. The reason for this was found after completion of the test of Bent #5R, when it was discovered that the longitudinal bars at the top plastic hinge zone of the columns had buckled. However, the level of peak load in the push and pull direction were approximately equal to that of Bent #6.

Damage assessment of repaired Bent #5R

Large cracks in the concrete were visible at the interface between the column and the beam cap, which reached 8 mm in width. These interface cracks propagated from the concrete into the FRP composite. Since the plastic hinge areas were already damaged during the test for Bent #5, removal of the FRP composite in these areas revealed the presence of large diagonal cracks as shown in Figs. 128 and 129. The FRP advanced composite layers delaminated in the - beam cap-column joint region, in a similar manner as for Bent #6 as shown in Fig. 99. Tensile failure of some of the 152 mm FRP composite U-straps was observed as shown in Fig. 130.

Upon removal of the FRP composite from the west-facing side at the top of the middle column, it was found that the longitudinal column bars had buckled as shown in Fig. 131 and 132. Since the applied load at the beam cap was in the push direction and the bars buckled in that direction, and since the load was in the pull direction when it was working against the buckling, this explains the difference in stiffness identified in Fig. 127. Figure 133 shows that not only did the bars buckle between the column ties, but in addition the concrete between the ties was pulverized and had fallen out; this was determined after the FRP composite sheet was removed. This is in contrast to the situation observed during testing of Bent #6 as was shown in Fig. 102. The difference is the fact that Bent #5R had already been damaged in the first test of Bent #5; however effective the epoxy grout injection and shotcrete were they could not replace the integrity of the as-built concrete of Bent #6.

The connection of the piles to the pile cap using 32 mm Dywidag bars shown in Fig. 10, was able to transfer the loads to the piles effectively with the development of radial cracks forming at the last load cycles as shown in Fig. 134. After demolition, the pile portion with the Dywidag bar was removed from one pile cap and the connection was examined. As Fig. 135 shows, the four #6 (19 mm) bars had buckled, the 32 mm Dywidag had yielded and was bent, and the anchor plate was also damaged. The rigid link beam between the pile cap and the footing shown in Fig. 12 as section B-B, suffered severe damage and extensive cracking as shown in Fig. 136; however, this did not occur until the last few cycles of the test.

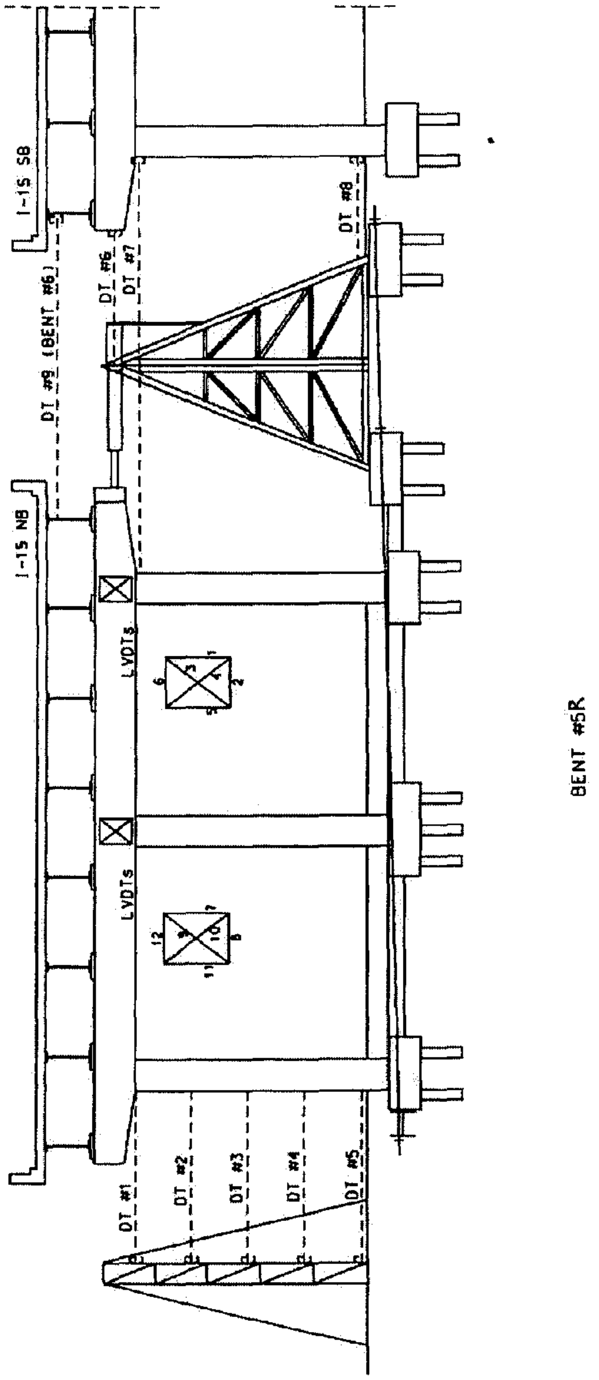

Figure 123. Displacement transducer and LVDT locations on Bent #5R

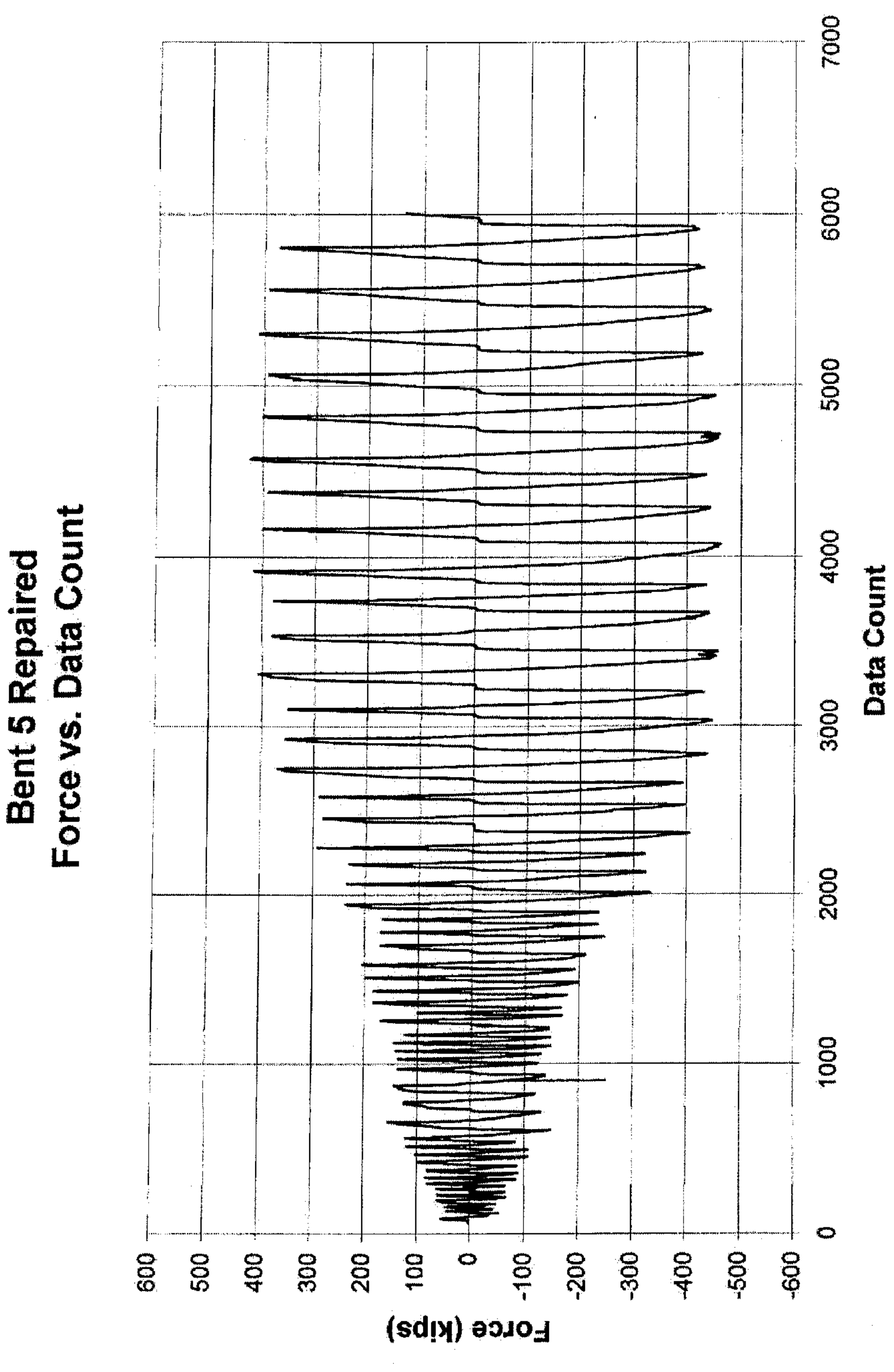

Figure 124. Actual applied lateral load history on Bent #5R (1 kip = 4.448 kN)

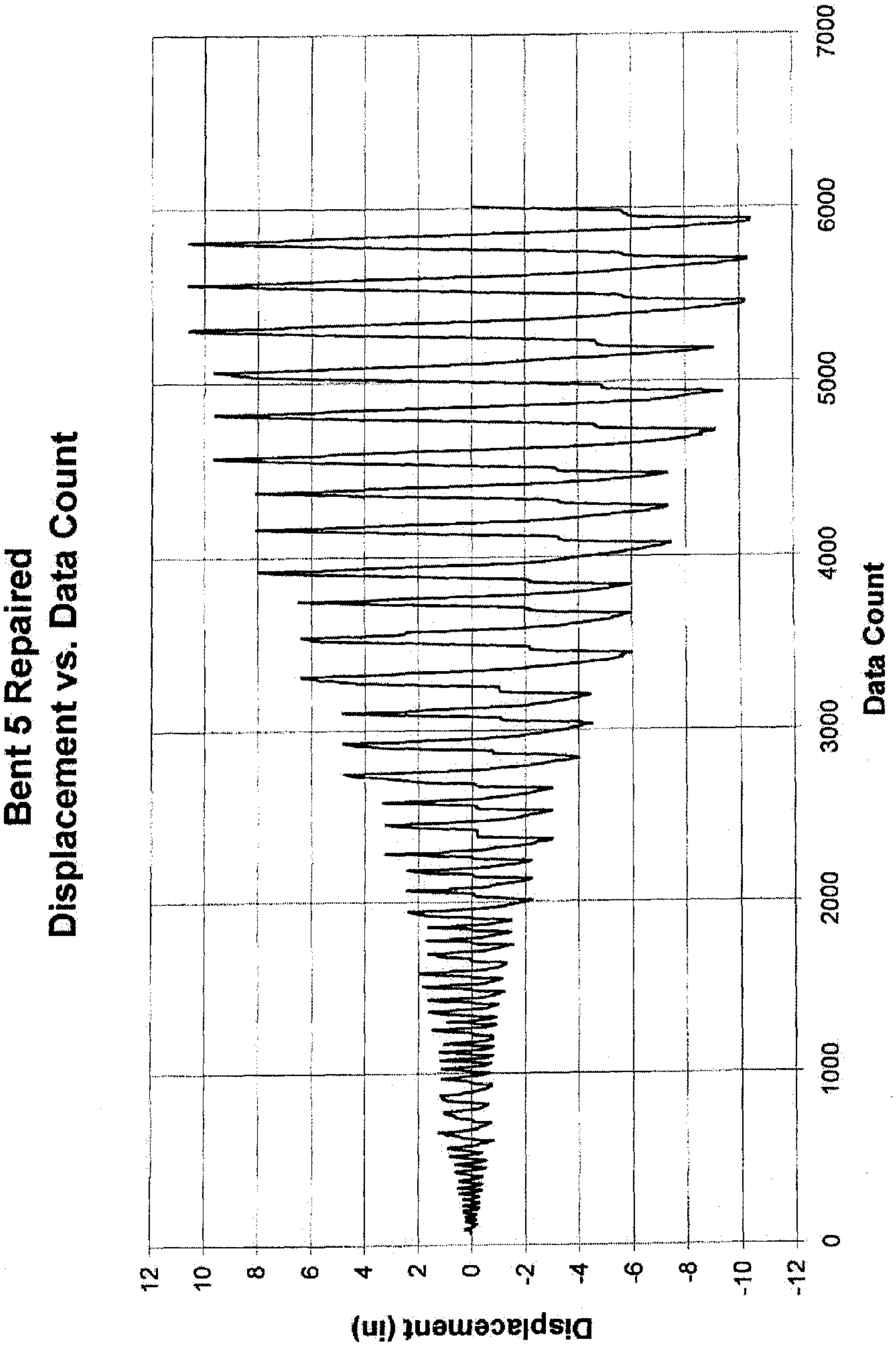

Figure 125. Applied lateral displacement history on Bent #5R (1 in. = 25.4 mm)

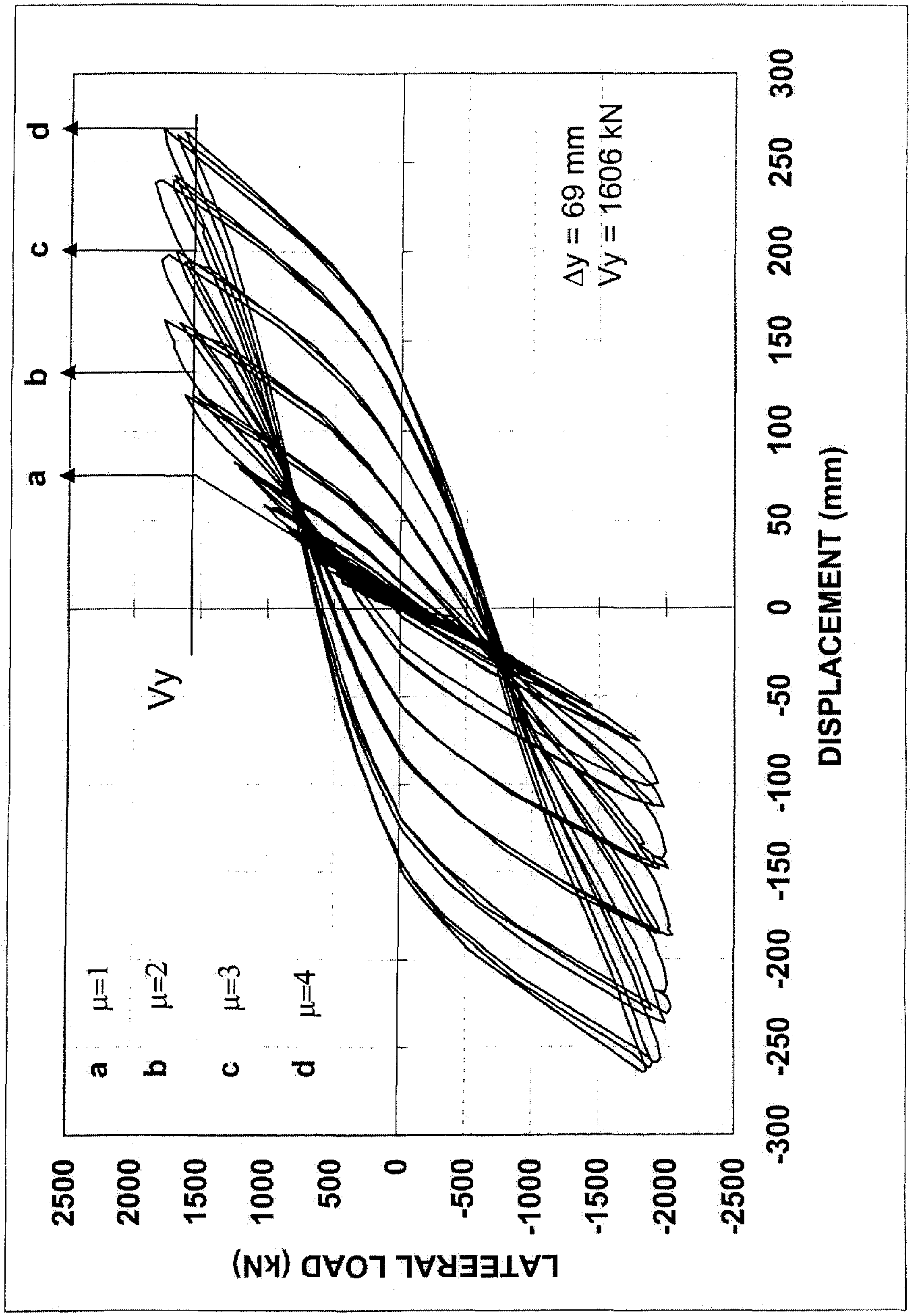

Figure 126. Hysteresis curves for Bent #5R

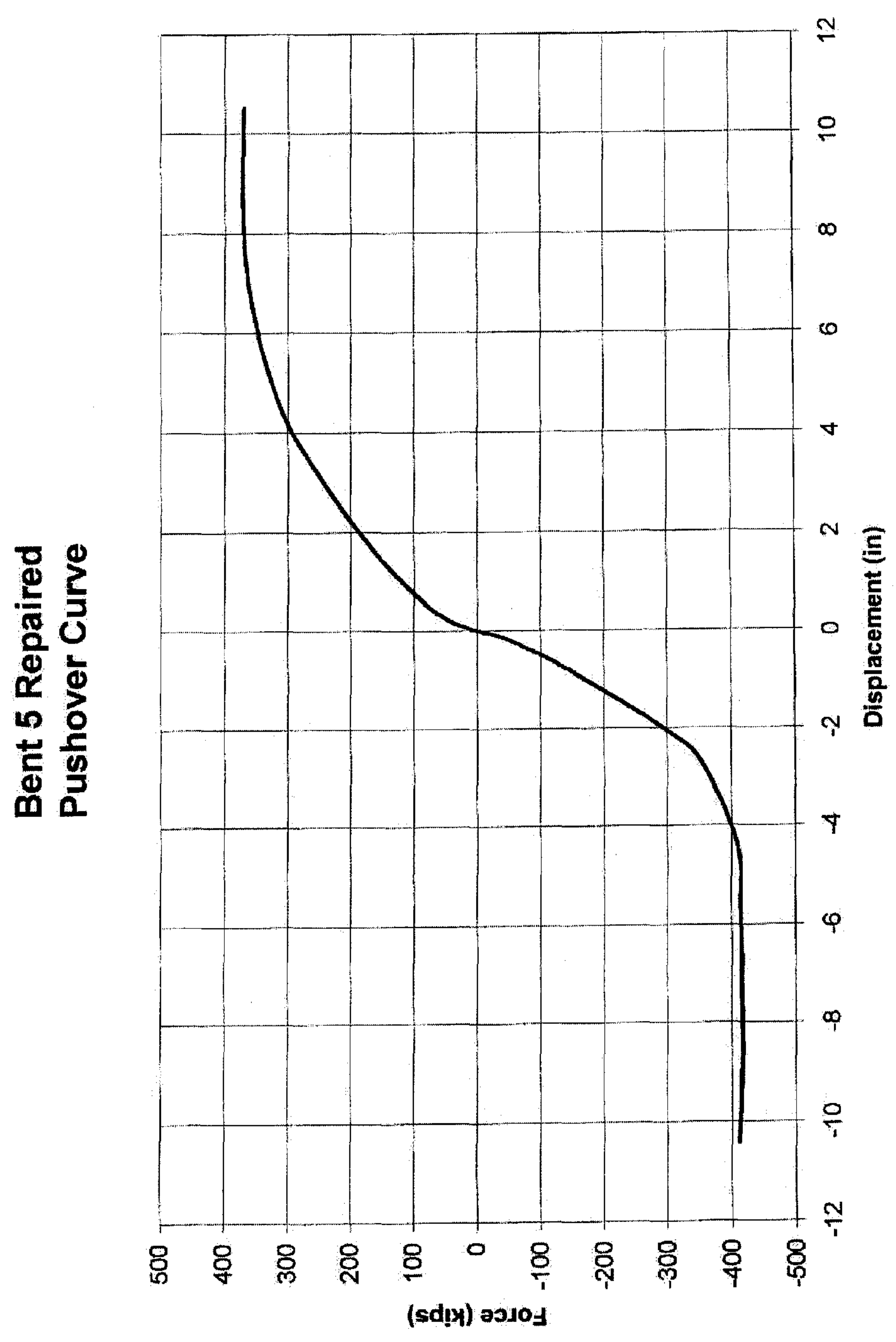

Figure 127. Envelope of hysteresis behavior for Bent #5R (1 kip = 4.448 kN)

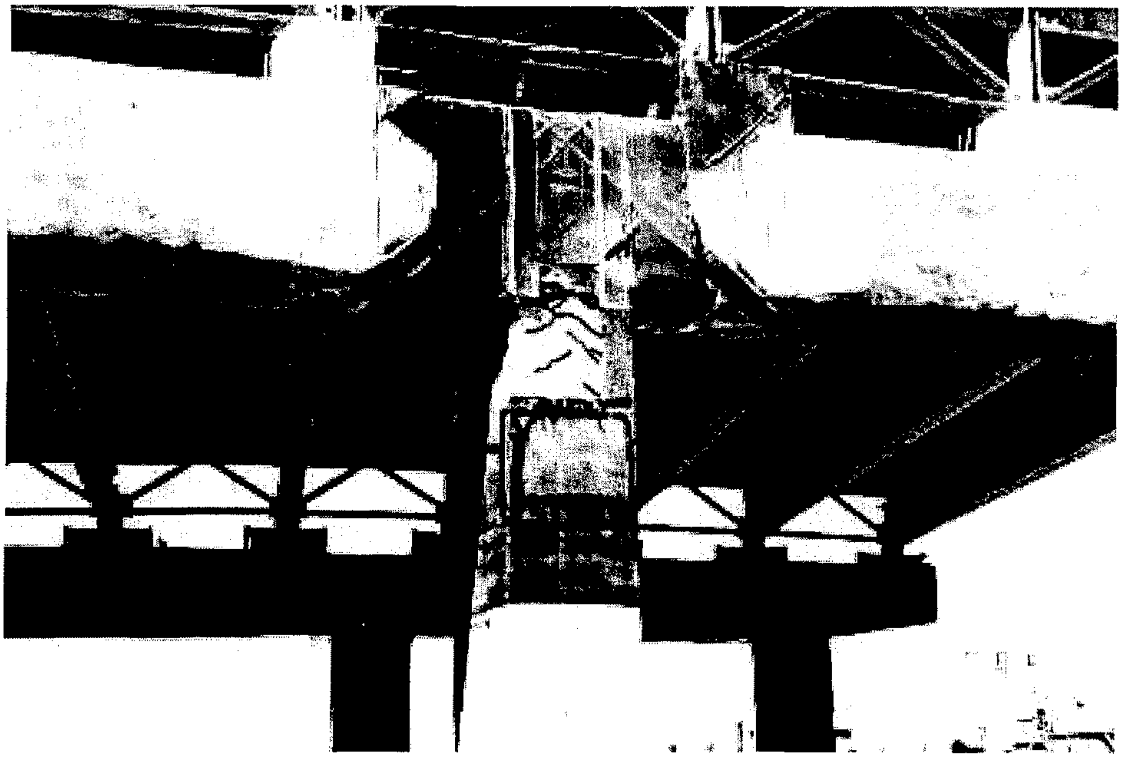

Figure 128. Diagonal cracks in plastic hinge region at the top of the middle column underneath the FRP composite

Figure 129. Close up of diagonal cracks in plastic hinge region of column

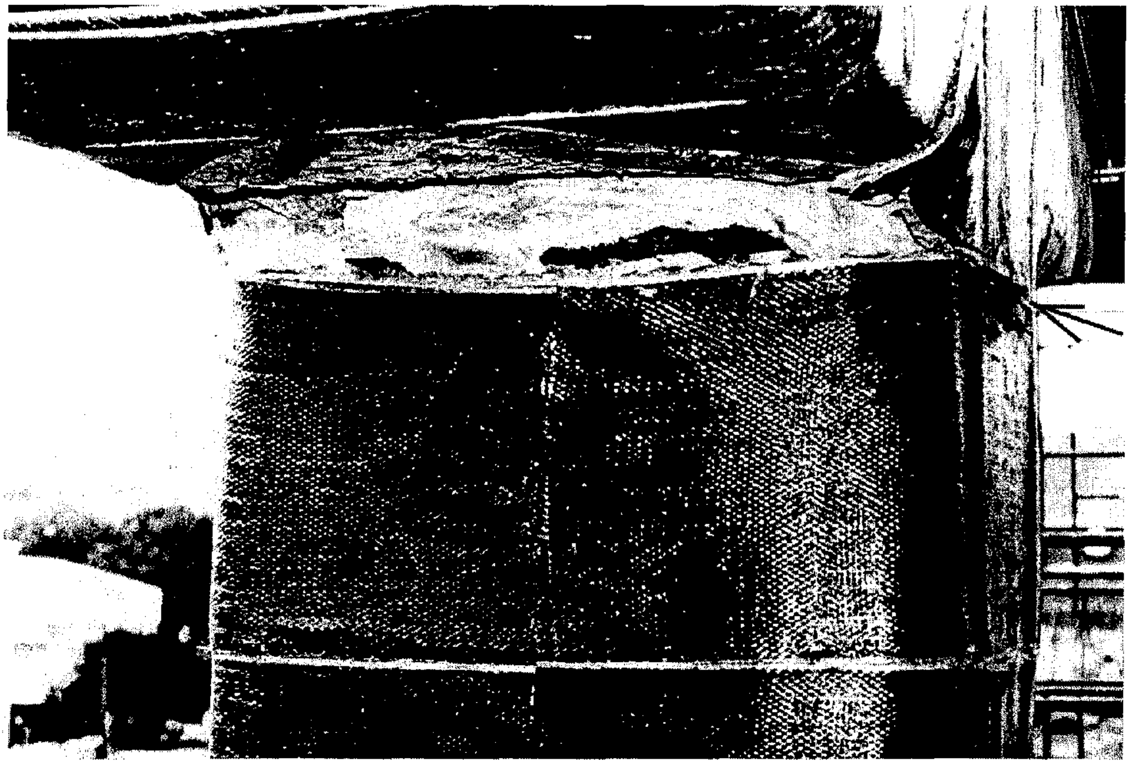

Figure 130. Tensile failure of FRP composite in U strap at the column

Figure 131. West-facing view of top of middle column after FRP composite was removed

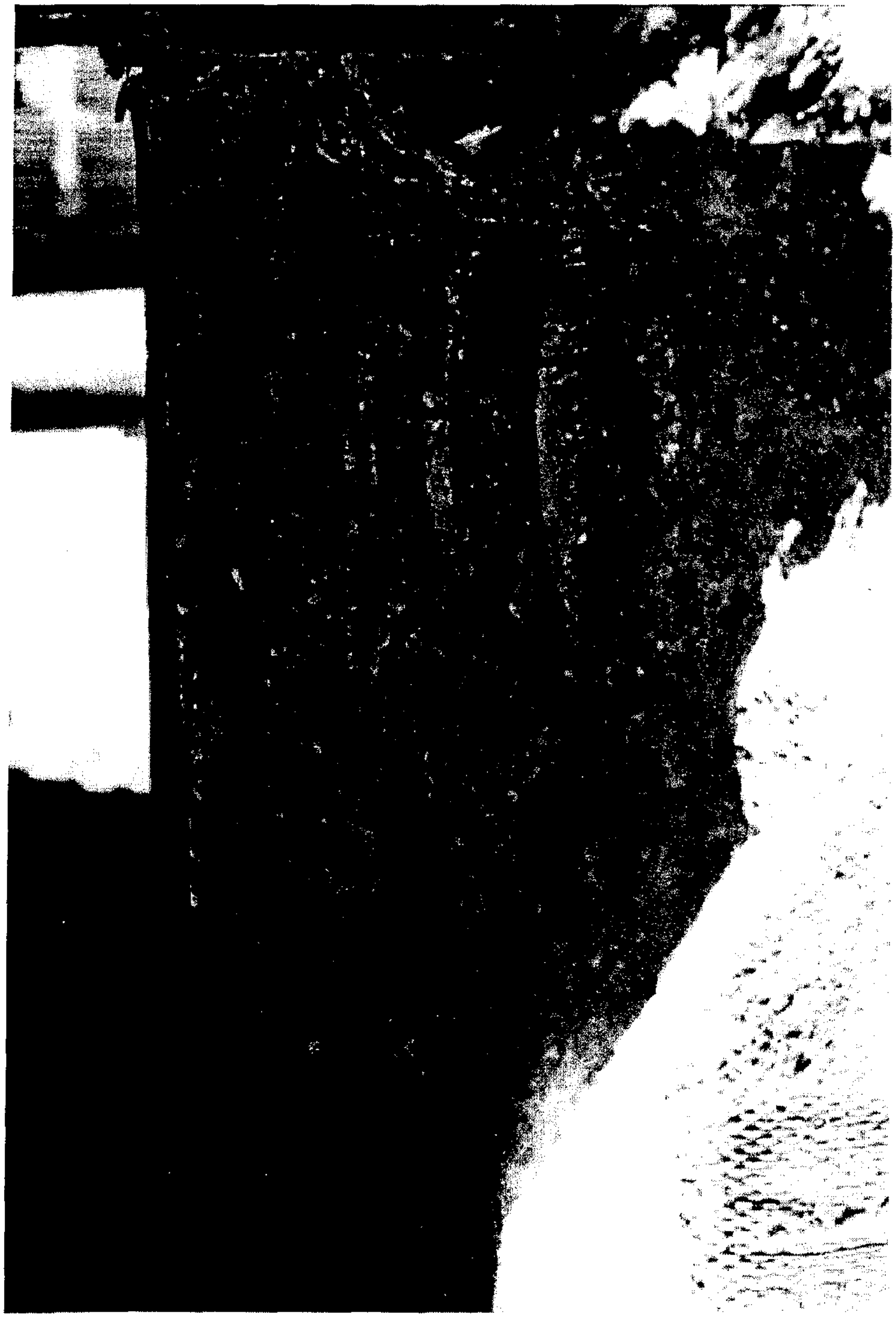

Figure 132. Buckling of longitudinal column bars on top of middle column

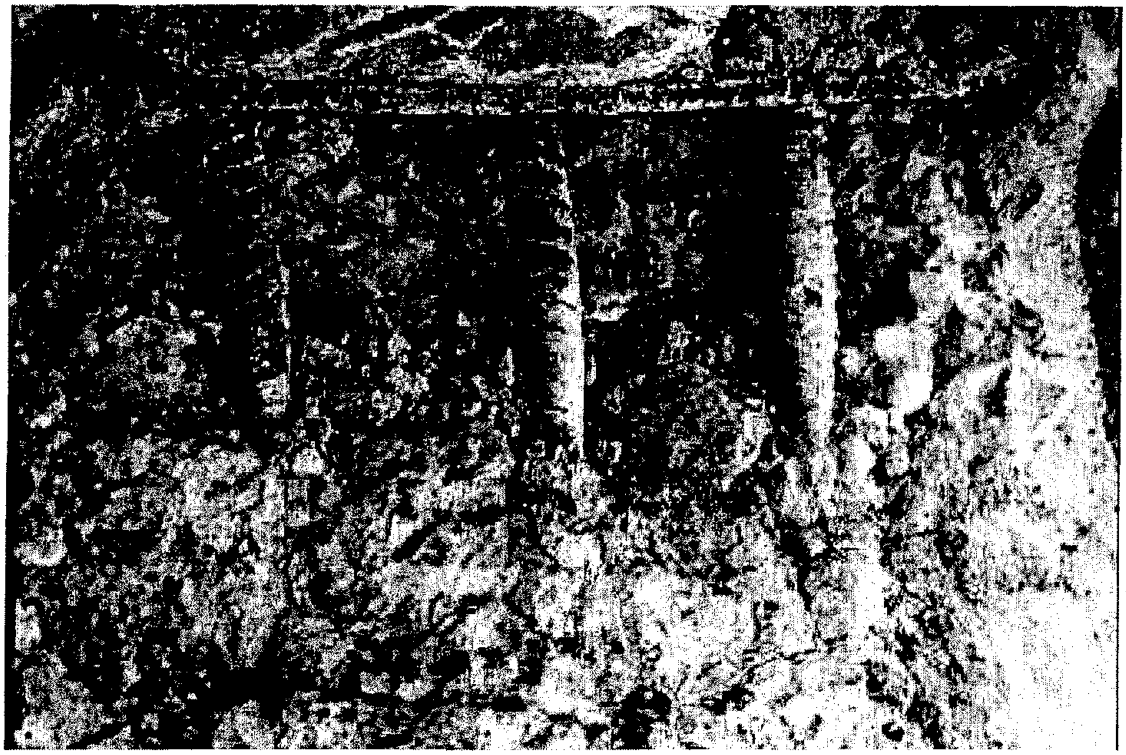

Figure 133. Pulverized concrete between ties of column of Bent #5R

Figure 134. Radial cracks at pile cap surface of Bent #5R

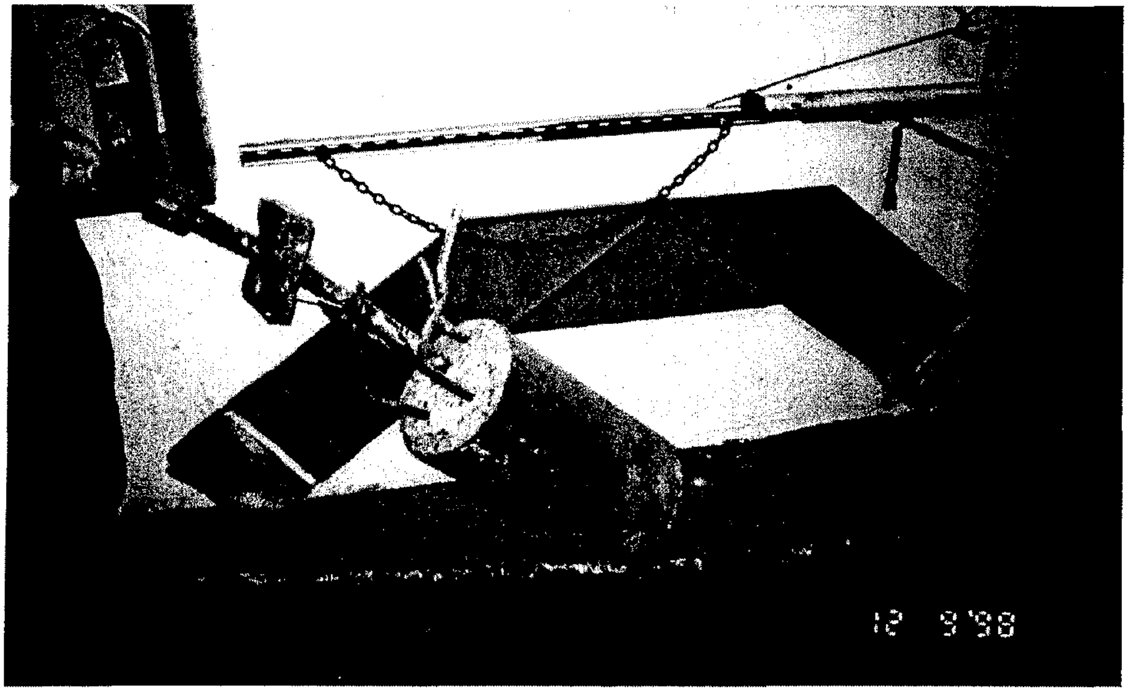

Figure 135. Damage of pile to pile cap connection

Figure 136. Damage in rigid link beam between pile cap and load frame footing

The distortion of the beam-column joints was determined from LVDT measurements. The shear strain in the center joint is shown in Fig. 137; the maximum strain is 0.056 which is approximately two times the strain observed in Bent #5 and slightly above the ultimate compressive strain usually obtained in reinforced concrete sections which is about 0.004. The shear strain is also shown at an exterior joint in Fig. 138, where the maximum strain is observed as 0.006. The principal tensile stresses at the interior beam cap-column joint were evaluated in a manner similar to that described for Bent #5, using equations (6.1) and (6.2). The principle tensile stress was found as 2.69 MPa (390 psi), which corresponds to a stress of $0.58\ (f'_c)^{0.5}$ *MPa or* $7.1\ (f'_c)^{0.5}$ *psi,* which is 35 percent higher than that developed in Bent #5. It is also approximately 42 percent higher than the stress predicted to cause joint degradation of $5(f'_c)^{0.5}$ *psi* or $0.42\ (f'_c)^{0.5}$ *MPa* (Priestley et al. 1996).

Strain gages were attached to the steel reinforcement in the columns, beam cap, the Dywidag bars, and the FRP composite. Figure 139 shows the location of the strain gages on all the steel and horizontal Dywidag bars in the foundation. Figure 140 shows the strain gage readings for gages 5 and 6 on the horizontal Dywidag bar shown in Fig. 139. These Dywidag bars are providing the tension forces in completing the load path for the structure and are shown in Fig. 12. As can be seen, the two bars have not yielded in this case, unlike the case for Bent #6. Figure 141 shows the strain gage readings from gage 11, which shows that the steel has yielded at the top of the center column in the plastic hinge region. Figure 142 shows the strain gage readings from gages 3 and 4 at the bottom of the exterior column in the plastic hinge region. As can be seen, both gages indicate steel yields relatively early in the loading cycles. The beam column joint at the top of the middle column was the most stressed of the joints in this test, as evidenced from the damage observed. The longitudinal bars in the joint debonded and slipped at the top of the joint. This is shown in Fig. 143, where the strain versus drift graph remains vertical at drifts between 0.1 and 0.6 percent. This is where the displacement of the bent is increasing, yet the reinforcement is not receiving any additional strain. This debonding occurred at the two exterior column joints but to a lesser extent.

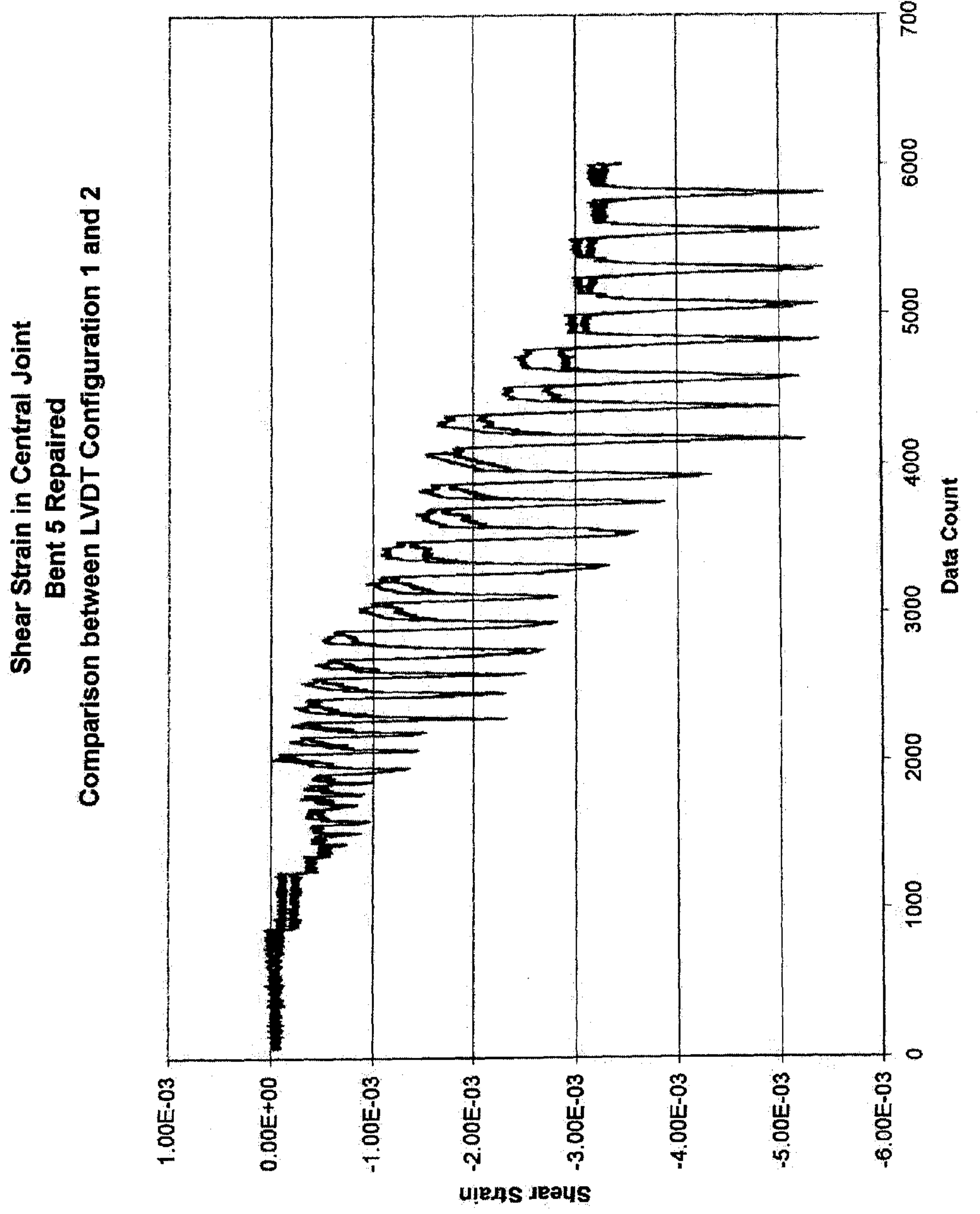

Figure 137. Shear strain at center beam cap-column joint of Bent #5R

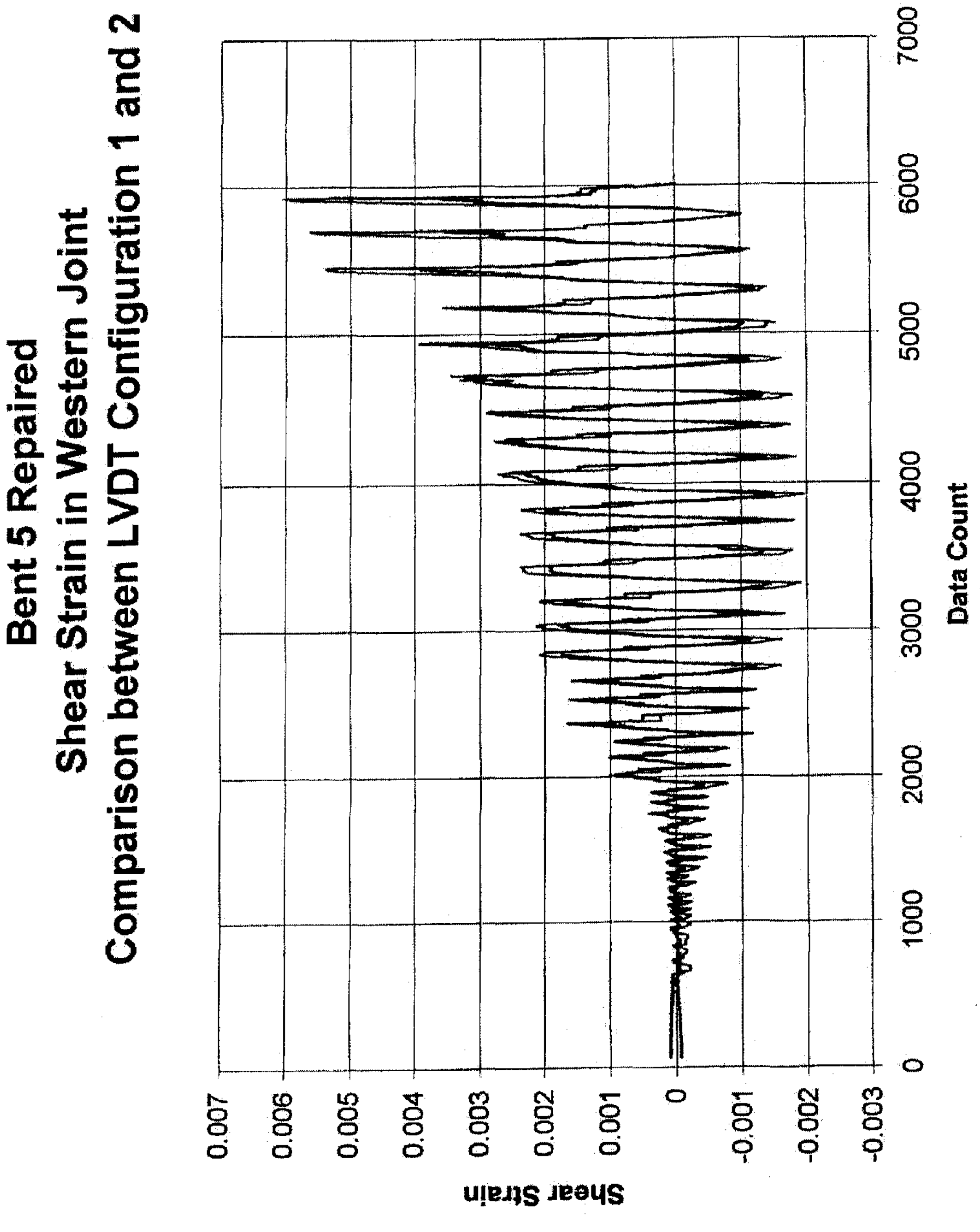

Figure 138. Shear strain at western beam cap-column joint of Bent #5R

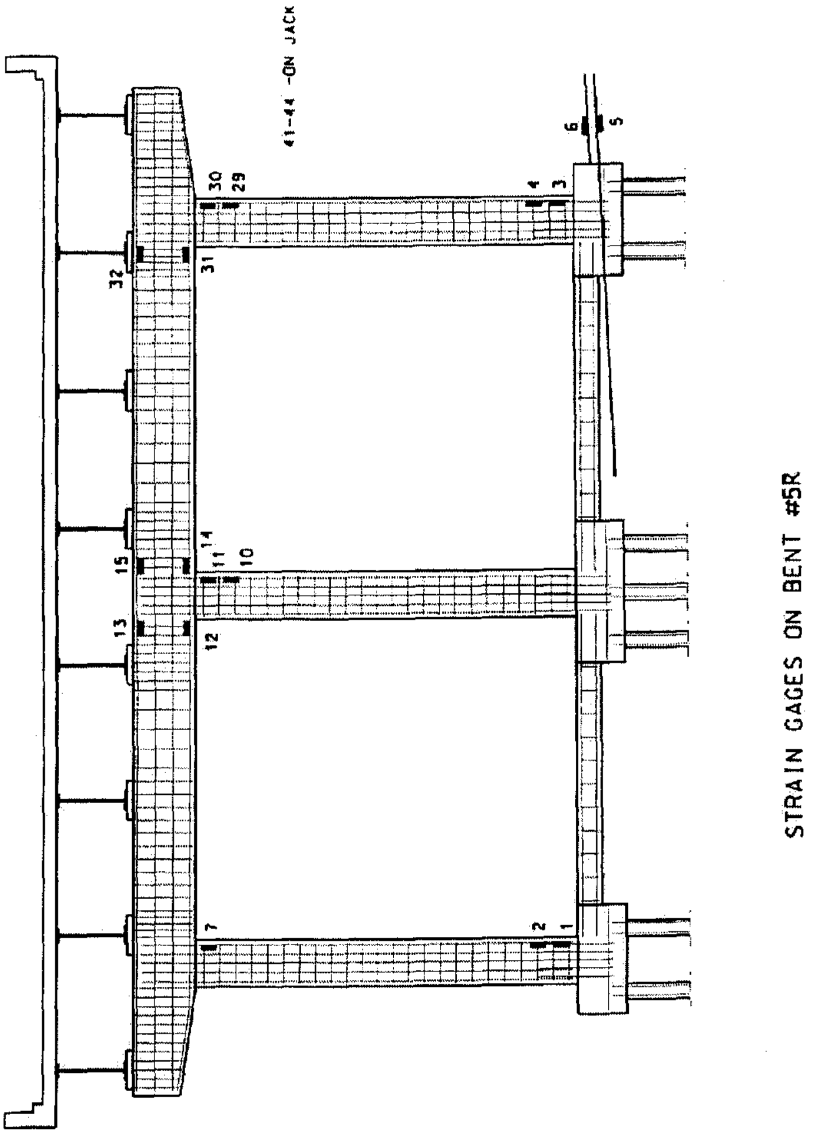

Figure 139. Strain gage locations on reinforcement of Bent #5R

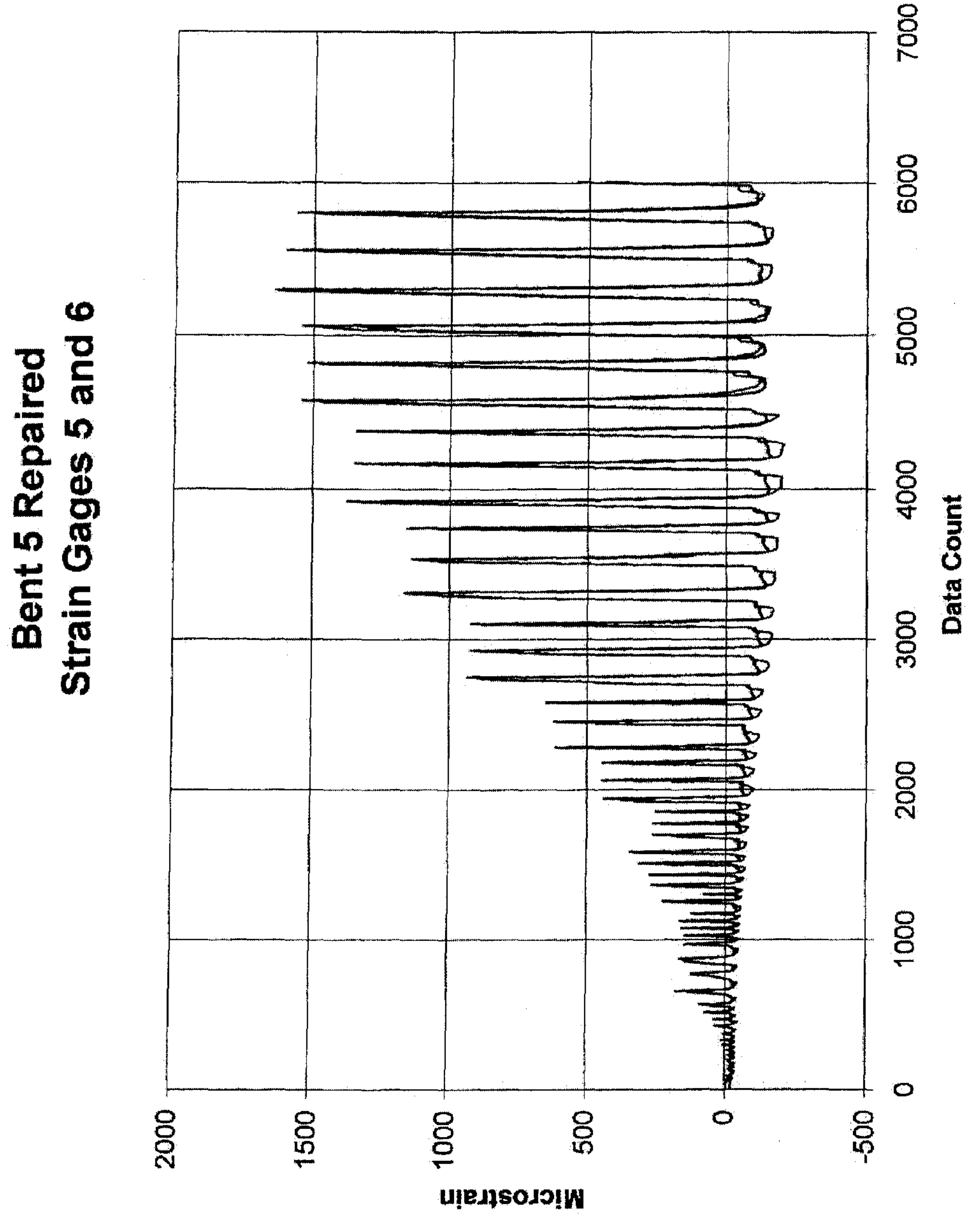

Figure 140. Strain gage readings on horizontal Dywidag bar

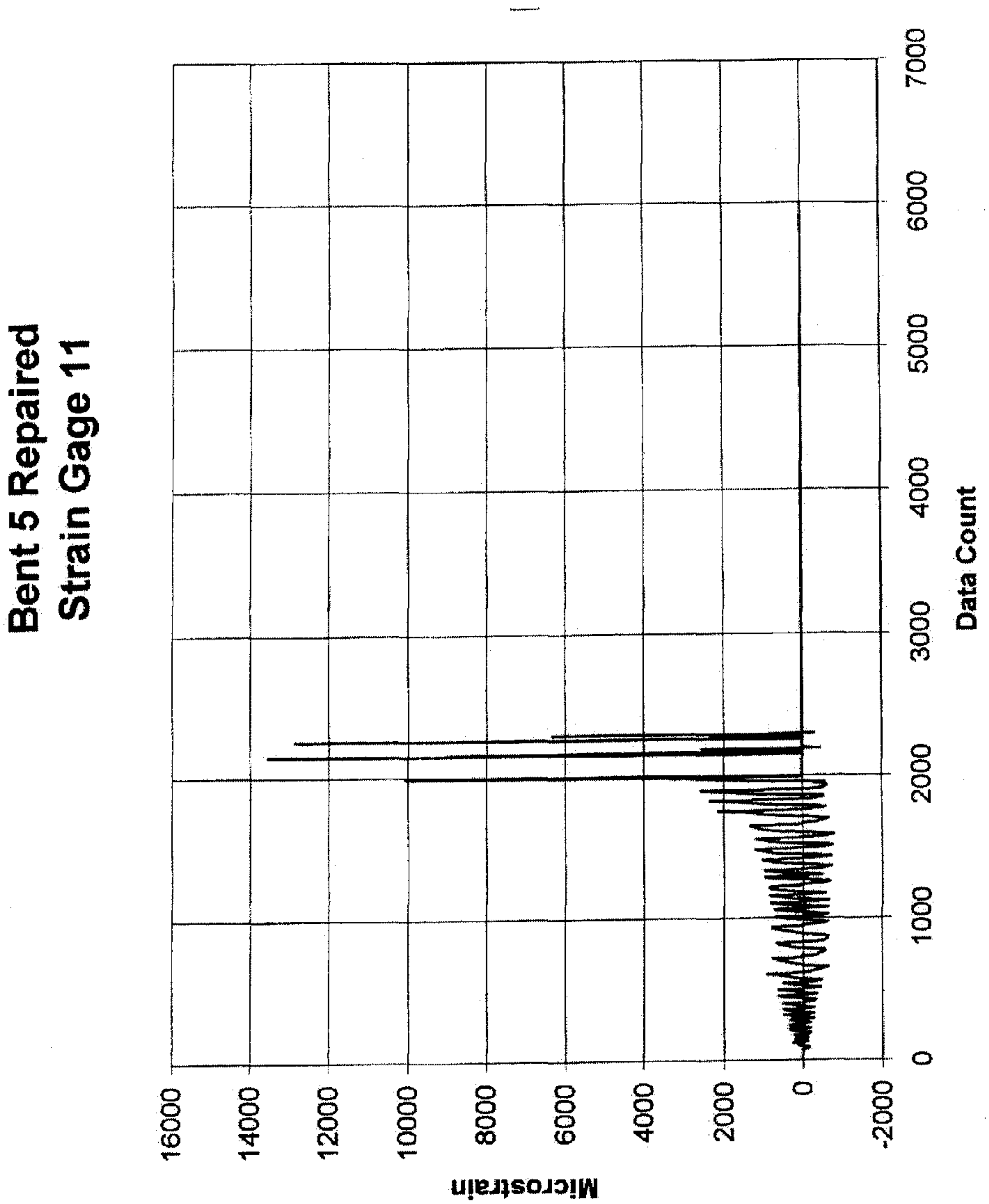

Figure 141. Strain gage at top of center column

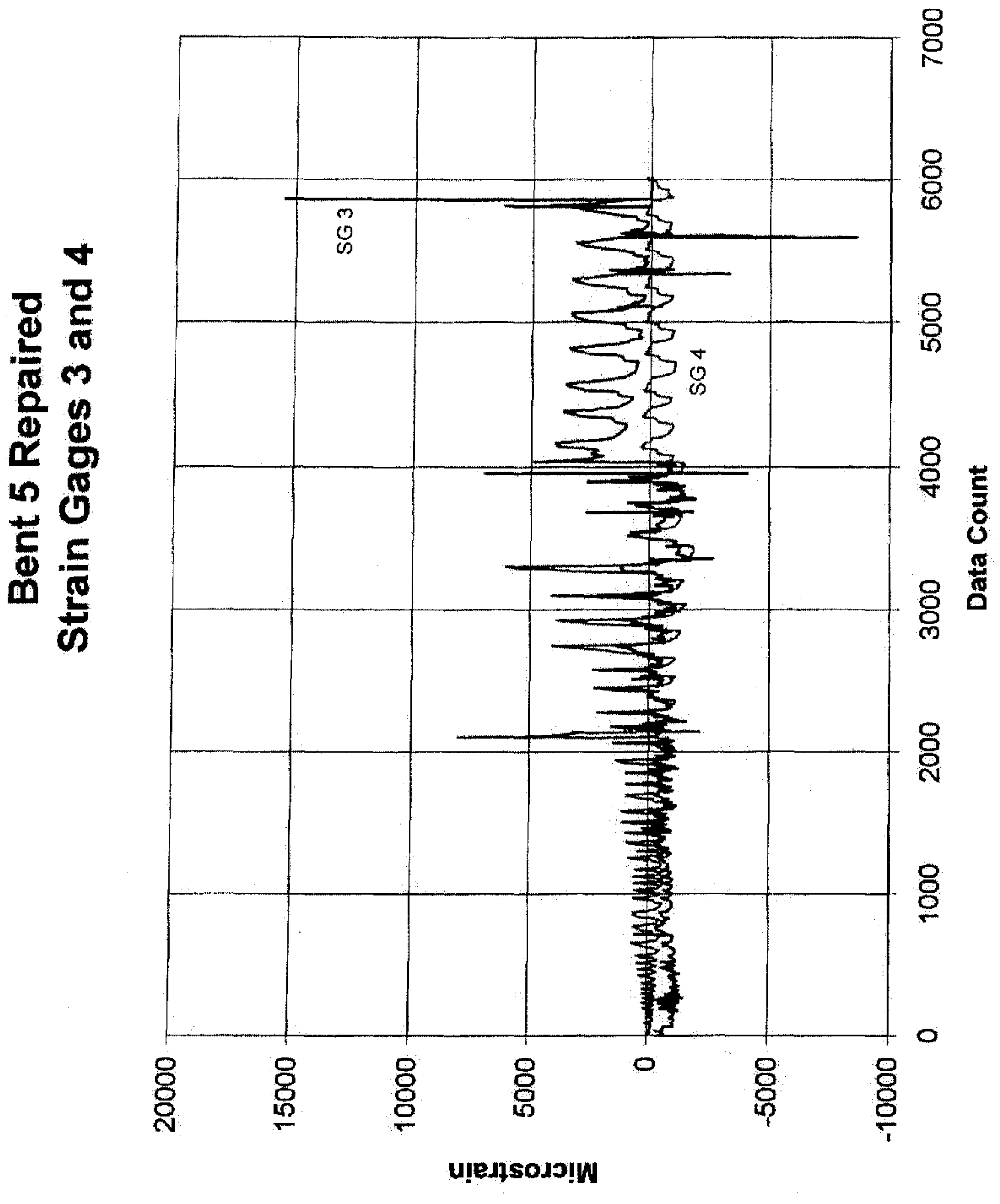

Figure 142. Strain gages 3 and 4 at bottom of exterior column

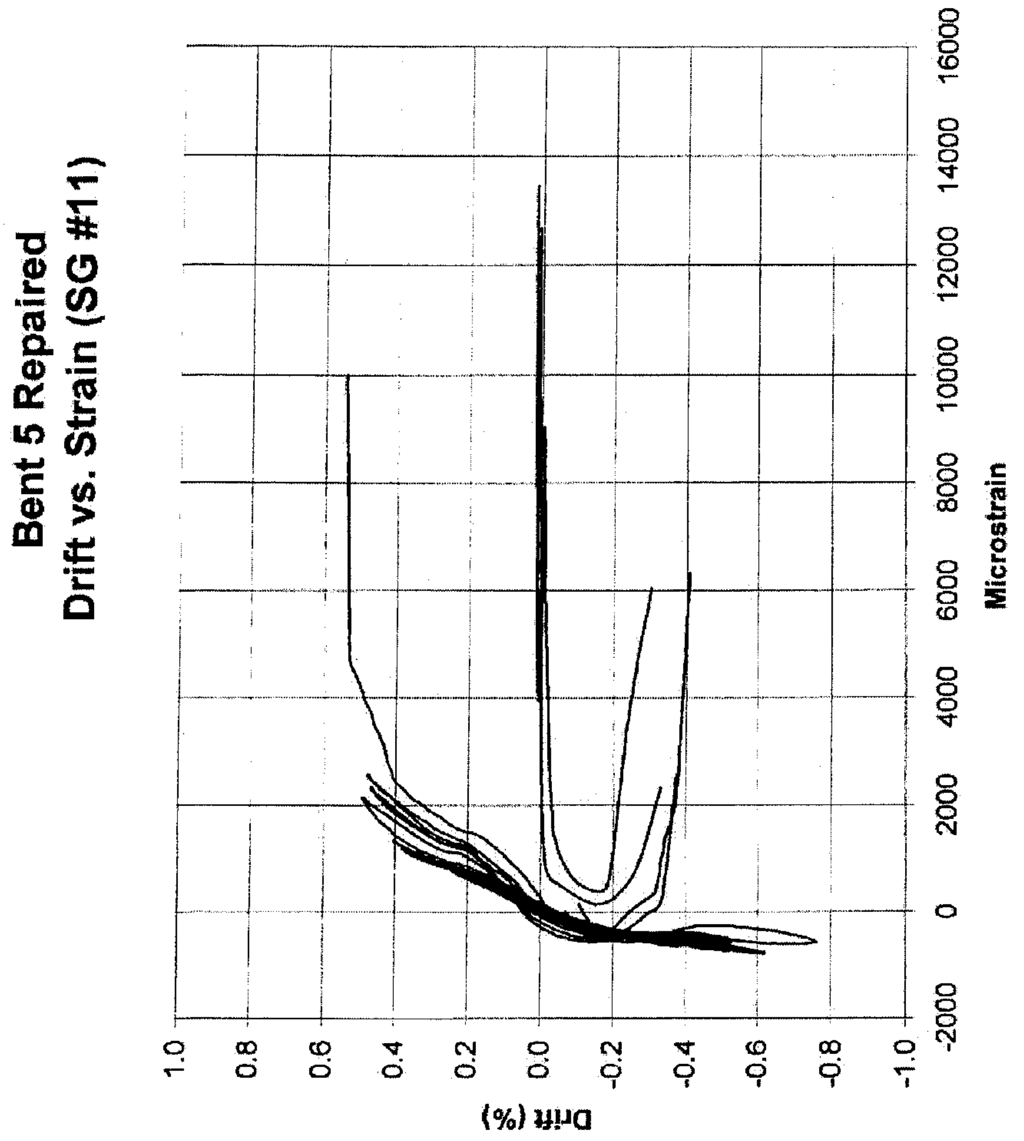

Figure 143. Column bar slippage at top of center column

Several strain gages were attached on the outer surface of the FRP composite. Figure 144 shows the location of the strain gages on the FRP composite in the joint and column regions for the middle and outer columns. Figure 145 shows the diagram of applied lateral force versus strain in the FRP composite. The force is the external load applied at the beam cap level, and the location of strain gage 20 is approximately at the mid-height of the middle joint as shown in Fig. 144. As Fig. 145 shows, the strain developed is not symmetrical in the push and pull directions and the maximum strain reached is 0.18 percent which is well below the maximum strain which can be developed in the FRP composite of 1 percent. The maximum strain in tension is approximately four times that in compression, and at approximately the same lateral load. On the other hand, at the exterior column joint, at strain gage locations 28 and 39, varying results were obtained as shown in Fig. 146. Strain gage 28 which is in the upper half of the joint reached a strain level of only 0.25 percent, whereas strain gage 39 in the lower half reached a maximum strain of 0.75 percent, which is approximately 75 percent of the maximum achievable strain. The variation in these strains depends on the stress field in the joint, however it also depends on the quality of the bond between the FRP composite and the concrete, which as Fig. 147 shows can vary from location to location. In most areas of the beam cap, a sufficiently good bond was observed. The water jet procedure is recommended after the grout epoxy injection and the application of shotcrete for an even better bond. This is critical in areas such as the beam cap-column joint where the FRP composite contribution depends on the bond between concrete and FRP composite.

The maximum strain in tension ranges from 4 to 12 times of that in compression. It should be noted that the strain range of 0.18 to 0.75 percent observed in the FRP composite in this test is beyond the yield strain of the steel reinforcement (0.14 percent) by a factor of 1.28 to 5.36 which demonstrates the versatility of the FRP composite and one of the reasons why higher ductility can be achieved. The other major reason is the achievement of higher confinement stresses, which result from the superior confinement offered by the FRP composite jackets in the columns.

The displacements of the exterior column were recorded throughout the test at 6 ft (1.829 m) intervals, as shown in Fig. 123 using displacement transducers DT1 to DT5. The envelopes of the displaced shape at various drift levels both in the push and pull direction are shown in Fig. 148. As can be seen from Fig. 148, initially up to a ductility of approximately 2.4 in push and 2.2 in pull, the displacement envelope resembles that of the as-built Bent #5 shown in Fig. 76. However, beyond this point and at increasingly higher ductility, the displaced shape begins to change shape and becomes more of an S-shape. After a ductility of 3.3 to 3.5, the S-shape becomes very pronounced and permanent deformation is evident. This is shown in Fig. 149, which shows the overall bent at a ductility approximately equal to 3.

The energy dissipated during the cyclic loading of the bridge bent represents a measure of the damage experienced by the bent. The cumulative dissipated energy was calculated as the area under the hysteresis loops and is shown in terms of the lateral load cycle number in Fig. 150. It can be seen that approximately 50% of the energy is dissipated in the last five cycles, which is similar to the energy dissipation of Bent #5 and Bent #6. A plot of the cumulative energy dissipation versus maximum displacement at each load step is shown in Fig. 151. The curve is almost linear up to a displacement of 100 mm (4 in.), after which the energy dissipation increases in an exponential manner. As observed in Fig. 150, half of the energy was dissipated after the load step corresponding to the maximum deformation of 8.5 in. (216 mm).

Comparing the performance of the as-built Bent #5 and the repaired Bent #5R, it can be seen that the FRP advanced composite retrofit significantly increased the ductility capacity of the as-built bent, and allowed the bent to achieve a higher lateral load capacity while maintaining a significant gravity load. This is significant, since Bent #5R was already damaged and repaired. In addition, the energy dissipated by Bent #5 is more than twice that dissipated by the as-built Bent #5. This proves that repair and rehabilitation of bridges with FRP composites, which were damaged in previous earthquakes is feasible and has merit.

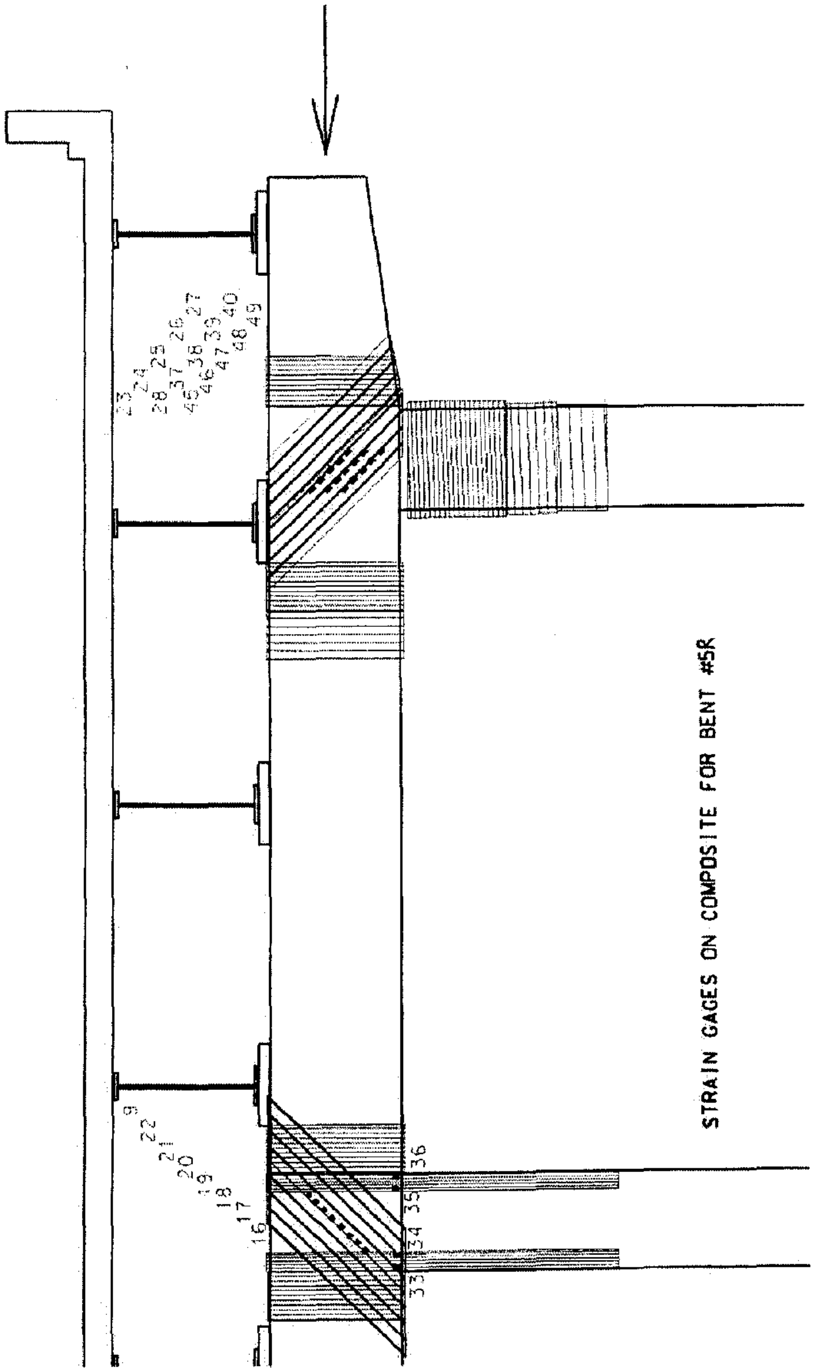

Figure 144. Strain gage locations on FRP composite for Bent #5R

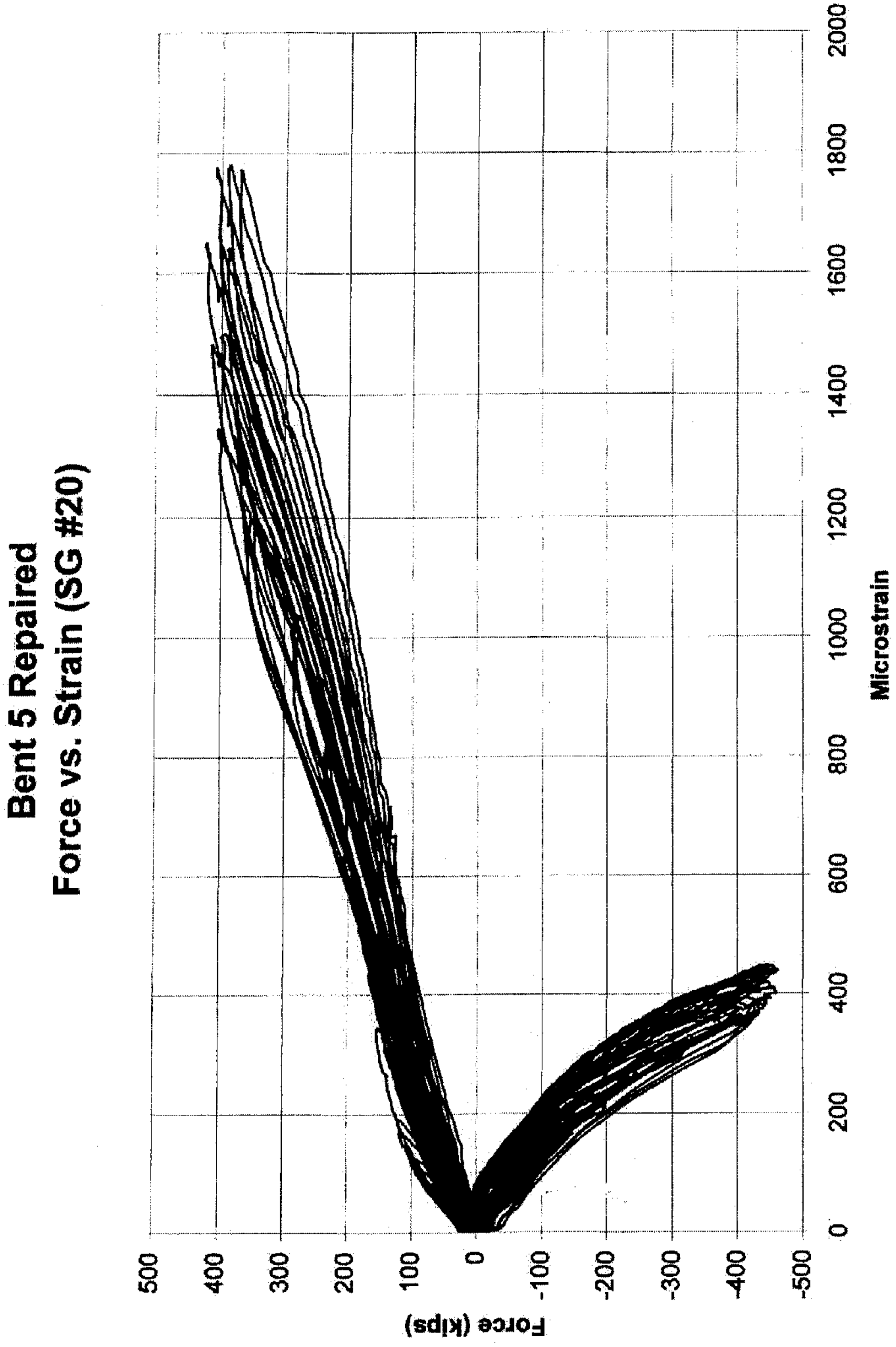

Figure 145. Strain versus force in the FRP composite for strain gage 20 in the middle beam cap-column joint (1 kip = 4.448 kN)

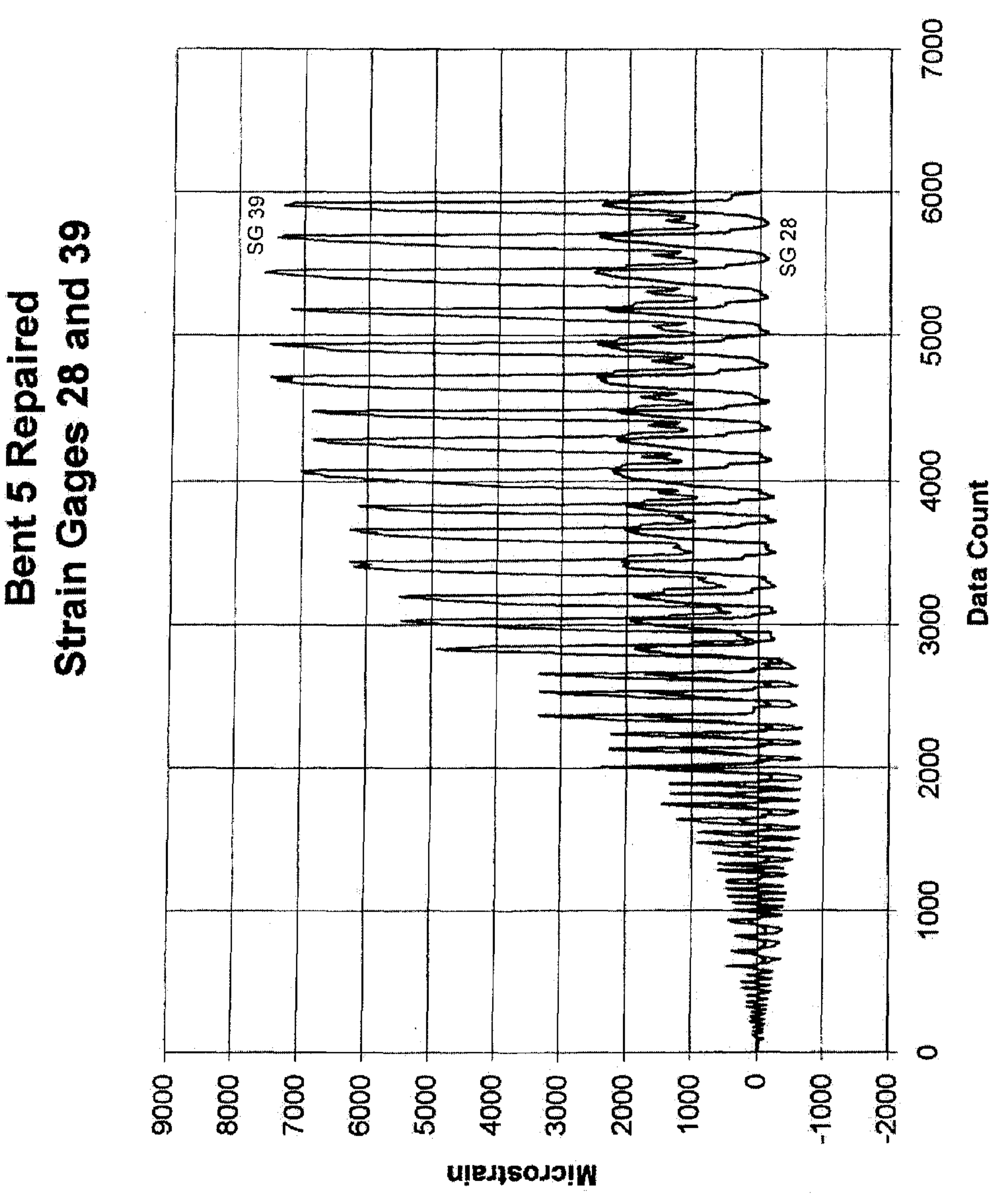

Figure 146. Strain gage histories for gages 28 and 39 in the FRP composite for the exterior beam cap-column joint

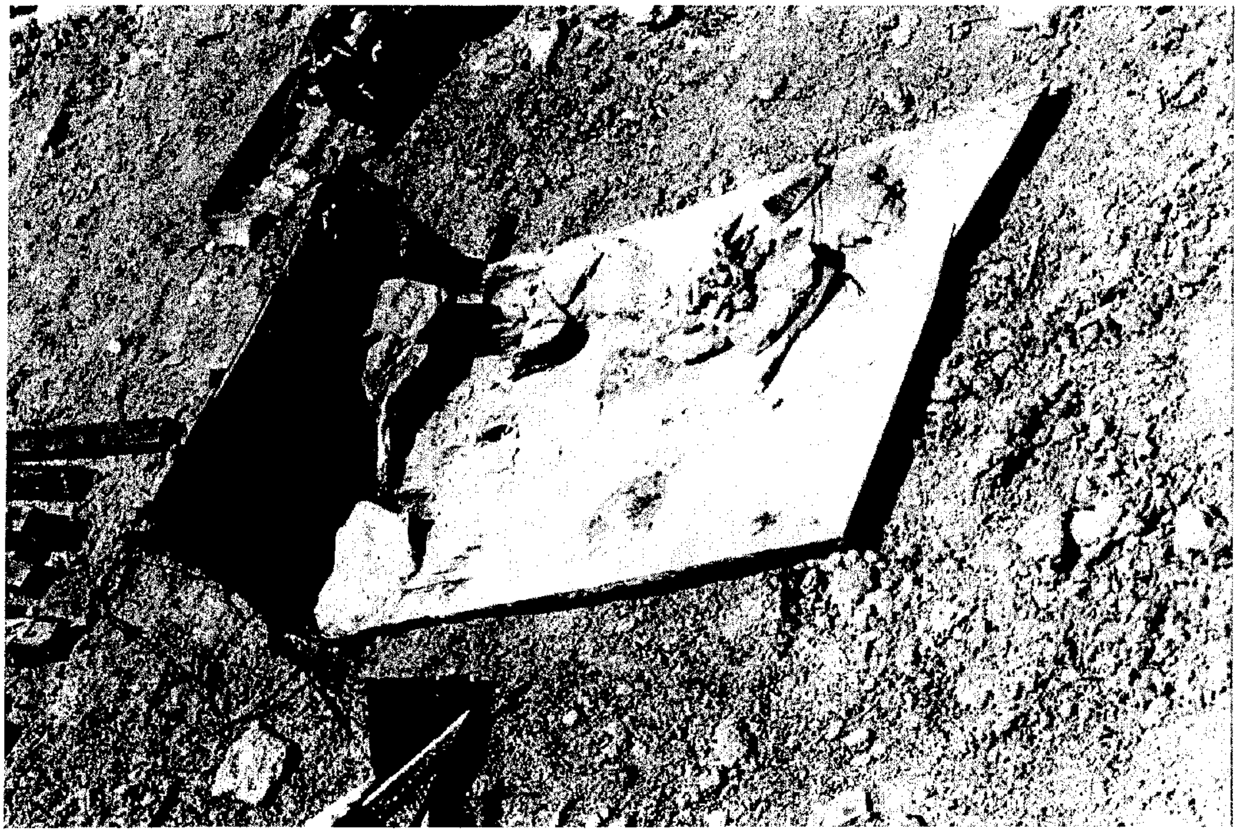

Figure 147. Variability of FRP composite to concrete bond

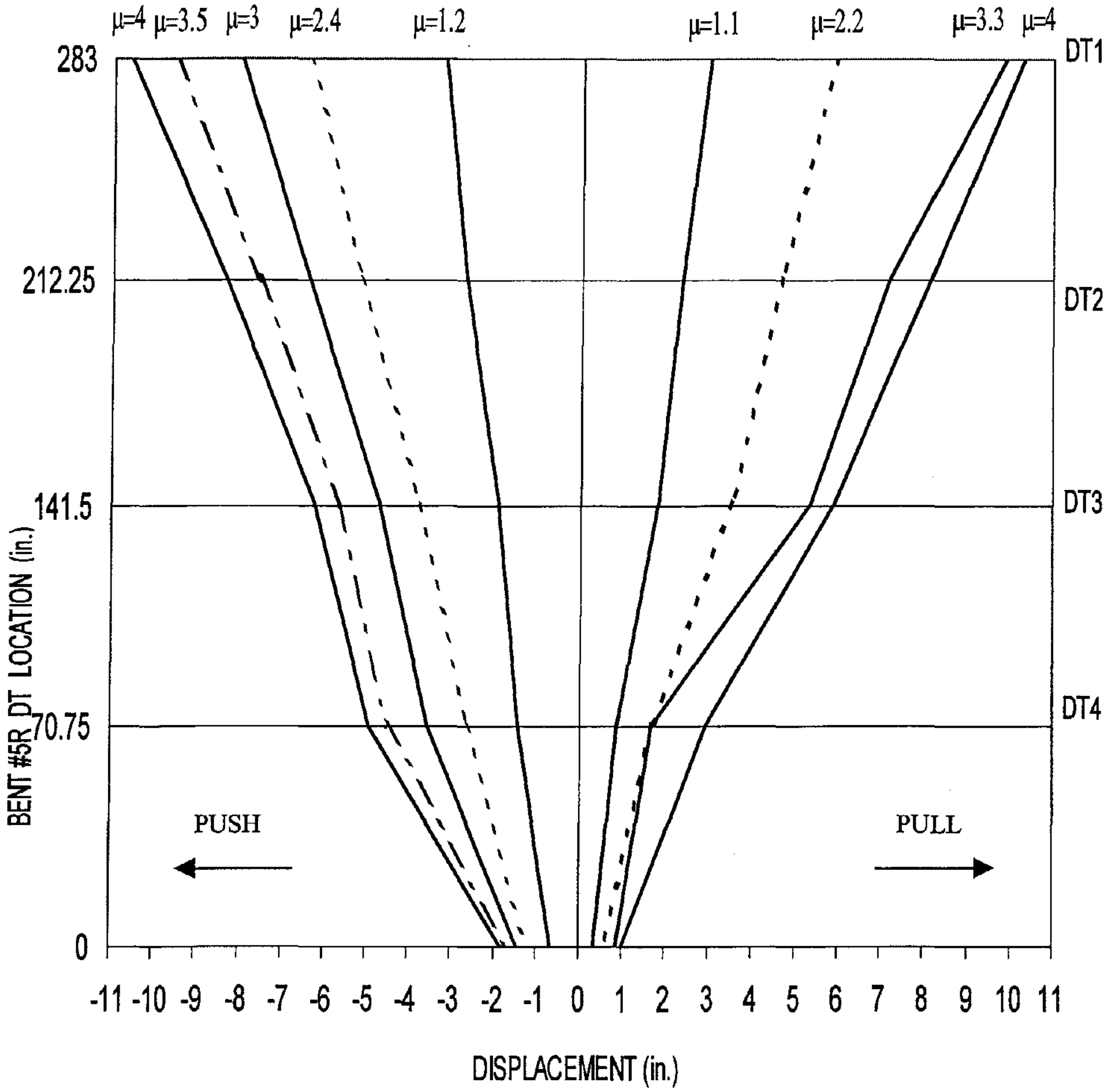

Figure 148. Displacement envelopes of exterior column of repaired Bent #5R
(1 in. = 25.4 mm)

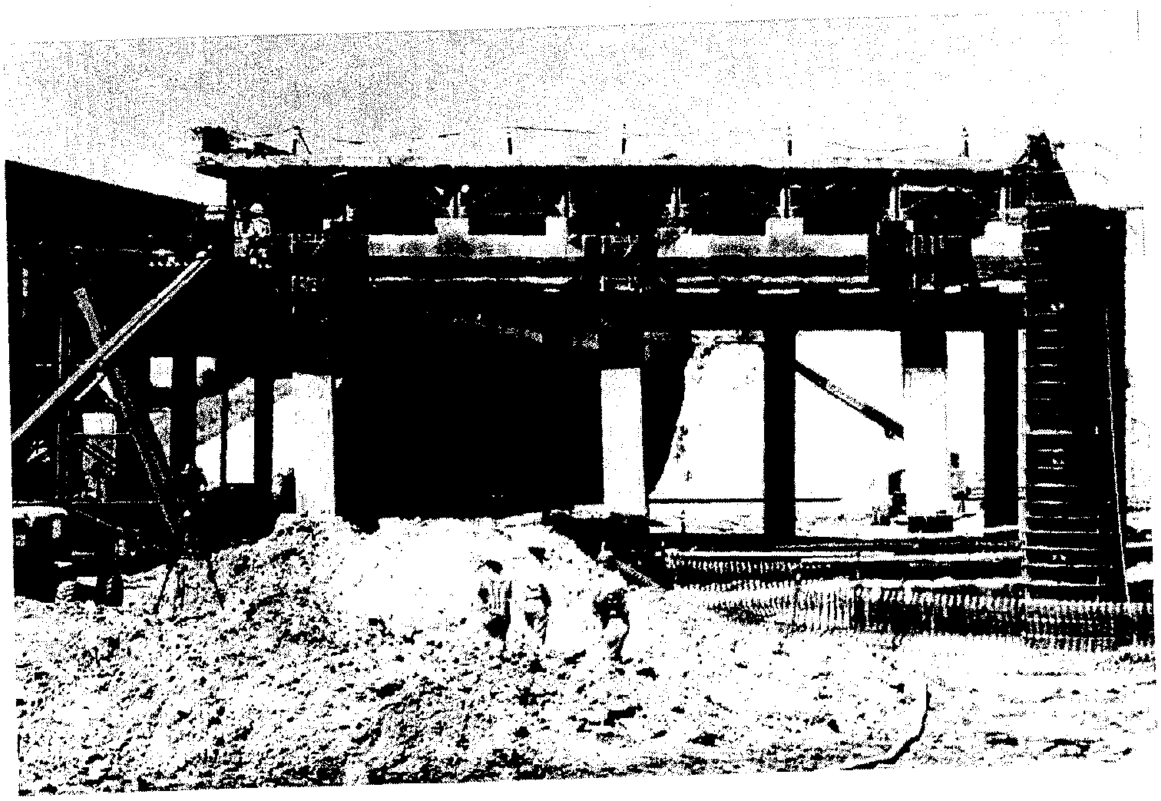

Figure 149. Displaced shape of Bent #5R at a ductility of 3

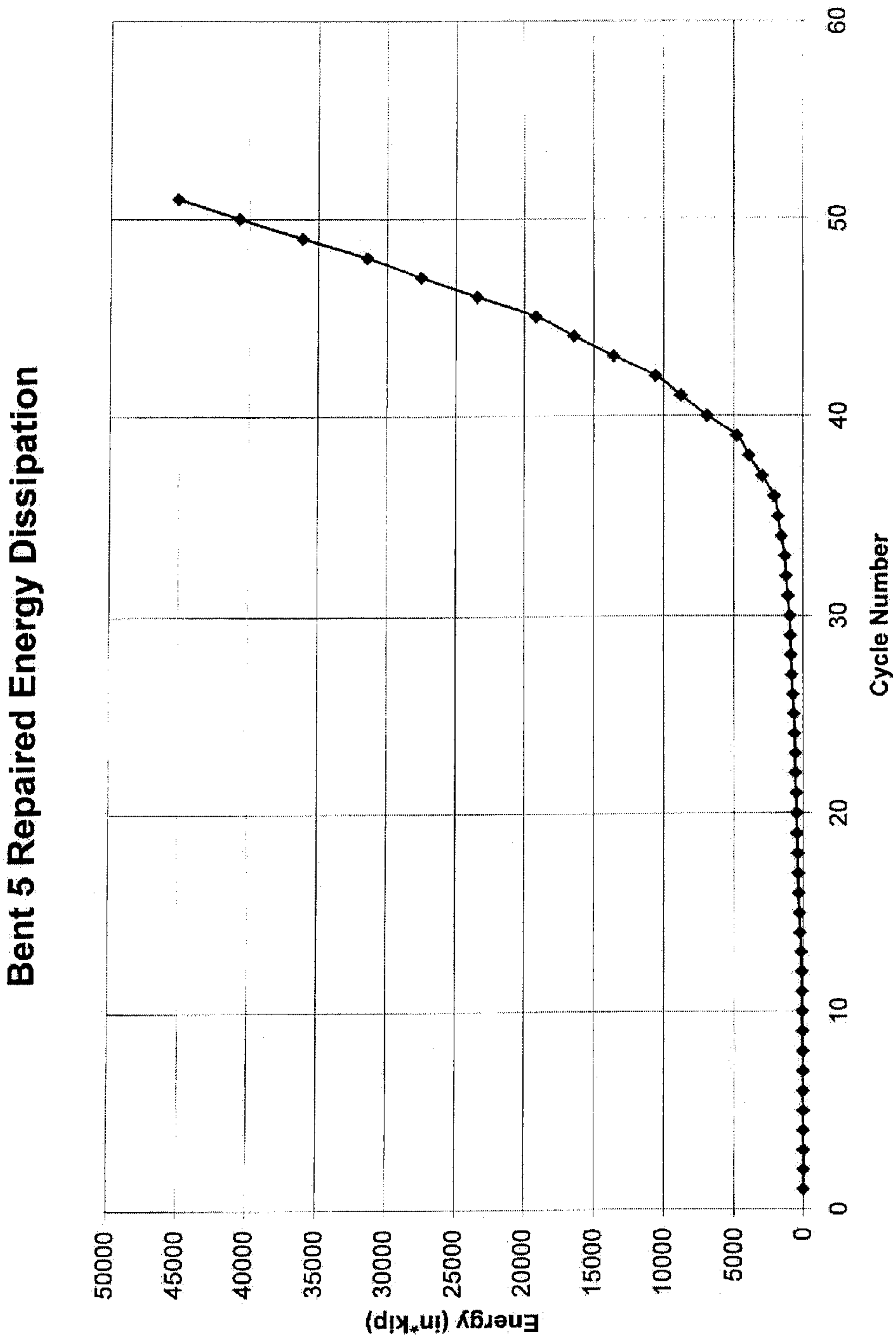

Figure 150. Cumulative energy dissipation of Bent #5R versus cycle number
(1 kip-in. = 0.113 kJ)

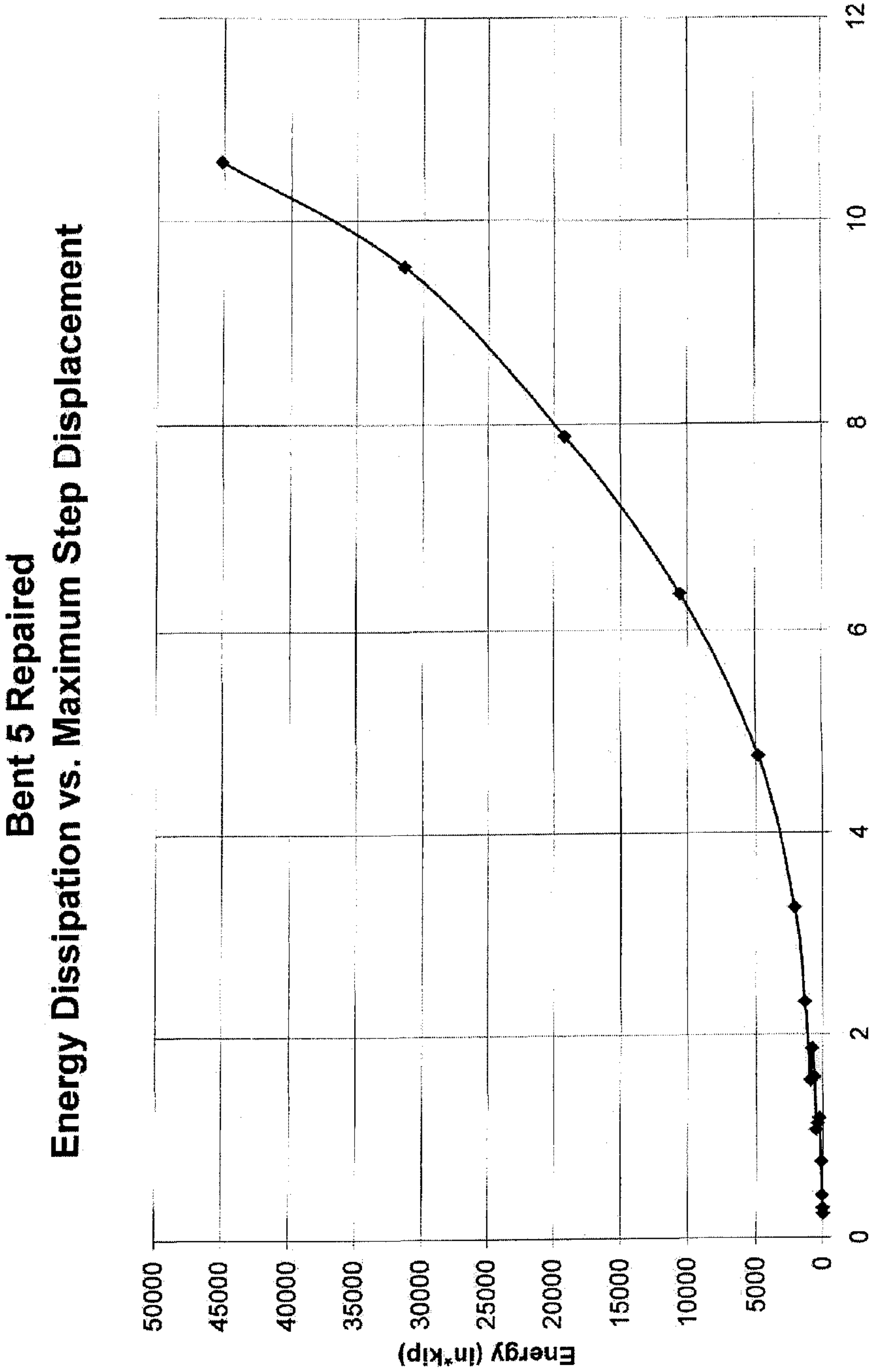

Figure 151. Cumulative energy dissipation of Bent #5R versus maximum load step displacement (1 kip-in. = 0.113 kJ)

9. ASSESSMENT OF PERFORMANCE AND CONCLUSIONS

The experimental evidence has shown that the seismic rehabilitation of the as-built bridge bent using FRP composites was successful. In this section, comparisons of the performance between the as-built and rehabilitated bent are made, in terms of existing design and rehabilitation guidelines.

Assessment of Performance

The assessment of Bent #5, which was in the as-built condition, involves determination of the following parameters:

(a) effective stiffness
(b) effective period
(c) reduction factor based on ductility
(d) lateral load based on demand
(e) lateral load and displacement capacity

Further comparisons are carried out regarding the as-built Bent #5 and retrofitted Bent #6.

Material Properties

The concrete and steel material properties assumed in the design were as follows: Concrete strength f'_c = 3,000 psi (21 MPa); steel stress at yield f_y = 40,000 psi (276 MPa). However, from laboratory tests on concrete cores and steel bars taken after the in-situ tests, the following properties were measured: f'_{ca} = 5,700 psi (39 MPa), and steel stress at yield f_{ya} = 48,500 psi (335 MPa), which represent an increase of 1.9 for the concrete and 1.2 for the steel, and are within the expected overstrength range. For example, the assessment strengths suggested by Priestley et al. (1996) are $1.5f'_c$ for concrete and $1.1f_y$ for steel.

Wind Load

According to the AASHO design criteria applicable at the time of construction, a transverse wind load equal to 50 psf (2.39 kPa) and a longitudinal load equal to 19 psf (0.91 kPa) were used to determine the wind loads applied to the bridge bent. The effective area normal to the wind load is calculated as follows:

(a) Concrete parapet = (45 x 842)/144 = 263 ft^2
(b) Steel girder = (49.5 x 842)/144 = 290 ft^2
(c) Concrete bent = (336 x 36)/144 = 84 ft^2

Total area normal to wind load = 637 ft^2

The total wind load is calculated as: P_{wind} = 637 x (50 + 19) = 44,000 lbs = 44 kip (196 kN). This is the load applied by the wind on one bent and it is much lower that the demand from the earthquake loads. In addition, the wind load demand is much less than the capacity of the bent.

Effective Period

In order to establish an approximate period for the bent, the true stiffness and weight of the bent must be known. In what follows, the effective stiffness of the bent is calculated based on the effective moment of inertia of the three columns, and the effective weight is calculated based on the weight of the deck, beam cap, and half the column weight as per the *Seismic Retrofitting Manual* (FHWA 1995).

The weight of each component is as follows:
- (a) Weight of deck = 8 x 54 x 2 = 864 kip
- (b) Weight of beam cap = (64.5 x 4 x 3) x 0.15 – (6.9 x 1 x 3) x 0.15 = 113 kip
- (c) Half of the column weight = 0.5 x 3 x (3 x 3 x 24) x 0.15 = 49 kip

Total dead load tributary to one bent W_{Tr}= 864 + 113 + 49 = 1026 kip (4564 kN).

The effective stiffness of each bent is calculated as follows, assuming fixed-fixed ends:

$$K_{eff} = 3x\frac{12\ EI_{eff}}{H^3} \tag{9.1}$$

where

$$I_{eff} = I_{elastic}\ x\ Crack\ Coefficient$$

$$E = 57{,}000\sqrt{f_c^{'}} = 57{,}000\sqrt{5{,}700} = 4{,}303\ ksi$$

Here, $I_{\text{elastic}} = (36)^4/12 = 139{,}968$, and H = 24 + 2 = 26 ft.

The axial load per column is equal to 594/3 = 198 kip, and the axial load ratio is $P/f'_c\,Ag = 198/(5.7 \times 36 \times 36) \cong 3\%$. The steel ratio of the column is $\rho = (16 \times 1.27)/(36 \times 36) = 1.6\%$. From these two parameters, and using the chart from Caltrans *Seismic Design Criteria* (Caltrans 1999), the crack coefficient was found equal to 0.4; the effective moment of inertia becomes equal to 139,968 x 0.4 = 55,987 in^4. From equation (9.1) the effective stiffness is K_{eff} = 286 kip/in. (50 kN/mm).

The effective period is obtained as

$$T = 2\pi\sqrt{\frac{1026}{286x386}} = 0.60\ s$$

Demand – Design Spectra for New I-15 South Temple Bridge

The 5% damped design spectra for the new South Temple I-15 Bridge are given in Fig. 152 for three recurrence intervals: (a) 10% exceedance in 50 years, (b) 10% exceedance in 100 years, and (c) 10% exceedance in 250 years. The design spectra include near-field directivity effects. The soil is soft in the area of South Temple Bridge and both the Wasatch and West Valley fault zones are aligned in the North-South direction, suggesting that directivity effects are potentially important at the longer periods. More information on the generation of these spectra is given in the new I-15 design study by Dames and Moore (1996).

The following spectral accelerations are thus obtained for the three recurrence intervals:
(a) 10% exceedance in 50 years, spectral acceleration $S_a = 0.563g$
(b) 10% exceedance in 100 years, spectral acceleration $S_a = 1.000g$
(c) 10% exceedance in 250 years, spectral acceleration $S_a = 1.667g$.
For an equivalent single-degree-of-freedom (SDOF), S_d, the spectral displacement can be obtained from the expression:

$$S_d = \frac{S_a T^2}{4\pi^2} \tag{9.2}$$

For the period derived above the implication is that the displacement demand on the As-built Bent #5 is as follows:
(a) 10% exceedance in 50 years, spectral displacement $S_d = 1.98$ in. (50 mm)
(b) 10% exceedance in 100 years, spectral displacement $S_d = 3.52$ in. (89 mm)
(c) 10% exceedance in 250 years, spectral displacement $S_d = 5.87$ in. (149 mm)

The Caltrans *Seismic Design Criteria* (Caltrans 1999), for multi-column Bents for newly constructed bridges suggest a maximum displacement ductility demand for design equal to $\mu_D = 5$. Bearing in mind that the as-built Bent was built in 1963, one expects that the displacement ductility would not meet these criteria; indeed the in-situ test showed that the displacement ductility of the as-built Bent 5 was $\mu_D = 2.8$. On the other hand, the retrofitted Bent 6 demonstrated a displacement ductility equal to $\mu_D = 6.3$, which actually exceeds the Caltrans requirements for new bridges.

The force reduction factor, or R factor, commonly used in design is defined in the *Seismic Retrofitting Manual* (FHWA 1995) as

$$R = 1 + 0.67(\mu_D - 1)\frac{T}{T_0} \le \mu_D \tag{9.3}$$

where T_0 = period corresponding to peak spectral response for the site. For long-period structures, $R = \mu_D$ is appropriate, implying an "equal displacement" approach. For shorter period structures, such as the present one, the "equal energy" approach is appropriate and

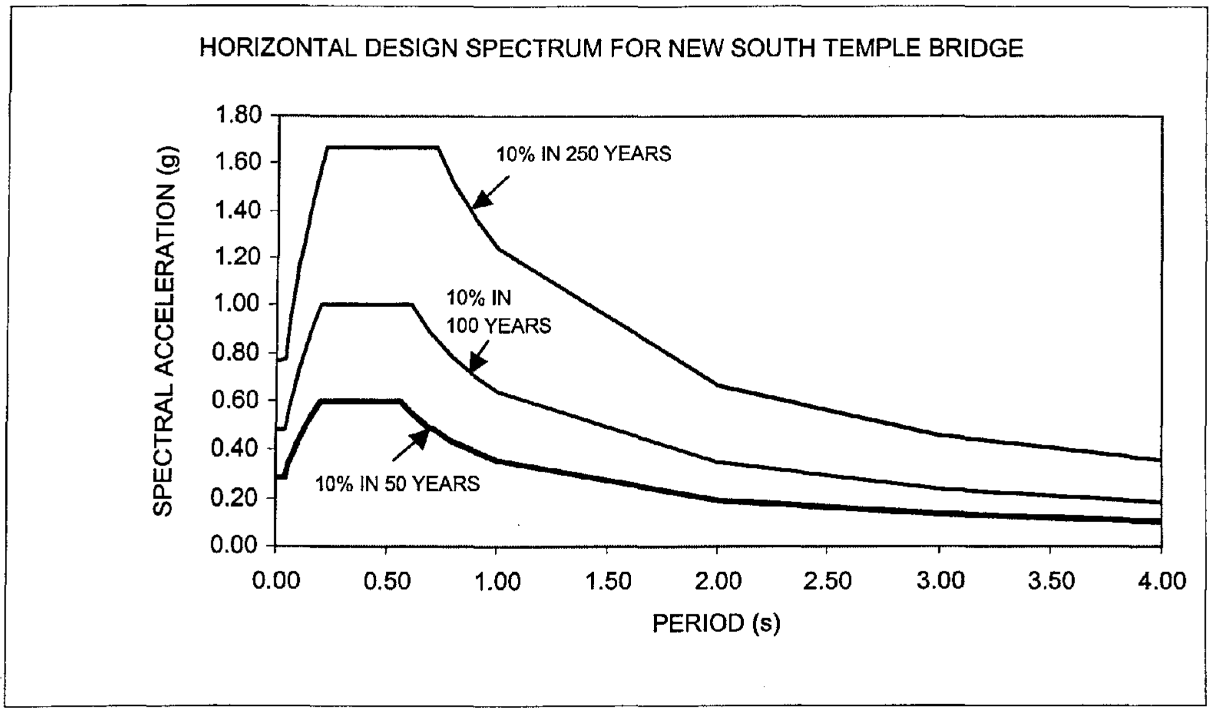

Figure 152. Design spectra for new I-15 Bridges

equation (9.2) is applicable. Here, the ratio T/T_0 is not readily obtained from the spectral acceleration curves since in the peak spectral response range the spectral acceleration has a flat portion in the short periods. For the current period of 0.6 s, using a ratio of $T/T_0 = 1$ is conservative for the 10% in 50 years earthquake, and the 10% in 100 years earthquake, and essentially correct for the 10% in 250 year earthquake design spectrum. Using a single-degree-of-freedom approximation, the reduced lateral forces are obtained for each design spectrum as follows for the as-built Bent 5:

$$V_{red} = \frac{S_a W_{Tr}}{R} \tag{9.4}$$

The reduced lateral forces for the three design spectra are shown in Table 1 for the As-built Bent #5. In addition, assuming an "equal energy" approach, the elastic displacements obtained from equation (9.2) must be increased to represent the elastoplastic system by an amount:

$$R_D = \frac{\mu_D}{\sqrt{2\mu_D - 1}} \tag{9.5}$$

The elastoplastic displacements of the equivalent SDOF systems are obtained as:

$$D_{ep} = R_D S_d \tag{9.6}$$

and are shown in Table 9.1.

Table 9.1. Reduced lateral forces and elastoplastic displacements for As-built Bent #5

Design Spectrum	**R Factor**	**Force kip (kN)**	**R_D Factor**	**Displacement in. (mm)**
10% in 50 Years	$2.2<\mu_D=2.8$	263 (1170)	1.2	2.38 (60)
10% in 100 Years	$2.2<\mu_D=2.8$	466 (2073)	1.2	4.22 (107)
10% in 250 Years	$2.2<\mu_D=2.8$	777 (3456)	1.2	7.04 (179)

From the capacity curve as shown in the hysteresis curve for Bent #5 the lateral force capacity is 337 kip (1500 kN) and the lateral displacement is 5.9 in. (150 mm). Therefore, as far as the bent's capacity, it is expected that the As-built Bent #5 will survive the 10% in 50 years earthquake, it will sustain damage if the 10% in 100 years earthquake occurs, and would probably collapse if the 10% in 250 years earthquake occurs.

A similar analysis is carried out for Bent #6. As can be observed from the hysteresis curves for Bent #5 and #6, there is not an appreciable increase in stiffness or weight in terms of the two bents, therefore the period is the same. Using equations (9.3) – (9.6), Table 9.2 for Bent #6 is obtained.

Table 9.2. Reduced lateral forces and elastoplastic displacements for Rehabilitated Bent #6

Design Spectrum	**R Factor**	**Force kip (kN)**	**R_D Factor**	**Displacement in. (mm)**
10% in 50 Years	$4.55<\mu_D=6.3$	127 (565)	1.85	3.66 (93)
10% in 100 Years	$4.55<\mu_D=6.3$	225 (1001)	1.85	6.51 (165)
10% in 250 Years	$4.55<\mu_D=6.3$	376 (1672)	1.85	10.86 (276)

From the capacity curve as shown in the hysteresis curve for Bent #6 the lateral force capacity is 437 kip (1943 kN) and the lateral displacement is 10.5 in. (267 mm). Therefore, as far as the bent's capacity, it is expected that the Retrofitted Bent #6 will survive the 10% in 50 years earthquake, the 10% in 100 years earthquake, and the 10% in 250 years earthquake with some damage due to large displacements. However, it is expected that even in this event the bridge will be functional and will carry the gravity loads, as was demonstrated in the in-situ tests.

Columns

Shear strength

According to the *Seismic Retrofitting Manual* (FHWA 1995) shear strength may be based on the following relationship for rectangular sections:

$$V_n = v_c A_e + A_v f_y \frac{d}{s} \cot\theta + 0.2P \tag{9.7}$$

where the first term is due to concrete shear-resisting mechanisms, the second term is due to shear carried by truss mechanisms, and the third term is the shear carried by axial compression.

The effective area $A_e = 0.8\ A_g$, for non-ductile regions

$$v_c = 3.5\sqrt{f_c^{'}}$$

and for plastic hinges with curvature ductility more than 4, which is the case here

$$v_c = 1.2\sqrt{f_c^{'}}$$

Using equation (7) results in the following calculated shear forces in the column:

(a) Non-ductile regions:
$V_n = 3.5\ (5{,}700)^{0.5} \times 0.8\ (36)^2 + 0.2\ (48{,}500)\ (36-3.5-.5-1.27/2)/12\ (1) + 0.2\ (545{,}000/3)$
$V_n = 336$ kip (1,494 kN)

(b) Within plastic hinge:
$V_n = 1.2\ (5{,}700)^{0.5} \times 0.8\ (36)^2 + 0.2\ (48{,}500)\ (36-3.5-.5-1.27/2)/12\ (1) + 0.2\ (545{,}000/3)$
$V_n = 156$ kip (694 kN)

On the other hand, the Caltrans *Seismic Design Criteria* (Caltrans 1999) specify that for new construction the column shear capacity is as follows:

$$V_n = V_c + V_s \quad ; \quad V_c = v_c \times A_e \tag{9.8}$$

The effective area $A_e = 0.8\ A_g$, and the concrete contribution is defined as follows:

(a) outside the plastic hinge zone

$$v_c = 3x Factor\ 2\ x\sqrt{f_c^{'}} \le 4\sqrt{f_c^{'}} \quad ; \quad Factor\ 2 = 1 + \frac{P_c}{2000A_g} < 1.5 \tag{9.9}$$

(b) inside the plastic hinge zone

$$v_c = Factor\ 1\ x\ Factor\ 2\ x\sqrt{f_c'} \le 4\sqrt{f_c'} \quad ; \quad Factor\ 1 = 0.3 \le \frac{\rho_s f_{yh}}{150} + 3.67 - \mu_D < 3 \tag{9.10}$$

The steel contribution is defined as: $V_s = A_v f_y d/s$. Using the Caltrans equations yields:

(a) outside the plastic hinge region:

$V_n = 3 \text{ x } [1+(545{,}000/3)/(2{,}000\text{x}36\text{x}36)] \text{ x } (5{,}700)^{0.5} \text{ x } 0.8\ (36)^2 + 0.2 \text{ x } 48{,}500 \text{ x } 31.365/12$
$V_n = 251 + 25 = 276$ kip (1228 kN)

(b) inside the plastic hinge region:

$V_n = [(4 \text{ x } 0.2/29\text{x}12) \text{ x } 48{,}500/150 + 3.67 - 2.8] \text{ x } [1+(545{,}000/3)/(2{,}000\text{x}36\text{x}36)]$
$\quad \text{x } (5{,}700)^{0.5} \text{ x } 0.8\ (36)^2 + 0.2 \text{ x } 48{,}500 \text{ x } 31.365/12$
$V_n = 135 + 25 = 160$ kip (712 kN)

It can be seen that the shear inside the plastic hinge region controls. The largest applied shear in the plastic hinge region during the test for Bent #5 was approximately 106 kip in the middle column, which is less than 156 kip. For Bent #6 the shear during the test was approximately 137 kip in the middle column, a figure that is close to 90% of the capacity. However, it should be noted that the additional FRP composite layers in the plastic hinge region added sufficient shear strength that shear failure was not a major concern during the tests.

Plastic hinge length

The analytical plastic hinge region in the Caltrans *Seismic Design Criteria* (Caltrans 1999) is defined as :

$$L_p = 0.08\,L + 0.15\,f_{ye}\,d_{bl} \ge 0.3\,f_{ye}\,d_{bl} \tag{9.11}$$

The corresponding expression from the *Seismic Retrofitting Manual* (FHWA 1995) is:

$$L_p = 0.08\,L + x\,d_{bl} \tag{9.12}$$

where $x = 6$ for Grade 40 rebar and $x = 9$ for Grade 60 rebar. As can be seen the two expressions are identical, equation (9.11) allowing a little more accuracy when f_{ye} is known with more precision. The analytical plastic hinge length is calculated as:

$L_p = 0.08\ (288/2) + 0.15\ (48.5)\ 1.27 = 20.8$ in.

From the in-situ test evidence, it was observed that the plastic hinge was located on the top of the middle column, on average 20 in. below the bottom face of the beam cap, as evidenced by the crack pattern.

Anchorage of longitudinal reinforcement

The longitudinal column bars extended all the way and into the footing and the beam cap for a certain distance. From in-situ measurements after the test, the extension of the column bars into the beam cap was equal to 34 in. (864 mm), and the extension of the column bars into the beam cap was 24 in. (607 mm). According to the *Seismic Retrofitting Manual* (FHWA 1995), the required effective anchorage length is:

$$l_a(d) = \frac{K_S d_b}{(1 + 2.5c/d_b + K_{tr})\sqrt{f_c'}} \geq 30d_b \tag{9.13}$$

where K_S = (48,500-11,000)/4.8 = 7813 psi; d_b = bar diameter =1.27 in.; c = lesser of the clear cover of the bar, or half the clear spacing between adjacent bars, here c = 2.71 in.; and K_{tr} = a function of the area of transverse reinforcing normal to potential splitting cracks, which for the present case is equal to zero, since no such reinforcement existed. Thus, the required effective anchorage length is:

$l_a(d) = (7813 \times 1.27)/(1+2.5 \times 2.71/1.27)\ (5700)^{0.5} = 20.8$ in. (528 mm) or

$l_a(d) = 30\ (1.27) = 38.1$ in. (968 mm) (controls)

Since the length provided into the beam cap was only 34 in. (864 mm), there is an anchorage failure, which was actually evidenced by bars pulling out from the concrete in the joint region of the beam cap. In the footing region, large radial cracks were observed and after demolition it was evident that bar pullout had occurred, which is justified by the fact that the 24 in. (607 mm) anchorage length provided is less than the required length of 38.1 in. (968 mm). The Caltrans *Seismic Design Criteria* (Caltrans 1999) do not apply here, since joint shear reinforcement requirements are not met.

As far as the pile-to-footing anchorage is concerned, the four Dywidag bars that were used were able to prevent pullout of the piles from the footing.

Splices in longitudinal reinforcement

It is well known that in areas of flexural yielding, columns with spliced reinforcement in the yielding zone may be subject to a rapid loss of flexural strength at the splice, unless closely spaced transverse reinforcement is provided. The key to preventing a splice failure is the presence of sufficient, closely spaced transverse reinforcement that will prevent initiation of splitting. The minimum area of transverse reinforcement required to prevent a splice failure is given in the *Seismic Retrofitting Manual* (FHWA 1995) as :

$$A_{tr}(d) = \frac{s f_y}{l_s f_{yt}} A_b \tag{9.14}$$

where s = spacing of transverse reinforcement = 12 in.; l_s = splice length = 25 in.; f_y , f_{yt} = yield stress of longitudinal and transverse reinforcement respectively = 48,500 psi; and A_b = area of spliced bar = 1.27 in^2. The required area is thus, $A_{tr}(d)$ = 0.61 in^2. (394 mm^2); the area provided is 0.2 in^2. (129 mm^2), which is much less than what is required.

According to the *Seismic Retrofitting Manual* (FHWA 1995), the clear spacing between spliced bars should not be more than 4 d_b = 4 x 1.27 = 5.08 in. (129 mm). Here, the clear spacing between bars is = 6.6825-1.27 = 5.41 in. (137 mm), which violates the requirement. In addition, the splice length should not be less than 1860 d_b $(f'_c)^{0.5}$ = 1860 (1.27)/(5,700)$^{0.5}$ = 31.3 in. (795 mm). Here, the splice length at the column – footing interface was only 25 in. (635 mm), which again violates the requirements. The Caltrans *Seismic Design Criteria* (Caltrans 1999) do not apply here, since splicing of flexural reinforcement is not permitted in critical regions of ductile elements. Evidence of lap splice failure was observed in all three tests.

Beam Cap

According to the *Seismic Retrofitting Manual* (FHWA 1995), the shear strength of the beam cap can be estimated by the expression identical to equation (9.8), where the concrete stress is :

$$v_c = (0.85 + 120\rho_\omega)\sqrt{f_c'} \le 2.4\sqrt{f_c'} \tag{9.15}$$

where ρ_ω=longitudinal tension steel ratio = 10 x 1.27 / (36 x 43.47) = 0.8%. The effective area is again 80% of the gross area of the cross-section. Hence, v_c = (0.85+120 x 0.008) (5,700)$^{0.5}$ = 137 psi (945 kPa); V_c = 0.8 (36) (48) (137) = 189 kip (841 kN). The contribution of the steel is given as : $V_s = A_v f_y d/s$ = 0.31 (48,500) (43.47)/11 = 59 kip (262 kN). Therefore, the nominal shear capacity is V_n = 189 + 59 = 248 kip (1103 kN). The shear obtained in the beam cap near the middle joint, during the in-situ test of Bent #5 was 160 kip (712 kN); during testing of Bent #6 the shear was 207 kip (921 kN), which is 84% of the capacity. However, it should be noted that FRP composite straps were used to resist additional shear in the beam cap near the joints, and therefore shear failure of the beam cap was prevented.

Beam Cap-column Joints

After the 1989 Loma Prieta earthquake, joint damage to several bridges indicated the real potential and possible collapse from this source. Diagonal cracks begin to develop when the principal tension stress exceeds 3.5 $(f'_c)^{0.5}$ = 3.5 (5,700)$^{0.5}$ = 264 psi (1820 kPa). The in-situ tests have shown that for Bent #5 the principal tensile stress was 287 psi (1979 kPa), and for Bent #6 it was 392 psi (2703 kPa). Therefore in both cases diagonal cracks were developed as seen in earlier photographs. However, it should be noted that Bent #6 had the FRP composite retrofit which was designed to pick up the difference in tensile stress from 392 psi (2703 kPa) to 287 psi (1979 kPa), i.e. it was designed to resist 105 psi (724 kPa) in tension.

According to the *Seismic Retrofitting Manual* (FHWA 1995), the shear capacity of the joint is :

$$V_{jh} = v_{cj}\, b\, h_c + A_{jh} f_y \tag{9.16}$$

$$v_{cj} = \sqrt{f_t (f_t - f_a)} \tag{9.17}$$

and where A_{jh} is the area of horizontal shear reinforcement between the top and bottom beam reinforcement in the joint region. In the present case, $A_{jh} = 0$ and the second term in equation (9.16) is equal to zero. For Bent #5, $f_t = 287$ psi (1979 kPa), $f_a = 86$ psi (593 kPa), and from equation (9.17) $v_{cj} = 240$ psi (1655 kPa). From equation (9.16), the shear capacity of the joint is $V_{jh} = 240\ (36)\ (36) = 311$ kip (1383 kN), which is less than the imposed shear demand of 337 kip (1499 kN). The FRP composite retrofit is used to compensate for the difference for Bent #6. The design of the FRP composite for strengthening the joint in shear was presented in section 7.

Overall performance

The performance of the three bents is evaluated by focusing on the envelopes of the experimentally obtained force-displacement relationships as shown in Fig. 153. It can be observed that the lateral load capacity of the rehabilitated Bent #6 was the highest, followed closely by that of the repaired bent. As Table 9.3 shows in detail, the ratio of the maximum lateral load to that of the as-built Bent #5 was 1.16 for Bent #6, and 1.15 for Bent #5R. The displacement ductility calculated using a bilinear model for the rehabilitated Bent #6 was 2.25 times the ductility of Bent #5, and the displacement ductility of the repaired Bent #5R was 1.43 times that of the as-built Bent #5. Another indicator of performance is the energy dissipated by the bent in each test. The rehabilitated Bent #6 and repaired Bent #5R showed exceptional energy disssipation due to the confinement provided by the carbon FRP composite. The ratios for Bent #6 and Bent #5R as compared to Bent #5 were 2.44 and 2.50, respectively. This is also described in more detail in Table 9.3, and Figs. 154 and 155. The beam cap–column joints were strengthened significantly by the application of the FRP composite. In the case of the rehabilitated Bent #6, the principal joint tensile stress was increased by a factor of 1.37, and that for the repaired Bent #5R was increased by a factor of 1.35. The joint shear strain was increased by a factor of 4.64 in the case of Bent #6 and a factor of 2.14 for Bent #5R.

A comparison of the theoretical pushover curve obtained from the DRAIN-2DX model and the actual hysteresis loops for Bent #5 and Bent #6 are shown in Fig. 156 and 157. It can be seen that the prediction for Bent #6 is very good, whereas the prediction for Bent #5 could be improved. More detailed models have been developed and are presented in a companion report (Cook, Lawton and Pantelides, 2000). It has been proven that the design goal of doubling the ductility of the as-built Bent #5 for the rehabilitated Bent #6 was met. Furthermore, even though Bent #5R was originally damaged, repair with FRP composites had restored the lateral load capacity and ductility and increased them by a considerable amount.

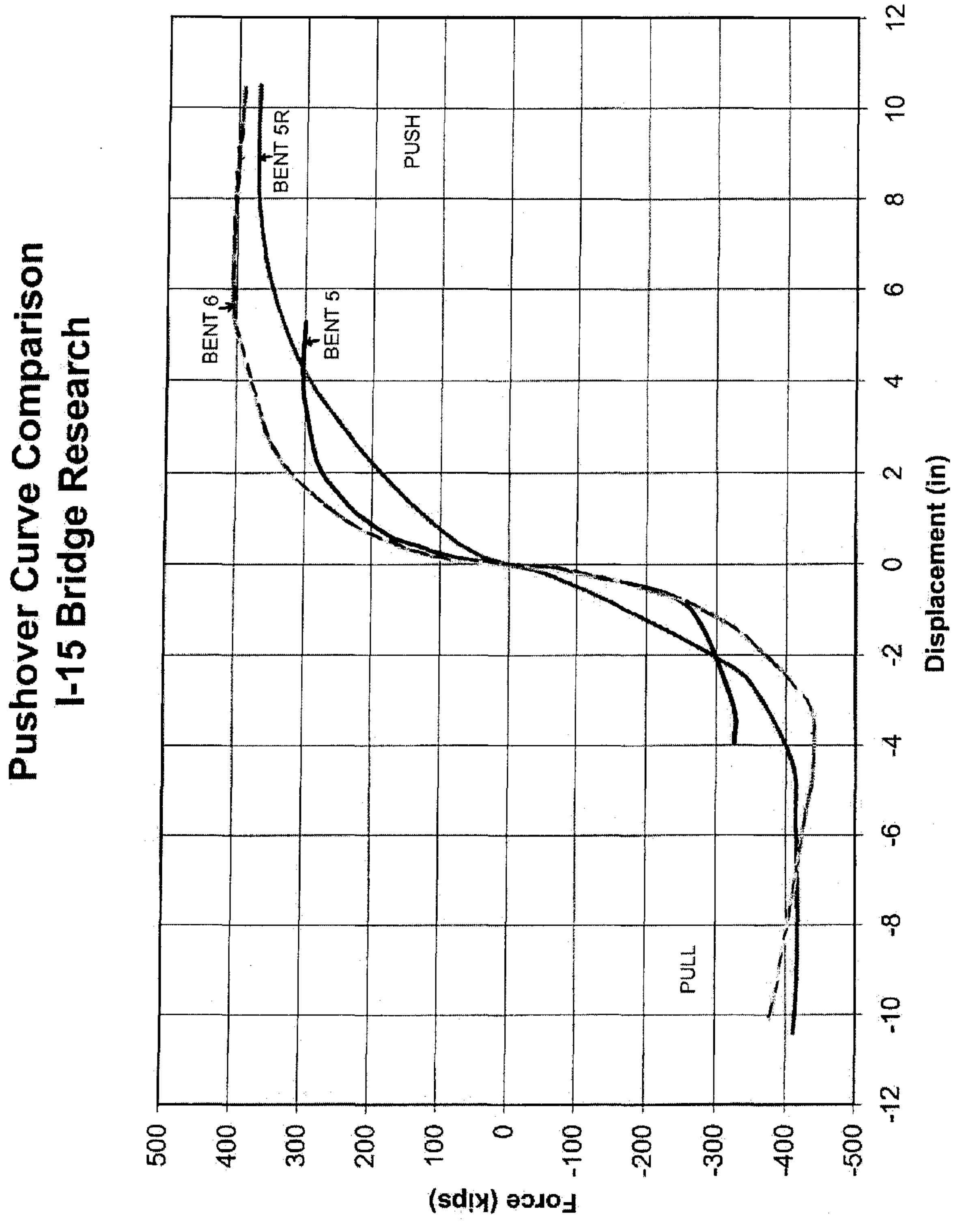

Figure 153. Comparison of envelopes of experimentally obtained lateral load-displacement relationship (1 kip = 4.448 kN, 1 in. = 25.4 mm)

Table 9.3. Performance comparisons between as-built, rehabilitated, and repaired bents

Quantity	**As-built Bent #5**	**Rehabilitated Bent #6**	**Repaired Bent #5R**	**Ratio of Bent #6 over Bent#5**	**Ratio of Bent #5R over Bent #5**
Displacement ductility	2.8	6.3	4.0	2.25	1.43
Lateral load capacity	315 kip (1401 kN)	364 kip (1619 kN)	361 kip (1606 kN)	1.16	1.15
Energy dissipation	18000 kip-in. 2034 kJ	38500 kip-in. 4350 kJ	45000 kip-in 5084 kJ	2.14	2.50
Principal joint tensile stress	$5.26(f'_c)^{0.5} psi$ $0.44(f'_c)^{0.5} MPa$	$7.20(f'_c)^{0.5} psi$ $0.60(f'_c)^{0.5} MPa$	$7.10(f'_c)^{0.5} psi$ $0.58(f'_c)^{0.5} MPa$	1.37	1.35
Joint shear strain	0.0028	0.0130	0.0060	4.64	2.14

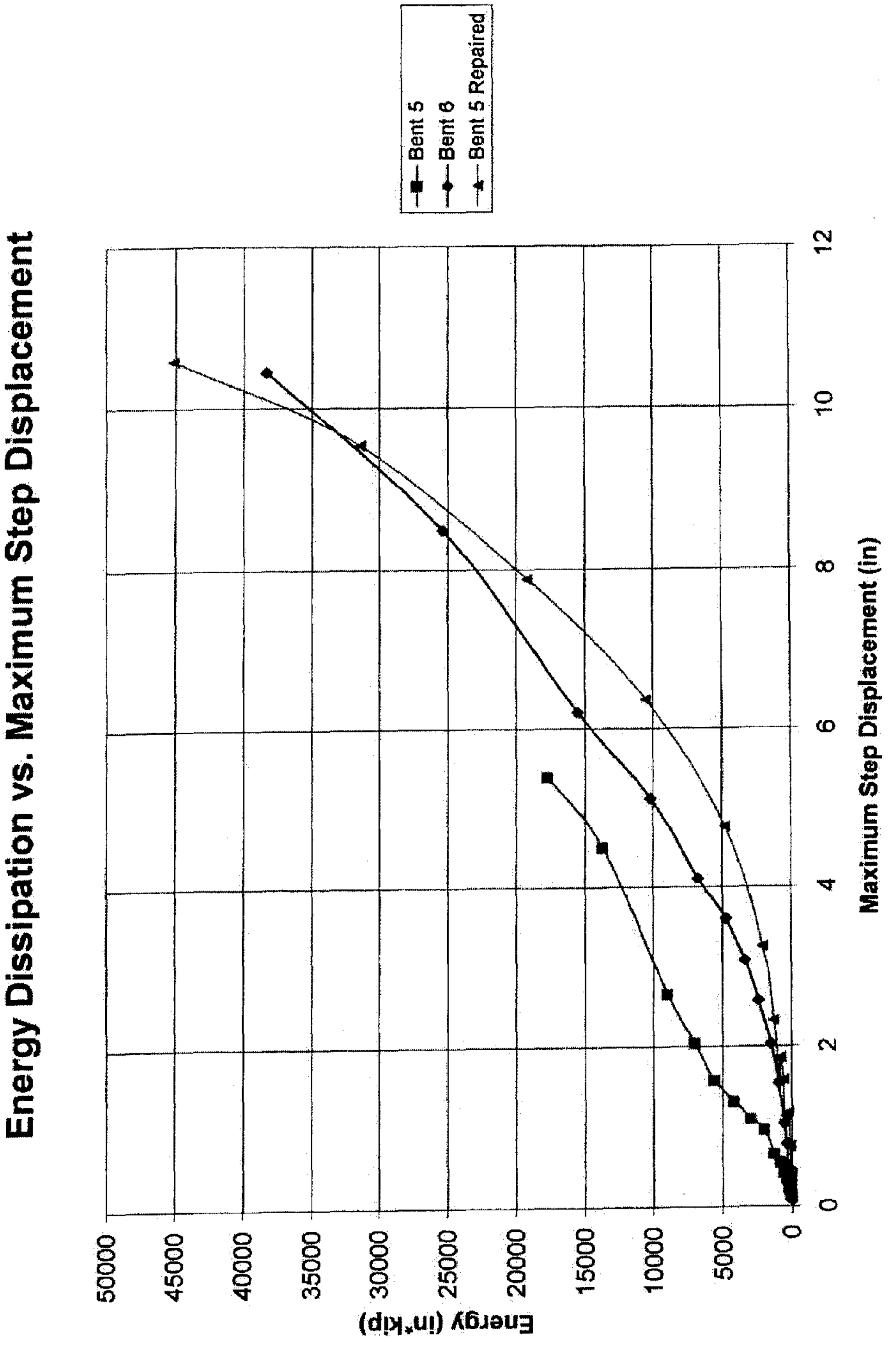

Figure 154. Comparison of dissipated energy versus maximum displacement
(1 kip-in. = 0.113 kJ, 1 in. = 25.4 mm)

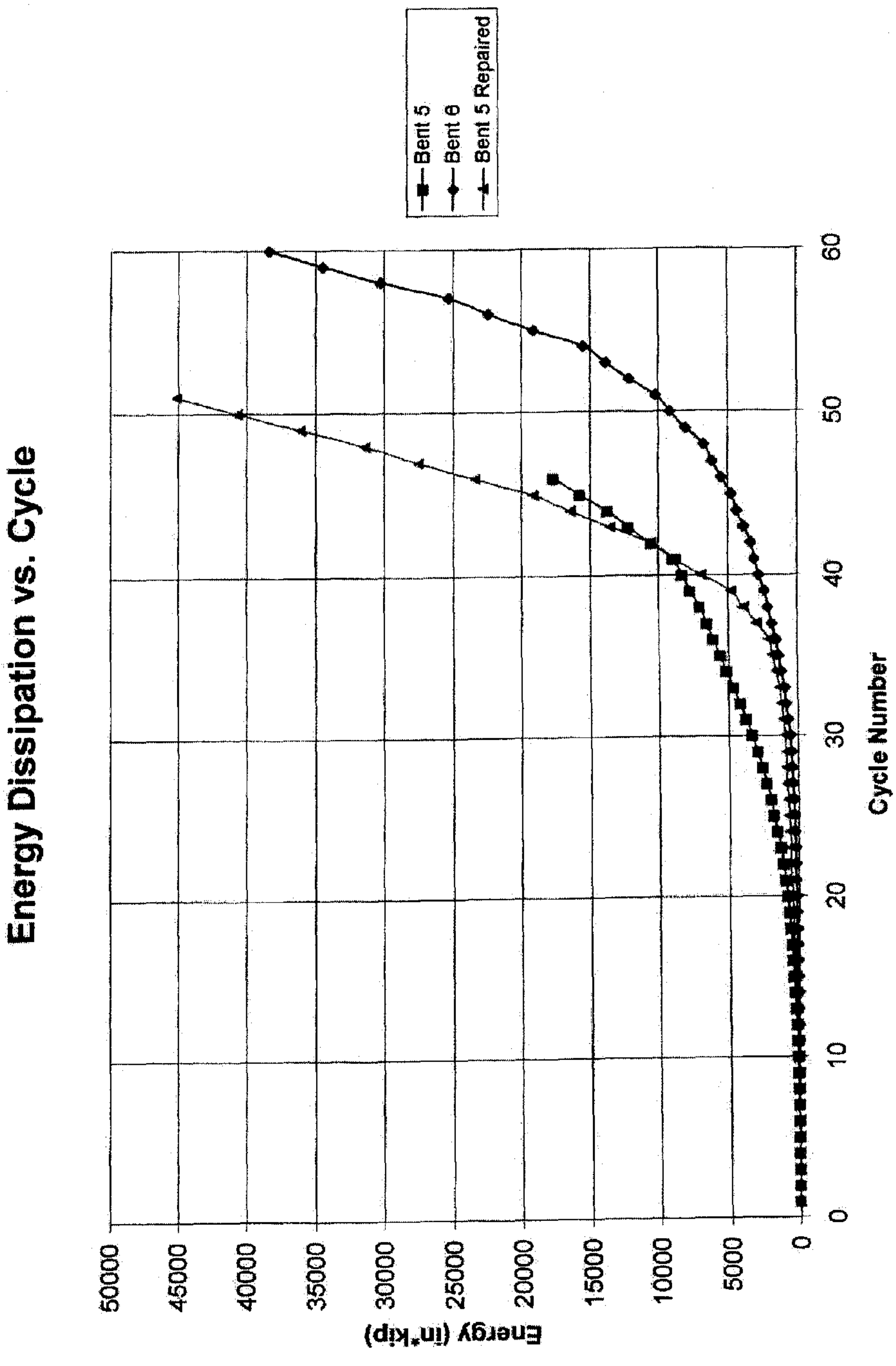

Figure 155. Comparison of dissipated energy versus cycle number
(1 kip-in. = 0.113 kJ, 1 in. = 25.4 mm)

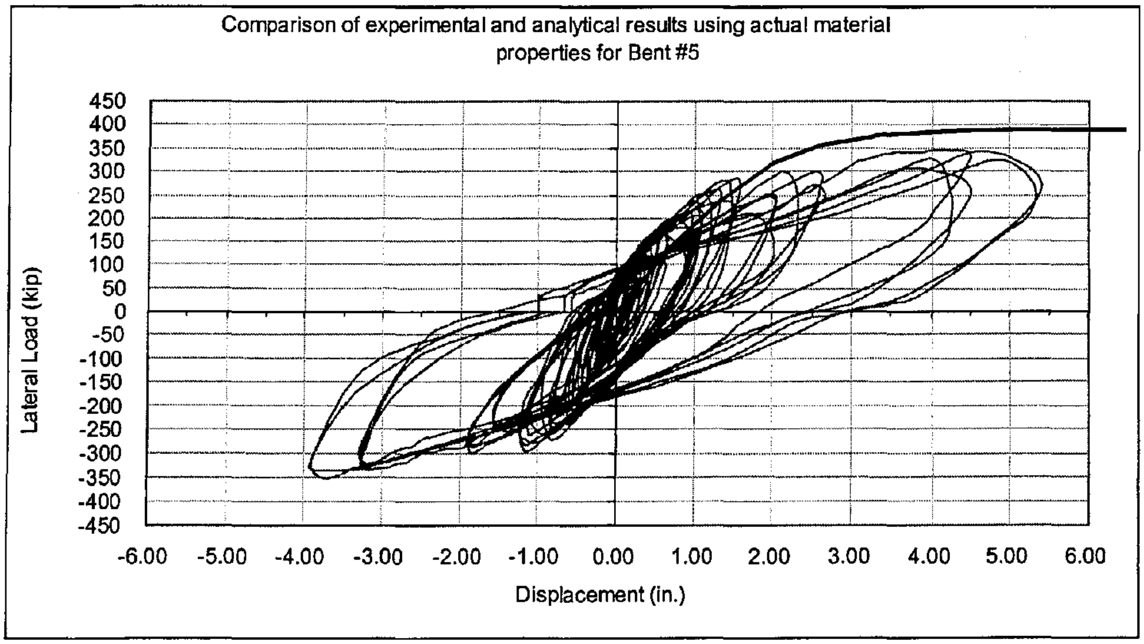

Figure 156. Comparison of experiment and analysis for Bent #5
(1 kip = 4.448 kN, 1 in. = 25.4 mm)

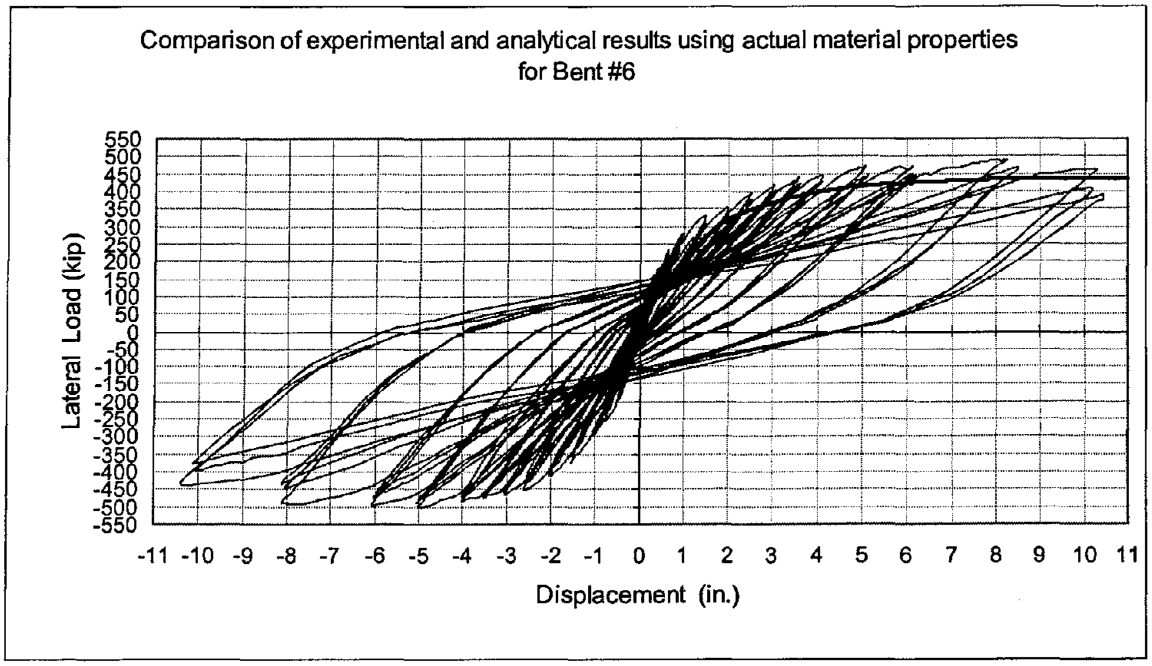

Figure 157. Comparison of experiment and analysis for Bent #6
(1 kip = 4.448 kN, 1 in. = 25.4 mm)

Conclusions

1. The lateral load and displacement capacity of the as-built Bent #5 was higher than expected due to redundancy and overstrength. In addition, the anchorage of the piles to the pile caps using epoxied high strength steel bars improved the performance which otherwise would not have been as good.

2. It is possible to design a seismic rehabilitation scheme using FRP composite materials to achieve a reasonable ductility increase. In the present case, a ductility increase of the performance of the as-built bent by a factor of 2 was set and it was achieved.

3. The loss of shear strength due to corrosion in the beam caps was of the order of 12 to 16 percent, which for the region adjacent to the column face was critical. However, the presence of double interior stirrups alleviates the problem to some extend.

4. The hysteretic behavior of the rehabilitated Bent #6 shows a substantial energy dissipation at a displacement ductility of 6.3, which reflects an increase by a factor of 2.25 compared to the as-is Bent #5; this is well above the target for the FRP composite design of doubling the displacement ductility. The lateral load capacity was also increased by a factor of 1.16. The dominant mode of failure of the FRP composite, was delamination from the concrete surface. However, the FRP composite U-straps over the beam cap failed in tension. Crack widths exceeded 6 mm in the beam cap to column interface.

5. The hysteretic behavior of the repaired Bent #5R shows a substantial energy dissipation at a displacement ductility of 4.0, which reflects an increase by a factor of 1.43 compared to the as-built bent. The lateral load capacity was also increased by 1.15. The dominant modes of failure of the FRP composite, were delamination from the concrete surface and tensile failure of the FRP composite U-straps. The vertical bars in the columns, near the joint had buckled, and crack widths in the concrete exceeded 6 mm.

6. The energy absorbed by the rehabilitated Bent #6 was substantially higher of that absorbed by the as-built Bent #5, by a factor of 2.14. The energy absorbed by the repaired Bent #5R was similarly higher compare to Bent #5, by a factor of 2.50. This reflects the increased capacity of both the rehabilitated and repaired bent to resist higher seismic demands as compared to the as-built bent.

7. The as-built Bent #5 had a principal tensile stress of $5.26\ (f'_c)^{0.5}\ psi$, or $0.44\ (f'_c)^{0.5}\ MPa$, which is higher than the stress predicted to cause joint degradation, i.e. $5\ (f'_c)^{0.5}\ psi$, or $0.42\ (f'_c)^{0.5}\ MPa$. The principal tensile stresses in the beam cap-column joint for the rehabilitated Bent #6 were higher than those of the as-built Bent #5 by a factor of 1.37. The principal tensile stresses in the beam cap-column joint for the repaired Bent #5R were higher than those of the as-built Bent #5 by a factor of 1.35. The joint shear strain in the as-built Bent #5 was at approximately 0.003. The joint shear strain in the rehabilitated Bent #6 was higher than that of the as-built Bent #5 by a factor of 4.56.

The joint shear strain in the repaired Bent #5R was higher than that of the as-built Bent #5 by a factor of 2.14.

8. The design spectra used in the design and construction of the new I-15 bridges were utilized to quantify the expected seismic demand for the 10 percent probability of exceedance earthquake for the 50 year, 100 year and 250 year event. A simplified analysis has shown that the rehabilitated Bent #6 would survive the 10 percent in 250 years earthquake with minor damage and the bridge would remain functional, largely due to the increased ductility provided by the FRP composite; on the other hand, the as-built Bent #5 would probably collapse in the 10 percent in 250 years earthquake, and sustain considerable damage in the 10 percent in 100 years earthquake.

9. Overall, it must be concluded that the FRP composite seismic retrofit was successful and it achieved its goals. In addition, the repair of a damaged bent using FRP composites actually improved the seismic performance to a level beyond the capacity of the bent in the as-built condition without FRP composites. This is significant because the results of this study show that even after an earthquake repair using FRP composites is possible and effective. Finally, it has also been demonstrated that traditional rehabilitation techniques, such as anchoring the piles to the pile cap using high strength steel bars, have to be considered along with the FRP composite rehabilitation in an effort to obtain a complete rehabilitation scheme.

10. Simple nonlinear pushover techniques were used to predict forces, displacements and stresses required for designing the FRP composite seismic retrofit. Moreover, the performance of the bents both with and without FRP composites during the tests was predicted in a satisfactory manner by nonlinear pushover techniques.

It is hoped that his report, along with the accompanying report on soil-structure interaction effects, will help engineers and transportation officials consider the use of FRP composite materials in actual seismic rehabilitation of bridges. Such an application is currently being implemented at the State Street Bridge on Interstate 80 in Slat Lake City.

REFERENCES

ACI 318 (1995). "ACI Committee 318. Building Code Requirements for Reinforced Concrete." (ACI 318-95). *Amer. Concr. Inst.,* Detroit, Mich.

ACI 352 (1991). "ACI Committee 352. Recommendations for Design of Beam-column Joints in Monolithic Reinforced Concrete Structures." (ACI 352R-91). *Amer. Concr. Inst.,* Detroit, Mich.

Alcocer, S.M., and Jirsa, O. (1993). "Strength of reinforced concrete frame connections rehabilitated by jacketing." *ACI Struct. J.,* 90(3), 249-261.

Arduini, M., and Nanni, A. (1997). "Behavior of precracked RC beams strengthened with carbon FRP sheets." *J. of Compos. for Constr.,* 1(2), 63-70.

ASTM (1996). "ASTM D 3039. Standard Test Method for Tensile Properties of Polymer Matrix Composite Materials." *Amer. Soc. For Test. Mater.* D3039/D 3039 M-95a.

Biddah, A., Ghobarah, A., and Aziz, T.S. (1997). "Upgrading of nonductile reinforced concrete frame connections." *J. Struct. Engrg.*, ASCE, 123 (8), 1001-1010.

Bollo, M.E., Mahin, S.A., Moehle, J.P., Stephen, R.M. and Qi, X. (1990). "Observations and implications of tests on the Cypress Street viaduct test structure." *Report No. UCB/EERC-90/21,* Univ. of Calif., Berkeley, Calif.

Buckle, I.G, Richardson, J.A., and Sveinsson, B.I. (1989). "Vertical response data from the Dominion Road bridge test", *Seismic Engineering:Research and Practice, ASCE Struct. Congress '89,* C.A. Kircher and A.K. Chopra, eds., San Francisco, Calif., 41-50.

California Department of Transportation (1999). "Caltrans Seismic Design Criteria – Version 1.1", California Department of Transportation, Engineering Service Center, Sacramento, Calif.

Chajes, M.J., Januszka, T.F., Mertz, D.R., Thomson, T.A., Jr., and Finch, W.W., Jr. (1995). "Shear strengthening of reinforced concrete beams using externally applied composite fabrics." *ACI Struct. J.,* 92(3), 295-303.

Computers and Structures, Inc. (1998). "SAP 2000 Three dimensional static and dynamic finite element analysis and design of structures", Berkeley, Calif.

Cook, C., Lawton, E. C., and Pantelides, C.P., (2000). "Soil structure-interaction effects on bridge bent tests at South Temple Bridge on Interstate 15", Research Report CVEEN 00-02, July 2000.

Dames and Moore (1996). “Seismic Hazard Analysis of the I-15 Corridor: 10600 South to 500 North, Salt Lake County, Utah”, Final Report prepared by Dames & Moore, Inc., Salt Lake City, September, 1996.

Douglas, B.M., and Reid, W.H. (1982). "Dynamic tests and system identification of bridges." *J. Struct. Engrg.,* ASCE 108(10), 2295-2312.

Douglas, B.M., Maragakis, E.A., and Nath, B. (1990). "Static deformations of bridges from quick-release dynamic experiments." *J. Struct. Engrg.,* ASCE 116(8), 2201-2213.

Eberhard, M.O., Marsh, M.L., O’Donovan, T., and Hjartarson, G. (1992). "Lateral-load tests of reinforced concrete bridge." *Transp. Res. Record No. 1371-* Bridge, Culvert and Tunnel Research, Nat. Res. Council, Washington, D.C., 92-100.

Federal Emergency Management Agency (1997). "NEHRP Guidelines for the Seismic Rehabilitation of Buildings." *FEMA 273 and FEMA 274*, Washington, D.C.

Federal Highway Administration (1995). “ Seismic retrofitting Manual for Highway Bridges”, U.S. Dept. of Transportation , Publication No. FHWA-RD-94-052, McLean, Virginia.

Gamble, W.L., and Hawkins, N.M. (1996). “Seismic retrofitting of bridge pier columns.” *Proc. Struct. Congress XIV*, ASCE, Vol. 1, 16-23, Chicago, Ill.

Gergely, I., Pantelides, C.P., Nuismer, R.J., and Reaveley, L.D. (1998). “Bridge pier retrofit using fiber-reinforced plastic composites.” *J. of Compos. for Constr.,* ASCE, 2(4), 165- 174.

Gergely, I., Pantelides, and Reaveley, L.D. (2000). “Shear strengthening of R/C T-joints using CFRP composites.” *J. of Compos. for Constr.,* ASCE, 4(2), 56-64.

Lawton, E.C., Fox, N.S., and Handy, R.L. (1994). "Control of settlement and uplift of structures using short aggregate piers." *ASCE Geotechnical Spec. Publ. SP-45, In-situ deep soil improvement,* 121-132.

Lowes, L.N., and Moehle, J.P. (1995). “Seismic behavior of retrofit of older reinforced concrete bridge T-joints.” *Rep. No. UCB/EERC-95/09,* Univ. of California, Berkeley, Calif.

Malek, A.M., and Saadatmanesh, H. (1998). "Ultimate shear capacity of RC beams strengthened with web-bonded FRP plates." *ACI Struct. J.,* 95(4), 391-399.

Norris, T., Saadatmanesh, H., and Ehsani, M.R. (1997). "Shear and flexural strengthening of R/C beams with carbon fiber sheets." *J. Struct. Engrg.*, ASCE, 123 (7), 903-911.

Pantelides, C. P., Gergely, I., Reaveley, L. D., and Nuismer, R. J. (1997). "Rehabilitation of cap beam-column joints with carbon fiber jackets." *Proc. of the Third Intern. Symp. on Non-Metallic (FRP) Reinforcement for Concrete Structures*, Sapporo, Japan, Vol. 1, 587-595.

Pantelides, C.P., and Reaveley, L.D. (1999). "In-Situ tests at South Temple Bridge on Interstate 15 – *Construction Report*", Research Report UUCVEEN 99-01, Feb. 1999, pp. 78.

Pantelides, C. P., Gergely, I., and Reaveley, L. D. (1999a). "Advanced composite retrofit design for R/C bridges." *Proc. of the Transportation Research Board 78th Annual Meeting*, Washington, D.C., Jan. 10-14, 1999.

Pantelides, C.P., Gergely, J., Reaveley, L.D., and Volnyy, V.A. (1999b). " Retrofit of R/C bridge pier with CFRP advanced composites." *J. Struct. Engrg.*, ASCE, 125(10), 1094-1099.

Prakash, V., Powell, G.H., and Filippou, F.C. (1992). "DRAIN-2DX Base Program User Guide." *Rep. No. UCB/SEMM-92/29,* Univ. of California, Berkeley, Calif.

Priestley, M.J.N., Seible, F., and Calvi, G.M. (1996). *Seismic Design and Retrofit of Bridges.* John Wiley & Sons, Inc., New York.

Priestley, M.J.N., Seible, F., MacRae, G.A., and Chai, Y.H. (1997). "Seismic assessment of the Santa Monica viaduct bent details." *ACI Struct. J.,* 94(5), 513-524.

Roberts, J.E. (1999). "Impact of Loma Prieta earthquake on seismic design of concrete bridges-California perspective", ACI International SP-187, *Seismic Response of Concrete Bridges*, ed. Krishnan, K., Farmington Hills, MI, SP 187-1, 1-16.

Saadatmanesh, H., and Ehsani, M.R. (1991). "RC beams strengthened with GFRP plates: experimental study." *J. Struct. Engrg.,* ASCE, 117(11), 3417-3433.

Saiidi, M., and Douglas, B.M. (1984). "Effect of design seismic loads on a highway bridge." *J. Struct. Engrg.*, ASCE, 110 (11), 2723-2735.

Seible, F., Hegemier, G., Priestley, M.J.N., Innamorato, D., Weeks, J., and Policelli, F. (1994). "Carbon fiber jacket retrofit test of shear bridge column, CRC-2." *Rep. No. ACTT-94/02,* Univ. of California, San Diego, La Jolla, Calif.

Seible, F., Priestley, M.J.N., Hegemier, G., and Innamorato, D. (1997). "Seismic retrofitting of RC columns with continuous carbon fiber jackets." *J. of Compos. for Constr.,* ASCE, 1(2), 52-62.

Seible, F., and Priestley, M.J.N. (1999). "Lessons learned from bridge performance during the Northridge earthquake", ACI International SP-187, *Seismic Response of Concrete Bridges*, ed. Krishnan, K., Farmington Hills, MI, SP 187-3, 29-55.

Sexsmith, R., Anderson, D., and English, D. (1997). "Cyclic behavior of concrete bridge bents." *ACI Struct. J.,* 94(2), 103-113.

Swamy, R.N., and Gaul, R. (1996). "Repair and strengthening of concrete members with adhesive bonded plates." *ACI Publ. SP-165,* Detroit, Mich.

Taylor, A.W. (1999). "Performance of reinforced concrete bridges in January 1995 Hyogoken Nanbu (Kobe) earthquake", ACI International SP-187, *Seismic Response of Concrete Bridges*, ed. Krishnan, K., Farmington Hills, MI, SP 187-4, 57-67.

Triantafillou, T.C. (1998). "Shear strengthening of reinforced concrete beams using epoxy-bonded FRP composites." *ACI Struct. J.*, 95(2), 107-115.

Zelinski, R. (1999). "Northridge earthquake influence on bridge design code", ACI International SP-187, *Seismic Response of Concrete Bridges*, ed. Krishnan, K., Farmington Hills, MI, SP 187-2, 17-28.

PB2001-101840

REPORT DOCUMENTATION PAGE

Form Approved
OMB No. 0704-0188

1. AGENCY USE ONLY (Leave Blank)	**1. REPORT DATE** July 2000	**1. REPORT TYPE AND DATES COVERED** Research

2. TITLE AND SUBTITLE

Seismic Rehabilitation of Concrete Bridges: Verification Using In-Situ Tests at South Temple Bridge on Interstate 15

2. FUNDING NUMBERS

3. AUTHOR(S)

Pantelides, C.P., Gergely, J., Marriott, N., and Reaveley, L.D.

4. PERFORMING ORGANIZATION NAMES(S) AND ADDRESS(ES)

University of Utah, Salt Lake City, Utah

3. PERFORMING ORGANIZATION REPORT NUMBER

UUCVEEN 00/1

5. SPONSORING/MONITORING AGENCY NAME(S) AND ADDRESS(ES)

NSF, FHWA, Utah Department of Transportation, Idaho National Engineering and Environmental Laboratory, University of Utah

4. SPONSORING/MONITORING AGENCY REPORT NUMBER

6. SUPPLEMENTARY NOTES

12a. DISTRIBUTION/AVAILABILITY STATEMENT

12b. DISTRIBUTION CODE

13. ABSTRACT (Maximum 200 words)

The report describes the results of three in-situ tests performed at the northbound lanes of the South Temple Bridge at Interstate 15 n Salt Lake City, Utah. The tests were performed on three reinforced concrete bents in 1998. The lateral load tests, simulating seismic excitations, were performed on: (a) a bent in the as-built condition, (b) a bent rehabilitated with Fiber Reinforced Polymer (FRP) composites, and (c) a repaired bent rehabilitated with FRP composites. The report includes the analysis and design of the FRP composite, experimental results for all three tests, and evaluation of the results and performance assessment. Overall, it is concluded hat the in-situ tests have confirmed that FRP composites are an effective method of improving the seismic performance of existing reinforced concrete bridges, which were not built to current seismic standards. In addition, FRP composites are effective for the repair of damaged bridges after an earthquake.

4. SUBJECT TERMS

14. NUMBER OF PAGES

15. PRICE CODE

5. SECURITY CLASSIFICATION OF REPORT None	**16. SECURITY CLASSIFICATION OF THIS PAGE**	**14. SECURITY CLASSIFICATION OF ABSTRACT**	**14. LIMITATION OF ABSTRACT**